

Feasibility studies on the production of new particles with preferential couplings to third generation fermions at the LHC

Cristian Fernando Rodríguez Cruz

August 24, 2025

CONTENTS

Contents	iii
INTRODUCTION	
1 STANDARD MODEL OF PARTICLE PHYSICS	1
1.1 Fields	3
1.2 Interactions and Symmetries	4
1.2.1 Example	6
1.3 Standard Model	7
1.3.1 Particle Content and Gauge Group	8
1.3.2 Gauge Bosons	10
1.3.3 Matter Fields	10
1.3.4 Electroweak Symmetry Breaking	11
1.4 Deficiencies of Standard Model and Evidence of New Physics	13
1.4.1 Theoretical problems	13
1.4.2 Cosmological problems	14
1.4.3 Phenomenological problems	15
2 PHENOMENOLOGICAL FRAMEWORK FOR LHC OBSERVABLES, SEARCHES AND ANALYSIS	17
2.1 Coordinate System and Collision Parameters	18
2.2 Detectors and Subsystems	20
2.2.1 Jets Reconstruction	21
2.2.2 τ Tagging at Multipurpose Detectors	23
2.2.3 B Tagging at Multipurpose Detectors	24
2.2.4 The CMS Detector	25
2.3 Phenomenological Pipeline	28
2.4 Measurement of the Power of an Analysis	28
3 BSM SIGNATURES IN DI-TAU FINAL STATES	31
3.1 A Simplified Model for the S_1 Scalar Leptoquark	31
3.2 A Simplified Model for the U_1 Vector Leptoquark	33
3.3 A simplified model for a Z'_{B-L} boson	40
3.4 Interference between the U_1 and Z'_{B-L} models	42
3.5 Single and Double Leptoquark Contributions	45
4 $U(1)_{T_R^3}$ GAUGE EXTENSION OF THE STANDARD MODEL	49
4.1 Experimental Considerations	50
4.2 The Minimal $U(1)_{T_R^3}$ Model	52
4.2.1 Scalar Potential	52
4.2.2 The Universal Seesaw Mechanism	53
4.2.3 Minimal UV-complete theory	54
4.3 Samples and Simulation	55
4.4 Data Analysis Using Machine Learning	59
4.5 Results	64
5 DISCUSSION AND RESULTS	71
5.1 U_1	71
5.2 Leptoquark	72
BIBLIOGRAPHY	73
PUBLICATIONS	83
On the sensitivity reach of vectorial leptoquark production with preferential couplings to third generation fermions at the LHC	85

INTRODUCTION

1

STANDARD MODEL OF PARTICLE PHYSICS

The standard model (SM) of particle physics is a quantum field theory (QFT) in which fundamental particles are excitations of interacting relativistic fields in the quantum vacuum (Greiner 2000). In this context, matter in nature is formed by particles that have a fermionic character, and their interactions are described by the gauge principle, where integer spin particles are defined as vector bosons, from the adjoint representation of a symmetry group (*gauge group*), are the messengers of the interaction (Pokorski 2000).

Specifically, the SM characterizes interactions through the gauge principle, where force-carrying particles (integer spin vector bosons) originate from the adjoint representation of symmetry groups (*gauge groups*) Pokorski 2000. This elegant formulation unifies three of the four fundamental forces in nature.

In this chapter, we contextualize the SM by introducing the basic concepts of quantum field theory, including the notion of fields and symmetries. We then present the particle content of the SM, its gauge group, and the Lagrangian density that describes its dynamics. Finally, we discuss the Higgs mechanism and its role in providing mass to the weak gauge bosons and fermions.

1.1 FIELDS

Relativistic quantum fields are degrees of freedom in QFT. Formally, they are *operator-valued functions of the spacetime that transform under a representation of the Lorentz group within an invariant subspace* (Tong 1995; Rodriguez 2018). The different representations of the Lorentz group are mainly characterized by their spin, and their fields obey a different equation of motion (see table 1.1).

In classical field theory, a variational principle is established which generates the equations that govern the dynamics of the different fields in a theory, *the equations of motion*. Hamilton's principle, or principle of minimal action, indicates that all possible physical configurations for a set of fields φ^I , with $I = 1, 2, 3, \dots, n$, are those where the integral of the action S is a minimal (Goldstein, Poole, and Safko 2001; José and Saletan 1998):

$$S = \int \mathcal{L}(\varphi^I, \partial_\mu \varphi^I) d^4x, \quad (1.1)$$

here, $d^4x = dx^0 dx^1 dx^2 dx^3$ and $x \equiv (ct, x^1, x^2, x^3) \equiv (x^0, x^1, x^2, x^3) \in \mathcal{M}^4$ are the space-time coordinates in the Minkowskian spacetime \mathcal{M}^4 , and the function $\mathcal{L}(\varphi^I, \partial_\mu \varphi^I)$ is called *the Lagrangian density* of a theory (Greiner 2000; Goldstein, Poole, and Safko 2001). The problem in classical field dynamics is to find the functions $\varphi^I(x)$ in a space-time \mathcal{M}^4 , fixing their boundary conditions. The solution to this classical problem is given by the Euler-Lagrange equations:

$$\frac{\partial \mathcal{L}}{\partial \varphi^I} - \frac{\partial}{\partial x^\mu} \frac{\partial \mathcal{L}}{\partial (\partial_\mu \varphi^I)} = 0, \quad (1.2)$$

and they are used to obtain the equations of motion of the set of fields φ^I (José and Saletan 1998).

In quantum field theory, the situation is more complicated: if we adopt the approach of quantization by path integrals (Martínez 2002; Weinberg 2005), the idea of an equation of motion vanishes and we go on to searching correlations between free particle states. However, the notion of action remains the cornerstone in the description of these observables. Explicitly, the correlation functions are calculated through the LSZ formula from the path integral (Walter Greiner 1996; Michael E. Peskin 1995):

$$\begin{aligned} Z[J] &= \langle \text{out}, 0 | 0, \text{in} \rangle \\ &= \mathcal{N} \int \mathcal{D}(\varphi, \bar{\varphi}) e^{iS[\varphi]} e^{i \int J_I \varphi^I d^4x} \\ &= \mathcal{N} \int \mathcal{D}(\varphi, \bar{\varphi}) e^{i \int d^4x \mathcal{L}} e^{i \int J_I \varphi^I d^4x}, \end{aligned} \quad (1.3)$$

taken over the space of fields φ with an appropriate measure $\mathcal{D}(\varphi, \bar{\varphi})$ and normalized by \mathcal{N} . The quantity Z is known as the partition function of the theory and gives the transition amplitude from the initial vacuum $|0, \text{in}\rangle$ to the final vacuum $|0, \text{out}\rangle$ in the presence of a source $J(x)$ producing particles (N. D. Birrell 1984). Therefore, the dynamics, at both the classical and quantum levels, in a theory are entirely determined by the Lagrangian density. Table 1.1 records the Lagrangian density for different types of free fields, i.e., non-interacting fields.

Name	Field	Spin	Free-Lagrangian
Klein-Gordón	ϕ	0	$\mathcal{L} = (\partial^\mu \bar{\phi} \partial_\mu \phi - m^2 \bar{\phi} \phi)$
Dirac	χ	1/2	$\mathcal{L} = \bar{\chi} (i \gamma^\mu \partial_\mu - m) \chi$
Maxwell	A^μ	1	$\mathcal{L} = -\frac{1}{4} F^{\mu\nu} F_{\mu\nu}$

Table 1.1: Some relevant representations of the Lorentz group in 4-dimensional space-time. In this notation $\eta_{\mu\nu} = \text{diag}(1, -1, -1, 1)$, γ^μ are the Dirac matrices, $F_{\mu\nu}^A = \partial_\mu A_\nu^A - \partial_\nu A_\mu^A + g f_{BC}^A A_\mu^B A_\nu^C$ is the strength field and the array of real numbers f_{AB}^C are the structure constants of the gauge group algebra (Freedman and Van Proeyen 2012), equations are written in natural units with $c = \hbar = 1$.

In this paradigm, our task is to propose a Lagrangian density for a set of fields that correctly models the propagation and interactions of fundamental particles.

1.2 INTERACTIONS AND SYMMETRIES

In quantum field theory, the form of the Lagrangian density is not arbitrary: it is shaped by a small set of physical and mathematical principles. These principles act as “rules” that guide the construction of consistent theories, ensuring both their internal consistency and their predictive power. In particular, if we want a relativistic and renormalizable theory, the Lagrangian must satisfy several conditions that strongly restrict the kind of terms that can appear.

To begin with, relativistic invariance demands that the equations of motion look the same in all inertial frames. This requirement is implemented by asking the action to be invariant under Poincaré transformations (Lahiri and Pal 2006). Equivalently, the Lagrangian density must transform as a Lorentz scalar and may change under translations at most by a total derivative (José and Saletan 1998).

Another basic condition is Hermiticity: the Lagrangian density must be Hermitian so that observables are real and the time evolution of the theory is unitary (Lahiri and Pal 2006; Michael E. Peskin 1995). In addition, dimensional analysis places further restrictions. In natural units, \mathcal{L} carries dimensions of [mass]⁴ (an energy density). This means that the interaction terms that we can add must be such that the overall operator has the correct dimension, which already rules out many possibilities.

In quantum field theory, loop corrections to scattering amplitudes typically produce divergences. A theory is called renormalizable if all these divergences can be absorbed into a redefinition of a *finite set* of physical parameters (such as masses and couplings). In practice, this requirement translates into a restriction on the operators that may appear in the Lagrangian: only terms of mass dimension ≤ 4 lead to renormalizable interactions. Higher-dimensional operators are still allowed, but they correspond to *effective* interactions that are suppressed at low energies and signal the presence of new physics at higher scales (Michael E. Peskin 1995; Weinberg 2005).

Summarizing, the main constraints that a relativistic and renormalizable Lagrangian density must satisfy are:

- **Poincaré (global) invariance:** the action must be invariant under Lorentz transformations and translations; the Lagrangian density is a Lorentz scalar and may change by at most a total derivative (Lahiri and Pal 2006; José and Saletan 1998).
- **Hermiticity:** \mathcal{L} must be Hermitian to ensure real observables and unitary evolution (Lahiri and Pal 2006; Michael E. Peskin 1995).
- **Mass dimension:** in natural units, \mathcal{L} has dimension [mass]⁴; interaction terms must be constructed accordingly.
- **Renormalizability:** demanding perturbative renormalizability restricts operators to dimension ≤ 4 , which in practice allows interactions built out of fields with spin 0, 1/2, or 1 and couplings of non-negative mass dimension (Michael E. Peskin 1995; Weinberg 2005).

In QFT, Poincaré invariance is assumed to be global. Promoting it to a local symmetry leads to gravity, with spin-2 fields (the graviton) as mediators. Perturbatively, such a theory is not renormalizable, so it lacks predictivity at high energies, although it can still be understood as an effective field theory.

These constraints drastically reduce the number of possible terms in the Lagrangian. As a result, the renormalizable interaction structures that typically arise are limited to: Yukawa couplings between fermions and scalars, scalar self-interactions (up to quartic order), and gauge interactions between matter fields and vector bosons.

At this point, we seem to have total freedom to mix these terms as possible interactions. However, the concept of symmetry has proven to be our most powerful ally for the construction of terms of interaction between fields. The procedure turns out to be simple; once a set of spin 0 and spin 1/2 fields has been established as part of the theory, these are organized to transform under a representation of a unitary gauge group G such that the Lagrangian density must be a global scalar of G . Then, once the global Lagrangian density is known, it is sought to “promote” symmetry to a local symmetry by a slight modification of associated kinematic terms (Pokorski 2000; Freedman and Van Proeyen 2012; Gallego 2016; Van Proeyen 1999; Martin 2012). This “promotion” is described in more detail below.

Given a Lagrangian density $\mathcal{L}(\varphi_i, \partial_\mu \varphi_i)$, a given field φ is said to be *globally symmetric* under unitary transformations, $\varphi_i \mapsto U_G(\varphi_i)$, if the action is invariant under the variations of the fields φ^I which are given, at infinitesimal level, by:

$$\delta_G(\theta)\varphi^I \approx i\theta^A(T_A)^I_J \varphi^J, \quad (1.4)$$

where θ^A are the parameters of the transformation \mathcal{U} and T_A are the representations of the generators of a unitary continuous group G . This considers an expansion of U at first order in θ^A . This group, G , supports unitary representations of the shape:

$$\mathcal{U}_G = U(\theta) = \exp(i\theta^A T_A). \quad (1.5)$$

The operators T_A satisfy a commutation relation according to the Lie algebra:

$$[T_A, T_B] = if_{AB}^C T_C, \quad (1.6)$$

where f_{AB}^C are the structure constants of G .

If invariance under local symmetry is desired, it is required to replace all the space-time derivatives ∂_μ that appear in \mathcal{L} by a new type known as *covariant derivatives* \mathcal{D}_μ , which implicitly bring the coupling of the given fields with new fields B_μ , known as *gauge fields*:

$$\partial_\mu \rightarrow \mathcal{D}_\mu = \partial_\mu - \delta_G(B_\mu) \implies \mathcal{L}(\varphi_i, \partial_\mu \varphi_i) \rightarrow \mathcal{L}(\varphi_i, \mathcal{D}_\mu \varphi_i; B_\mu). \quad (1.7)$$

Term $\delta_G(B_\mu)$ is called *connection* and it introduces a *gauge field* B_μ^A for each generator T_A of G (note that $\delta_T(B_\mu) \equiv iB_\mu^A T_A$). The covariant derivative is defined such that its transformation is of the form

$$\mathcal{D}'_\mu = U \mathcal{D}_\mu U^\dagger, \implies \mathcal{D}_\mu(\varphi) \rightarrow U \mathcal{D}_\mu(U^\dagger \varphi). \quad (1.8)$$

For this, it is enough that B_μ^C transforms as

$$\delta_G(\theta) B_\mu^C = \theta^A f_{AB}^C B_\mu^B + \partial_\mu \theta^C. \quad (1.9)$$

Since additional fields have been introduced, and, in order to implement local symmetry, it is necessary to construct a kinetic Lagrangian for such fields. Following the ideas of Yang and Mills based on the antisymmetric curvature tensor which is defined as

$$F_{\mu\nu}^C T_C = F_{\mu\nu} = -[\mathcal{D}_\mu, \mathcal{D}_\nu] = \left(\partial_\mu B_\nu^C - \partial_\nu B_\mu^C + f_{AB}^C B_\mu^A B_\nu^B \right) T_C, \quad (1.10)$$

and with it the kinetic Lagrangian for gauge fields is generalized as:

$$\mathcal{L} = -\frac{\delta_{AB}}{4g^2} F_{\nu\mu}^A F^{\nu\mu B},$$

where g is known as the gauge coupling constant which indicates the strength of the interaction. Usually, the gauge fields are rescaled so that the coefficient of the kinetic term is 1/4 and g appears in the covariant derivative.

1.2.1 EXAMPLE

As a way of illustration let us consider a renormalizable theory with a real scalar ϕ and a Dirac spinor ψ so that both are non-interacting, and suppose that this theory is globally invariant under phase transformations, i.e. the fields $\varphi \in \{\phi, \psi\}$ transform as $\varphi \mapsto e^{i\theta} \hat{Q}\varphi$ such that $\hat{Q}\psi = q\psi$ and $\hat{Q}\phi = 0\phi = 0$. The free lagrangian density for the real scalar field and the Dirac field is

$$\mathcal{L}_{\text{free}} = \frac{1}{2} \partial^\mu \phi \partial_\mu \phi - \frac{1}{2} \mu^2 \phi^2 + \bar{\psi} (i\gamma_\mu \partial^\mu - m) \psi \quad (1.11)$$

If we want to add globally symmetric interaction terms, the scalar potential must be an expansion in the fields of order four at maximum, so that it remains

renormalizable. The linear term of the potential does not contribute to the action, and the quadratic term of the potential is contained by the mass term. Whereas, a fermionic potential is not allowed since the only term renormalizable is precisely the term of mass. A cross term is allowed $\sim \phi\bar{\psi}\psi$, which is called *Yukawa coupling*, then the globally invariant Lagrangian is

$$\begin{aligned}\mathcal{L}_{\text{global}} &= \frac{1}{2}\partial^\mu\phi\partial_\mu\phi - V(\phi) + \bar{\psi}(i\gamma_\mu\partial^\mu - m)\psi + k_1\phi\bar{\psi}\psi, \\ V(\phi) &= \frac{\mu^2}{2!}\phi^2 + \frac{\alpha}{3!}\phi^3 + \frac{\lambda}{4!}\phi^4.\end{aligned}\quad (1.12)$$

Promoting to local,

$$\mathcal{L}_{\text{local}} = \frac{1}{2}\mathcal{D}^\mu\phi\mathcal{D}_\mu\phi - V(\phi) + \bar{\psi}(i\gamma_\mu\mathcal{D}^\mu - m)\psi + k_1\phi\bar{\psi}\psi - \frac{1}{4g^2}F_{\mu\nu}F^{\mu\nu}, \quad (1.13)$$

where,

$$\mathcal{D}_\mu\varphi = (\partial_\mu - igA_\mu Q)\varphi \implies \begin{cases} \mathcal{D}_\mu\phi = \partial_\mu\phi, \\ \mathcal{D}_\mu\psi = \partial_\mu\psi - igqA_\mu\psi. \end{cases} \quad (1.14)$$

With these ingredients, we are ready to approach the standard model Lagrangian.

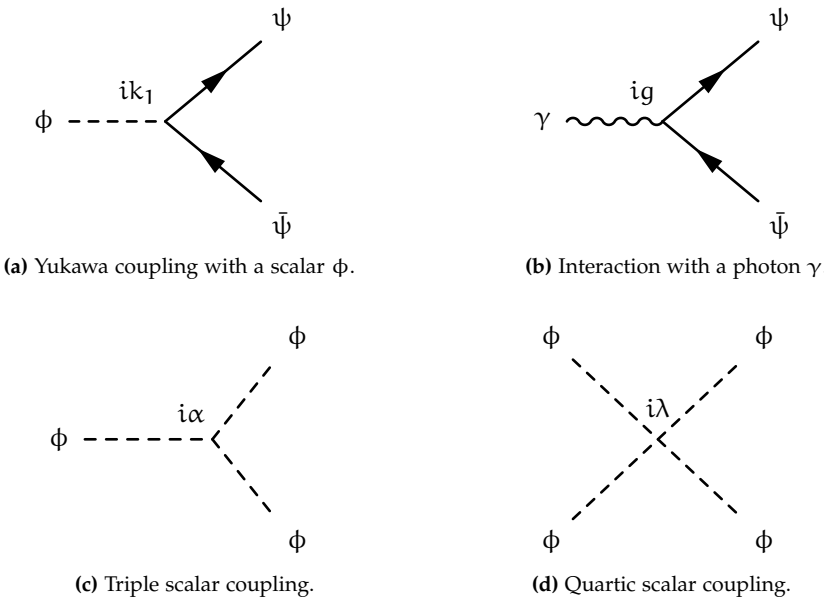


Figure 1.1: Feynman diagrams for Yukawa coupling, gauge boson coupling and quartic scalar coupling.

1.3 STANDARD MODEL

Fragment extracted and adapted from (Robinson 2011)

To contextualize the SM let me place us in 1965. Tomonaga, Feynman, and Schwinger have just won the Nobel prize for their independent contributions on the development of the Quantum Electrodynamics theory (“Physics: 1963-1970” 1972). They calculated the magnetic moment of the electron and other observables using quantum field theory and renormalization to separate out the infinities of the theory from a finite contribution (Dyson 1949) showing that renormalized

gauge theories agree with experiment up to very high precision (to more than 13 significant digits)(Zyla et al. 2020).

Unfortunately, in 1965, the models explaining radioactive decay and the strong interaction were not renormalizable. The leading theory was called *the chiral V – A universal model of weak decays* featuring four-fermion interactions in the combination of vector minus axial currents. The V – A model could not be mathematically broken down into a finite and an infinite component. Although gauge theory and renormalization explained the interaction of electrons with photons, gauge theory was not able to address the strong and weak forces. These forces were known to be short-range forces. To make a force have a short range in QFT, the mediating boson needed a mass. The Yukawa theory of scalar fields included such a term as an early model for the strong force with short range. The force law then fell off as $\exp(-rm)/r^2$ with both the classic inverse square law multiplied by an exponential dampening with distance parameterized by the mass m. To give a gauge boson A_μ a short range, the Lagrangian would need a mass term such as $m_A^2 A_\mu A^\mu$. This term violates gauge symmetry because when $A \mapsto A_\mu + \epsilon_\mu$ we see that $A_\mu A^\mu \neq A'_\mu A'^\mu$. Naively, one would think that gauge symmetry blocks all gauge bosons from having mass; and therefore, all gauge theories (Abelian and the non-Abelian ones) would obey force laws that scale as $1/r^2$. This would mean that all gauge theories would represent long-range forces similar to gravity and electromagnetism (each of which is mediated by a massless boson)¹. There are two known solutions to this quandary:

1. The Higgs mechanism which gives renormalizable gauge bosons mass without violating gauge symmetry.
2. A spontaneously created mass gap phenomena associated with non-Abelian gauge theories, which is not fully understood yet, and seems to be related to the confinement of individual quarks.

The SM chooses (1) the Higgs mechanism for the weak force, and (2) for QCD.

1.3.1 PARTICLE CONTENT AND GAUGE GROUP

First, let us talk about the chiral nature of particles: Massive half-spin particles are described at the fundamental level by a Dirac spinorial field, see table 1.1. However, Dirac spinors do not transform under an irreducible representation of the Lorentz group. Spinors can be decomposed into two components that do transform under irreducible representations of the Lorentz group: two *Weyl spinors*. The left and right chiral projectors, P_L and P_R , take a Dirac spinor and project it onto each of these invariant subspaces. For a massless Dirac spinor, the left and right components are dynamically decoupled, *i.e.* which are independent fields obeying independent Lagrangian densities; for example, the left component of a massless spinor has the Lagrangian $\mathcal{L} = -i\bar{\psi}\partial^\mu P_L \psi$ (For more details see Appendix A at (Rodriguez 2018)).

The discovery of parity asymmetry in radioactive decays (Wu et al. 1957) indicates that the chiral description of weak interactions couples differently to the

¹ In 1954 when Yang was first giving a presentation on non-Abelian gauge theories, Pauli interrupted the talk. Pauli wanted to know what the mass of the non-Abelian gauge boson was. Pauli was so insistent that Yang eventually sat down. Pauli realized that a mass term violated gauge symmetry; the mass terms were needed for short-range forces; non-Abelian gauge theories seemed like they should have long-range forces; and therefore, they probably do not explain strong or weak forces. In short, people no less than Pauli felt gauge symmetry's properties made them unlikely candidates for the a short-range force needed to explain the strong and weak forces (Robinson 2011)

left and right chiral components of half-spin particles. Indeed, the chirality of the fermionic spectrum is possibly one of the deepest properties of the Standard Model. Describing particles in terms of Dirac spinors, it means that left- and right-chirality components actually have different EW quantum numbers. This is compatible with a gauge symmetry only if half-spin particles are considered to be massless, at least without a Dirac mass $m\bar{f}_R f_L + h.c.$. Nevertheless, half-integer spin fundamental particles, such as the electron, have a well-measured mass. Therefore, the reconciliation of chiral asymmetry and mass lies in the Higgs mechanism, where the masses of the particles result from an effective Yukawa coupling with a scalar, the Higgs boson.

With this in mind, the SM has a content of matter fields from three generations (or families) of quarks q and leptons ℓ , described as Weyl 2-component spinors, with the structure

$$q_L = \begin{pmatrix} u_L^i \\ d_L^i \end{pmatrix}, u_R^i, d_R^i, \quad \ell_L = \begin{pmatrix} \nu_L^i \\ e_L^i \end{pmatrix}, e_R^i; \quad i = 1, 2, 3. \quad (1.15)$$

All these particles transform under a group $U(1)$ with different associated (hyper)charges. The doublets formed by the left components of the fields transform under the representation of two components of a $SU(2)$ group. The right components do not transform under $SU(2)$, therefore they are singlets. In addition, each quark in q_L transforms as color triplets under $SU(3)$, while u_R, d_R transforms as conjugate triplets. Leptons, on the other hand, turn out to be colored singlets. Gauge quantum numbers of the Standard Model fermions are shown in table 1.2.

Field	$SU(3)_C$	$SU(2)_L$	$U(1)_Y$	$U(1)_{EM}$
$q_L^i = (u^i, d^i)_L$	3	2	+1/3	(2/3, -1/3)
u_R^i	3	1	+4/3	+2/3
d_R^i	3	1	-2/3	-1/3
$\ell_L^i = (\nu^i, e^i)_L$	1	2	-1	(0, -1)
e_R^i	1	1	-2	-1
$H = (H^+, H^0)$	1	2	+1	(+1, 0)

Table 1.2: Gauge quantum numbers of Standard Model quarks, leptons and the Higgs scalar.

Then, we consider the Standard Model as a quantum field theory based on a gauge group

$$G_{SM} = SU(3)_C \times SU(2)_L \times U(1)_Y, \quad (1.16)$$

with $SU(3)_C$ describing strong interactions via Quantum Chromodynamics (QCD), and $SU(2)_L \times U(1)_Y$ describing electroweak (EW) interactions. Gauge vector bosons that result from taking this group locally are eight gluons (G^a) from each t^a color-generator of $SU(3)_C$, and a linear combination of the three (W^\pm, Z) weak bosons and the (γ) electromagnetic photon from the tree T^i isospin-generators of $SU(2)_L$ and Y hyper-charge-generator of $U(1)_Y$.

Electroweak symmetry is spontaneously broken into electromagnetic symmetry $U(1)_{EM}$ via the Higgs mechanism and the Higgs boson H . The hypercharges Y of the Standard Model fermions in table 1.2 are related to their usual electric charges by the Gell-Mann Nishijima relation (Nakano and Nishijima 1953)

$$Q_{EM} = \frac{1}{2}Y + T_3, \quad (1.17)$$

where $T_3 \doteq \text{diag}(\frac{1}{2}, -\frac{1}{2})$ is an $SU(2)_L$ generator. Thus, they reproduce electric charge quantization, e.g. the equality in magnitude of the proton and electron charges. Although these hypercharge assignments look rather ad hoc, their values are dictated by the quantum consistency of the theory ².

1.3.2 GAUGE BOSONS

The Lie algebra of the gauge group $SU(3) \times SU(2) \times U(1)$ is

$$\begin{aligned} [t^a, t^b] &= if^{abc}t_c, \\ [T^i, T^j] &= ie^{ijk}T_k, \\ [T^i, Y] &= [t^a, T^j] = [t^a, Y] = 0, \end{aligned} \quad (1.18)$$

where f^{abc} and e^{ijk} are the structure constants of $SU(3)$ and $SU(2)$. And therefore, the gauge fields G_μ , W_μ , and B_μ must transform in the adjoint representation

$$\begin{aligned} \delta B_\mu &= \partial_\mu \theta \\ \delta W_\mu^i &= \partial_\mu \theta^i - g e^{ijk} \theta^j W_\mu^k \\ \delta G_\mu^a &= \partial_\mu \epsilon^a - g_s f^{abc} \epsilon^b G_\mu^c \end{aligned} \quad (1.19)$$

then the curvature strength tensors are

$$\begin{aligned} G_{\mu\nu}^a &= \partial_\mu G_\nu^a - \partial_\nu G_\mu^a + g_s f^{abc} G_\mu^b G_\nu^c \\ W_{\mu\nu}^i &= \partial_\mu W_\nu^i - \partial_\nu W_\mu^i + g e^{ijk} W_\mu^j W_\nu^k \\ B_{\mu\nu} &= \partial_\mu B_\nu - \partial_\nu B_\mu \end{aligned} \quad (1.20)$$

and the “kinetic” term for gauge fields in the Lagrangian is

$$\mathcal{L}_{\text{Gauge}} = -\frac{1}{4} G_{\mu\nu}^a G_a^{\mu\nu} - \frac{1}{4} W_{\mu\nu}^i W_i^{\mu\nu} - \frac{1}{4} B_{\mu\nu} B^{\mu\nu}. \quad (1.21)$$

while these kinetic terms induce vertices between gauge bosons and in turn do not take into account the masses for such vector bosons, the Higgs mechanism produces the masses for them and gives us the linear combination to the physical bosons W^\pm , Z , γ :

$$\begin{cases} W_\mu^+ = \frac{1}{\sqrt{2}} (W_\mu^1 - iW_\mu^2) \\ W_\mu^- = \frac{1}{\sqrt{2}} (W_\mu^1 + iW_\mu^2) \\ Z_\mu = c_w W_\mu^3 - s_w B_\mu \\ A_\mu = s_w W_\mu^3 + c_w B_\mu \end{cases} \quad \text{where} \quad \begin{cases} s_w = \sin \theta_w = \frac{g}{\sqrt{g^2 + g'^2}}, \\ c_w = \cos \theta_w = \frac{g'}{\sqrt{g^2 + g'^2}}. \end{cases} \quad (1.22)$$

where to avoid confusion with Dirac matrices, we denote as A_μ to the electromagnetic potential.

1.3.3 MATTER FIELDS

We refer to the fermionic fields of the SM as the matter fields. We distinguish fermions in these two categories: leptons, fermions that do not have strong

² It is indeed easy to check that these are (modulo an irrelevant overall normalization) the only (family independent) assignments canceling all potential triangle gauge anomalies.

interaction, and quarks that interact both strongly and electroweakly. In table 1.3, we can see that there are six leptons, three charged and three neutral: each charged lepton has an associated neutrino forming between them doublets of $SU(2)_L$ and similarly for quarks.

According to the SM, there are three generations of fermions. Each generation contains a doublet of leptons and a doublet of quarks. Among generations, particles differ by their flavour quantum number and mass, but their strong and electrical interactions are identical. Moreover, the flavour quantum number is a quantity conserved by all interactions except for the weak interaction. Each generation is more massive than the previous one. The second and third generations are unstable and they disintegrate into the first generation. This is why ordinary matter is composed of the first generation. All three generations are produced in nuclear reactors, colliders, and cosmic rays.

Fermion categories		Elementary particle generation		
Type	Subtype	First	Second	Third
Quarks (q)	up-type	(u) up	(c) charm	(t) top
	down-type	(d) down	(s) strange	(b) bottom
Leptons (ℓ)	charged	(e) electron	(μ) muon	(τ) tauon
	neutral	(ν_e) e-neutrino	(ν_μ) μ -neutrino	(ν_τ) τ -neutrino

Table 1.3: Three generations of fermions according to the Standard Model of particle physics. Each generation containing two types of leptons and two types of quarks.

Under all the constraints on local gauge invariance and renormalizability of the theory, the fermionic Lagrangian for SM is given by

$$\mathcal{L}_{\text{Fer}} = i\bar{\ell}_L^j \not{\partial} \ell_L^j + i\bar{e}_R^j \not{\partial} e_R^j + i\bar{q}_L^j \not{\partial} q_L^j + i\bar{u}_R^j \not{\partial} u_R^j + i\bar{d}_R^j \not{\partial} d_R^j \quad (1.23)$$

where $\not{\partial} \equiv \gamma^\mu \not{\partial}_\mu$ with covariant derivative

$$\not{\partial}_\mu = \partial_\mu - ig_s t_a G_\mu^a - ig T_i W_\mu^i - ig' \frac{Y}{2} B_\mu, \quad (1.24)$$

and gauge fields G^a , W^i , and B acting on each kind of fermion via

$$\begin{aligned} \not{\partial}_\mu \ell_L^i &= \left(\partial_\mu - ig T_j W_\mu^j + i \frac{g'}{2} B_\mu \right) \ell_L^i \\ \not{\partial}_\mu e_R^i &= \left(\partial_\mu - ig' B_\mu \right) e_R^i \\ \not{\partial}_\mu q_L^i &= \left(\partial_\mu - ig_s t_a G_\mu^a - ig T_j W_\mu^j - i \frac{g'}{6} B_\mu \right) q_L^i \\ \not{\partial}_\mu u_R^i &= \left(\partial_\mu - ig_s t_a G_\mu^a - i \frac{2g'}{3} B_\mu \right) u_R^i \\ \not{\partial}_\mu d_R^i &= \left(\partial_\mu - ig_s t_a G_\mu^a + i \frac{g'}{3} B_\mu \right) d_R^i \end{aligned} \quad (1.25)$$

which couples the fermions to the gauge bosons.

1.3.4 ELECTROWEAK SYMMETRY BREAKING

In the SM, the electroweak symmetry $SU(2)_L \times U(1)_Y$ is spontaneously broken down to the electromagnetic $U(1)_{\text{EM}}$ symmetry by a complex scalar Higgs field

transforming as a $SU(2)_L$ doublet $H = (H^+, H^0)$ and with hypercharge +1. Its dynamics is parametrized in terms of a potential, devised to trigger a non-vanishing Higgs vacuum expectation value (vev) v

$$V = -\mu^2 |H|^2 + \lambda |H|^4 \Rightarrow v^2 \equiv \langle |H| \rangle^2 = \mu^2 / 2\lambda. \quad (1.26)$$

The vev defines the electrically neutral direction and is set to $\langle H^0 \rangle \simeq 170 \text{ GeV}$ in order to generate the vector boson masses. Simultaneously it produces masses for quarks and leptons through the Yukawa couplings

$$\mathcal{L}_{\text{Yuk}} = y_u^{ij} \bar{q}_L^i u_R^j H^* + y_d^{ij} \bar{q}_L^i d_R^j H + y_\ell^{ij} \bar{\ell}_L^i e_R^j H + \text{h.c.} \quad (1.27)$$

where $y_{u,d,\ell}$ are 3×3 complex coupling matrices. These interactions are actually the most general consistent with gauge invariance and renormalizability, and accidentally are invariant under the global symmetries related to the baryon number B and the three family lepton numbers L_i ³. When H acquires a vacuum expectation value, $\langle H \rangle = (0, v/\sqrt{2})$, \mathcal{L}_{Yuk} yields mass terms for the quarks and leptons. For quarks, the physical states are obtained by diagonalizing $y_{u,d}$ by four unitary matrices, $V_L^{u,d}$, as $M_{\text{diag}}^f = V_L^f Y^f V_R^{f\dagger} (v/\sqrt{2})$, $f = u, d$. As a result, the charged-current W^\pm interactions couple to the physical u_{Lj} and d_{Lk} quarks with couplings given by

$$\begin{aligned} \mathcal{L}_{\text{Fer}} &\supset \frac{-g}{\sqrt{2}} (\bar{u}_L, \bar{c}_L, \bar{t}_L) \gamma^\mu W_\mu^+ V_{\text{CKM}} \begin{pmatrix} d_L \\ s_L \\ b_L \end{pmatrix} + \text{h.c.}, \\ V_{\text{CKM}} &\equiv V_L^u V_L^{d\dagger} = \begin{pmatrix} V_{ud} & V_{us} & V_{ub} \\ V_{cd} & V_{cs} & V_{cb} \\ V_{td} & V_{ts} & V_{tb} \end{pmatrix}. \end{aligned} \quad (1.28)$$

However, in both flavour-changing charged and neutral currents, the weak interaction at play deals with lepton flavours in a universal manner. This property is known as *Lepton Flavour Universality*; whereas quarks are treated on a different footing due to the CKM matrix. This universality of lepton couplings is assumed when determining the CKM parameters, in particular to combine results from semileptonic and leptonic decays that involve e, μ , and/or τ leptons.

The Lagrangian of the scalar sector is simply

$$\mathcal{L}_H = \mathcal{D}_\mu H^\dagger \mathcal{D}^\mu H - V(H^\dagger, H) \quad (1.29)$$

where $\mathcal{D}_\mu H = (\partial_\mu + igT_a W_\mu^a + ig' \frac{Y}{2} B_\mu) H$, then

$$\begin{aligned} \mathcal{L}_{\langle H \rangle} &= -\frac{1}{8} \begin{pmatrix} 0 & v \end{pmatrix} \begin{pmatrix} gW_\mu^3 - g'B_\mu & g(W_\mu^1 - iW_\mu^2) \\ g(W_\mu^1 + iW_\mu^2) & -gW_\mu^3 - g'B_\mu \end{pmatrix}^2 \begin{pmatrix} 0 \\ v \end{pmatrix} \\ &= -\frac{1}{8} v^2 V_\mu^T \begin{pmatrix} g^2 & 0 & 0 & 0 \\ 0 & g^2 & 0 & 0 \\ 0 & 0 & g^2 & -g'g \\ 0 & 0 & -g'g & g'^2 \end{pmatrix} V^\mu \end{aligned} \quad (1.30)$$

where $V_\mu^T = (W_\mu^1, W_\mu^2, W_\mu^3, B_\mu)$. Diagonalizing this mass matrix, we have that the mass eigenvalues are $0, -\frac{1}{8}v^2g^2, -\frac{1}{8}v^2g^2$, and $-\frac{1}{8}v^2(g^2 + g'^2)$. The massless

³ Regarding the Standard Model as an effective theory, non-renormalizable operators violating these symmetries may, however, be present.

boson is the photon, the most massive is the Z boson, and the two intermediate vectors correspond to the bosons W^+ and W^- , that transform under a representation of the unbroken generator Q_{EM} .

Having said that, so far, it is enough to understand how the standard model of particle physics as a relativistic field theory describes the interactions of fundamental matter articles via the fundamental forces, mediated by the force carrying particles, the vector bosons. The Higgs boson, also a fundamental Standard Model particle, plays a central role in the mechanism that determines the masses of the photon and weak bosons, as well as the rest of the standard model particles.

Since then, the standard model has faced several experimental tests and has had unprecedented success in explaining the measurements made so far; it has also been a powerful predictive theory. The Standard model has proven successfully at describing many features of nature that we measure in our experiments. The most famous example is the agreement of the Standard Model prediction and the experimental measurement of the electron magnetic dipole moment to within twelve significant figures of accuracy (Odom et al. 2006). The 2012 discovery of the Higgs boson was the culmination of almost fifty years of searching for the particle first predicted to exist in 1965 and first incorporated into the Standard Model in 1967 with Glashow, Weinberg, and Salam's unification of the electromagnetic and weak forces (Weinberg 1967; Glashow 1961). With the 2012 Higgs discovery, the full predicted particle spectrum of the Standard Model was finally observed.

1.4 DEFICIENCIES OF STANDARD MODEL AND EVIDENCE OF NEW PHYSICS

Pending to be updated

While these and other successes of the Standard Model are an achievement for the field of particle physics, it is well known that this cannot be the ultimate theory of fundamental particles and interactions. Even though the Standard Model is currently the best description there is of the subatomic world, it does not explain the complete picture; there are also important questions that it does not answer and it is also surrounded by different irregularities. Some of them are completely incompatible with the current Standard Model, and strongly suggest that the Standard Model requires a consistent extension to solve experimental and theoretical problems that we will label as the cosmological problems, phenomenological problems, and theoretical problems. Below we will list very briefly the main representatives of these categories.

1.4.1 THEORETICAL PROBLEMS

HIERARCHY PROBLEM Is the problem concerning the large discrepancy between aspects of the weak force and gravity. Both of these forces involve constants of nature, the Fermi constant for the weak force and the Newtonian constant of gravitation for gravity. If the Standard Model is used to calculate the quantum corrections to Fermi's constant, it appears that Fermi's constant is surprisingly large and is expected to be closer to Newton's constant unless there is a delicate cancellation between the bare value of Fermi's constant and the quantum corrections to it.

In the Standard Model context, the Higgs boson is much lighter than the energy scale on which the standard model is considered valid (ideally the Plank mass), and the quantum corrections to the Higgs mass are on the

order of this energy scale; it would inevitably make the Higgs and fermions masses huge, comparable to the scale at which new physics appears, unless there is an incredible fine-tuning cancellation between the quadratic radiative corrections and the bare mass. This level of fine-tuning is deemed unnatural.

STRONG CP PROBLEM QCD Lagrangian supports a term associated with the strength tensor dual for gluons that break CP symmetry in the strong interaction sector. Experimentally, however, no such violation has been found, implying that the coefficient of this term is fine tuned to zero.

QUANTUM TRIVIALITY Suggests that it may not be possible to create a consistent quantum field theory involving elementary scalar Higgs particles because for high momentum particles the renormalization presents inconsistencies unless the renormalization of the charges becomes null, and therefore not interacting, *i.e.* trivial. Nevertheless, because the Higgs boson plays a central role in the Standard Model of particle physics, the question of triviality in Higgs models is of great importance.

NUMBER OF PARAMETERS AND UNEXPLAINED RELATIONS In total, the standard model has too many free parameters (19 in total) that are obtained experimentally, and there are indications that several of them may be correlated, however the origin of these correlations is beyond the standard model.

For example, Yoshio Koide's empirical formula (Rivero and Gsponer 2005)

$$\frac{m_e + m_\mu + m_\tau}{(\sqrt{m_e} + \sqrt{m_\mu} + \sqrt{m_\tau})^2} = 0.666661(7) \approx \frac{2}{3}$$

seems to indicate that there is a way to predict the masses of leptons.

1.4.2 COSMOLOGICAL PROBLEMS

GRAVITY Although the Standard Model describes the three important fundamental forces at the subatomic scale, it does not include gravity. However, at larger scales, gravity becomes present and is described by Einstein's theory of general relativity, in which gravity rather than a force is a property that measures the deformation of spacetime then, the most of the conventional machinery of perturbative QFT is profoundly incompatible with the general relativistic framework (Rovelli 2007), and a theory of quantum gravity with which we are enabled to perform calculations has yet to be discovered.

DARK MATTER Within the framework of Einstein's general relativity, the cosmological standard model (Λ CDM) is, like the standard model of particle physics, one of the most successful theories of the 20th century. Λ CDM it is based on a very specific density of matter that can be explained with ordinary matter from the standard model of particles, baryonic matter; according to Λ CDM, in addition to baryonic matter, there is a kind of matter five times more abundant than baryonic matter, which does not interact electrically (therefore it is dark) and non-relativistic (therefore it is cold), known as cold dark matter (CDM). Yet, the Standard Model does not supply any fundamental particles that are good dark matter candidates.

DARK ENERGY Moreover, according to Lambda CDM only 31% of the energy that makes up the universe is matter, the remaining 69% of the universe's

energy should consist of the so-called dark energy, a constant energy density for the vacuum (Λ). If we try to explain dark energy in terms of vacuum energy only from the standard model lead to a mismatch of 120 orders of magnitude (Adler, Casey, and Jacob 1995), sometimes called *The Worst Theoretical Prediction in the History of Physics* (M. P. Hobson 2005); a bit sensationalist title to indicate the fact that we do not fully understand the composition of the particle spectrum of the universe.

MATTER-ANTIMATTER ASYMMETRY In the observable universe there is more matter than antimatter. In 1967, Andrei Sakharov proposed a set of three necessary conditions that a baryon-generating interaction must satisfy to produce matter and antimatter at different rates (Sakharov 1967). While the standard model can satisfy these three conditions (Hooft 1976; Cline 2006), it satisfies them at three different energy scales and therefore presents difficulties in the capability to explain the matter-antimatter asymmetry (Robinson 2011).

1.4.3 PHENOMENOLOGICAL PROBLEMS

NEUTRINO MASSES In the standard model, the right chiral component of neutrinos is not part of the composition of fermionic fields because if they were present they would not interact and consequently neutrinos have no mass. However, the precision measurement (Abe et al. 2008) of the mixing matrix for neutrino oscillations has shown that neutrinos change flavour in free flight and in turn that the three neutrino flavours cannot have identical mass, meaning that all three cannot have zero mass. There is no single way to extend the standard model to include masses to neutrinos and even more to explain their value so close to zero and results in the open problem confirmed at the phenomenological level present in the standard model.

ANOMALOUS B-MESONS DECAY A B-meson is a bound state made up of an quark-antiquark pair where one of them comes from a b-quark. Various experimental results (Lees et al. 2012; Aaij et al. 2015; Altmannshofer and Straub 2015; Hurth, Mahmoudi, and Neshatpour 2016a; LHCb Collaboration et al. 2021) have suggested a surplus over Standard Model predictions in its decays to D-mesons along with a τ , ν_τ doublet. While none of them have reached the statistical threshold of 5σ to declare a break from the standard model, the Capdevila's meta-analysis of all available data reported a 5.0σ deviation from SM (Capdevila et al. 2018).

ANOMALOUS MAGNETIC DIPOLE MOMENT OF MUON Unlike the extraordinary agreement between theory and experiment with the magnetic dipole moment of the electron (Odom et al. 2006); in the case of the muon, the measurement of Fermilab's Muon g-2 experiment has presented an apparent discrepancy with an accuracy of 4.2σ (Blum et al. 2013; Abi et al. 2021) which strengthen evidence of new physics in the muon sector and apparently in the violation of lepton universality of the standard model.

ANOMALOUS MASS OF THE W BOSON Results from the CDF Collaboration, reported in April 2022, indicate that the mass of a W boson exceeds the mass predicted by the Standard Model with a significance of 7σ (Collaboration et al. 2022). However, this very highly accurate result, unlike the anomaly in B-meson Decay, is in tension with the results of Atlas, LHCb, LEP and Do II (Aaboud et al. 2018; R. Aaij et al. 2022; Schael et al. 2006; Abazov et al.

2012). Certainly, a review of all the information we possess so far must be done to determine if this anomaly is a window into new physics beyond the standard model.

CCA AND $q\bar{q} \rightarrow e^+e^-$ It has been observed that certain nuclear beta decays happen less frequently than expected (Hardy and Towner 2020). This tension, called the Cabibbo Angle anomaly (CAA), displays a significance around 3σ (Zyla et al. 2020), and can again be interpreted as a sign that electrons and muons behave more differently than predicted by the SM (Crivellin and Hoferichter 2020). Furthermore, the CMS experiment at CERN observed more very high-energetic electrons in proton-proton collisions ($q\bar{q} \rightarrow e^+e^-$) compared to muons than expected (collaboration 2021).

2

PHENOMENOLOGICAL FRAMEWORK FOR LHC OBSERVABLES, SEARCHES AND ANALYSIS

Since its formulation, the Standard Model (SM) has proven remarkably successful in describing the fundamental particles and interactions, and its parameters have been measured with increasing precision over several decades; however, as we have commented in the last chapter, various theoretical and experimental observations suggest that the SM is incomplete and certain details of the standard model seem to demand a better explanation, motivating the exploration of new physics (NP) beyond the standard model (BSM) and in turn methods in the search for this new physics. This pursuit requires both the development of theoretical models and the design of experimental strategies to test them. Particle physics phenomenology plays a crucial role in this endeavor by bridging theoretical predictions with experimental observations, feasibility and searches, particularly in high-energy experiments such as those conducted at the Large Hadron Collider (LHC), as well as in high-precision low-energy measurements.

The LHC is a proton-proton (pp) collider that has been operating since 2009, achieving center-of-mass collision energies ranging from 7 TeV to 13.6 TeV. During its Run I (2010-2013), the LHC reached 7 TeV in 2010-2011 and 8 TeV in 2012, leading to landmark discoveries such as the Higgs boson in 2012. Run II (2015-2018) operated at 13 TeV and achieved an instantaneous luminosity of $1.5 \times 10^{34} \text{ cm}^{-2} \text{ s}^{-1}$, yielding approximately 1000 top-quark pairs and 50 Higgs bosons per minute. Run III (2022-2025) is currently underway with collisions at a record energy of 13.6 TeV and even higher luminosities. Following this, the High-Luminosity LHC (HL-LHC) is expected to begin operations around 2029. This major upgrade aims to increase the integrated luminosity by more than an order of magnitude, targeting up to 3 ab^{-1} of data per experiment. The HL-LHC will significantly enhance the sensitivity to rare processes, improve the precision of Standard Model measurements, and boost the discovery potential for BSM phenomena.

These collisions take place at four main interaction points, each equipped with a sophisticated particle detector designed to record and analyze the outcomes. Two of the largest and most comprehensive experiments at the LHC are the Compact Muon Solenoid (CMS) and ATLAS detectors. Both are multipurpose detectors with broad physics programs, designed to explore a wide range of phenomena. They perform precision measurements within the electroweak sector of the SM, investigate the dynamics of quarks and gluons (including through heavy-ion collisions), and carry out extensive searches for BSM signatures using pp collision data. While CMS and ATLAS differ in their detector designs and reconstruction strategies, their physics goals are largely overlapping, and their results are complementary. Throughout this work, phenomenological studies and comparisons are primarily developed in the context of CMS, although several results from ATLAS are also referenced, given the close alignment in sensitivity and scope.

2.1 COORDINATE SYSTEM AND COLLISION PARAMETERS

To fully describe the CMS experiment, some of its parameters should be outlined. Measurements performed at CMS adopt the coordinate system whose origin lies at the collision point, with the y -axis pointing vertically upward, the x -axis pointing radially inward towards the centre of the LHC and the z -axis along the beam direction. The azimuthal angle ϕ is measured in the xy -plane from the x -axis and the polar angle, θ , is measured from the z -axis, as shown in the Fig. 2.1.

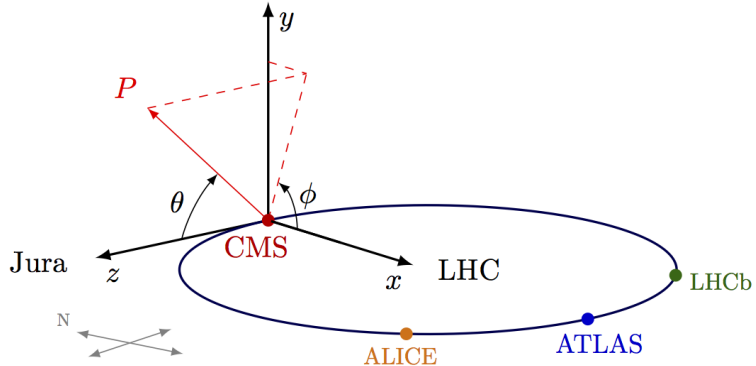


Figure 2.1: Coordinate system employed by the CMS experiment (retrieved from (Neutelings n.d.)).

The event rate R for a physical process (e.g., $pp \rightarrow X$) is governed by the accelerator's luminosity \mathcal{L} and the process cross section σ . Luminosity quantifies the performance of a collider to produce interactions, establishing the proportionality,

$$\frac{dR}{dt} = \mathcal{L}\sigma, \quad (2.1)$$

where σ (typically measured in barns, $1\text{ b} = 10^{-24}\text{ cm}^2$) encodes the interaction probability. For LHC proton bunches colliding head-on with Gaussian transverse profiles, the instantaneous luminosity is (Herr and Muratori 2006; Thomson 2013):

$$\mathcal{L} = \frac{fN_b}{4\pi} \frac{N_1 N_2}{\sigma_x \sigma_y} \quad (2.2)$$

Here, $N_{1,2}$ are proton counts per bunch, f is the bunch collision frequency, N_b is the number of bunches, and $\sigma_{x,y}$ are transverse beam widths.

Integrating \mathcal{L} over time yields the total integrated luminosity L , linking directly to the observed event count N :

$$L = \int \mathcal{L} dt \quad \Rightarrow \quad N = L\sigma. \quad (2.3)$$

The Gaussian beam approximation in (2.2) ignores hourglass effects (beam divergence near interaction points) and dynamic $\sigma_{x,y}$ variations during fills. CMS mitigates these via real-time luminosity monitoring using pixel clusters (collaboration 2021), with systematic uncertainties below 2%. High \mathcal{L} also introduces pileup—multiple pp interactions per bunch crossing—which complicates η/ϕ measurements but is corrected using vertex isolation algorithms.

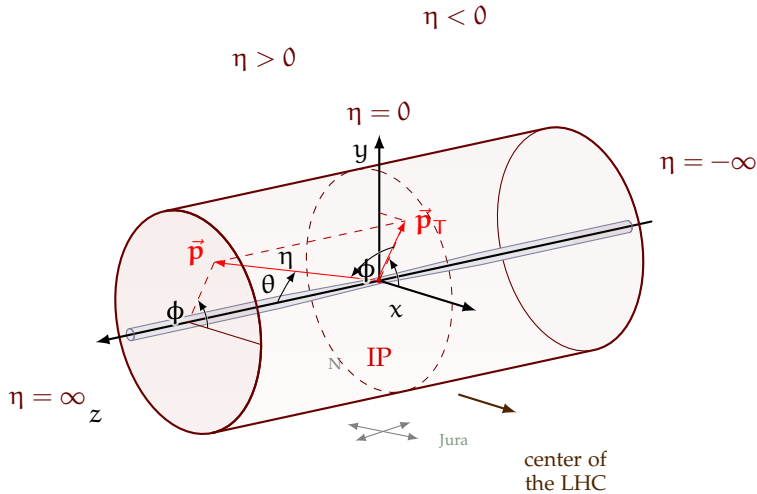


Figure 2.2: Detailed reparametrization of the coordinate system employed by the CMS experiment (retrieved from (Neutelings n.d.))

The following variables are related to the particles being produced rather than the accelerator.

DECAY WIDTH (Γ) The decay rate is the probability that a given particle will decay per unit time. Since a particle can have multiple decay modes, the total decay rate is the sum of the decay rates for each mode (Thomson 2013). The relative frequency of a decay mode is the branching ratio, given by

$$\text{BR}(j) = \frac{\Gamma(j)}{\Gamma}.$$

CROSS-SECTION (σ) The cross-section is a measure of the probability that an interaction will occur from a collision. It is a quantum-mechanical analogue of the "effective size" of the particles involved in an interaction.

PSEUDO-RAPIDITY (η) Instead of using the polar angle, CMS measurements involve the pseudo-rapidity, defined by

$$\eta = -\ln \left(\tan \frac{\theta}{2} \right)$$

The main advantage of using the pseudo-rapidity is that distributions over it tend to be closer to a uniform distribution than those over the polar angle, see Fig. 2.2. Furthermore, the difference in pseudo-rapidity is invariant under Lorentz boosts along the beam direction (Thomson 2013).

TRANSVERSE MOMENTUM (p_T) Refers to the component of momentum which is perpendicular to the beam line. It is usually preferred over full momentum because momentum along the beamline may just be left over from the beam particles, while the transverse momentum is always associated with whatever physics happened at the vertex, see Fig. 2.2.

MISSING TRANSVERSE ENERGY AND MOMENTUM (E_T^{miss} & p_T^{miss}) Missing energy and momentum refers to the energy and momentum that is not detected but is expected to be there as a consequence of energy conservation and momentum conservation. This momentum is often carried by particles that do not interact electromagnetically or strongly and are therefore difficult to

detect (Thomson 2013). Missing energy and momentum provides an indirect measurement of undetectable particles in hadron colliders such as neutrinos. Missing momentum reconstructions focus on the transverse direction, where total momentum is expected to be zero.

2.2 DETECTORS AND SUBSYSTEMS

A typical collider experiment comprises several main detector subsystems that are used jointly to detect and measure the properties of particles produced in the collision. A *schematic representation* of such a generic multipurpose detector is shown in Fig. 2.3. The detector is typically composed of several concentric layers, each designed to measure different properties of the particles produced in the collisions.

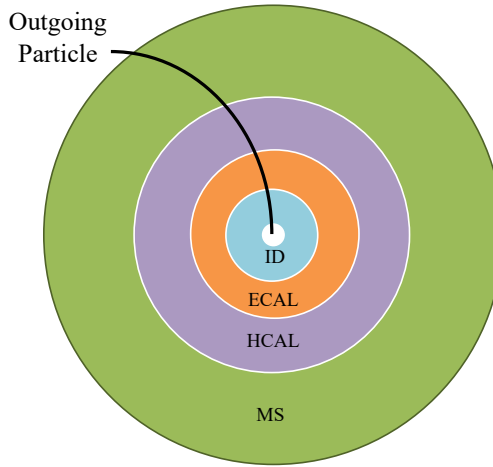


Figure 2.3: Schematic representation of transversal section of a generic multipurpose detector. The innermost subsystem, called the inner detector (ID), is used to measure the trajectories of charged particles, the electromagnetic calorimeter (ECAL) measures the energy of photons and electrons, the hadronic calorimeter (HCAL) measures the energy of hadrons, and the muon system (MS) measures the trajectories of muons. The missing transverse energy (MET) is measured by combining information from all subsystems..

The innermost subsystem, called the inner detector (ID), is designed to detect electrically charged particles that are long-lived enough to traverse the ID. The most common such particles from the SM are two charged leptons (the electron e^- and the muon μ^-) and three hadrons (the pion π^+ , kaon K^+ , and proton p^+). Regions of ionization produced by such a particle in solid-state or gaseous detector sensors are detected as spatial hits that are fit into a trajectory, referred to as a **track**. The direction and curvature of the track in a magnetic field yield the particle's momentum vector and electric charge. In some detectors, the ID is enclosed in a Cherenkov-light detector used to measure the velocity of the tracked particles. Combined with the momentum measurement in the ID, this yields the particle mass with sufficient resolution to differentiate between pions, kaons, and protons in a relevant momentum range.

After passing through the tracker, particles produced in the collisions typically enter an electromagnetic calorimeter (ECAL), designed to measure the energies

of photons, electrons and positrons. The energy measurement exploits the properties of electromagnetic shower production via photon radiation and e^+e^- pair production, resulting from the interaction of energetic particles with the ECAL material.

Hadrons deposit energy via hadronic interactions with the detector material. Since this process involves large fluctuations and a variety of energy-deposition mechanisms, precise hadron-energy measurement is achievable only at high-energy colliders, where fluctuations are effectively averaged out. In particular, high-energy quarks and gluons hadronize into a collimated spray of hadrons known as a **jet**. Containing the jet requires use of a deep hadronic calorimeter (HCAL) beyond the ECAL. While a jet can be identified solely in the calorimeters, its energy is nowadays measured from a combination of the momenta of tracks in the ID and the signals integrated in the ECAL and HCAL.

The signals from the calorimeters, known as **towers**, are grouped into jets using a jet clustering algorithm. If a hadronic particle is neutral, it will not leave a track in the ID, but it will still deposit energy in the towers. So, the towers are used to measure the energy of neutral particles, such as photons and neutral hadrons, while the ID tracks are used to measure the energy of charged particles. This approach is known as particle flow (PF) reconstruction and provides a more accurate measurement of the energy of jets.

Muons do not undergo hadronic interactions, and are heavy enough that they lose energy due to ionization at a low rate. Therefore, they lose only a few GeV while traversing a typical LHC-detector calorimeter. Using this property to identify them, a muon system (MS) is built outside the calorimeter. In high-energy collider detectors, the MS is usually immersed in a magnetic field in order to measure the momenta of muons. Tracks reconstructed in the MS are often combined with tracks in the ID to obtain a high-quality momentum measurement.

When studying final states that include long-lived, weakly interacting particles, such as neutrinos in the SM or dark matter candidates in BSM models, an important reconstructed quantity is missing momentum. Using three-momentum conservation and the approximate hermeticity of the detector, it is possible to measure the momentum imbalance in the event and to infer the combined momentum of the invisible set of particles. Since the interacting partons in proton collisions generally carry different fractions of the momenta of the incoming hadrons and many of the particles produced fall outside of the acceptance of the sensitive detector, the summed momenta of measured final-state particles along the beam axis z are not expected to cancel. Therefore, experiments at the LHC measure the missing transverse momentum, denoted E_T^{miss} known as Missing Energy Transverse (MET), where momentum balance is assumed only in the $x-y$ plane transverse to the beam direction.

Collider detectors are mostly designed and constructed for optimal detection of SM particles produced in the collision. However, they can also be used to search for new physics (NP) beyond the SM. In this case, the detector is used to search for signatures of NP, such as new particles or interactions that are not predicted by the SM. The detector subsystems are designed to be sensitive to a wide range of particles and interactions, allowing for the detection of a variety of NP signatures.

2.2.1 JETS RECONSTRUCTION

Quarks and gluons are never observed as free particles because of colour confinement. Nevertheless, perturbative QCD treats them as the relevant short-distance degrees of freedom: factorization theorems and asymptotic freedom justify com-

puting hard-scattering matrix elements for incoming and outgoing partons even though QCD becomes non-perturbative at low scales. The strong coupling α_s grows large and effectively “blows up” around the confinement scale Λ_{QCD} ; consequently something must happen to quarks and gluons before they reach the detector. In practice the gluon and all quarks except the top hadronize, producing cascades of baryons and mesons that themselves undergo further decays. At the LHC these hadrons typically carry energies comparable to the electroweak scale, and relativistic boosts tend to collimate their decay products into narrow bunches. Those collimated collections of hadrons are the jets we measure at hadron colliders and the objects we use to infer the partons produced in the hard interaction.

Phenomenologically one usually assumes that each high-energy parton yields a jet and that the measured jet four-momentum can, to useful accuracy, be related to the original parton four-momentum. Jets are therefore defined operationally using recombination (clustering) algorithms such as Cambridge-Aachen or the (anti-) k_T family. Experimentally this means grouping a large number of energy depositions (or particle-flow candidates) observed in the calorimeters and tracker into a much smaller set of jets or subjets. Nothing in the raw detector data, however, indicates a priori how many jets there should be: the clustering procedure and the choice of a resolution scale fix the outcome. In practice one must either specify the desired number of final jets or choose a resolution/stop criterion (for example a distance parameter R , a clustering distance cut, or a jet-mass/subjet-resolution threshold) that determines the smallest substructure to be considered a separate parton-like object.

Modern reconstruction at the LHC typically uses particle-flow (PF) candidates as input together with infrared- and collinear-safe clustering algorithms to define jet four-momenta. The anti- k_T algorithm ([Cacciari:2008gp](#)), implemented in FastJet ([Cacciari:2011ma](#)), is widely used in ATLAS and CMS; it groups candidates by proximity in the rapidity–azimuth (y, ϕ) plane with a typical distance parameter $R \sim 0.4\text{--}0.6$ and is relatively insensitive to soft radiation and pileup. After clustering, jet energy corrections (JEC) derived from simulation and in-situ calibrations compensate for detector response, pileup, and underlying-event effects, while jet-substructure and tagging algorithms help infer the flavour and origin of the initiating parton.

Jet algorithms

Recombination (or sequential clustering) algorithms formalise the intuitive idea that parton showering produces collinear and soft splittings: two nearby and kinematically compatible subjets are merged if they are more likely to have originated from a single parton. A practical implementation requires a measure of “distance” between objects; common choices combine an angular separation in the rapidity–azimuth plane, ΔR_{ij} , with a transverse-momentum weighting. Typical distance measures are

$$\begin{aligned} k_T : \quad y_{ij} &= \frac{\Delta R_{ij}}{R} \min(p_{T,i}, p_{T,j}), \quad y_{iB} = p_{T,i}, \\ C/A : \quad y_{ij} &= \frac{\Delta R_{ij}}{R}, \quad y_{iB} = 1, \\ \text{anti-}k_T : \quad y_{ij} &= \frac{\Delta R_{ij}}{R} \min(p_{T,i}^{-1}, p_{T,j}^{-1}), \quad y_{iB} = p_{T,i}^{-1}. \end{aligned}$$

The parameter R balances jet–jet and jet–beam criteria and sets the geometric size of jets; in LHC analyses typical values are $R \sim 0.4\text{--}0.7$ depending on the physics target.

Two operational modes are useful to distinguish. In an exclusive algorithm one supplies a resolution scale y_{cut} and proceeds iteratively:

1. compute $y^{\min} = \min_{i,j}\{y_{ij}, y_{iB}\}$;
2. if $y^{\min} = y_{ij} < y_{\text{cut}}$ merge i and j and repeat;
3. if $y^{\min} = y_{iB} < y_{\text{cut}}$ remove i as beam radiation and repeat;
4. stop when $y^{\min} > y_{\text{cut}}$ and keep remaining subjets as jets.

An inclusive algorithm omits y_{cut} and instead declares a subjet a final-state jet when its jet-beam distance is the smallest quantity; iteration continues until no inputs remain. Inclusive algorithms therefore produce a variable number of jets, while exclusive algorithms deliver a scale-dependent fixed set.

A practical question is how to combine the kinematics of merged objects. The most common choice in modern experiments is the E-scheme: four-vectors are added, which preserves energy-momentum and yields a physical jet mass useful for substructure and boosted-object tagging. An alternative is to sum three-momenta and rescale the energy to enforce a massless jet; this can be appropriate when the analysis targets massless parton kinematics, but it discards potentially useful jet-mass information.

From a theoretical and experimental viewpoint important properties are infrared and collinear safety: a jet algorithm should give stable results under emission of soft particles or collinear splittings. The k_T , C/A and anti- k_T families are constructed to satisfy these requirements. Their practical behaviour differs: k_T naturally follows the physical shower history (soft-first clustering), C/A is purely geometric (useful for declustering and substructure studies), while anti- k_T produces regular, cone-like jets that are robust and convenient experimentally.

Corrections for pileup and the underlying event are necessary at the LHC. These corrections depend on the jet area (a well-defined concept for sequential algorithms) and are typically performed by estimating an event-wide transverse-momentum density and subtracting the corresponding contribution proportional to the jet area. Finally, because inclusive algorithms can produce jets arbitrarily close to the beam, a minimum jet p_T threshold (commonly 20–100 GeV depending on the analysis) is imposed to ensure experimental observability and theoretical control.

2.2.2 τ TAGGING AT MULTIPURPOSE DETECTORS

The τ lepton decays hadronically with a probability of $\sim 65\%$, producing a narrow “ τ -jet” that contains only a few charged and neutral hadrons. Hadronic decays are dominated by one- and three-prong topologies and often include neutral pions that promptly convert to photons, giving a sizable electromagnetic fraction in the calorimeters. When the τ momentum is large compared to its mass the decay products are highly collimated: for $p_T > 50$ GeV roughly 90% of the visible energy is contained within a cone of radius $R = \sqrt{(\Delta\eta)^2 + (\Delta\varphi)^2} = 0.2$. These properties motivate the use of small signal cones and narrow isolation annuli in reconstruction.

Identification exploits three complementary classes of observables:

- Calorimetric isolation and shower-shape variables: hadronic τ decays deposit localized energy in ECAL+HCAL. Experiments use isolation sums and shape ratios to quantify peripheral activity. Example variables are

$$\Delta E_T^{12} = \frac{\sum_{0.1 < \Delta R < 0.2} E_{T,j}}{\sum_{\Delta R < 0.4} E_{T,i}}, \quad P_{ISOL} = \sum_{\Delta R < 0.40} E_T - \sum_{\Delta R < 0.13} E_T,$$

which suppress QCD jets that populate the isolation ring.

- Charged-track isolation and prong topology: the few, collimated charged tracks of a τ allow powerful selections. A common procedure defines a matching cone of radius R_m around the calorimeter jet axis to select candidate tracks above a p_T^{\min} threshold. The leading track (tr_1) is found and a narrow signal cone R_S around tr_1 is used to count associated tracks (1 or 3 prongs preferred). A larger isolation cone R_I is scanned for additional tracks: if no extra tracks with Δz_{impact} consistent with tr_1 are found, the candidate is isolated. Typical CMS/ATLAS choices are $R_S \sim 0.07\text{--}0.15$, $R_I \sim 0.3\text{--}0.4$, and $p_T^{\min} \sim 1\text{--}2$ GeV, although values depend on analysis and working point.
- Lifetime and vertexing observables: the finite τ lifetime ($c\tau \approx 87$ μm) produces displaced tracks and, for multi-prong decays, a reconstructible secondary vertex. Impact-parameter significances (2D or 3D) and secondary-vertex properties (mass, flight length significance) are used to separate genuine taus from prompt jets or leptons.

Additional discriminants include the invariant mass of the visible decay products computed from tracks and calorimeter clusters (with care to avoid double counting), electromagnetic energy fractions (sensitive to $\pi^0 \rightarrow \gamma\gamma$), and dedicated shower-strip grouping for nearby photons. For example, invariant-mass reconstruction commonly uses a jet cone $\Delta R_{\text{jet}} \lesssim 0.4$ while excluding calorimeter clusters matched to tracks by a minimum separation $\Delta R_{\text{track}} \gtrsim 0.08$ to reduce double counting.

Reconstruction algorithms combine these inputs. CMS's Hadron-Plus-Strips (HPS) and modern DeepTau methods explicitly build decay-mode hypotheses and use strip-clustering of photons plus multivariate or deep-learning discriminators to reject jets, electrons and muons (**CMS:2022ydz**; **CMS_DeepTau**). ATLAS employs analogous calorimeter+track based MVAs and BDTs (**ATLAS:2022fgo**). Typical working points trade efficiency versus background: medium points often give τ_h efficiencies of order 50–70% with light-jet misidentification rates in the per-mille to percent range, depending on kinematics and pileup.

Practical implementations tune cone sizes, isolation thresholds and MVA inputs to the kinematic region and analysis goals; the choice of working point is driven by the signal-to-background optimization for the search or measurement at hand.

2.2.3 B TAGGING AT MULTIPURPOSE DETECTORS

Jets originating from bottom quarks (b-jets) exhibit several distinctive properties that enable their identification. The relatively long lifetime of b hadrons (order 1.5 ps) produces displaced charged tracks and often reconstructible secondary vertices a few millimetres from the primary interaction point. The large b-hadron mass yields decay products with sizable transverse momentum relative to the jet axis, and semileptonic branching fractions produce soft electrons or muons inside the jet. These features form the basis for b-tagging.

Practical algorithms exploit individual signatures or combine them:

- **Track-counting:** counts tracks with large impact-parameter significance to identify a b-like topology.
- **Jet-probability:** evaluates the compatibility of the jet’s track impact-parameter distribution with the primary vertex hypothesis.
- **Secondary-vertex:** explicitly reconstructs displaced vertices and uses their kinematic properties (decay length significance, vertex mass).
- **Soft-lepton taggers:** identify low- p_T leptons inside jets from semileptonic b decays.

Modern taggers combine many observables in multivariate or deep-learning classifiers to maximize discrimination power. Contemporary approaches exploit rich, low-level inputs (track-by-track and PF-candidate information, vertex features and kinematics) and advanced network architectures:

- Deep feed-forward networks (e.g. DeepCSV/DeepJet) ingest a large set of high-level and per-track inputs to produce powerful binary or multi-class discriminants that separate b, c and light-flavour jets.
- Sequence models and recurrent networks (RNN-based taggers) process an arbitrary ordered list of track-level variables, improving sensitivity by directly exploiting per-track correlations and order-dependent information (impact-parameter sequences, track kinematics).
- Graph- and set-based architectures and combined particle+vertex networks (sometimes referred to as “DeepFlavour”-style models) aggregate heterogeneous inputs and return per-flavour probabilities, enabling natural multi-classification and calibrated operating points.

These developments yield measurable performance gains: modern deep classifiers typically improve b efficiency at fixed mistag rate (or reduce mistag rates at fixed efficiency) relative to classical taggers. The continuous output of such networks permits analyses to choose operating points (loose/medium/tight) corresponding to desired efficiencies or mistag targets. Calibration remains essential: data-driven scale factors derived from control samples (e.g. $t\bar{t}$, multijet, dilepton) are applied to correct simulation, and systematic uncertainties from the calibration, flavour composition and kinematic extrapolation are propagated to physics results.

Examples in use are CMS DeepCSV / DeepJet and ATLAS MV2 / DL1 ([CMS:2017wtu](#); [ATLAS:2019bwq](#)), which illustrate the transition from expert-designed high-level variables to large-scale machine learning leveraging low-level detector information. Typical medium working points yield b-tag efficiencies of order 60–80% with light-jet misidentification rates at or below the percent level; the precise choice of working point is tuned per-analysis to optimise sensitivity while accounting for calibration and systematic uncertainties.

2.2.4 THE CMS DETECTOR

Particularly the CMS multi-purpose detector has a length of 21.6 meters, with a diameter of 14.6 meters and weights 12500 tonnes. The detector is composed of a set of different sub-detectors as seen in figure 2.4. The CMS detector has a cylindrical shape and it is divided into two main sections: barrel and endcaps.

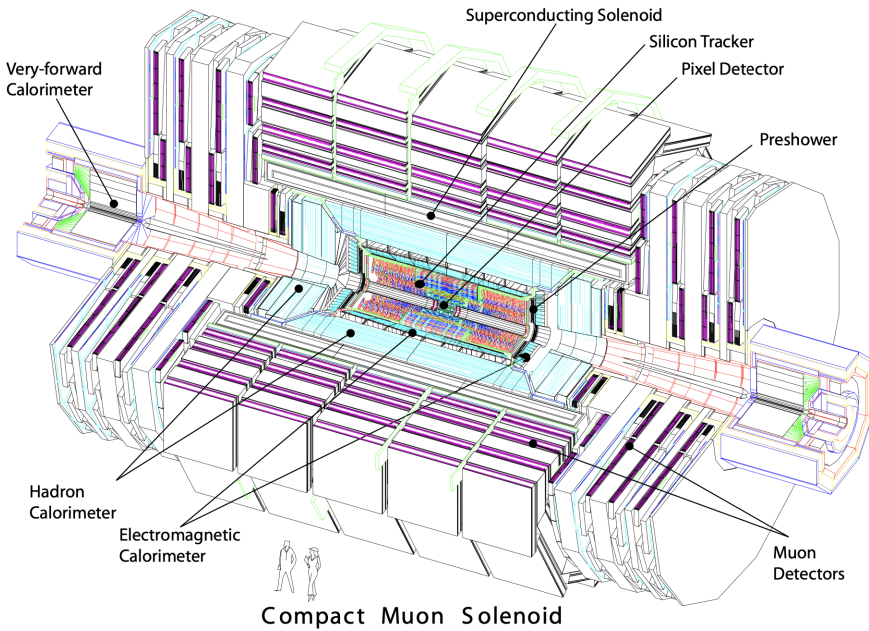


Figure 2.4: Diagram of the CMS detector showing inner components (retrieved from (Collaboration 2008))

The different sub-detectors are located concentrically in layers (Collaboration 2008). The inner most layer has a pixel detector made out of silicon, used for the reconstruction of primary and secondary vertices from electrically charged particles that decay promptly within this sub-detector volume. The pixel detector is followed by a sub-detector made of silicon strips, known as the tracker detector, used for the reconstruction of trajectories of electrically charged particles. Following the tracker detector, are found the electromagnetic (ECAL) and hadron (HCAL) calorimeters, used to measure both energy and direction of the particles undergoing electromagnetic and strong interactions, respectively. The ECAL detector is a modular device composed of lead-tungsten crystals, highly efficient to produce electromagnetic showers after interacting with charged particles. The emerging photons from the showers are measured using photo-diodes, that collect the light produced from the signal and convert it into an electric signal. This signal is then used by software tools to detect the energy and direction of the corresponding particles (Collaboration 2008). The ECAL is made of non magnetic materials such as copper and steel, which are characterized by heavy nuclei favoring strong interactions. Following a similar functioning as ECAL, hadronic particles enter the calorimeter, interact with the non-magnetic layers producing hadronic showers. These showers are then detected by plastic scintillators and their signals are transformed into electric pulses. These signals are then analyzed to estimate the energy and direction of the original particles (Collaboration 2008).

The next layer of the detector consists of a superconducting solenoid, which surrounds the previous sub-detectors. This solenoid is made of a niobium-titanium alloy that is refrigerated to 2 K by using liquid helium, producing a uniform magnetic field of 3.8 T inside the barrel (Collaboration 2008). This magnetic field is used to measure the momentum of electrically charged particles as it induces curvatures in their trajectories.

Finally, the last set sub-detectors conform the muon detector system. This system is made of three different detector technologies, that allow to reconstruct the trajectory of the muons with a fast trigger response, and are alternated with iron

returning yokes of steel to enclose the magnetic field produced by the solenoid. The trigger is a date-filtering system composed of hardware and software algorithms, designed to collect interesting events from the proton-proton collisions. The muon detectors have a total of 1400 chambers distributed in 250 drift tubes, 540 cathode strip chambers that track the position of a muon and provide a trigger, as well as 610 resistive plate chambers that give a redundant trigger, which quickly decide over the event storage (Collaboration 2008).

Due to its cylindrical geometry, the CMS detector is divided into a central barrel region and two forward endcaps, which define the detector acceptance in terms of the pseudorapidity. The barrel region provides coverage for $|\eta| \lesssim 1.5$, while the endcap regions extend the acceptance up to $1.5 \lesssim |\eta| \lesssim 2.5$ for most subsystems (Collaboration 2008).

This geometrical segmentation impacts the overall detection efficiency. For example, the pixel and silicon strip trackers are more efficient in the barrel, where multiple tracking layers are crossed perpendicularly by particles. In the endcaps, particles cross detector layers at shallow angles, leading to reduced hit multiplicity and, consequently, lower tracking efficiency and resolution. Similar considerations apply to the ECAL and HCAL subsystems, where the granularity and material budget have been optimized to compensate for the non-uniform geometry, maintaining energy resolution across η .

Muon identification and momentum reconstruction also exhibit regional differences. The drift tubes (DTs), which offer high spatial resolution, are only installed in the barrel, while cathode strip chambers (CSCs) and resistive plate chambers (RPCs) cover the endcap regions. The combination of technologies ensures redundancy and robust triggering throughout the full detector acceptance. However, due to the higher background levels and increased radiation in the endcaps, the performance of muon reconstruction tends to be better in the barrel. For muons (electrons), the assumed identification efficiency is 95% (85%), with a 0.3% (0.6%) mis-identification rate (**CMS-PAS-FTR-13-014**; **CMS_MUON_17001**; **CMS_EGM_17001**).

Following reference (**CMS_BTV2016**), we use a flat identification efficiency for b jets of 70% across the entire p_T spectrum with misidentification rate of 1%. These values correspond with the “medium working point” of the CMS algorithm to identify b jets, known as DeepCSV. We also explored the “Loose” (“Tight”) working point using an efficiency of 85% (45%) and mis-identification rate of 10% (0.1%).

For the performance of τ_h identification in DELPHES, we consider the latest technique described in (**CMS_DeepTau**), which is based on a deep neural network (i.e. DeepTau) that combines variables related to isolation and τ -lepton lifetime as input to identify different τ_h decay modes. Following (**CMS_DeepTau**), we consider three possible DeepTau “working points”: (i) the “Medium” working point of the algorithm, which gives a 70% τ_h -tagging efficiency and 0.5% light-quark and gluon jet mis-identification rate; (ii) the “Tight” working point, which gives a 60% τ_h -tagging efficiency and 0.2% light-quark and gluon jet mis-identification rate; and (iii) the “VTight” working point, which gives a 50% τ_h -tagging efficiency and 0.1% light-quark and gluon jet mis-identification rate. Similar to the choice of b-tagging working point, the choice of τ_h -tagging working point is determined through an optimization process which maximizes discovery reach. The “Medium” working point was ultimately shown to provide the best sensitivity and therefore chosen for this study.

2.3 PHENOMENOLOGICAL PIPELINE

The contributions of signal and background events in this work are estimated using Monte Carlo (MC) simulations, a widely adopted methodology for studying hypothetical signals from new physics models and assessing their observability in experiments such as the LHC. Monte Carlo simulations allow us to:

- Perform automated calculations, such as cross-sections and decay widths.
- Conduct feasibility studies before data collection.
- Estimate event selection efficiency and acceptance.
- Predict background event rates.
- Distinguish between different signal hypotheses.

The simulation process is modular, comprising several distinct stages that mimic the experimental pipeline. Model implementation is done using `FeynRules` (v2.3.43) ([Christensen:2008py](#); [Alloul:2013bka](#)), which translates the Lagrangian of the new physics scenario into a Universal FeynRules Output (UFO) format containing Feynman rules. This output, along with a parameter card specifying numerical values for the free parameters, is used as input to the `MadGraph5_aMC@NLO` (v3.5.7) ([Alwall:2014bza](#); [Alwall:2014hca](#)) framework.

Within `MadGraph`, the process begins with generating the matrix elements and Feynman diagrams for a given process. Then, using the `MadEvent` submodule, hard scattering events are produced. Samples are generated for proton-proton collisions at center-of-mass energies of $\sqrt{s} = 13\text{ TeV}$ and $\sqrt{s} = 13.6\text{ TeV}$, using the `NNPDF3.0 NLO` ([NNPDF:2014otw](#)) set for parton distribution functions (PDFs). The full squared amplitude (SDE) strategy is employed for phase-space integration to correctly handle strong interference effects, such as those involving a Z' boson.

The output of `MadEvent` is stored in the Les Houches Event (LHE) format, containing the four-momenta of all final-state particles. The generation is optimized through configuration of the `run_card`, ensuring that only detectable final-state partons are included, which avoids wasting computational resources on events that will be rejected by detector simulation.

Subsequently, the parton-level events are passed to `PYTHIA` (v8.2.44) ([Sjostrand:2014zea](#)), which simulates parton showers, fragmentation, and hadronization. This step translates partons into stable hadrons and resonances. The resulting events, saved in `HepMC2` format, are then processed by `DELPHES` (v3.4.2) ([deFavereau:2013fsa](#)), a fast detector simulation framework. `DELPHES` emulates the CMS detector response, using detector geometry and reconstruction performance input cards to simulate tracking, calorimetry, and particle identification. The final output is stored in `ROOT` format, ready for data analysis.

From this point onward, the analysis closely mirrors that of real experimental data, including event selection, reconstruction of physical objects (e.g., jets, leptons), and tagging of specific particle candidates like b -jets, light jets, and hadronic taus.

2.4 MEASUREMENT OF THE POWER OF AN ANALYSIS

In high-energy physics experiments, data is often discretized into bins (e.g., histograms of collision events versus energy or momentum) to test competing hypotheses. The fundamental framework compares two scenarios: the *null hypothesis* (H_0), representing background-only processes (b_i in each bin i), and the *alternative*

hypothesis (H_1), including both signal and background ($s_i + b_i$). Given the Poissonian nature of event counts n_i , the likelihood for observing the data under each hypothesis is:

$$\mathcal{L}(n_i | \lambda_i) = \frac{e^{-\lambda_i} \lambda_i^{n_i}}{n_i!}, \quad \text{where } \lambda_i = \begin{cases} b_i & \text{for } H_0, \\ s_i + b_i & \text{for } H_1. \end{cases} \quad (2.4)$$

The Neyman-Pearson lemma (NeymanPearson1933) provides a rigorous framework for hypothesis testing by establishing that the *likelihood ratio* $Q = \mathcal{L}(\text{data} | H_1)/\mathcal{L}(\text{data} | H_0)$ is the most powerful test statistic for distinguishing between two simple hypotheses, H_0 and H_1 . This forms the basis for quantifying the evidence for new physics signals against known backgrounds. For binned analyses in particle physics, we define the likelihood ratio Q_i for each bin i as,

$$Q_i = \frac{\mathcal{L}(n_i | s_i + b_i)}{\mathcal{L}(n_i | b_i)} = e^{-s_i} \left(1 + \frac{s_i}{b_i}\right)^{n_i}, \quad (2.5)$$

where n_i is the observed event count, s_i the expected signal, and b_i the expected background in bin i .

The test statistic for the full analysis is constructed as the product of individual bin likelihood ratios:

$$Q = \prod_{i=1}^N Q_i, \quad (2.6)$$

where N is the total number of bins. Under this formulation, each bin is treated as an independent experiment, allowing us to analyze the data in a modular way. This is particularly useful when combining results from multiple search channels or energy ranges. If we take the logarithm of the likelihood ratio this property turns into an additive form and, by the Wilks' theorem (Wilks1938), the asymptotic distribution of the test statistic $-2 \ln Q$ under the background-only hypothesis (H_0) follows the χ^2 distribution facilitating p-value calculations and hypothesis testing. So, for convenience and connection to asymptotic distributions, we consider the logarithmic form:

$$-2 \ln Q = -2 \sum_{i=1}^N \ln Q_i = 2 \sum_{i=1}^N \left[s_i - n_i \ln \left(1 + \frac{s_i}{b_i}\right) \right]. \quad (2.7)$$

Then, the practical implementation of the Neyman-Pearson lemma in particle physics leads to the definition of a test statistic t that quantifies the evidence for a signal against the background-only hypothesis, constructed as

$$t = -2 \ln Q = \sum_{i=1}^N [2s_i - 2n_i w_i] \quad (2.8)$$

where N is the total number of bins and $w_i = \ln(1 + s_i/b_i)$ is the optimal weight for bin i .

The discovery significance κ quantifies the statistical separation of t if n is distributed according to the background-only hypothesis (H_0) versus the signal-plus-background hypothesis (H_1), normalized by the standard deviation of the H_1 distribution,

$$\kappa = \frac{\langle t \rangle_{H_0} - \langle t \rangle_{H_1}}{\sigma_{H_1}}. \quad (2.9)$$

The expected behavior differs under the signal-plus-background (H_1) and background-only (H_0) hypotheses:

- Under H_1 ($n_i \sim \text{Pois}(s_i + b_i)$):

$$\langle -2 \ln Q \rangle_{s+b} = \sum_i [2s_i - 2(s_i + b_i)w_i] \implies \sigma_{s+b}^2 = 4 \sum_i (s_i + b_i)w_i^2. \quad (2.10)$$

- Under H_0 ($n_i \sim \text{Pois}(b_i)$):

$$\langle -2 \ln Q \rangle_b = \sum_i [2s_i - 2b_i w_i] \implies \sigma_b^2 = 4 \sum_i b_i w_i^2 \quad (2.11)$$

Substituting in κ gives a useful expression for the discovery significance,

$$\kappa = \frac{\sum s_i w_i}{\sqrt{\sum (s_i + b_i) w_i^2}} \quad (2.12)$$

It quantifies the separation between the signal+background ($s+b$) and background-only hypotheses in units of standard deviations (σ), where $\kappa = 5$ corresponds to the traditional 5σ discovery threshold, $\kappa = 3$ to a 3σ evidence to the traditional anomaly detection threshold, and $\kappa = 1.69$ to the 95% confidence level (CL) exclusion limit.

This figure of merit automatically optimizes sensitivity through the logarithmic weights $w_i = \ln(1 + s_i/b_i)$, which naturally emphasize bins with either high signal-to-background ratios (s_i/b_i) or large absolute signal contributions (s_i). In asymptotic limits, κ simplifies to intuitive forms: for dominant signals ($s_i \gg b_i$), it approaches $\sqrt{\sum s_i}$ (Poisson counting), while in background-dominated regimes ($s_i \ll b_i$), it reduces to an inverse-variance-weighted sum $\sum s_i / \sqrt{\sum b_i (s_i/b_i)^2}$. This dual behavior ensures optimal discrimination power across all signal regimes.

In practice, we must take into account systematic effects by incorporating nuisance parameters into the likelihood and profiling over uncertainty ranges. The power calculation can be extended to include systematic uncertainties by modifying the denominator as,

$$\kappa_{\text{sys}} = \frac{\sum_i s_i w_i}{\sqrt{\sum_i [(s_i + b_i) + \sigma_{\text{sys,signal},i}^2 + \sigma_{\text{sys,bkg},i}^2] w_i^2}}, \quad (2.13)$$

where σ_{sys} terms represent the systematic uncertainties on signal and background predictions.

3

BSM SIGNATURES IN DI-TAU FINAL STATES

3.1 A SIMPLIFIED MODEL FOR THE \tilde{S}_1 SCALAR LEPTOQUARK

Leptoquarks (LQs) are hypothetical bosonic particles that couple simultaneously to a quark and a lepton, thereby mediating lepton-quark interactions at a single vertex. They arise naturally in various extensions of SM, including grand unified theories and models with extended gauge symmetries, and have attracted renewed interest as a possible explanation for observed flavor anomalies and hints of lepton flavor non-universality.

To ensure Lorentz invariance, the interaction vertex involving a leptoquark, a quark, and a lepton must form a scalar or vector operator. Among these possibilities, scalar leptoquarks (scalar-LQs) provide a minimal and renormalizable framework without requiring new gauge interactions, making them an ideal starting point for simplified model studies.

The classification of scalar leptoquarks is determined by their transformation properties under the SM gauge group $SU(3)_C \times SU(2)_L \times U(1)_Y$. For simplicity, we focus on scalar-LQs that are singlets under $SU(2)_L$, so that the model contains a single new scalar degree of freedom. This constraint leads to interactions involving two fermions of the same chirality, which requires charge conjugation of one of the fields to build a Lorentz scalar.

There are two classes of gauge-invariant, renormalizable operators that couple such a singlet scalar-LQ to SM fermions. These are:

1. $I_1 = \bar{q}_L^C \epsilon \ell_L$ and $I'_1 = \bar{u}_R^C e_R$, where q_L and ℓ_L are left-handed quark and lepton doublets, respectively, and u_R , e_R are right-handed singlets. Both I_1 and I'_1 are $SU(2)_L$ singlets, transform as color triplets under $SU(3)_C$, and carry hypercharge $Y = -2/3$.
2. $\tilde{I}_1 = \bar{d}_R^C e_R$, a gauge-invariant operator involving two right-handed singlets. It is also a color triplet and an $SU(2)_L$ singlet, but with hypercharge $Y = -8/3$.

The corresponding leptoquark representations are:

1. $S_1 \doteq (\bar{\mathbf{3}}, \mathbf{1}, 2/3)$, consistent with the first set of operators.
2. $\tilde{S}_1 \doteq (\bar{\mathbf{3}}, \mathbf{1}, 8/3)$, associated with the second invariant.

In models with flavor alignment or preferential couplings to third-generation fermions, S_1 typically couples to $b\nu_\tau$ and $t\tau$ vertices. However, processes like $pp \rightarrow \tau^+\tau^-$ suffer suppression due to the low parton density of the top quark in the proton.

In contrast, the \tilde{S}_1 leptoquark allows for direct couplings to b quarks and τ leptons via a term of the form $\bar{d}_R^C \tilde{S}_1 e_R$. Despite the relatively small b -quark content in the proton, these channels remain accessible at the LHC.

For these reasons, this section focuses on the simplified model containing only the scalar leptoquark \tilde{S}_1 . The most general renormalizable Lagrangian for the \tilde{S}_1 leptoquark extends the SM one by

$$\mathcal{L} \supset |D_\mu \tilde{S}_1|^2 + \tilde{y}_{ij} \bar{d}_R^C i \tilde{S}_1 e_R^j + \tilde{z}_{ij} \bar{u}_R^C i \tilde{S}_1^* u_R^j + \text{h.c.} + V_{\text{ext}}(\tilde{S}_1, H) \quad (3.1)$$

Note that \tilde{z} must be antisymmetric (due to fermionic statistics) and is typically assumed to vanish or be highly suppressed to avoid large FCNCs.

where \tilde{y}, \tilde{z} are complex Yukawa matrices in the flavor space, D_μ is the covariant derivative acting on the \tilde{S}_1 field as

$$D_\mu \tilde{S}_1 = \partial_\mu \tilde{S}_1 + ig_s T^a G_\mu^a \tilde{S}_1 + i \frac{4}{3} g' B_\mu \tilde{S}_1, \quad (3.2)$$

and V_{ext} is the extension of the SM Higgs potential to include the leptoquark field given by

$$V_{\text{ext}} = \mu_{\tilde{S}_1}^2 |\tilde{S}_1|^2 + \lambda_{\tilde{S}_1} |\tilde{S}_1|^4 + \lambda_{H\tilde{S}_1} |H|^2 |\tilde{S}_1|^2, \quad (3.3)$$

such that the full scalar potential reads

$$V = \underbrace{-\mu^2 |H|^2 + \lambda |H|^4}_{\text{SM Higgs}} + \underbrace{\mu_{\tilde{S}_1}^2 |\tilde{S}_1|^2 + \lambda_{\tilde{S}_1} |\tilde{S}_1|^4}_{\text{scalar-LQ self-interactions}} + \underbrace{\lambda_{H\tilde{S}_1} |H|^2 |\tilde{S}_1|^2}_{\text{Higgs portal}}. \quad (3.4)$$

After EWSB, $H \rightarrow (0, (\nu + h)/\sqrt{2})^T$, the $H\tilde{S}_1$ interactions become interactions between the physical Higgs boson h and the leptoquark \tilde{S}_1 as

$$\mathcal{L}_{\text{int}} \supset \lambda_{H\tilde{S}_1} v h |\tilde{S}_1|^2 + \frac{1}{2} \lambda_{H\tilde{S}_1} h^2 |\tilde{S}_1|^2 \quad (3.5)$$

and a mass shift for the leptoquark field

$$\Delta m_{\tilde{S}_1}^2 = \frac{1}{2} \lambda_{H\tilde{S}_1} v^2 \implies m_{\tilde{S}_1}^2 = \mu_{\tilde{S}_1}^2 + \frac{1}{2} \lambda_{H\tilde{S}_1} v^2. \quad (3.6)$$

Additionally, from the covariant derivative as $B_\mu = c_W A_\mu - s_W Z_\mu$, the \tilde{S}_1 interactions with the SM gauge bosons are given by

$$\mathcal{L} \supset \frac{4}{3} e [(\partial_\mu \tilde{S}_1^*) \tilde{S}_1 - \tilde{S}_1^* (\partial_\mu \tilde{S}_1)] A^\mu + \left(\frac{4}{3} e \right)^2 A_\mu A^\mu |\tilde{S}_1|^2 \quad (3.7)$$

$$\mathcal{L} \supset -\frac{4}{3} g_1 s_W [(\partial_\mu \tilde{S}_1^*) \tilde{S}_1 - \tilde{S}_1^* (\partial_\mu \tilde{S}_1)] Z^\mu + \left(\frac{4}{3} g_1 s_W \right)^2 Z_\mu Z^\mu |\tilde{S}_1|^2. \quad (3.8)$$

For preferential couplings to third-generation fermions in the lepton-quark vertices, we assume the texture of the Yukawa matrix \tilde{y}_{33} is such that $\tilde{y}_{33} \gg \tilde{y}_{ij}$ for $i, j \neq 3$. This results in a preferential decay of the scalar-LQ into $b\tau$ final states, with branching ratio $\text{BR}(\tilde{S}_1 \rightarrow b\tau) \approx 1$ for large scalar-LQ masses.

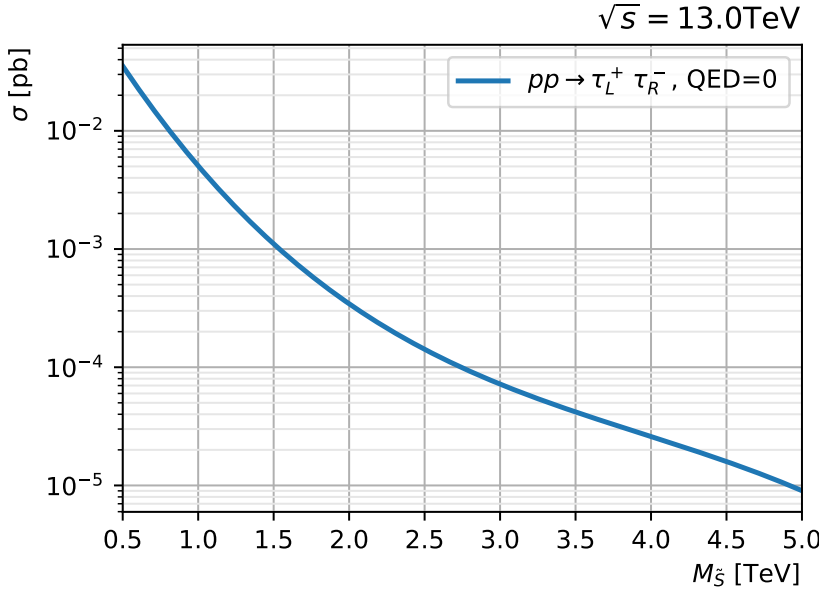


Figure 3.1: Cross section for scalar leptoquark (scalar-LQ) pair production decaying to $\tau^+\tau^-$ final states, showing different τ polarization configurations as a function of scalar-LQ mass at $\sqrt{s} = 13.0$ TeV. The coupling is fixed to $\tilde{y}_{33} = 1.0$.

It is worth noting that, due to the right-handed structure of the Yukawa interaction the scalar leptoquark \tilde{S}_1 couples only to right-chiral tau leptons. As a result, the dominant contribution to the $\tau^+\tau^-$ final state originates from the configuration where the outgoing taus have opposite helicities, specifically $\tau_L^+\tau_R^-$. This polarization asymmetry provides a characteristic signature that could be probed using polarization-sensitive observables, such as the asymmetry in the charged energy of the products of the τ decay. Figure 3.1 shows the integrated production cross sections at $\sqrt{s} = 13.0$ TeV assuming a fixed coupling $\tilde{y}_{33} = 1.0$.

S

3.2 A SIMPLIFIED MODEL FOR THE U_1 VECTOR LEPTOQUARK

In contrast to what is done for the scalar-LQ, vector couplings between fermions of the same helicity are allowed without resorting to the charge conjugation matrix. In this way, the inclusion of a single vectorial LQ (vector-LQ) with signatures in the di-tau final state channel requires a vector that transforms as $U_1 \doteq (\bar{\mathbf{3}}, \mathbf{1}, 4/3)$ under the SM group.

Extending the SM with a massive U_1 vector-LQ is not straightforward, as one has to ensure the renormalizability of the model. Most of the theoretical community has focused on extensions of the Pati-Salam (PS) models which avoid proton decay, such as the scenario found in (Assad, Fornal, and Grinstein 2018). Other examples include PS models with vector-like fermions (Calibbi, Crivellin, and Li 2018; Blanke and Crivellin 2018; Iguro et al. 2021), the so-called 4321 models (Di Luzio, Greljo, and Nardecchia 2017; Greljo and Stefanek 2018; Luzio et al. 2018), the twin PS² model (King 2021; Fernández-Navarro and King 2023), the three-site PS³ model (Bordone et al. 2018a; Bordone et al. 2018b; Fuentes-Martín et al. 2022), as well as composite PS models (Gripaios 2010; Barbieri, Murphy, and Senia 2017; Barbieri and Tesi 2018).

However, in what follows, we shall restrict ourselves to a simplified non-renormalizable lagrangian for a gauge vector-LQ, understood to be embedded into a more complete model. The SM is thus extended by adding the following terms featuring the U_1 vector – LQ :

The couplings in the second line of Eq. (3.9) can be found in the literature as $g_s \rightarrow g_s(1 - \kappa_U)$ and $g' \rightarrow g'(1 - \tilde{\kappa}_U)$, in order to take into account the possibility of an underlying strong interaction.

$$\begin{aligned} \mathcal{L}_{U_1} = & -\frac{1}{2} U_{\mu\nu}^\dagger U^{\mu\nu} + M_U^2 U_{1\mu}^\dagger U_1^\mu \\ & -ig_s U_{1\mu}^\dagger T^a U_{1\nu} G^{a\mu\nu} - i\frac{2}{3}g' U_{1\mu}^\dagger U_{1\nu} B^{\mu\nu} \\ & + \frac{g_U}{\sqrt{2}} \sum_{ij} [U_{1\mu} (\beta_L^{ij} \bar{Q}_i \gamma^\mu L_i + \beta_R^{ij} \bar{d}_R^i \gamma^\mu e_R^j) + h.c.] \end{aligned} \quad (3.9)$$

where $U_{\mu\nu} \equiv \mathcal{D}_\mu U_{1\nu} - \mathcal{D}_\nu U_{1\mu}$, and $\mathcal{D}_\mu \equiv \partial_\mu + ig_s T^a G_\mu^a + i\frac{2}{3}g' B_\mu$. As evidenced by the second line above, we assume that the vector – LQ has a gauge origin.

The tight constraints from low-energy observables, such as $\Delta F = 2$ amplitudes and lepton flavor violating processes, motivates the following choice of the β_L and β_R matrices, which are 3×3 matrices in flavor space:

$$\beta_L = \begin{pmatrix} 0 & 0 & \beta_L^{d\tau} \\ 0 & 0 & \beta_L^{s\tau} \\ 0 & \beta_L^{b\mu} & 1 \end{pmatrix}, \quad \beta_R = \begin{pmatrix} 0 & 0 & 0 \\ 0 & 0 & 0 \\ 0 & 0 & \beta_R^{b\tau} \end{pmatrix}. \quad (3.10)$$

Several works have studied the structure of the β_L and β_R matrices and the choice above is consistent with the breaking of $U(2)$ symmetry in the flavor space (Cornella et al. 2021a; Assad, Fornal, and Grinstein 2018; Calibbi, Crivellin, and Li 2018; Blanke and Crivellin 2018).

The third and fourth lines in Eq. (3.9) shows the vector – LQ interactions with SM fermions, with coupling g_U , which we have chosen as preferring the third generation. These are particularly relevant for the vector – LQ decay probabilities, as well as for the single-vector – LQ production cross-section. The $\beta_L^{s\tau}$ parameter, which is the vector – LQ $\rightarrow s\tau$ coupling in the β_L matrix (see marginpar), is chosen to be equal to 0.2, following the fit done in (Cornella et al. 2021a), in order to simultaneously solve the $R_{D^{(*)}}$ anomaly and satisfy the $p p \rightarrow \tau^+ \tau^-$ constraints. Although $\beta_L^{s\tau}$ technically alters the single-vector – LQ production cross-section and vector – LQ branching fractions, we have confirmed that a value of $\beta_L^{s\tau} = 0.2$ results in negligible impact on our collider results, and thus is ignored in our subsequent studies.

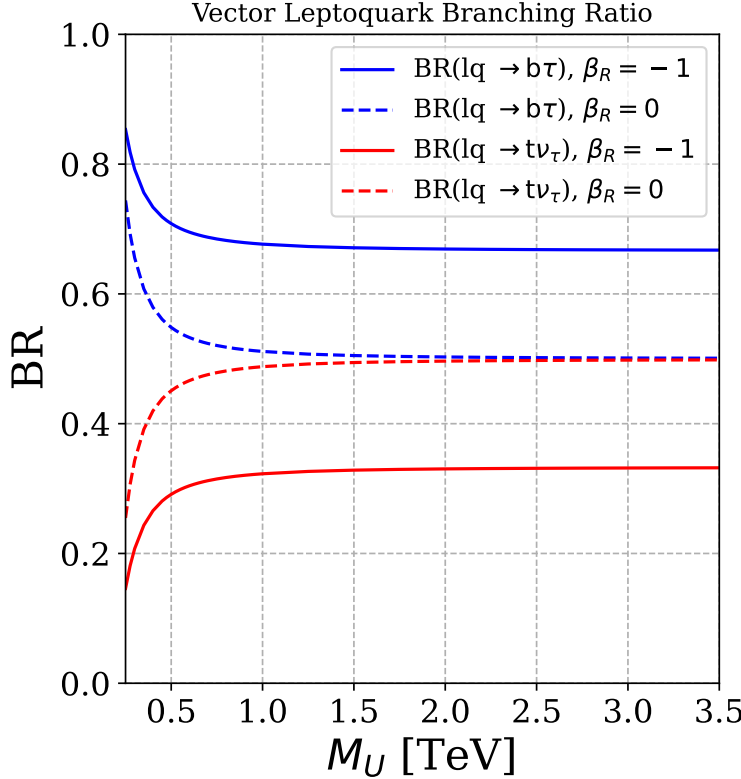


Figure 3.2: The vector – LQ $\rightarrow b\tau$ and vector – LQ $\rightarrow t\nu$ branching ratios for $\beta_R^{b\tau} = 0$ (solid lines) and $\beta_R^{b\tau} = -1$ (dashed lines).

The vector – LQ right-handed coupling is modulated with respect to the left-handed one by the $\beta_R^{b\tau}$ parameter. The choice of $\beta_R^{b\tau}$ is important phenomenologically, as it affects the vector – LQ branching ratios, as well as the single-vector – LQ production cross-section. To illustrate the former, Figure 3.2 (top) shows the vector – LQ $\rightarrow b\tau$ and vector – LQ $\rightarrow t\nu$ branching ratios as functions of the vector – LQ mass, for two values of $\beta_R^{b\tau}$. For large vector – LQ masses, we confirm that with $\beta_R^{b\tau} = 0$ then $\text{BR}(\text{vector – LQ} \rightarrow b\tau) \approx \text{BR}(\text{vector – LQ} \rightarrow t\nu) \approx \frac{1}{2}$. However, for $\beta_R^{b\tau} = -1$, as was chosen in (Cornella, Fuentes-Martín, and Isidori 2019), the additional coupling adds a new term to the total amplitude, leading to $\text{BR}(\text{vector – LQ} \rightarrow b\tau) \approx \frac{2}{3}$. The increase in this branching ratio can thus weaken bounds from vector – LQ searches targeting decays into $t\nu$ final states, which motivates exploring the sensitivity in $b\tau$ final states exclusively. Note that although a $\text{BR}(\text{vector – LQ} \rightarrow b\tau) \approx 1$ scenario is possible by having the vector – LQ couple exclusively to right-handed currents (i.e., $g_U \rightarrow 0$, but $g_U \beta_R^{b\tau} \neq 0$), it does not solve the observed anomalies in the $R_{D^{(*)}}$ ratios. Therefore, although some LHC searches assume $\text{BR}(\text{vector – LQ} \rightarrow b\tau) = 1$, we stress that in our studies we assume values of the model parameters and branching ratios that solve the $R_{D^{(*)}}$ ratios.

Having $\beta_L^{s\tau}$ different from zero also opens new decay channels. These, however, are either suppressed by $\beta_L^{s\tau}$ and powers of λ_{CKM} . In any case, this effect would decrease $\text{BR}(\text{vector – LQ} \rightarrow b\tau)$ and $\text{BR}(\text{vector – LQ} \rightarrow t\nu)$ by less than 3%.

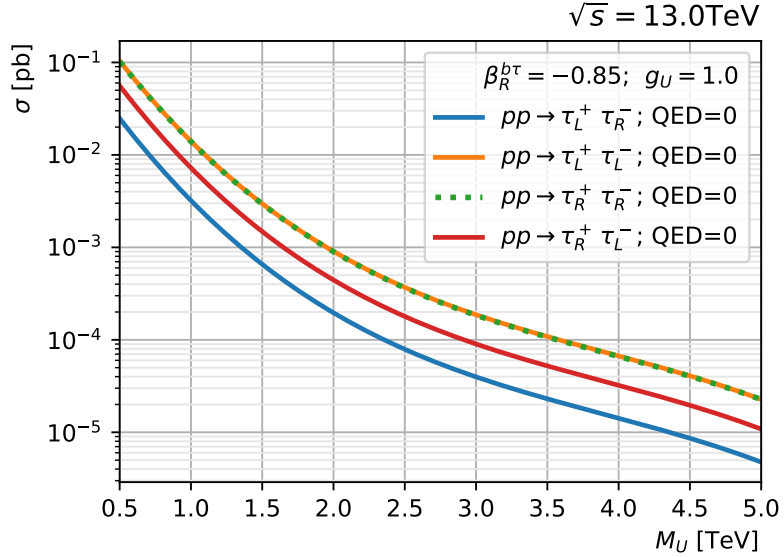


Figure 3.3: Cross section to $\tau^+\tau^-$ final states mediated for a vector-LQ in t-channel, showing different τ polarization configurations as a function of vector-LQ mass at $\sqrt{s} = 13.0\text{TeV}$. The couplings are fixed to $g_U = 1.0$ and $\beta_R^{b\tau} = -0.85$.

Unlike the scalar leptoquark (S_1) model, the vector leptoquark (U_1) couples to both left- and right-handed chiral currents, allowing for distinct polarization configurations in the $b\bar{b} \rightarrow \tau^+\tau^-$ final states. This feature is critical for collider phenomenology, as it influences the kinematic distributions of the final-state particles. The squared amplitudes for each polarization configuration in the center-of-mass frame can be expressed as follows:

$$|\mathcal{M}(\tau_L^+\tau_L^-)|^2 \propto g_U^4 (\tanh \eta + 1)^2, \quad (3.11)$$

$$|\mathcal{M}(\tau_L^+\tau_R^-)|^2 = |\mathcal{M}(\tau_R^+\tau_L^-)|^2 \propto 4g_U^4 \beta_R^2, \quad (3.12)$$

$$|\mathcal{M}(\tau_R^+\tau_R^-)|^2 \propto g_U^4 (\tanh \eta + 1)^2 \beta_R^4, \quad (3.13)$$

where η denotes the pseudorapidity of the τ lepton with respect to the incident b -quark direction, or equivalently, the pseudorapidity of the anti- τ lepton with respect to the incident \bar{b} -quark direction. Figure 3.3 shows the η -integrated production cross sections computed for an intermediate benchmark point with fixed couplings $g_U = 1.0$ and $\beta_R^{b\tau} = -0.85$.

We define the polarization asymmetry \mathcal{P}_{τ^-} of the τ lepton as the difference between the right-handed and left-handed contributions, normalized by their sum:

$$\mathcal{P}_{\tau^-} = \frac{|\mathcal{M}_R|^2 - |\mathcal{M}_L|^2}{|\mathcal{M}_R|^2 + |\mathcal{M}_L|^2} = \frac{(\tanh(\eta) + 1)^2 (\beta_R^4 - 1)}{(\tanh(\eta) + 1)^2 (1 + \beta_R^4) + 8\beta_R^2}, \quad (3.14)$$

could be probed using polarization-sensitive observables like the asymmetry in the charged energy of the products of the τ decay.

$$|\mathcal{M}_R|^2 = \frac{1}{2} \left(|\mathcal{M}(\tau_R^+\tau_R^-)|^2 + |\mathcal{M}(\tau_L^+\tau_R^-)|^2 \right), \quad (3.15)$$

$$|\mathcal{M}_L|^2 = \frac{1}{2} \left(|\mathcal{M}(\tau_L^+\tau_L^-)|^2 + |\mathcal{M}(\tau_R^+\tau_L^-)|^2 \right). \quad (3.16)$$

Figure 3.4 shows the polarization asymmetry \mathcal{P}_{τ^-} of the τ lepton as a function of its pseudorapidity η for different values of the $\beta_R^{b\tau}$ parameter. The asymmetry is

maximal for $\beta_R^{b\tau} = -1$, which corresponds to the scenario where the vector – LQ couples exclusively to right-handed currents, and minimal for $\beta_R^{b\tau} = 0$, where the vector – LQ couples only to left-handed currents. The polarization asymmetry is sensitive to the choice of $\beta_R^{b\tau}$, and thus can be used to probe the underlying BSM model.

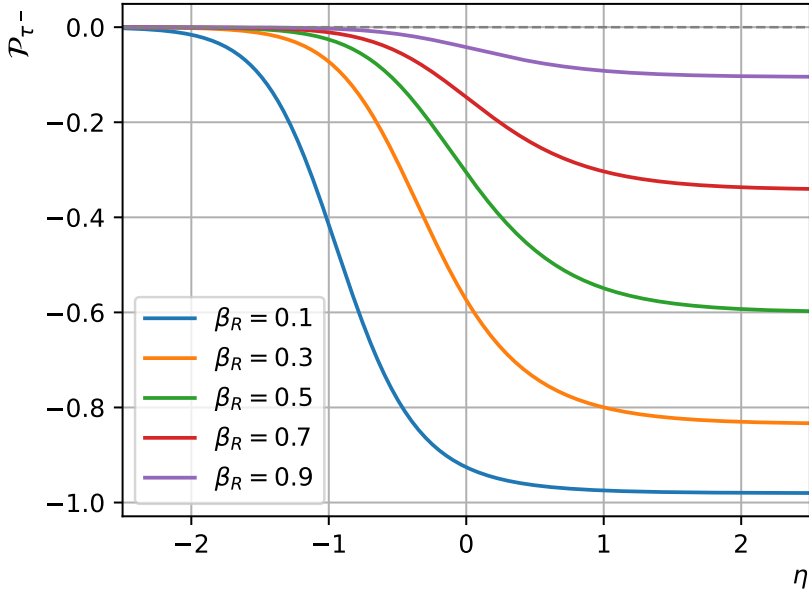


Figure 3.4: The polarization asymmetry P_{τ^-} of the τ lepton as a function of its pseudorapidity η for different values of the $\beta_R^{b\tau}$ parameter.

Going to the detector frame, in pp collisions we do not have a well-defined direction for the incoming b-quark due to we do not know which proton the b-quark comes from. So in average, we must promediate the two proton directions,

$$\mathcal{P}_{\tau^-}^{\text{avg}} = \frac{1}{2} (\mathcal{P}_{\tau^-}(\eta) + \mathcal{P}_{\tau^-}(-\eta)). \quad (3.17)$$

Figure 3.5 shows the average polarization asymmetry $\mathcal{P}_{\tau^-}^{\text{avg}}$ of the τ lepton as a function of its pseudorapidity η for different values of the $\beta_R^{b\tau}$ parameter. The polarization has a strong non-null dependence on η mainly for small values of $\beta_R^{b\tau}$, where the polarization asymmetry is maximal. For larger values of $\beta_R^{b\tau}$, the polarization asymmetry becomes less sensitive to the pseudorapidity, and the average polarization asymmetry approaches a constant value near zero. This signature is particularly relevant to differentiate the vector-LQ model from the scalar-LQ model, where the polarization asymmetry is always zero due to the right-handed structure of the Yukawa interaction.

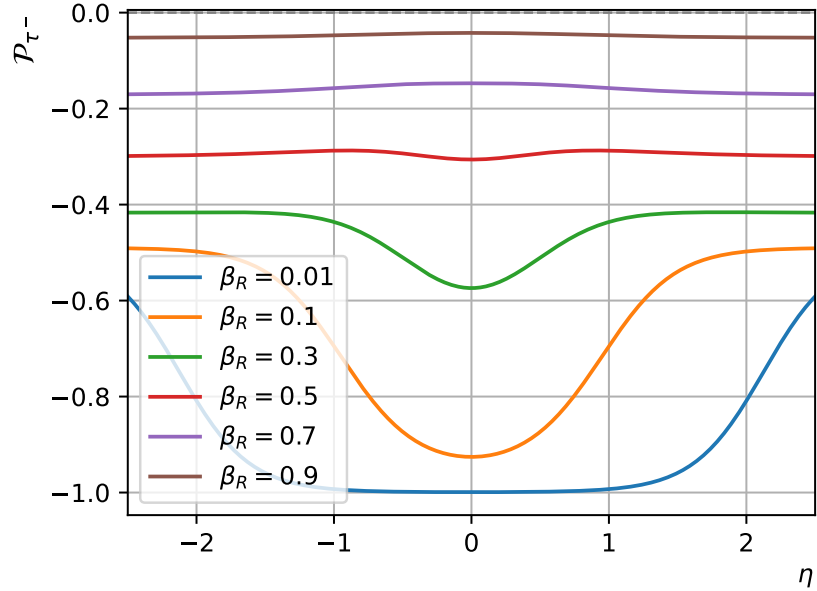


Figure 3.5: The average polarization asymmetry P_{τ}^{avg} of the τ lepton as a function of its pseudorapidity η for different values of the $\beta_R^{b\tau}$ parameter.

The simulated signal and background events are initially filtered using selections which are motivated by experimental constraints, such as the geometric constraints of the CMS detector, the typical kinematic thresholds for reconstruction of particle objects, and the available triggers. The remaining events after the preliminary event selection criteria are used to train and execute a BDT algorithm for each signal point in the $\{M_U, g_U\}$ space, in order to maximize the probability to detect signal amongst background events. The BDT algorithm is implemented using the `scikit-learn` ([pedregosa_scikit-learn_2011](#)) and `xgboost` (XGB) ([chen_xgboost_2016](#)) python libraries. We use the XGBClassifier class from the xgboost library, a 10-fold cross validation using the scikit-learn method (GridCV¹) for a grid in a hyperparameter space with 75, 125, 250, and 500 estimators, maximum depth in 3, 5, 7, 9, as well as learning rates of 0.01, 0.1, 1, and 10. For the cost function, we utilize the default mean square error (MSE). Additionally, we use the tree method based on the approximate greedy algorithm (histogram-optimized), referred to as `hist`, with a uniform sample method. These choices allow us to maximize the detection capability of the BDT algorithm by carefully tuning the hyperparameters, selecting an appropriate cost function, and utilizing an optimized tree construction method.

For both channels and each $\{M_U, g_U\}$ signal point, the binary XGB classifier was trained (tested) with 20% (80%) of the simulated events, for each signal and background MC sample. Over forty kinematic and topological variables were studied as input for the XGB. These included the momenta of b jets and $\tau_{h,\ell}$ candidates; both invariant and transverse masses of pairs of τ objects and of b τ combinations; angular differences between b jets, between τ objects, and between the $\tau_{h,\ell}$ and b jets; and additional variables derived from the missing momentum in the events. After studying correlations between variables and their impact on the performance of the BDT, we found that only eight variables were necessary and responsible for the majority of the sensitivity of the analysis.

¹ GridCV is a method that allows to find the best combination of hyperparameter values for the model, as this choice is crucial to achieve an optimal performance.

The variable that provides the best signal to background separation is the scalar sum of the p_T of the final state objects ($\tau_h, \tau_{h/\ell}$) and the missing transverse momentum, referred to as S_T^{MET} :

$$S_T^{\text{MET}} = |\vec{p}_T^{\text{miss}}| + \sum_{\tau_h, \tau_{h/\ell}} |\vec{p}_T| \quad (3.18)$$

The S_T^{MET} variable has been successfully used in LQ searches at the LHC, since it probes the mass scale of resonant particles involved in the production processes. Other relevant variables include the magnitude of the vectorial difference in p_T between the two lepton candidates ($|\Delta \vec{p}_T|_{\tau_h \tau_{h/\ell}}$), the $\Delta R_{\tau_h \tau_{h/\ell}}$ separation between them, the reconstructed dilepton mass $m_{\tau_h \tau_{h/\ell}}$, and the product of their electric charges ($Q_{\tau_h} \times Q_{\tau_{h/\ell}}$). We also use the $|\Delta \vec{p}_T|$ between the τ_h candidate and \vec{p}_T^{miss} , and (if applicable) the $|\Delta \vec{p}_T|$ between the τ_h candidate and the leading b jet. For the final states including two τ_h candidates, the one with the highest p_T is used.

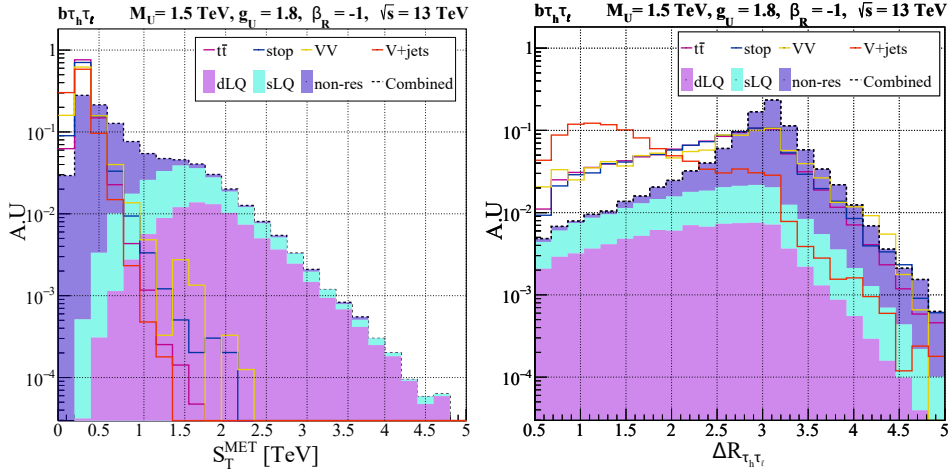


Figure 3.6: $S_T^{\text{MET}}, \Delta R_{\tau_h \tau_\ell}$, signal and background distributions for the $\tau_h \tau_\ell$ channel. The signal distributions are generated for a benchmark sample with LQ mass of 1.5 TeV maximally coupled to right-handed currents assuming a coupling $g_U = 1.0$.

Figure 3.6 shows some relevant topological distributions...

Figure 3.7: The BDT output for the $\tau_h \tau_\ell$ channel, showing the signal and background distributions for a benchmark sample with LQ mass of 1.5 TeV maximally coupled to right-handed currents assuming a coupling $g_U = 1.0$. The BDT output is defined as the logarithm of the ratio of the probability of the event being signal over the probability of it being background.

Figure 3.7

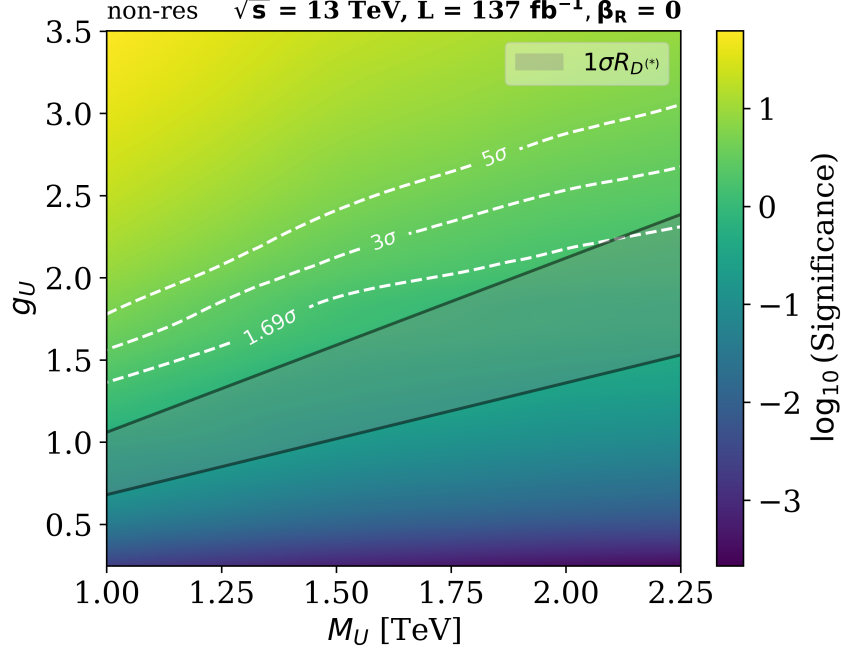


Figure 3.8: The significance of the $\tau\tau$ signal, as a function of the LQ mass and coupling g_U , for the non-resonant production of $\tau\tau$ final states at $\sqrt{s} = 13.0$ TeV, with an integrated luminosity of 137 fb^{-1} .

Figure 3.8...

3.3 A SIMPLIFIED MODEL FOR A Z'_{B-L} BOSON

Hypothetical heavy neutral bosons, such as the Z' boson, are a common feature in many BSM models. They arise from extended gauge symmetries and can couple to fermions in ways that differ from the SM Z boson. Assuming a $U(1)_{B-L}$ extension of the SM gauge group, the Z' boson can couple to fermions through a gauge interaction that is proportional to their baryon minus lepton number ($B - L$). This coupling can lead to new interactions and processes that are not present in the SM, such as flavor-changing neutral currents or enhanced production of certain final states depending on the symmetry breaking pattern and the mass of the Z' boson. Additionally, we could consider textures in the flavor space of the Z' couplings, which can lead to preferential couplings to specific generations of fermions and to avoid large flavor-changing neutral currents (FCNCs) we assume that they are diagonal in the flavor space.

Accordingly, we assume the Z' only couples to third-generation fermions. Our simplified model is thus extended by:

$$\begin{aligned} \mathcal{L}_{Z'} &= -\frac{1}{4} Z'_{\mu\nu} Z'^{\mu\nu} + \frac{1}{2} M_{Z'}^2 Z'_{\mu} Z'^{\mu} \\ &+ \frac{g_{Z'}}{2\sqrt{6}} Z'^{\mu} (\zeta_q \bar{Q}_3 \gamma_{\mu} Q_3 - 3\zeta_{\ell} \bar{L}_3 \gamma_{\mu} L_3) \end{aligned} \quad (3.19)$$

$$+ \zeta_t \bar{t}_R \gamma_{\mu} t_R + \zeta_b \bar{b}_R \gamma_{\mu} b_R - 3\zeta_{\tau} \bar{\tau}_R \gamma_{\mu} \tau_R \quad (3.20)$$

where the constants $M_{Z'}$, $g_{Z'}$, ζ_q , ζ_t , ζ_b , ζ_{ℓ} , ζ_{τ} , are model-dependent.

Unlike the U_1 vector leptoquark, the polarization of the τ lepton implies the opposite polarization of the anti- τ lepton, due to their production in the same chiral

line. To differentiate the contributions of each ζ parameter, we have calculated the amplitudes for the different initial and final state polarizations, which are given by:

$$|\mathcal{M}(b_L \bar{b}_R \rightarrow \tau_L^+ \tau_L^-)|^2 \propto g_Z^4 \zeta_\ell^2 \zeta_q^2 (1 + \tanh \eta)^2, \quad (3.21)$$

$$|\mathcal{M}(b_R \bar{b}_L \rightarrow \tau_R^+ \tau_L^-)|^2 \propto g_Z^4 \zeta_\ell^2 \zeta_b^2 (1 - \tanh \eta)^2, \quad (3.22)$$

$$|\mathcal{M}(b_L \bar{b}_R \rightarrow \tau_L^+ \tau_R^-)|^2 \propto g_Z^4 \zeta_\tau^2 \zeta_q^2 (1 - \tanh \eta)^2, \quad (3.23)$$

$$|\mathcal{M}(b_R \bar{b}_L \rightarrow \tau_L^+ \tau_R^-)|^2 \propto g_Z^4 \zeta_\tau^2 \zeta_b^2 (1 + \tanh \eta)^2. \quad (3.24)$$

Figure 3.9 shows the integrated production cross sections at $\sqrt{s} = 13.0$ TeV for a fixed set of couplings $g_{Z'} = 1.0$, $\zeta_\ell = 1.0$, $\zeta_q = 1.0$, $\zeta_b = 0.8$, and $\zeta_\tau = 0.6$. The cross section is sensitive to the choice of the couplings, and thus can be used to probe the underlying BSM model.

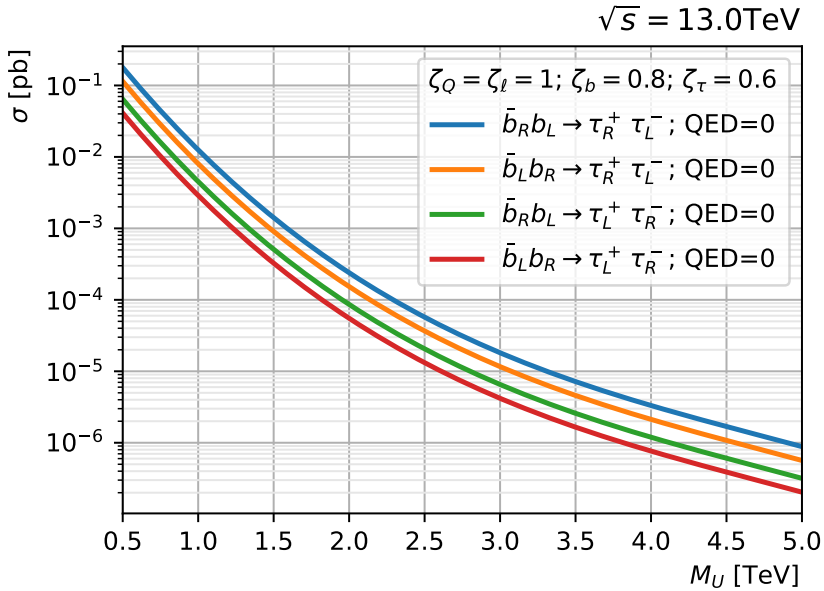


Figure 3.9: Cross section for Z' production decaying to $\tau^+ \tau^-$ final states, showing different τ polarization configurations as a function of Z' mass at $\sqrt{s} = 13.0$ TeV. The couplings are fixed to $g_{Z'} = 1.0$, $\zeta_\ell = 1.0$, $\zeta_q = 1.0$, $\zeta_b = 0.8$, and $\zeta_\tau = 0.6$.

The polarization asymmetry \mathcal{P}_{τ^-} of the τ lepton can be defined in a similar way as for the U_1 vector leptoquark, but now it is sensitive to the different couplings ζ_ℓ , ζ_q , ζ_b , and ζ_τ . The polarization asymmetry is given by:

$$\mathcal{P}_{\tau^-} = \frac{|\mathcal{M}_R|^2 - |\mathcal{M}_L|^2}{|\mathcal{M}_R|^2 + |\mathcal{M}_L|^2} \quad (3.25)$$

$$= \frac{(1 + \tanh \eta)^2 (\zeta_\tau^2 \zeta_b^2 - \zeta_\ell^2 \zeta_q^2) + (1 - \tanh \eta)^2 (\zeta_\tau^2 \zeta_q^2 - \zeta_\ell^2 \zeta_b^2)}{(1 + \tanh \eta)^2 (\zeta_\tau^2 \zeta_b^2 + \zeta_\ell^2 \zeta_q^2) + (1 - \tanh \eta)^2 (\zeta_\tau^2 \zeta_q^2 + \zeta_\ell^2 \zeta_b^2)}, \quad (3.26)$$

where we have defined the right-handed and left-handed contributions as

$$|\mathcal{M}_R|^2 = \frac{1}{2} \left(|\mathcal{M}(b_R \bar{b}_L \rightarrow \tau_L^+ \tau_R^-)|^2 + |\mathcal{M}(b_L \bar{b}_R \rightarrow \tau_L^+ \tau_R^-)|^2 \right), \quad (3.27)$$

$$|\mathcal{M}_L|^2 = \frac{1}{2} \left(|\mathcal{M}(b_R \bar{b}_L \rightarrow \tau_R^+ \tau_L^-)|^2 + |\mathcal{M}(b_L \bar{b}_R \rightarrow \tau_R^+ \tau_L^-)|^2 \right). \quad (3.28)$$

Similarly, the polarization of $t\bar{t}$ observables in Z'_{B-L} will depend on the couplings ζ_q , ζ_b , and ζ_t , and can be used to measure the parameters of the underlying BSM model.

3.4 INTERFERENCE BETWEEN THE U_1 AND Z'_{B-L} MODELS

The presence of a Z' boson in LQ models has been justified in various papers, for example, in ([Baker:2019sli](#)). The argument is that minimal extensions of the SM which include a massive gauge U_1 LQ, uses the gauge group $SU(4) \times SU(3)' \times SU(2)_L \times U(1)_{T_R^3}$. Such an extension implies the presence of an additional massive boson, Z' , and a color-octet vector, G' , arising from the spontaneous symmetry breaking into the SM. Naively, the LQs are associated to the breaking of $SU(4) \rightarrow SU(3)_{[4]} \times U(1)_{B-L}$, the G' arises from $SU(3)_{[4]} \times SU(3)' \rightarrow SU(3)_c$, and the Z' comes from the breaking of $U(1)_{B-L} \times U(1)_{T_R^3} \rightarrow U(1)_Y$. Notice that the specific pattern of breaking, and the relations between the masses and couplings, are connected to the specific scalar potential used. The Z' in particular can play an important role in the projected LQ discovery reach, as it can participate in $p p \rightarrow \tau\tau$ production by s-channel exchange, both resonantly and as a virtual mediator. To study the effect of a Z' on the $p p \rightarrow \tau\tau$ production cross-sections and kinematics, we extend our benchmark Lagrangian in Eq. (3.9) with further non-renormalizable terms involving the Z' boson according to ([3.19](#)).

We study two extreme cases for the Z' mass, following ([GINO_PhysRevD.102.115015](#)), namely $M_{Z'} = \sqrt{\frac{1}{2}} M_U < M_U$ and $M_{Z'} = \sqrt{\frac{3}{2}} M_U > M_U$. We also assume the LQ and Z' are uniquely coupled to left-handed currents, i.e. $\zeta_q = \zeta_\ell = 1$ and $\zeta_t = \zeta_b = \zeta_\tau = 0$. With these definitions, Figure 3.10 shows the effect of the Z' on the $\tau\tau$ production cross-section, considering $g_U = 1$, $\beta_R = 0$, and different $g_{Z'}$ couplings. On the top panel, the cross-sections corresponding to the cases where $M_{Z'} = \sqrt{\frac{1}{2}} M_U$ are shown. As expected, the $\tau\tau$ production cross-section for the inclusive case (i.e., $g_{Z'} \neq 0$) is larger than that for the LQ-only non-res process ($g_{Z'} = 0$, depicted in blue). This effect increases with $g_{Z'}$ and, within the evaluated values, can exceed the LQ-only cross-section by up to two orders of magnitude. In contrast, a more intricate behaviour can be seen in the bottom panel of Figure 3.10, which corresponds to $M_{Z'} = \sqrt{\frac{3}{2}} M_U$. Here, for low values of M_U , a similar increase in the cross-section is observed. However, for higher values of M_U , the inclusive $p p \rightarrow \tau\tau$ cross-section is smaller than the LQ-only $\tau\tau$ cross-section. This behaviour suggests the presence of a dominant destructive interference at high masses, leaving its imprint on the results.

In order to further illustrate the effect, Figure 3.11 shows the relative kinematic interference (RKI) as a function of the reconstructed invariant mass $m_{\tau\tau}$, for $g_{Z'} = 1$ and varying values of M_U . The RKI parameter is defined as

$$RKI(m_{\tau\tau}) = \frac{1}{\sigma_{LQ+Z'}} \left[\frac{d\sigma_{LQ+Z'}}{dm_{\tau\tau}} - \left(\frac{d\sigma_{LQ}}{dm_{\tau\tau}} + \frac{d\sigma_{Z'}}{dm_{\tau\tau}} \right) \right], \quad (3.29)$$

where σ_X is the production cross-section arising due to contributions from X particles. For example, $\sigma_{LQ+Z'}$ represents the inclusive cross-section where both virtual LQ and s-channel Z' exchange contribute. For both cases, we can observe the presence of deep valleys in the RKI curves when $m_{\tau\tau} \rightarrow 0$, indicating destructive interference between the LQ and the Z' contributions. This interference generates a suppression of the differential cross-section for lower values of $m_{\tau\tau}$ and, therefore, in the integrated cross-section.

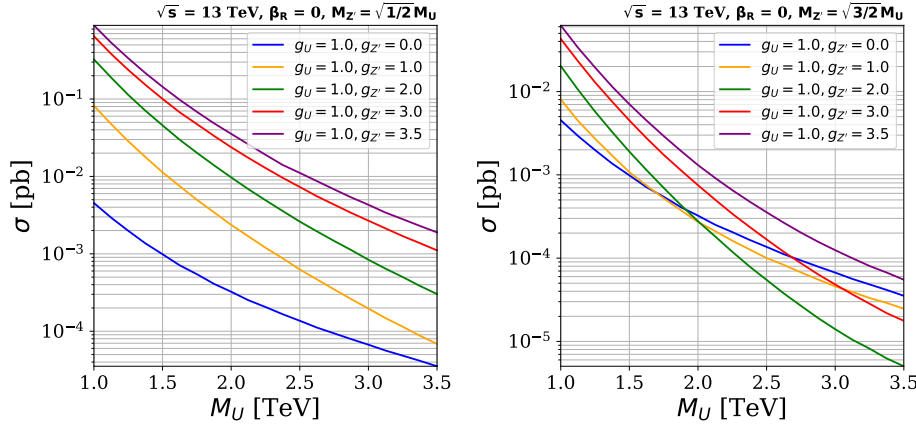


Figure 3.10: $\tau\tau$ cross-section as a function of the LQ mass for different values of g_U and $g_{Z'}$. The estimates are performed at $\sqrt{s} = 13$ TeV, $\beta_R = 0$, $M_{Z'} = \sqrt{1/2}M_U$ (left), and $M_{Z'} = \sqrt{3/2}M_U$ (right).

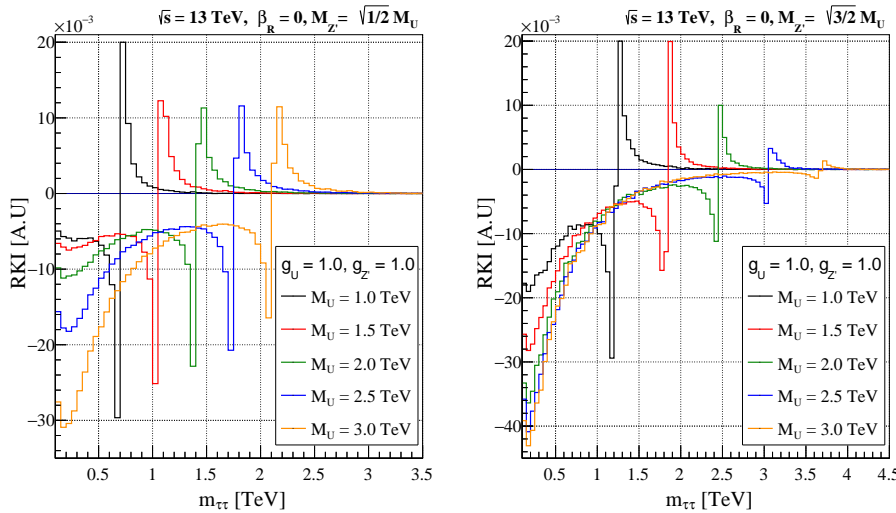


Figure 3.11: The relative kinematic interference (RKI), as a function of the reconstructed mass of two taus, for different LQ masses. The studies are performed assuming $\sqrt{s} = 13$ TeV, $\beta_R = 0$, $g_U = 1.0$, $g_{Z'} = 1.0$, $M_{Z'} = \sqrt{1/2}M_U$ (left), and $M_{Z'} = \sqrt{3/2}M_U$ (right).

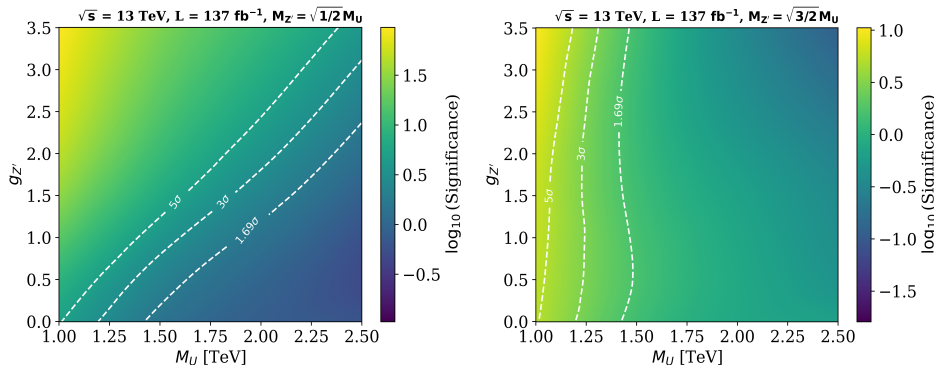


Figure 3.12: Change on the non-res signal significance for different Z' coupling scenarios and LQ masses. The estimates are performed at $\sqrt{s} = 13.0$ TeV, $\beta_R = 0$, $g_U = 1.8$, $M_{Z'} = \sqrt{1/2}M_U$ (top), and $M_{Z'} = \sqrt{3/2}M_U$ (bottom).

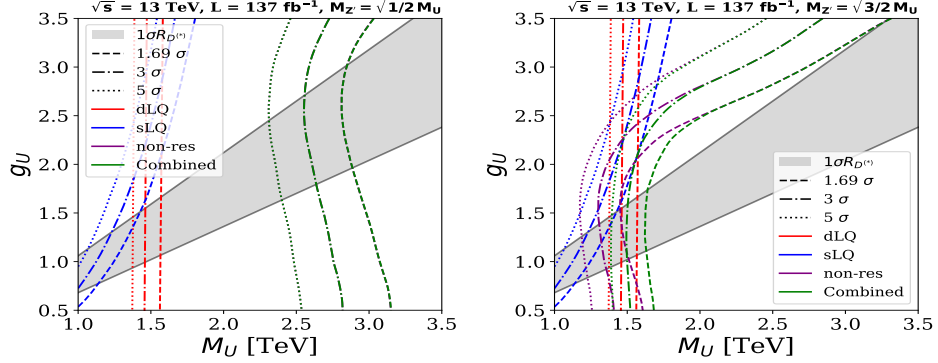


Figure 3.13: Signal significance for different coupling scenarios and LQ masses, for all channels, with an additional Z' contribution to non-res production. We set $\beta_R = 0$ and $g_{Z'} = 3.5$, taking $M_{Z'}^2$ equal to $M_U^2/2$ ($3M_U^2/2$) on the top (bottom) panel.

The change in sensitivity on the non-res signal significance due this interference effect with the Z' boson is shown in Figure 3.12. We consider two opposite cases for the Z' mass: $M_{Z'}^2 = M_U^2/2$ (top) and $M_{Z'}^2 = 3M_U^2/2$ (bottom). Our results are shown on the $g_{Z'} - M_U$ plane, for a fixed $g_U = 1.8$ and $\beta_R = 0$. For the $M_{Z'}^2 = M_U^2/2$ scenario, there is an overall increase in the total cross-section, with a larger $g_{Z'}$ implying a larger sensitivity. This means that our ability to probe smaller values of g_U could be enhanced, as a given observation would be reproduced with both a specific g_U and vanishing $g_{Z'}$, or a smaller g_U with large $g_{Z'}$. Thus, for a large enough $g_{Z'}$, it could be possible to enhance non-res to the point that the entire region favoured by B-anomalies could be ruled out. In contrast, for $M_{Z'}^2 = 3M_U^2/2$ the cross-section is strongly affected by the large destructive interference, such that a larger $g_{Z'}$ does not necessarily imply an increase in sensitivity. In fact, as can be seen in the bottom panel, for large M_U the significance is reduced as $g_{Z'}$ increases, leading to the opposite conclusion than above, namely, that a large $g_{Z'}$ could reduce the effectiveness of non-res.

The impact of the above can be seen in Figure 3.13, which shows our previous sensitivity curves on the $M_U - g_U$ plane, but this time with a Z' contribution to non-res. We use the same values of $M_{Z'}$ as before, but fix $g_{Z'} = 3.5$. For smaller $M_{Z'}$ (top), the non-res contribution is enhanced so much, that both sLQ and dLQ play no role whatsoever in determining the exclusion region. We find that, for small g_U , the sensitivity is dominated by Z' production such that, since M_U is related to $M_{Z'}$, LQ masses up to ~ 3 TeV are excluded. This bound is slightly relaxed for larger values of g_U , which is attributed to destructive interference effects due to an increased LQ contribution.

The bottom panel of Figure 3.13 shows that case where $M_{Z'}$ is larger than M_U . As expected from our previous discussion, the behaviour and impact of non-res is modified. For small g_U , we again have the pure Z' production dominating the non-res cross-section, leading to a null sensitivity on g_U , similar to what happens in dLQ. In contrast, for very large g_U , we find that the pure LQ non-res production is the one that dominates, and we recover sensitivity regions with a slope similar to those shown in Figures 3.14-3.18, shifted towards larger values of g_U . For intermediate values of this coupling, the destructive interference have an important effect again, twisting the exclusion region slightly towards the left. Still, even in this case, we find that sLQ plays a marginal role in defining the combined exclusion region, and that the final result again depends primarily on dLQ and non-res production.

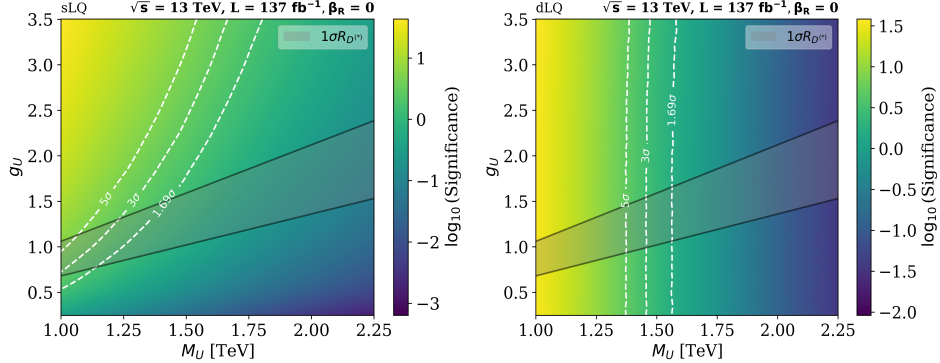


Figure 3.14: Signal significance for different coupling scenarios and LQ masses, without right-handed currents, using the combination of all search channels. The results pertaining to sLQ, dLQ and non-res production are displayed respectively from the top. These results are for $\sqrt{s} = 13 \text{ TeV}$ and 137 fb^{-1} .

3.5 SINGLE AND DOUBLE LEPTOQUARK CONTRIBUTIONS

The expected signal significance for sLQ, dLQ and non-res production, and their combination, is presented in Figure 3.14. Here, the significance is shown as a heat map in a two dimensional plane of g_U versus M_U , considering exclusive couplings to left-handed currents, *i.e.* $\text{BR}(\text{LQ} \rightarrow b \text{ fi}) = \frac{1}{2}$. The dashed lines show the contours of constant signal significance. The 1.69σ contour represents exclusion at 95% confidence level, and the $3-5\sigma$ contours represent potential discovery. The grey band defines the set of $\{M_U, g_U\}$ values that can explain the B-meson anomalies, $C_U \sim 0.01$ for this scenario. The estimates are performed under the conditions for the second run, RUN-II, of the LHC ($\sqrt{s} = 13 \text{ TeV}$ and $L = 137 \text{ fb}^{-1}$). We find that the dLQ interpretation plot (Figure 3.14 second from the top) does not depend on g_U , which is expected due to dLQ production arising exclusively from interactions with gluons. For this reason, the dLQ production process provides the best mode for discovery when g_U is small. On the other hand, the non-res channel is more sensitive to changes in the coupling parameter g_U , as its production cross-section depends on g_U^4 . Therefore, the non-res production process provides the best mode for discovery when g_U is large. These results confirm the expectations from previous analyses (see for instance [Schmaltz:2018nls](#)), in the sense that the dLQ and non-res processes complement each other nicely at low and high g_U scenarios. The sLQ channel combines features from both the dLQ and non-res channels, in principle making it an interesting option to explore different scenarios and gain a better understanding of LQ properties, but the evolution of the signal significance in the full phase space is more complicated as it involves resonant LQ production with a cross-section that depends non-trivially on M_U , g_U , and the LQ coupling to gluons. However, Figure 3.14 shows that the sLQ production process can provide complementary and competitive sensitivity to the non-res and dLQ processes, in certain parts of the phase space. The top panel of Figure 3.15 presents the sensitivity of all signal production processes combined, and compares our expected exclusion region with the latest one from the ATLAS Collaboration [ATLAS_7A](#). The comparison suggests that our proposed analysis strategy provides better sensitivity than current methods being carried out at ATLAS, especially at large values of g_U . In particular, we find that with the pp data already available from RUN-II, our expected exclusion curves begin to probe solutions to the B-anomalies for LQ masses up to 2.25 TeV.

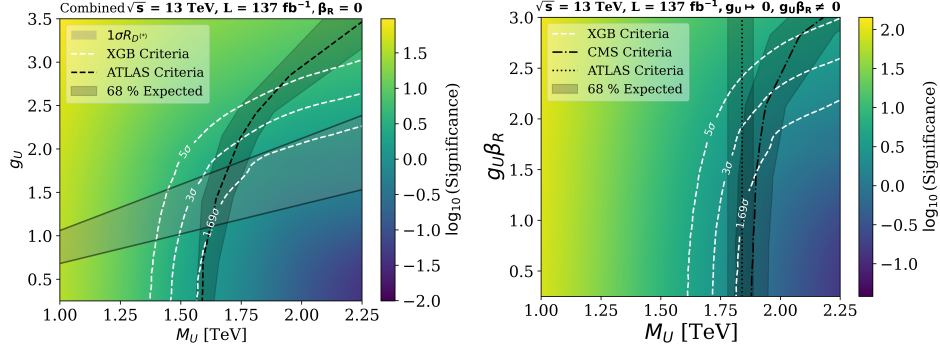


Figure 3.15: The top (bottom) panel shows signal significance comparison with ATLAS ATLAS_7A (CMS and ATLAS LQS_CMS_2022_results_comparison; ATLAS_Vertical_Line) background only hypothesis, for the combination of all channels, with uniquely coupling to left-handed (right-handed) currents. The estimates are performed at $\sqrt{s} = 13$ TeV and 137 fb^{-1} .

Figure 3.15 shows the expected signal significance considering $\text{BR}(\text{LQ} \rightarrow b \text{ fi}) = 1$, in order to compare our analysis with the corresponding results from the CMS LQS_CMS_2022_results_comparison and ATLAS ATLAS_Vertical_Line Collaborations. Let us emphasize again that $\text{BR}(\text{LQ} \rightarrow b \text{ fi})$ depends on β_R , as illustrated on the top panel of Figure 3.2. Thus, although the $\text{BR}(\text{LQ} \rightarrow b \text{ fi}) = 1$ scenario is a possible physical case, it does not solve the observed anomalies in the $R_{D^{(*)}}$ ratios, as it corresponds to the case where LQs couple exclusively to right-handed currents.

With this in mind, the scenario studied by CMS in LQS_CMS_2022_results_comparison considers couplings only to left-handed currents, setting artificially the condition $\text{BR}(\text{LQ} \rightarrow b \text{ fi}) = 1$. In order to compare, we scale the efficiency \times acceptance of our selection criteria for $\beta_R = 0$, by a factor of 2.0 for s LQ and 4.0 for d LQ. According to Figure 3.15, the ML approach that we have followed again suggests an optimization of the signal and background separation, having the potential of improving the regions of exclusion (1.69σ) with respect to that of CMS. In the bottom panel of the Figure we have also included a similar exclusion by ATLAS ATLAS_Vertical_Line. However, since ATLAS only considers d LQ production in the analysis, the results are not entirely comparable, so are included only as a reference.

We now turn to the role of β_R , and our capacity of probing the regions solving the B-meson anomalies. Figure 3.16 shows the maximum significant contours, under LHC RUN-II conditions, for the different LQ production mechanisms and their combination, considering scenarios with only left-handed currents ($\beta_R = 0$, top) and with maximal right-handed currents ($\beta_R = -1$, bottom). We find a noticeable improvement in signal significance in all channels when taking $\beta_R = -1$, as is expected from the increase in $\text{BR}(\text{LQ} \rightarrow b \text{ fi})$ branching ratio and production cross-sections (see Figure 3.2). However, the region solving the B-meson anomalies also changes, preferring lower values of g_U , such that in both cases we find ourselves just starting to probe this region at large M_U .

The combined significance contours for the different BR scenarios that have been considered is presented in Figure 3.17. These contours illustrate the regions of exclusion for the three cases of interest, namely exclusive left-handed currents ($\text{BR}(\text{LQ} \rightarrow b \text{ fi}) = \frac{1}{2}$, $\beta_R = 0$), maximal left and right couplings ($\text{BR}(\text{LQ} \rightarrow b \text{ fi}) = \frac{2}{3}$, $\beta_R = -1$), and exclusive right-handed currents ($\text{BR}(\text{LQ} \rightarrow b \text{ fi}) = 1$, $g_U \rightarrow 0$, $g_U \beta_R = 1$). For small g_U , we find that the exclusive right-handed

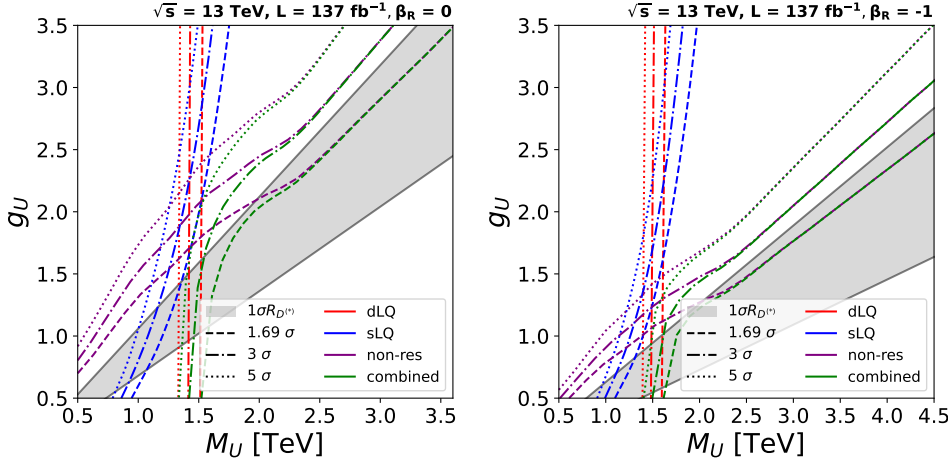


Figure 3.16: Signal significance for different coupling scenarios and LQ masses for all channels. This plot summarizes our results with $\beta_R = 0$ (without right-handed currents) and $\beta_R = -1$ (maximally coupled to right-handed currents). The estimates are performed at $\sqrt{s} = 13 \text{ TeV}$ and 137 fb^{-1} .

scenario is most sensitive, while the exclusive left-handed case is the worst. The reason for this is that this region is excluded principally by dLQ production, such that having the largest branching ratio is crucial in order to have a large number of events. For larger couplings, both exclusive scenarios end up having similar exclusion regions, with the $\beta_R = -1$ case being significantly more sensitive. The reason in this case is that the exclusion is dominated by non-res, which has a much larger production cross-section if both currents are turned on.

In order to finalise our analysis of the LQ-only model, we show in Figure 3.18 the expected combined significance in the relatively near future. For this, considering $\sqrt{s} = 13.6 \text{ TeV}$, we show contours for the sensitivity corresponding to integrated luminosities of 137 fb^{-1} , 300 fb^{-1} , and 3000 fb^{-1} , for scenarios with only left-handed currents (top) and with maximal coupling to right-handed currents (bottom). Note that for $\beta_R = 0$ ($\beta_R = -1$), couplings g_U close to 3.18 (1.85) and $M_U = 5.0 \text{ TeV}$ can be excluded with 1.69σ significance for the high luminosity LHC era, allowing us to probe the practically the entirety of the B-meson anomaly favored region. Note that the background yields for the high luminosity LHC might be larger due to pileup effects. Nevertheless, as it was mentioned in Section ??, we have included a conservative 10% systematic uncertainty associated with possible fluctuations on the background estimations. Although effects from larger pileup might be significant, they can be mitigated by improvements in the algorithms for particle reconstruction and identification, and also on the data-analysis techniques.

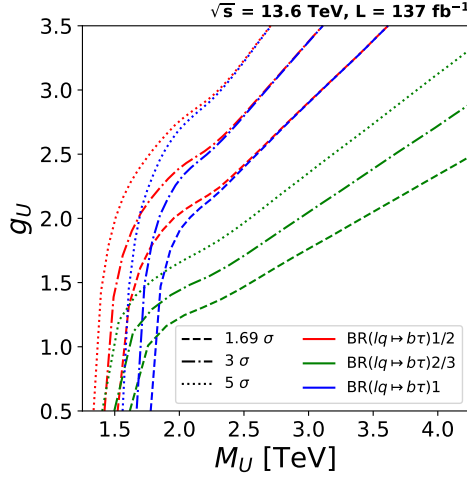


Figure 3.17: Signal significance for different coupling scenarios and LQ masses, considering the case without coupling to right-handed currents $\text{BR}(\text{LQ} \rightarrow b \text{ fi}) = \frac{1}{2}$, the case maximally coupled to right- and left-handed currents $\text{BR}(\text{LQ} \rightarrow b \text{ fi}) = \frac{2}{3}$, and the case uniquely coupled to right-handed currents $\text{BR}(\text{LQ} \rightarrow b \text{ fi}) = 1$. The estimates are performed at $\sqrt{s} = 13 \text{ TeV}$ and 137 fb^{-1} .

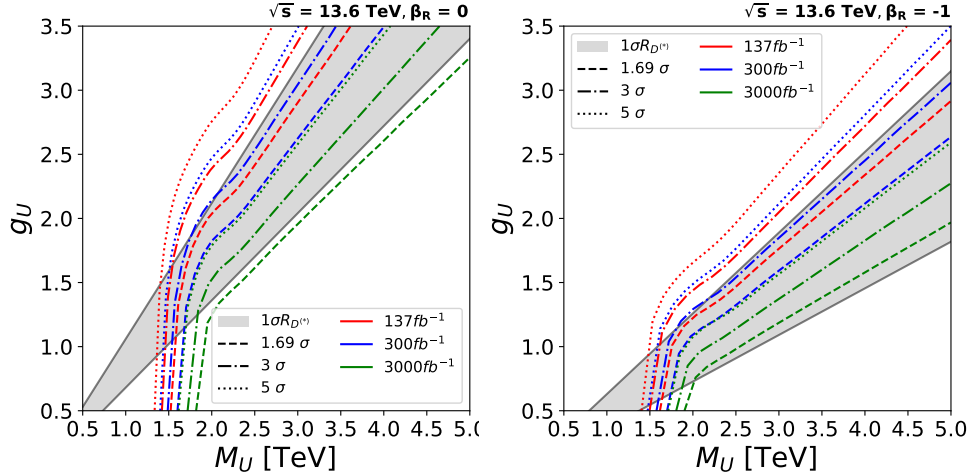


Figure 3.18: Projected signal significance for different coupling scenarios and LQ masses maximally coupled to right-handed currents. The estimates are performed at $\sqrt{s} = 13.6 \text{ TeV}$, 137 fb^{-1} , 300 fb^{-1} and 3000 fb^{-1} .

4

$U(1)_{T_R^3}$ GAUGE EXTENSION OF THE STANDARD MODEL

Minimal extensions to the SM, considering new $U(1)_X$ symmetry groups, are among the most studied BSM scenarios. For example, the $U(1)_{T_R^3}$ symmetry, where families of right-handed fermions of the SM and possible extensions, such as right-handed neutrinos, are charged, was originally studied in the context of left-right symmetry models (**MohapatraPati1975; SenjanovicMohapatra1975**; Assad, Fornal, and Grinstein 2018). In these studies, $U(1)_{T_R^3}$ is identified as the subgroup of $SU(2)_R$ defined by its diagonal (electric-charge neutral) generator, T_R^3 . In addition, it is often suggested that $U(1)_{T_R^3}$ is a subspecies of a $U(1)_{B-L}$ symmetry since the breaking of the $U(1)_{B-L} \times U(1)_{T_R^3}$ leads to the $U(1)_Y$ symmetry. This naturally motivates the presence of a massive and electrically neutral Z' gauge boson (**Michaels:2020fzj; Dev:20210tb; Florez2023**; Luzio et al. 2018; Baker et al. 2019). However, in the breaking of $U(1)_{B-L} \times U(1)_{T_R^3} \rightarrow U(1)_Y$, it follows that the Higgs doublet H , since it is a singlet of $U(1)_{B-L}$, acquires its hypercharge by inheritance from a charge under $U(1)_{T_R^3}$. Consequently, the vacuum expectation value (VEV) of H couples both symmetry-breaking scales for $U(1)_Y$ and $U(1)_{T_R^3}$. Alternatively, these symmetry-breaking scales can be decoupled by adding an additional $U(1)_G$ group where fermions of the SM are singlets and H is not. Therefore, the hypercharge comes from $U(1)_G$ for the H and from $U(1)_{T_R^3}$ for fermions, *i.e.* $Y = Q_{T_R^3} + \frac{1}{2}Q_{B-L} + Q_G$ (**Dutta:2022qvn**). Moreover, one can ask for scenarios where the hypercharge is not related to the $U(1)_{T_R^3}$ charge.

Recently, theoretical and phenomenological efforts have emerged around scenarios where the low-energy gauge symmetry of the SM is extended by appending the Abelian gauge group $U(1)_{T_R^3}$, whose spontaneous symmetry-breaking is not linked to the electroweak one (**Dutta2019; Dutta2020; Dutta2020b; Dutta2022; PhysRevD.107.095019; Dutta2023**). In these scenarios, the gauge boson of $U(1)_{T_R^3}$ is associated with a massive dark photon A' whose longitudinal mode arises from a Higgs-like mechanism involving a complex scalar field, ϕ . This field is a singlet under the SM group, with its CP-odd component associated with the A' mass and the CP-even giving rise to a dark Higgs, ϕ' . To cancel gauge anomalies, a right-handed ν_R neutrino must be included for each generation of the SM that couples to $U(1)_{T_R^3}$. Furthermore, to correctly explain the origin of fermion masses in a UV-complete theory, a set of new vector-like quarks ($\chi_u, \chi_d, \chi_\ell, \chi_\nu$) must be included. These new particles are singlets under $U(1)_{T_R^3}$ and charged like SM right-handed fermions, as in the universal see-saw mechanism (**Berezhiani; Chang1987; Davidson1987; Rajpoot1987; Babu1989; Babu1990**).

In this phenomenology study, we devise a LHC search strategy for the light GeV-scale scalar boson ϕ' produced in association with a heavy TeV-scale χ_u , the partner particle of the top quark, through a previously unexplored production and final state channel. Particularly, we explore the production of $pp \rightarrow t\chi_u\phi'$, in

contrast to $pp \rightarrow TT \rightarrow t\phi't\phi'$ with hadronic (**Bhardwaj_2022; Bhardwaj_2022_2; Bardhan_2023**) di-photon decays. Due to the non-trivial $\chi - t - \phi'$ coupling, processes where the final state includes $t\chi_u\phi'$ are allowed in pp colliders through the $\chi_u - t$ fusion, see Figure 4.3. Since the χ_u couples to SM quarks and gluons, it can be produced in large quantities. Furthermore, its energetic decay products can be detected alongside the ϕ' mediator particle that has significant transverse momentum. Therefore, if the ϕ' decays into SM particles that are observable in the detector's central region, this strategy can be very effective at reducing the SM background, and thus improve the long-term LHC discovery reach for heavy top partners and GeV-scale mediators, which are typically hard to detect using conventional methods at hadron colliders. Moreover, since it is possible to have $\chi_u \rightarrow t\phi'$ decays (and $\bar{\chi}_u \rightarrow \bar{t}\phi'$), the same $pp \rightarrow t\chi_u\phi'$ state may arise from $\chi_u\bar{\chi}_u$ production diagrams with quantum chromodynamic (QCD) vertices, where one χ_u decays to $t\phi'$, as shown in Figure 4.4. As a consequence, the energetic products from $\chi_u\bar{\chi}_u$ decays can be readily detected, particularly when they occur alongside a mediator particle that carries substantial transverse momentum, providing greater sensitivity than that of searches where either χ_u or ϕ' are considered in isolation.

We probe the scenario where the scalar ϕ' has family non-universal fermion couplings, as was suggested in (**Dutta2020**), and thus can address several issues with the SM. We focus on the ϕ' decay to a pair of muons since, at the experimental level, muons generally have high reconstruction and identification efficiencies, which allow for the development of relatively low $p_T(\mu)$ triggers, and provide clean signatures to remove the copious QCD multijet SM background. A key component of this study is the development of an analysis strategy utilizing a machine learning (ML) algorithm based on Boosted Decision Trees (BDT) (**friedman_greedy_2001**). The event classifier's output is employed to conduct a profile-binned likelihood test, which is used to determine the overall signal significance for each model examined in the analysis. The effectiveness of BDTs and other ML algorithms has been validated in numerous experimental and phenomenological studies (**Ai:2022qvs; ATLAS:2017fak; Biswas:2018snp; Chung:2020ysf; Feng:2021eke; ttZprime; Chigusa:2022svv; Florez2023; Arganda2024; Ajmal_2024; Dutta_2015**). Our findings indicate that the BDT algorithm significantly enhances signal significance.

The rest of this chapter is structured as follows. Section 4.2 discusses details of the minimal $U(1)_{T_R^3}$ model. Section 4.1 provides an overview of current relevant results at the LHC. Section 4.3 explains how the Monte Carlo (MC) simulation samples are produced for this study. In Section 4.4 we discuss the motivation and details of our machine learning workflow, and in Section 4.5, the main results are presented.

4.1 EXPERIMENTAL CONSIDERATIONS

The ATLAS and CMS collaborations at CERN have conducted various searches for heavy vector-like quarks (T). These searches utilized pp collisions at center-of-mass energies of $\sqrt{s} = 8$ and 13 TeV. The studies primarily focused on T production through gluon-mediated QCD processes, either in pair production from quark-antiquark annihilation (Figure 4.1) or in single-T production from electroweak processes involving associated quarks (Figure 4.2).

In those studies, T decays into bW , tZ , or tH have been considered. In the context of T pair production, $T\bar{T}$, via QCD processes, the cross sections are well-known and solely depend on the mass of the vector-like quark. Assuming a narrow T

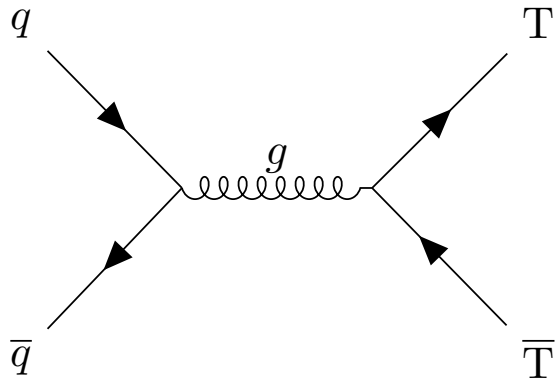


Figure 4.1: Representative Feynman diagram for $T\bar{T}$ pair production via gluon-mediated QCD processes.

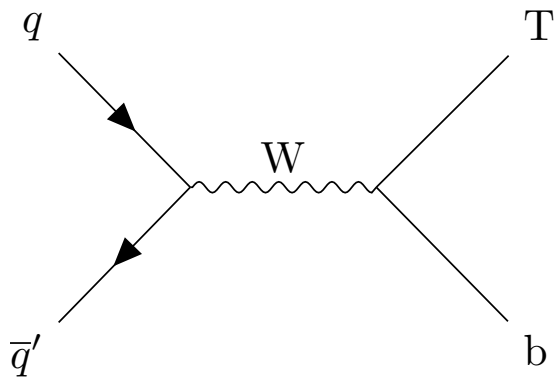


Figure 4.2: Representative Feynman diagram for single T production via electroweak processes.

decay width ($\Gamma/m(T) < 0.05$ or 0.1) and a 100% branching fraction to bW , tZ , or tH , these searches have set stringent bounds on $m(T)$, excluding masses below almost 1.5 TeV at 95% confidence level (**CMS:2024bni**; **CMS:2024qdd**; **ATLAS:2022ozf**; **ATLAS:2023bfh**; **ATLAS:2022hnn**; **ATLAS:2022tla**; **ATLAS:2023pja**; **ATLAS:2024fdw**).

The most recent analysis from the CMS collaboration probes T -quark production via $pp \rightarrow Tqb$, in final states with $T \rightarrow tZ$ or $T \rightarrow tH$, considering scenarios with preferential couplings to third-generation fermions. The analysis sets 95% confidence level upper limits of 68–1260 fb on the production cross section, for T masses ranging from 600–1200 GeV (**CMS:2024qdd**). The latest studies from ATLAS probe vector-like quarks using the single- T production mode with the $T \rightarrow tH$ decay channel leading to a fully hadronic final state (**ATLAS:2022ozf**), the single- T production mode with the $T \rightarrow tZ$ decay channel leading to a multileptonic final state (**ATLAS:2023bfh**), the TT pair production mode with various T decay channels leading to multileptonic final states (**ATLAS:2022hnn**), and the TT pair production mode with various T decay channels leading to a single lepton plus missing momentum final state (**ATLAS:2022tla**; **ATLAS:2023pja**). The multilepton search offers the greatest sensitivity in most of the phase space, but the missing transverse energy based search has better sensitivity for low branching fraction $\mathcal{B}(T \rightarrow Wb)$ and high $\mathcal{B}(T \rightarrow Ht)$. These searches have similar sensitivities for the singlet and doublet models, resulting in exclusion bounds for masses below about 1.25 TeV and 1.41 TeV, respectively.

A key consideration in the model interpretations summarized above is that the T branching fractions depend on the chosen model. The excluded mass range is less restrictive for specific branching fraction scenarios, such as $\{\mathcal{B}(T \rightarrow tZ), \mathcal{B}(T \rightarrow bW), \mathcal{B}(T \rightarrow tH)\} = \{0.2, 0.6, 0.2\}$, excluding masses below about 0.95 TeV. Moreover, if the $T \rightarrow \phi't$ decay is allowed, or if the branching fractions $\mathcal{B}(T \rightarrow tH/bW)$ are lower, the limits previously quoted must be re-evaluated. The authors of Ref. (**Cacciapaglia:2019zmq**) emphasize that bounds on $m(T)$ can be around 500 GeV when $T \rightarrow t\phi'$ decays are permitted. Therefore, to facilitate a comprehensive study, benchmark scenarios in this paper are considered down to $m(\chi_u) = 500$ GeV.

4.2 THE MINIMAL $U(1)_{T_R^3}$ MODEL

4.2.1 SCALAR POTENTIAL

In this model, the SM is extended by the Abelian gauge symmetry $U(1)_{T_R^3}$, where only right-handed fermions are charged. We assume two independent Higgs mechanisms, one with a Higgs doublet H for electroweak symmetry breaking and the other with a Higgs singlet ϕ for the $U(1)_{T_R^3}$ symmetry breaking. Both scalars have independent vacuum expectation values (VEVs), $\langle H \rangle = v_h/\sqrt{2}$ and $\langle \phi \rangle = v_\phi/\sqrt{2}$, allowing us to express the doublet and singlet Higgs fields, following a Kibble parametrization, as

$$H = \begin{pmatrix} G_+ \\ \frac{1}{\sqrt{2}}(v_h + \rho_0 + iG_0) \end{pmatrix} \quad (4.1)$$

$$\phi = \frac{1}{\sqrt{2}}(v_\phi + \rho_\phi + iG_\phi). \quad (4.2)$$

In Eqs.4.1 and Eq.4.2, G_\pm , G_0 , and G_ϕ are the Goldstone bosons that allow the SM W^\pm and Z bosons and the dark photon A' , associated with the $U(1)_{T_R^3}$ symmetry,

to acquire mass. The ρ_h and ρ_ϕ are an orthogonal mixture of the SM Higgs boson and the dark Higgs

$$\begin{pmatrix} h \\ \phi' \end{pmatrix} = \begin{pmatrix} \cos \alpha & -\sin \alpha \\ \sin \alpha & \cos \alpha \end{pmatrix} \begin{pmatrix} \rho_0 \\ \rho_\phi \end{pmatrix}, \quad (4.3)$$

that results from the diagonalization of the mass matrices arising from the gauge invariant potential

$$\begin{aligned} \mathcal{V}(\phi, H) = & \mu_H^2 H^\dagger H + \mu_\phi^2 \phi^* \phi \\ & + \lambda (H^\dagger H)(\phi^* \phi) + \lambda_H (H^\dagger H)^2 + \lambda_\phi (\phi^* \phi)^2. \end{aligned} \quad (4.4)$$

The tadpole equations are given from the minimization of the potential as

$$\frac{\partial \mathcal{V}}{\partial H} = \frac{v_h}{\sqrt{2}} \left(\mu_H^2 + \lambda_H v_h^2 + \frac{1}{2} \lambda v_\phi^2 \right) = 0, \quad (4.5)$$

$$\frac{\partial \mathcal{V}}{\partial \phi} = \frac{v_\phi}{\sqrt{2}} \left(\mu_\phi^2 + \lambda_\phi v_\phi^2 + \frac{1}{2} \lambda v_h^2 \right) = 0. \quad (4.6)$$

The masses of the scalar bosons can be written as

$$m_{h,\phi'}^2 = \frac{1}{2} \left(\lambda_H v_h^2 + \lambda_\phi v_\phi^2 \right) \pm \sqrt{\lambda^2 v_h^2 v_\phi^2 + \left(\lambda_H v_h^2 - \lambda_\phi v_\phi^2 \right)^2}, \quad (4.7)$$

and the mixing angle α as

$$\tan 2\alpha = \frac{-\lambda v_h v_\phi}{\lambda_\phi v_\phi^2 - \lambda_H v_h^2}. \quad (4.8)$$

If we invert this relations, we can express the quartic couplings in terms of the masses and mixing angle as

$$\lambda_H = \frac{m_{\phi'}^2 + m_h^2 + (m_{\phi'}^2 - m_h^2) \cos(2\alpha)}{4v_h^2}, \quad (4.9)$$

$$\lambda_\phi = \frac{m_{\phi'}^2 + m_h^2 + (m_{\phi'}^2 - m_h^2) \cos(2\alpha)}{4v_\phi^2}, \quad (4.10)$$

$$\lambda = \frac{m_{\phi'}^2 - m_h^2}{2v_h v_\phi} \sin(2\alpha). \quad (4.11)$$

So, we have four free parameters in the scalar potential, the masses of the physical scalar bosons m_h and $m_{\phi'}$, the mixing angle α , and the VEV of the dark Higgs v_ϕ . In a similar way that the v_h is fixed by de mass of the electroweak gauge bosons, the v_ϕ can be fixed by the mass of the dark photon A' , which is given by $m_{A'}^2 = g_{T_R^3}^2 v_\phi^2$, where $g_{T_R^3}$ is the gauge coupling of the $U(1)_{T_R^3}$ group. Depending on the range of values of $g_{T_R^3}$ this gauge boson correspond to a Z' boson or a dark photon. In this chapter, we will assume that the $g_{T_R^3}$ is small enough so that the A' boson can be considered as a dark photon.

4.2.2 THE UNIVERSAL SEESAW MECHANISM

In the model, each electrically charged SM fermion f has a mass protected by both VEVs. In turn, they acquire mass from the mixture with a vector-like fermion χ_f , which is charged as the right-handed component of the respective SM fermion, in

a UV complete theory. The terms in the Lagrangian density that contribute to the mass of physical fermions are,

$$\begin{aligned} -\mathcal{L} \supset & Y_{f_L} \bar{f}'_L \chi'_{fR} H + Y_{f_R} \bar{\chi}'_{fL} f'_R \phi^* + m_{\chi'_f} \bar{\chi}'_{fL} \chi'_{fR} \\ & + \text{h.c.} \end{aligned} \quad (4.12)$$

Therefore, in the vacuum, the mass matrix is

$$M_f = \begin{pmatrix} 0 & Y_{f_L} v_h / \sqrt{2} \\ Y_{f_R} v_\phi / \sqrt{2} & m_{\chi'_f} \end{pmatrix}. \quad (4.13)$$

The left- and right-handed components of the physical fermions (f, χ_f) are given by two rotations $\mathcal{R}(\theta_{f_{L,R}})$ as,

$$\begin{pmatrix} f_{L,R} \\ \chi_{f_{L,R}} \end{pmatrix} = \begin{pmatrix} \pm \cos \theta_{f_{L,R}} & \mp \sin \theta_{f_{L,R}} \\ \sin \theta_{f_{L,R}} & \cos \theta_{f_{L,R}} \end{pmatrix} \begin{pmatrix} f'_{L,R} \\ \chi'_{f_{L,R}} \end{pmatrix}, \quad (4.14)$$

in a way that $\mathcal{R}(\theta_{f_L}) M_f \mathcal{R}^{-1}(\theta_{f_R}) = \text{diag}(m_f, m_{\chi_f})$ up to a phase. Assuming real parameters, the physical masses and the mixing angles are given by

$$m_f m_{\chi_f} = \frac{(Y_{f_L} v_h)(Y_{f_R} v_\phi)}{2}, \quad (4.15)$$

$$m_f^2 + m_{\chi_f}^2 = m_{\chi'_f}^2 + \frac{1}{2} (Y_{f_L}^2 v_h^2 + Y_{f_R}^2 v_\phi^2), \quad (4.16)$$

$$\tan \theta_{f_{L,R}} = \frac{\sqrt{2}}{m_{\chi'_f}} \left(\frac{Y_{f_{L,R}} v_{h,\phi}}{2} - \frac{m_f^2}{Y_{f_{L,R}} v_{h,\phi}} \right). \quad (4.17)$$

The Yukawa interactions of the physical fermions with the scalar bosons have the form

$$-\mathcal{L}_{\text{yuk}} = h \bar{\Psi}_{f_L} \mathcal{Y}_h \Psi_{f_R} + \phi' \bar{\Psi}_{f_L} \mathcal{Y}_\phi \Psi_{f_R}, \quad (4.18)$$

with $\Psi_f = (f, \chi_f)^T$, and the matrices $\mathcal{Y}_{f_{L,R}}$ given by

$$\mathcal{Y}_h = \frac{1}{\sqrt{2}} \mathcal{R}(\theta_{f_L}) (Y_{f_L} \sigma_+ \cos \alpha - Y_{f_R} \sigma_- \sin \alpha) \mathcal{R}^{-1}(\theta_{f_R}) \quad (4.19)$$

$$\mathcal{Y}_\phi = \frac{1}{\sqrt{2}} \mathcal{R}(\theta_{f_L}) (Y_{f_L} \sigma_+ \sin \alpha + Y_{f_R} \sigma_- \cos \alpha) \mathcal{R}^{-1}(\theta_{f_R}), \quad (4.20)$$

where $\sigma_\pm = (\sigma_1 \pm i\sigma_2)/2$ are the ladder Pauli matrices.

4.2.3 MINIMAL UV-COMPLETE THEORY

The model must provide non-zero masses for all the SM fermions and be free of gauge anomalies. So, we must have at least one full generation of vector-like fermions $\{\chi_u, \chi_d, \chi_e, \chi\}$ and the right-handed component of the SM neutrinos, ν_R , charged as shown in Table 4.1 for each SM generation. Therefore, the Yukawa interactions in the UV-complete theory must be of the form

$$\begin{aligned} -\mathcal{L} \supset & Y_{Lu}^{ij} \bar{q}_L^{i'} \chi_{uR}^{j'} \tilde{H} + Y_{Ru}^{ij} \bar{\chi}_{uL}^{i'} u_R^{j'} \phi^* + m_{\chi_u}^{ij} \bar{\chi}_{uL}^{i'} \chi_{uR}^{j'} \\ & + Y_{Ld}^{ij} \bar{q}_L^{i'} \chi_{dR}^{j'} H + Y_{Rd}^{ij} \bar{\chi}_{dL}^{i'} d_R^{j'} \phi + m_{\chi_d}^{ij} \bar{\chi}_{dL}^{i'} \chi_{dR}^{j'} \\ & + Y_{Le}^{ij} \bar{l}_L^{i'} \chi_{eR}^{j'} H + Y_{Re}^{ij} \bar{\chi}_{eL}^{i'} l_R^{j'} \phi + m_{\chi_e}^{ij} \bar{\chi}_{eL}^{i'} \chi_{eR}^{j'} \\ & + Y_{Lv}^{ij} \bar{l}_L^{i'} \chi_{vR}^{j'} \tilde{H} + Y_{Rv}^{ij} \bar{\chi}_{vL}^{i'} \nu_R^{j'} \phi^* + m_{\chi_v}^{ij} \bar{\chi}_{vL}^{i'} \chi_{vR}^{j'} \\ & + \text{h.c.}, \end{aligned} \quad (4.21)$$

where the i index runs over the three generations of fermions. The simultaneous diagonalization of the mass matrices of each fermion sector will have a similar structure to the one presented in Eqs. 4.15 and 4.16 and the Yukawa matrices will have a similar structure of Eqs. 4.19 and 4.20 but codifying the CKM matrix. For the neutrino sector, the structure of the mass matrix will be more complicated due to the presence of the additional Majorana mass term for the vector-like neutrino χ'_ν .

Field	$SU(3)_C$	$SU(2)_L$	$U(1)_Y$	$U(1)_{T_R^3}$
q'_L	3	2	$1/6$	0
ℓ'_L	1	2	$-1/2$	0
H	1	2	$1/2$	0
u'_R^c	3	1	$-2/3$	-2
d'_R^c	3	1	$1/3$	2
ℓ'_R^c	1	1	1	2
ν'_R^c	1	1	0	-2
ϕ	1	1	0	2
χ'_{u_L}	3	1	$2/3$	0
χ'_{u_R}	3	1	$-2/3$	0
χ'_{d_L}	3	1	$-1/3$	0
χ'_{d_R}	3	1	$1/3$	0
χ'_{ℓ_L}	1	1	-1	0
χ'_{ℓ_R}	1	1	1	0
χ'_{ν_L}	1	1	0	0
χ'_{ν_R}	1	1	0	0

Table 4.1: Minimal field content of the model and their representations under the SM and $U(1)_{T_R^3}$ gauge groups.

4.3 SAMPLES AND SIMULATION

The minimal $U(1)_{T_R^3}$ model described in Sec. 4.2 is implemented *at tree level* into the FeynRules package (**Alloul:2013bka**), which generates the Feynman rules and exports them into a Universal FeynRules Output (UFO) (**Degrade:2011ua**). The resulting UFO is utilized as input for a generator to produce the MC samples. Both signal and background events are generated with the `MadGraph5_aMC@NLO v3.2.0` program (**Alwall:2014hca; Alwall:2014bza**) at leading order (LO) in QCD, considering pp beams colliding with a center-of-mass energy of $\sqrt{s} = 13.6$ TeV. Each signal and background sample is generated separately, with no interference effects between the signal and background considered. The impact of these interference effects has been evaluated, and for all values of χ_u and ϕ' masses considered, the effect on the signal plus background cross section is found to be less than < 0.5%. Additionally, the effect on the shape of the b-jet p_T distribution is less than 6% for $p_T < 300$ GeV and less than 2% for b-jet $p_T > 300$ GeV. We use the NNPDF3.0 NLO (**NNPDF:2014otw**) set for parton distribution functions (PDFs) for all event generation. Parton-level events are then interfaced with PYTHIA (v8.2.44) (**Sjostrand:2014zea**) to account for parton showering and hadronization processes. Finally, we use DELPHES (v3.4.2) (**deFavereau:2013fsa**) to simulate smearing and other detector effects using the CMS detector geometric configurations and parameters for particle identification and reconstruction, using the CMS input

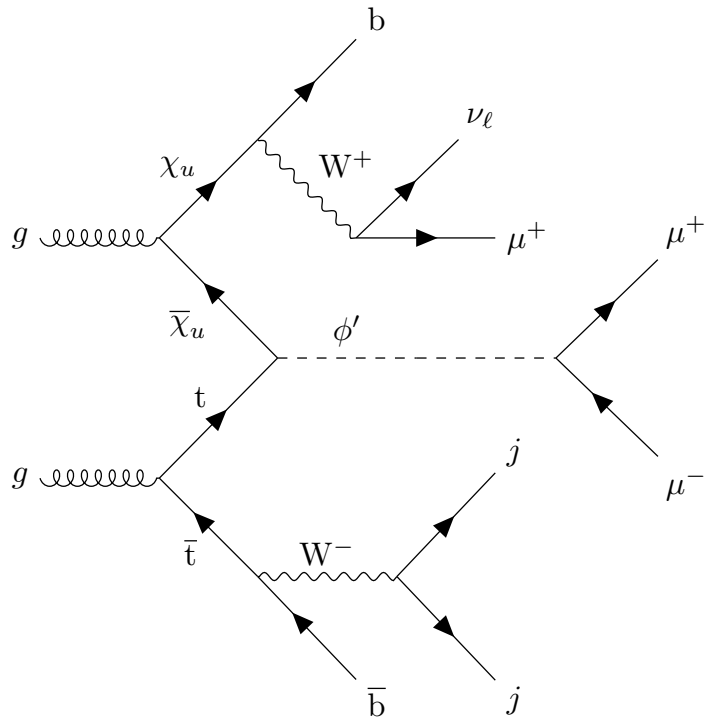


Figure 4.3: Representative Feynman diagram for the production of a ϕ' boson in association with a χ_u vector-like quark through the fusion of a top quark and χ_u vector-like quark. Once again, the ϕ' decays to a pair of muons, the top quark decays fully hadronically, and the χ_u decays semi-leptonically to muons, neutrinos and b-jets.

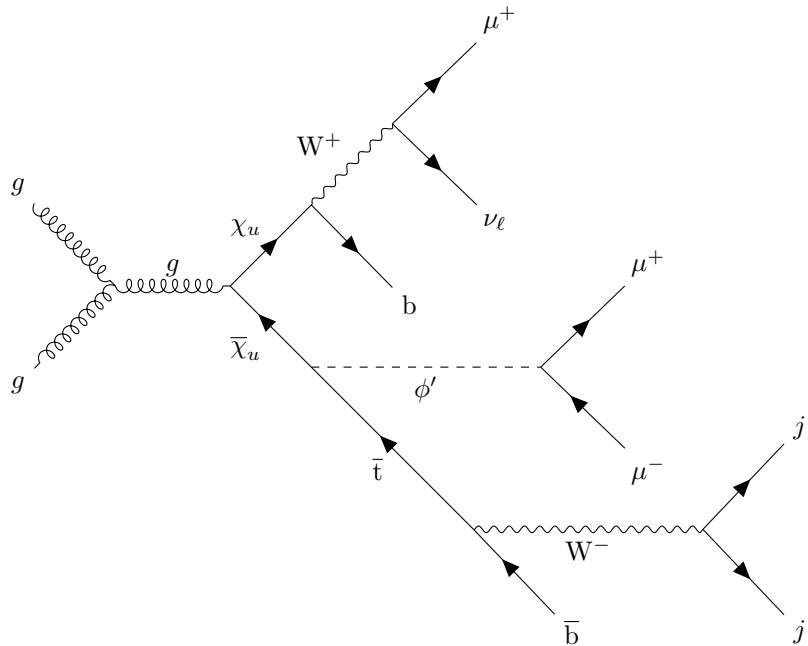


Figure 4.4: Representative Feynman diagram for the production of a ϕ' boson in association with a χ_u vector-like quark through the fusion of a gluon pair from incoming protons. The ϕ' decays to a pair of muons, the top quark that decays fully hadronically, and the χ_u decay semi-leptonically to muons, neutrinos and jets.

card with 140 average pileup interactions. All signal cross sections used in this analysis are obtained requiring the following kinematic criteria on leptons (ℓ), b quarks, and light-quark/gluon jets (j) at parton level in MadGraph: $p_T(\ell) > 35$ GeV, $|\eta(b)| < 2.5$, $|\eta(\ell)| < 2.3$, $p_T(j) > 20$ GeV, and $|\eta(j)| < 5$. These parton-level selections were applied exclusively to the signal processes to restrict event generation to the relevant phase space regions. For background processes, these default parton level requirements in MadGraph were imposed: $p_T(\ell) > 10$ GeV, $|\eta(\ell)| < 2.5$, $p_T(j) > 20$ GeV, $|\eta(j)| < 5$, and $|\eta(b)| < 5$. This ensures that the phase space regions for the background near the analysis-level selection criteria are adequately described after parton showering since the pre-selections at the analysis level are more stringent than the parton-level requirements. Furthermore, we use the MLM algorithm for jet matching and jet merging. The parameters x_{qcut} and q_{cut} of the MLM algorithm are set to 30 and 45 respectively to ensure continuity of the differential jet rate as a function of jet multiplicity. Each simulated signal and background sample is produced separately at LO, with one million events at the generation level, neglecting potential interference effects between the signal and background due to the suppression caused by the different orders of magnitude in the coupling constants of the signal and background.

Signal samples are generated considering the production of a ϕ' boson, an associated χ_u vector-like quark, and a top quark ($pp \rightarrow \chi_u t \phi'$), inclusive in both α and α_s (see Figures 4.3-4.4). We have used the implementation of the $U(1)_{T_R^3}$ model in Ref. (Dutta2023). Signal samples were created considering coupling values of $Y_{t_R} = Y_{t_L} = 2\sqrt{2}$ in the range of masses $m(\phi') \in \{5, 10, 50, 100, 325\}$ GeV for the dark higgs and $m(\chi_u) \in \{0.50, 0.75, 1.0, 1.5, 2.0, 2.5\}$ TeV for the vector-like quark χ_u (PhysRevD.108.095006). The production cross section for $pp \rightarrow \chi_u t \phi'$ is highly dependent on the choice of the Yukawa couplings in the Lagrangian. The $\chi_u - t$ fusion process shown in Figure 4.3 is dominated by the Y_{t_R} coupling. However, the decay $\chi_u \rightarrow t \phi'$ shown in Figure 4.4 is inversely proportional to the Y_{t_L} coupling. This effect is shown in Figure 4.5, which displays the total signal cross section, as a function of Y_{t_R} and Y_{t_L} , for a benchmark point with $m(\phi') = 100$ GeV and $m(\chi_u) = 1.0$ TeV.

We target signal events where the top quark decays hadronically into a bottom quark and two jets ($t \rightarrow bW \rightarrow bq\bar{q}'$), the χ_u decays semileptonically into a b quark, lepton, and neutrino (via $\chi_u \rightarrow bW$ and $W \rightarrow \mu\nu_\mu$), and the ϕ' produces two muons. We note that the scalar ϕ' particle could result from the mixture of the SM Higgs boson and additional scalar fields, and the Yukawas of the fermions could additionally arise from the mixing of the SM fermions with additional copies of the associated vector-like fermions. Therefore, the ϕ' branching ratios are dependent on the chosen mechanism and model by which this mixture occurs, see for example, Refs. (Cacciapaglia_2023; Calibbi:2009pv; Blankenburg, Isidori, and Jones-Perez 2012; Jones-Perez 2013). For the purpose of this work, and similar to Refs. (Dutta2020; Dutta2023), the considered benchmark signal scenarios have $\mathcal{B}(\chi_u \rightarrow b W)$ of about 0.5 and $\mathcal{B}(\phi' \rightarrow \mu^+ \mu^-) = 1.00$. Figure 4.6 shows the production cross section in fb, as a function of $m(\phi')$ and $m(\chi_u)$ masses, assuming the aforementioned decays, branching ratios, and couplings.

We note that for the parameter space of focus in this paper, the total mass of the $t-\chi_u$ system is larger than $m(\phi')$, thus the large rest energy of the $t-\chi_u$ system is converted into potentially large momentum values for the ϕ' . Similarly, the t -quark produced through the χ_u-t fusion interaction can also have large momentum values, and thus in some cases the hadronic t decay products cannot be fully reconstructed independently of each other. This results in three possible t reconstruction scenarios: a fully merged scenario where the $W \rightarrow jj$ system and

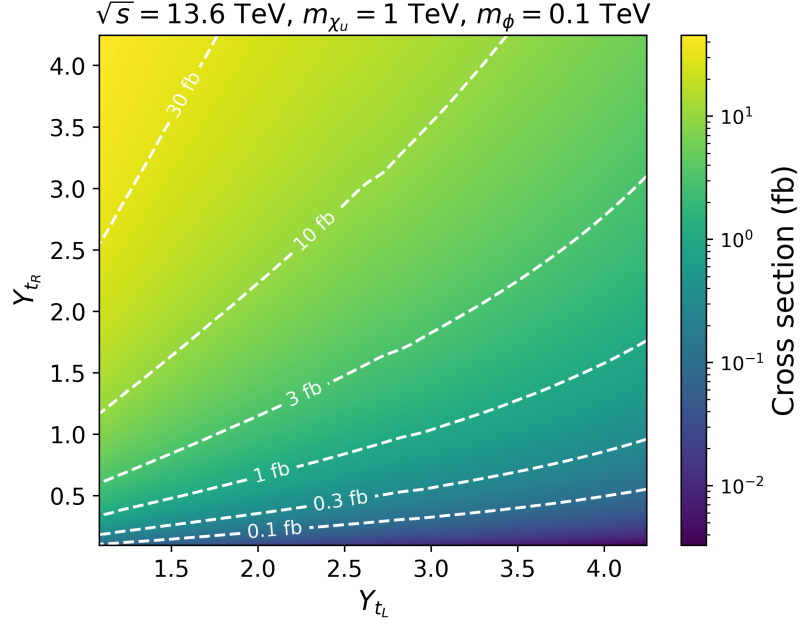


Figure 4.5: Signal production cross section, $\text{pp} \rightarrow \chi_u t \phi'$, in the Y_{t_R} versus Y_{t_L} plane, for a benchmark point with $m(\phi') = 100 \text{ GeV}$ and $m(\chi_u) = 1.00 \text{ TeV}$. The white-dashed contours show specific cross section values in the two dimensional plane.

the b quarks are very collimated and reconstructed as a single “fat jet” (henceforth referred to as a FatJet, FJ); a partially merged scenario, where the decay products of the W boson form a single FatJet but the b quark can still be separately identified; and an un-merged scenario where all decay products can be independently identified. Jets are clustered using the anti- k_t algorithm (Cacciari_2008) using the FastJet (v3.4.2) (Cacciari_2012) package with a distance parameter of $R = 0.4$ for standard jets and $R = 0.8$ for fat jet objects. Each scenario has an associated identification efficiency and misidentification rate, which depends on the choice of the boosted t/W algorithm (our choice of efficiency and misidentification rates is described later).

Based on the above details, the final state of interest in this paper consists of three muons (two from the ϕ' decay and one from the χ_u decay), a (possibly boosted) top-tagged system, at least one b-tagged jet, and large missing transverse momentum (\vec{p}_T^{miss}). For the partially merged and un-merged scenarios, there will be two b quarks present in the final state (one of which is part of the top tagged system).

We consider background sources from SM processes which can give similar objects in the final state as those expected for signal. Several background sources were considered and studied, such as QCD multijet events, production of vector boson pairs (VV : WW, ZZ, WZ), vector boson triplets (VVV : WWZ, WZZ, ZZZ, WWW), top-quark pairs in association with weak bosons ($t\bar{t}X$), and $t\bar{t}\bar{t}\bar{t}$ processes. The dominant sources of SM background events are from the $t\bar{t}X$, ZZW, and $t\bar{t}\bar{t}\bar{t}$ processes. The $t\bar{t}X$ background is primarily associated production of a Z/γ^* from $t\bar{t}$ fusion processes. The ZZW process becomes a background when one Z decays $b\bar{b}$, another Z decays to a pair of muons, and the W decays to a muon and a neutrino. Events from ZZW and $t\bar{t}\bar{t}\bar{t}$ have been combined, after being weighted by their corresponding production cross section. The combination is presented as the “ $b\bar{b}\mu\mu\nu\nu$ ” background in the remainder of this paper. The $t\bar{t}X$ process is presented

Background Process	Cross-Section σ [pb]
$pp \rightarrow t\bar{t}\mu^+\mu^-$	2.574×10^{-3}
$pp \rightarrow b\bar{b}\mu\mu\nu$	4.692×10^{-4}

Table 4.2: A summary of dominant SM backgrounds produced by pp collisions and their cross sections in pb, as computed by MadGraph with $n = 10^6$ events.

as part of the “ $t\bar{t}\mu^+\mu^-$ ” background. Table 4.2 shows the production cross sections for the dominant background sources. The rest of the aforementioned background processes do not contribute meaningfully in our context, accounting for $\ll 1\%$ of the total expected background yield.

The identification of leptons, boosted top quarks, and bottom quarks plays an important role in the ability to identify signal events, the ability to minimize the rate of SM backgrounds, and thus also the discovery reach in the high-luminosity environment of the LHC. It is worth noting that the reconstruction and identification of leptons and the decay products of the top/bottom quarks may be non-trivial at the High-Luminosity LHC (HL-LHC) due to the presence of a potentially large number of secondary pp interactions (pileup). The impact of pileup on the new physics discovery reach, and the importance of pileup mitigation at CMS and ATLAS has been outlined in many papers, for example in Ref. (CMS-PAS-FTR-13-014). We note the expected performance of the upgraded ATLAS and CMS detectors for the HL-LHC is beyond the scope of this work; however, the studies presented here do attempt to provide reasonable expectations by conservatively assuming some degradation in lepton and hadron identification efficiencies, using Ref. (CMS-PAS-FTR-13-014) as a benchmark, and considering the case of 140 average pileup interactions.

For muons with $|\eta| < 1.5$, the assumed identification efficiency is 95% with a 0.3% misidentification rate (CMS-PAS-FTR-13-014; CMS_MUON_17001). The performance degrades linearly with η for $1.5 < |\eta| < 2.5$, and we assume an identification efficiency of 65% with a 0.5% misidentification rate at $|\eta| = 2.5$. Similarly, the charged hadron tracking efficiency, which contributes to the jet clustering algorithm and missing transverse momentum (\vec{p}_T^{miss}) calculation, is 97% for $1.5 < |\eta| < 2.5$, and degrades to about 85% at $|\eta| = 2.5$. These potential inefficiencies due to the presence of secondary pp interactions contribute to how well the lepton and top kinematics can be reconstructed. Following Refs. (CMS:2020poo; ATLAS:2018wis), we consider the “Loose” working point for the identification of the fully merged (partially merged) t decays, which results in 80-85% top (W) identification efficiency and 11-25% misidentification rate, depending on the FatJet transverse momentum (p_T^{FJ}). Following Ref. (CMSbttag), we consider the “Loose” working point of the DeepCSV algorithm (Bols et al. 2020), which gives a 70-80% b-tagging efficiency and 10% light quark mis-identification rate. The choice of boosted t/W and b-tagging working points is determined through an optimization process that maximizes discovery reach. It is noted the contribution from SM backgrounds with a misidentified boosted t/W is negligible, and thus our discovery projections are not sensitive to uncertainties related to the boosted t/W misidentification rates.

4.4 DATA ANALYSIS USING MACHINE LEARNING

The analysis of signal and background events is performed utilizing machine learning techniques. A machine learning-based approach offers sizeable advantages

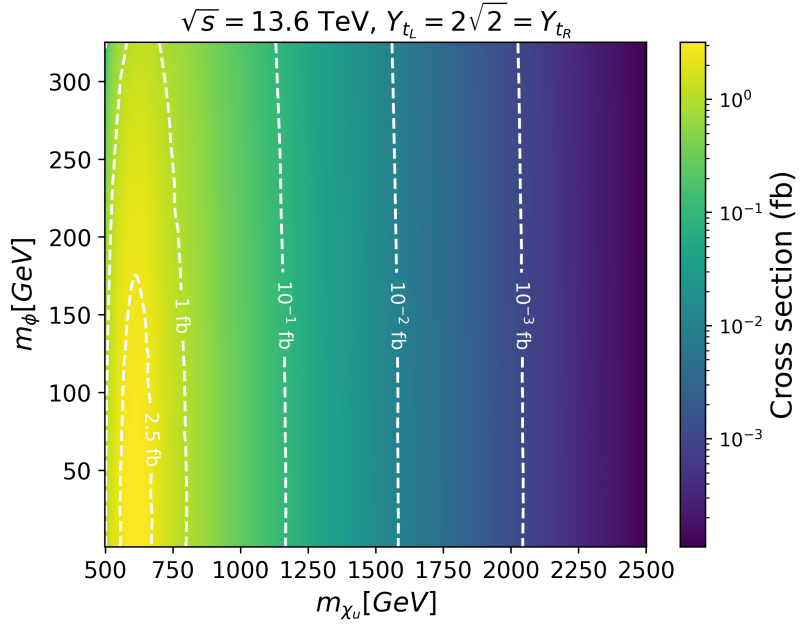


Figure 4.6: Projected cross section (fb) plot for $\text{pp} \rightarrow t\chi_u\phi'$ and subsequent decay as a function of $m(\chi_u)$ and $m(\phi')$.

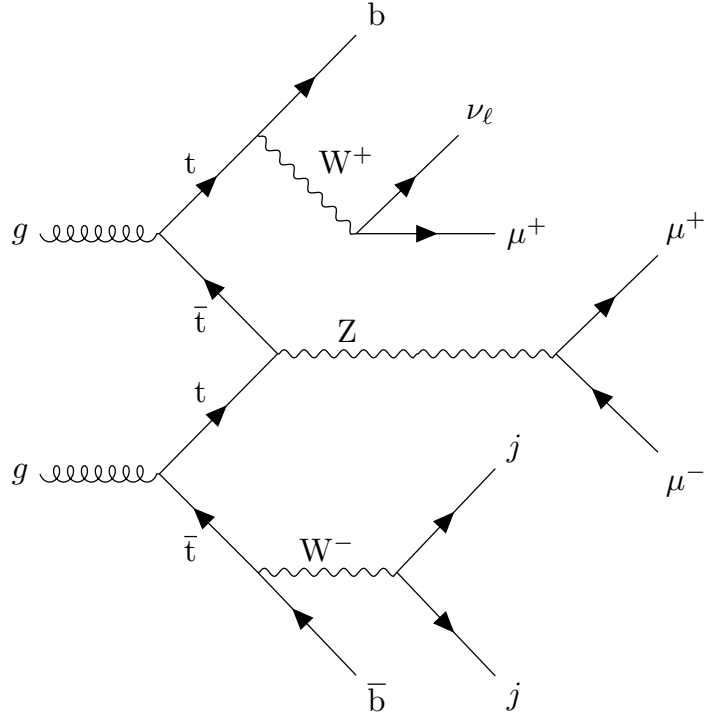


Figure 4.7: Representative Feynman diagram for a background event. A Z boson is produced in association with a top quark through the fusion of a top, anti top pair from incoming protons. The Z boson subsequently decays to a pair of muons and the two spectator top quarks decay semi-leptonically and purely hadronically to muons, neutrinos and jets, resulting in the same final states as the signal event.

when compared to traditional event classification techniques. Unlike conventional methods, machine learning models have the capability to simultaneously consider all kinematic variables, allowing them to efficiently navigate the complex and high-dimensional space of event kinematics. Consequently, machine learning models can effectively enact sophisticated selection criteria that take into account the entirety of this high-dimensional space. This makes them ideal for high-energy physics applications.

The BDT method is a powerful machine learning technique that has proven its effectiveness in various applications, particularly in the field of collider physics. In this method, decision trees are trained greedily in a sequential manner, with each tree focusing on learning the discrepancies or residuals between its predictions and the expected values obtained from the previously trained tree. This iterative process aims to progressively minimize errors, making BDTs a particularly effective approach for enhancing model performance.

In the context of collider physics, BDTs have demonstrated their utility in addressing classification problems. In particular, BDTs can effectively discriminate between signal and background events, enabling accurate and efficient event classification. Their ability to handle subtle non-linear relationships within the data with high interpretability makes BDTs a valuable tool to handle large amounts of data with a large number of parameters for each event.

The first step in our workflow involves the use of a specialized `MadAnalysis Expert Mode C++` script (Conte, Fuks, and Serret 2013). This script extracts essential kinematic and topological information from the simulated samples. The script will process the aforementioned variables contained within these files and transform them into a structured and informative CSV (Comma-Separated Values) format that can be used to train our machine learning models. These kinematic variables include crucial details about the events, such as particle momenta, energies, and topologies, providing the fundamental building blocks for our machine learning analysis. Figure 4.13 shows the features that are used for training the machine learning models and their importance for a benchmark point.

To account for the differential significance of various events, we apply cross-section weighting. This ensures that the relative importance of signal and background events is appropriately balanced in the dataset. This weighting is crucial for addressing the varying likelihood of observing different types of events in high-energy physics experiments. The prepared and weighted datasets are then passed to our `MadAnalysis Expert Mode C++` script, where the simulated signal and background events are initially filtered, before being passed to the CSV file for use by the machine learning algorithm. The filtering process requires at least one well-reconstructed and identified b-jet candidate, at least one jet (regular or FJ) not tagged as a b jet, and exactly three identified muons. The filtering selections are motivated by experimental constraints, such as the geometric constraints of the CMS/ATLAS detectors, the typical kinematic thresholds for the reconstruction of particle objects, and the available lepton triggers which also drive the minimal kinematic thresholds. Selected jets must have $p_T > 30 \text{ GeV}$ and $|\eta(j)| < 5.0$, while b-jet candidates with $p_T > 20 \text{ GeV}$ and $|\eta(b)| < 2.5$ are chosen. The μ object must pass a $p_T > 35 \text{ GeV}$ threshold and be within a $|\eta(\ell)| < 2.3$. We will refer to this filtering criteria as pre-selections. The efficiency of the pre-selections depends on $m(\phi')$ and $m(\chi_u)$, but is typically about 25-30% for the signal samples. Events passing this pre-selection are used as input for the machine learning algorithm, which classifies them as signal or background, using a probability factor.

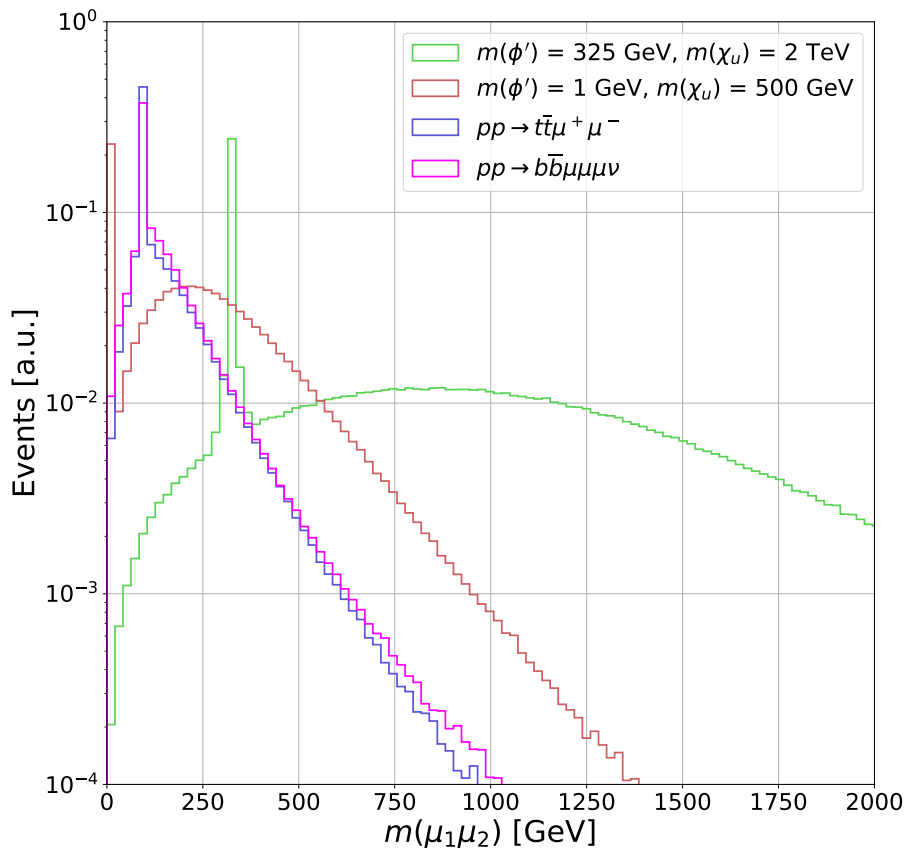


Figure 4.8: Invariant mass distribution of the muon pair with the highest and second highest transverse momentum. The distributions are shown for the two main SM background processes and two signal benchmark points.

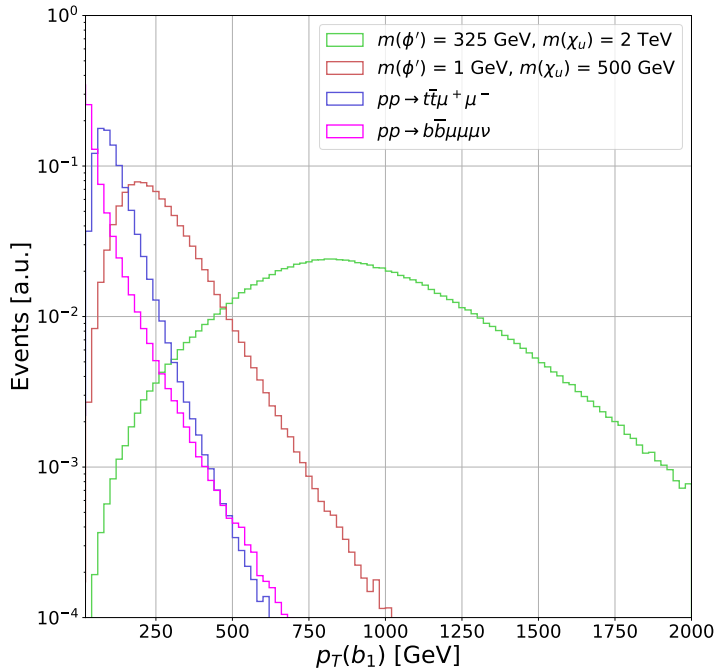


Figure 4.9: Transverse momentum distribution of the leading b-quark jet candidate. The distributions are shown for the two main SM background processes and two signal benchmark points.

Model	Train/Test Acc.	Training Time
BDT	N.A./0.9993	6s
Neural Network 1	0.9999/0.9997	1h 58m
Neural Network 2	0.9999/0.9998	2h 12m
Neural Network 3	0.9999/0.9998	2h 32m

Table 4.3: Train/test results for the ML models.

We explore the performance of a diverse set of machine learning models, specifically three neural networks of differing architectures and a BDT algorithm. To ensure robust model assessment, we employed a standard 90-10 train-test split of the dataset, partitioning it into a 90% portion for training and a 10% portion for testing. This division allows us to gauge the generalization capabilities of our models on unseen data.

The training and evaluation of the BDT were carried out in a high-performance computing environment. Specifically, an Nvidia A100 GPU was used. The canonical PyTorch ([paszke2019](#)) deep learning framework was employed for configuring, training, and evaluating the neural networks. PyTorch is well-regarded for its flexibility and performance in deep learning applications.

For the BDT algorithm, we used hyperparameters $\eta = 0.3$, $\gamma = 0$, and $\text{max_depth} = 6$. The XGBoost ([chen_xgboost_2016](#)) library was used for the implementation of the Boosted Decision Tree algorithm. It offers high efficiency, optimization, and interpretability, making it a suitable choice for this particular task.

It is worth mentioning that we experimented with deep neural networks of various architectures. Although we found that they yield similar signal sensitivity to the BDT, the complex nature of the studies in this work (particle objects consid-

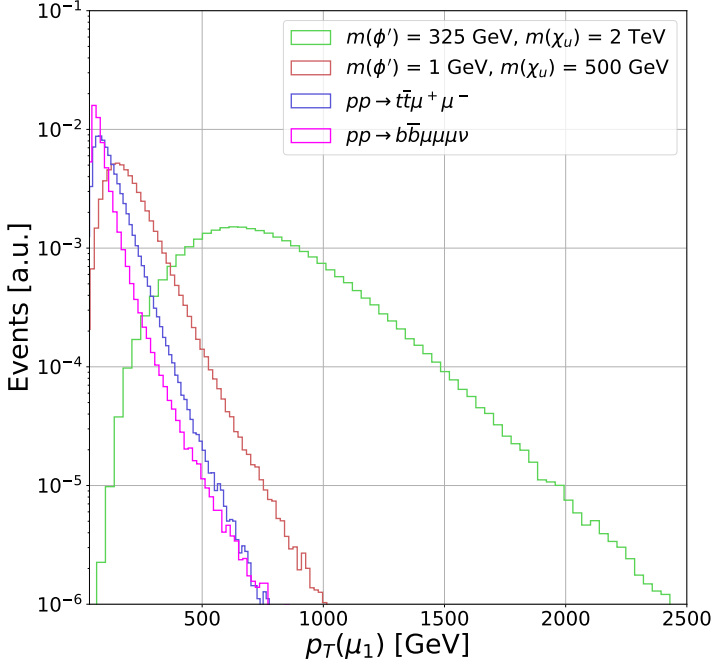


Figure 4.10: Transverse momentum distribution of the leading muon candidate. The distributions are shown for the two main SM background processes and two signal benchmark points.

ered, experimental constraints in a high luminosity LHC, etc.) motivates the use of a BDT over a deep neural network because of its usefulness, efficiency, and simplicity in understanding the machine learning output in addition to significantly shorter training times. Therefore, we perform our proceeding analysis using the BDT. The outcomes of our model training and evaluation are presented in Table 3.

4.5 RESULTS

Figures 4.8, 4.9, and 4.10 show relevant kinematic distributions for two benchmark signal points and the dominant SM backgrounds, using the subset of events passing the pre-selections defined above. The signal benchmark points in these figures are $m(\phi') = 325$ GeV, $m(\chi_u) = 2$ TeV, and $m(\phi') = 1$ GeV, $m(\chi_u) = 500$ GeV. The distributions are normalized such that the area under the curve is unity. These distributions correspond to the reconstructed mass, $m(\mu_1, \mu_2)$, between the two muon candidates with the highest transverse momentum (μ_1 and μ_2), the transverse momentum of the b-jet candidate with the highest transverse momentum $p_T(b_1)$, and the muon candidate with the highest transverse momentum $p_T(\mu_1)$, respectively. These distributions are among the variables identified by the BDT algorithm with the highest signal to background discrimination power (see Figure 4.13).

As can be seen from Figure 4.8, the ϕ' mass can be reconstructed through its associated muon decay pair, which is observed as a peak in the $m(\mu_1, \mu_2)$ distribution around the expected $m(\phi')$ value, and has low- and high-mass tails which are a consequence of cases where the leading and/or subleading muon is not from the ϕ' decay, but rather from the associated W boson from the χ_u decay. For the backgrounds, muons come from Z (W) decays. Therefore, the $m(\mu_1, \mu_2)$ background distributions show a peak near $m_{W/Z}$, combined with a

broad distribution indicative of the combination of two muon candidates from different decay vertices. We note that the $\phi' \rightarrow \mu^+ \mu^-$ decay width depends on the square of the $\phi' \rightarrow \mu^+ \mu^-$ coupling and $\frac{m_\mu^2}{m(\phi')^2}$ and is thus suppressed by the relatively small muon mass. For the new physics phase space considered in this paper, the ϕ' decay width is less than 1% of the ϕ' resonant mass. Furthermore, as indicated previously, the signal/background interference effects are small and negligible compared to effects from experimental resolution. Therefore, the width of the $m(\mu_1, \mu_2)$ signal distributions is driven by the experimental resolution in the reconstruction of the muon momenta, as well as the probability that the two leading muons are the correct pair from the ϕ' decay. Since the probability that the two highest- p_T muons are the correct pair from the $\phi' \rightarrow \mu^+ \mu^-$ decay depends on $m(\phi')$ and $m(\chi_u)$, it is important to include all possible combinations of dimuon pairs (i.e., $m(\mu_1, \mu_3)$ and $m(\mu_2, \mu_3)$) in the training of the BDT.

Figure 4.9 shows the distribution for the b-jet candidate with the highest p_T , $p_T(b_1)$, for the same simulated samples shown in Figure 4.8. Based on the signal topology and our choice of parameter space (i.e., $m(\chi_u) > m_t$), it is expected that the leading b-jet candidate comes from the χ_u decay, with an average p_T close to $\frac{m(\chi_u) - m_W}{2}$, as observed in Figure 4.9. For the $t\bar{t}\mu^+ \mu^-$ background, the b-jet candidates come from top-quark decays. Therefore, their average transverse momentum is expected to be $\frac{m_t - m_W}{2} \approx 45$ GeV, as observed in Figure 4.9. On the other hand, the b-jet candidates for the $b\bar{b}\mu\mu\nu$ background can come from off-mass-shell Z^*/γ^* , and thus typically have an even softer spectrum in comparison to the $t\bar{t}\mu^+ \mu^-$ background.

Figure 4.10 shows the distribution for the muon candidate with the highest p_T , $p_T(\mu_1)$. Similar to Figure 4.9, when $m(\chi_u) > m_t$ it is expected that the leading muon candidate comes from the χ_u decay, with an average p_T of approximately $\frac{m(\chi_u) - m_W}{4}$, as observed in Figure 4.10. For the major SM backgrounds, the muon candidates come from $Z/W/\gamma^*$ decays. Therefore, their average transverse momentum is expected to be much lower, $\frac{m_{Z/W}}{4} \approx 40 - 45$ GeV. This kinematic feature provides a nice handle to discriminate high $m(\chi_u)$ signal events amongst the large SM backgrounds, which have lower average $p_T(\mu)$ constrained by the SM weak boson masses.

In addition to these aforementioned variables in Figures 4.8-4.10, several other kinematic variables were included as inputs to the BDT algorithm. In particular, 27 such variables were used in total, and these included the momenta of b and muon candidates; invariant masses of pairs of muons; angular differences between b jets and between the muons.

As mentioned above, the variables $m(\mu_i, \mu_j)$ for $i, j \neq 1$ provide some additional discrimination between signal and background when the leading muons are not a ϕ' decay candidate. The angular separation variables, such as $\Delta R(\mu_i, \mu_j)$, are designed to be sensitive to lower mass ϕ' , since the low rest mass of those particles means they acquire more boost, and thus smaller angular separation ΔR between the muon candidates. The trained BDT returns the discriminating power of each of its inputs, and the feature importance for each variable is shown in Figure 4.13 for a signal benchmark point with $m(\phi') = 325$ GeV and $m(\chi_u) = 2000$ GeV.

Figure 4.11 shows the distributions for the output of the BDT algorithm, normalized to unity, for the representative signal benchmark point of $m(\phi') = 1$ GeV, $m(\chi_u) = 0.5$ TeV and the two dominant backgrounds. The output of the BDT algorithm is a value between 0 and 1, which quantifies the likelihood that an event is either background-like (BDT output near 1) or signal-like (BDT output near 0). Figure 4.12 illustrates the true positive rate (TPR), defined as the probability of

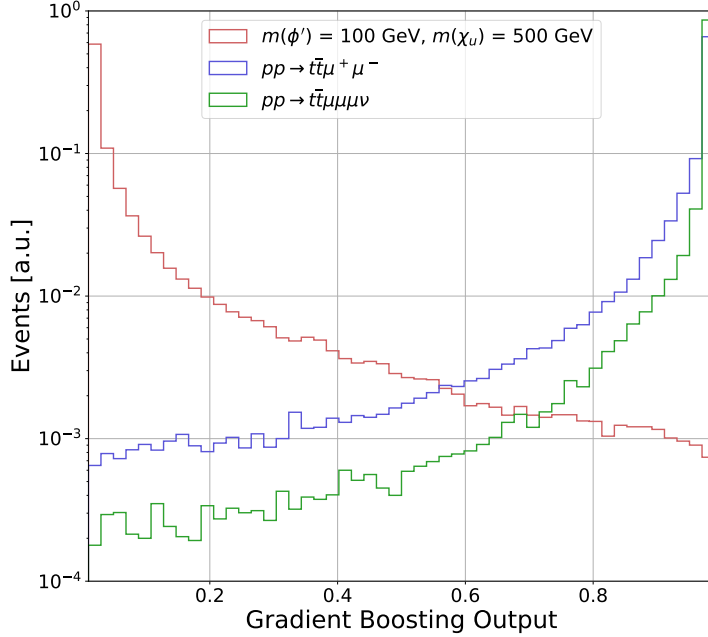


Figure 4.11: Output of the gradient boosting algorithm for a benchmark $m(\phi') = 100$ GeV and $m(\chi_u) = 500$ GeV signal, and dominant backgrounds. The distributions are normalized to unity.

correctly selecting signal events using the BDT output, plotted against the false positive rate (FPR), defined as the probability of incorrectly selecting background events. For example, for $m(\phi') = 100$ GeV and $m(\chi_u) = 500$ GeV, when signal events are selected at 65% probability, the background is selected at about 10^{-3} probability. We note that the primary discriminating feature between the signal and background is the boosted b-jet p_T coming from the χ_u vector-like quark. The p_T of said b jet increases with $m(\chi_u)$, peaking at around $[m(\chi_u) - m(W)]/2$. This enhanced boost increases the separation between signal and background, improving the performance of the BDT algorithm as $m(\chi_u)$ increases.

The outputs from the BDT machine learning algorithm are used to perform a profile-bin likelihood analysis to estimate the signal significance for a luminosity of 3000 fb^{-1} , corresponding to the expected amount of collected data by the end of the LHC era. For this purpose, the BDT distributions are normalized to cross section times pre-selection efficiency times luminosity for the different signal models. The significance is then calculated using the expected bin-by-bin yields of the BDT output distribution in a profile likelihood fit, using the ROOTFit ([Butterworth:2015oua](#)) package developed by CERN. The expected signal significance Z_{sig} is calculated using the probability of obtaining the same test statistic for the signal plus background and the signal-null hypotheses, defined as the local p-value. Similar to Refs. ([Florez:2021zoo](#); [Florez:2019tqr](#); [Florez:2018ojp](#); [Florez:2017xhf](#); [VBFZprimePaper](#); [Florez:2016lwi](#); [Leonardi_2020](#)), the significance corresponds to the point where the integral of a Gaussian distribution between Z_{sig} and ∞ results in a value equal to the local p-value. The estimation of Z_{sig} incorporates systematic uncertainties. The uncertainty values have been included as nuisance parameters, considering lognormal priors for normalization and Gaussian priors for uncertainties associated with the modeling of the shapes similar to Refs. ([natalia2021longtermlhcdiscoveryreach](#); [PhysRevD.103.095001](#)).

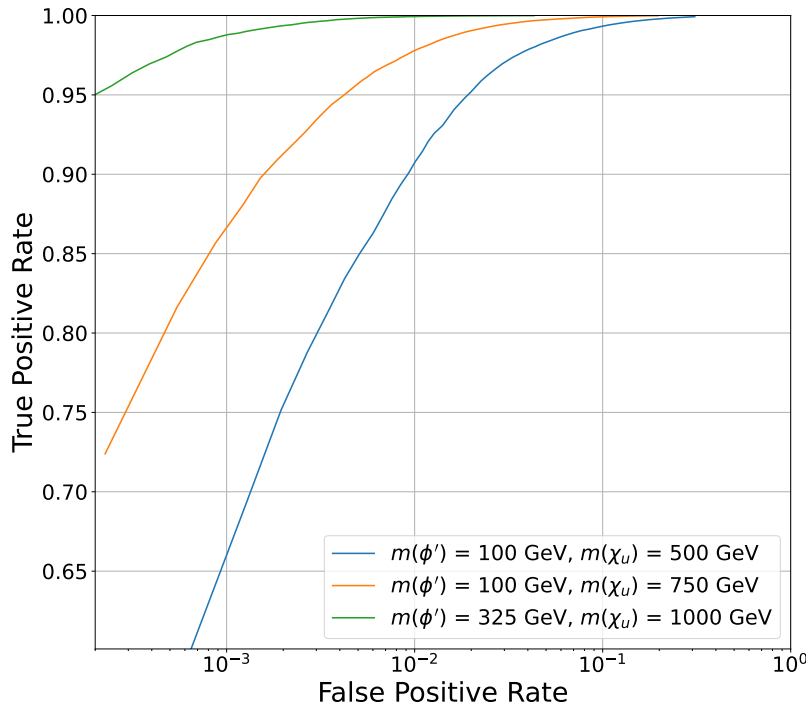


Figure 4.12: Receiver operating characteristic curve of the BDT algorithm for three different signal benchmark scenarios.

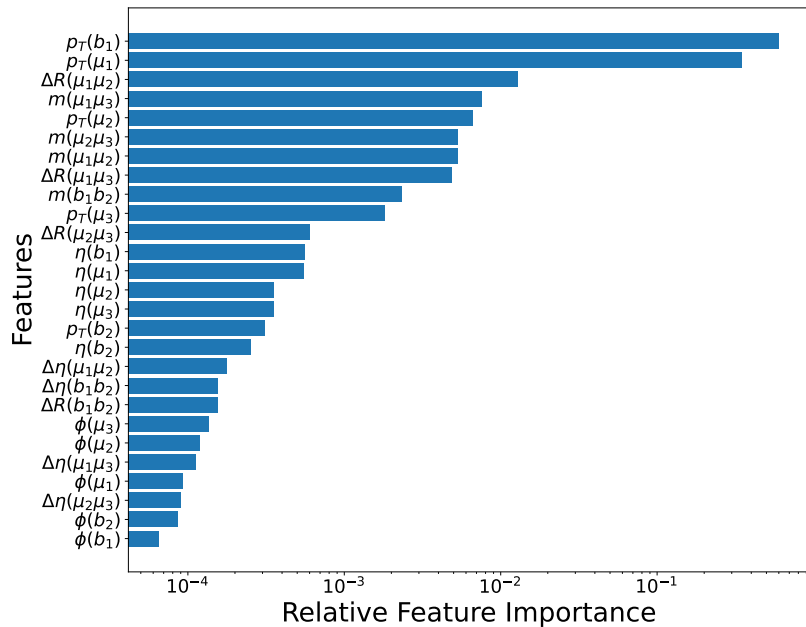


Figure 4.13: Relative importance of features in training for a benchmark signal scenario with $m(\phi') = 325 \text{ GeV}$ and $m(\chi_u) = 2000 \text{ GeV}$.

The systematic uncertainties that have been included result from experimental and theoretical constraints. A 1-5% systematic uncertainty, depending on the simulated MC sample, has been included to account for the choice of Parton Distribution Function (PDF) set. The systematic uncertainty effect was incorporated following the PDF4LHC ([Butterworth:2015oua](#)) recommendations. This systematic uncertainty has a small impact on the expected event yields for signal and background, but it does not affect the shape of the BDT output distribution. We additionally considered theoretical uncertainties related to the absence of higher-order contributions to the signal cross sections, which can change the pre-selection efficiencies and the shapes of kinematic variables used as inputs to the BDT algorithm. This uncertainty was calculated by varying the renormalization and factorization scales by $\times 2$, and studying the resulting change in the bin-by-bin yields of the BDT distributions. They are found to be at most 2% in a given bin.

Regarding experimental uncertainties, following experimental measurements from CMS on the estimation of the integrated luminosity, a conservative 3% effect has been included ([lumiRef](#)). A 5% systematic uncertainty associated with the reconstruction and identification of b-quark jets has been included, independent of p_T and η of the b-jet candidates. According to Ref. ([CMSbtag](#)), this uncertainty is correlated between signal and background processes with genuine b-jets and is also correlated across BDT bins for each process. For muons, we include a 2% uncertainty associated with the reconstruction, identification, and isolation requirements, and a 3% systematic uncertainty to account for scale and resolution effects on the momentum and energy measurement. We consider jet energy scale uncertainties ranging from 2-5%, contingent on η and p_T , resulting in shape-based uncertainties on the BDT output distribution. Jet energy scale uncertainties were assumed to range from 1-5%, contingent on η and p_T . These assumptions lead to shape-based uncertainties on the BDT output distribution, varying from 1-2%. Additionally, we include a 10% systematic uncertainty to account for errors in the signal and background predictions. Considering all the various sources of systematic uncertainties, our conservative estimate yields a total effect of about 20%.

Figure 4.14 shows the expected signal significance considering an integrated luminosity of 3000 fb^{-1} . The significance is shown as a heat map in a two-dimensional plane for different ϕ' and χ_u masses. The x-axis corresponds to $m(\chi_u)$, the y-axis to $m(\phi')$, and the heat map to $\log_{10}(Z_{\text{sig}})$. The white dashed lines are contours of constant signal significances of 1.69σ , 3σ and 5σ to represent regions of possible exclusion, evidence of new physics, and discovery, respectively. Under these conditions, ϕ' (χ_u) masses ranging from 1 to 325 GeV (500 to 1800 GeV) can be probed. The range for a discovery with 5σ signal significance varies from χ_u masses from $m(\chi_u) = 770$ - 1100 GeV , depending $m(\phi')$. For large $m(\chi_u)$, the significance is almost independent of $m(\phi')$ because the primary discriminating feature—the boosted b-quark originating from ϕ' —is driven predominantly by the large $m(\chi_u)$, with the kinematic impact of $m(\phi')$ being relatively negligible.

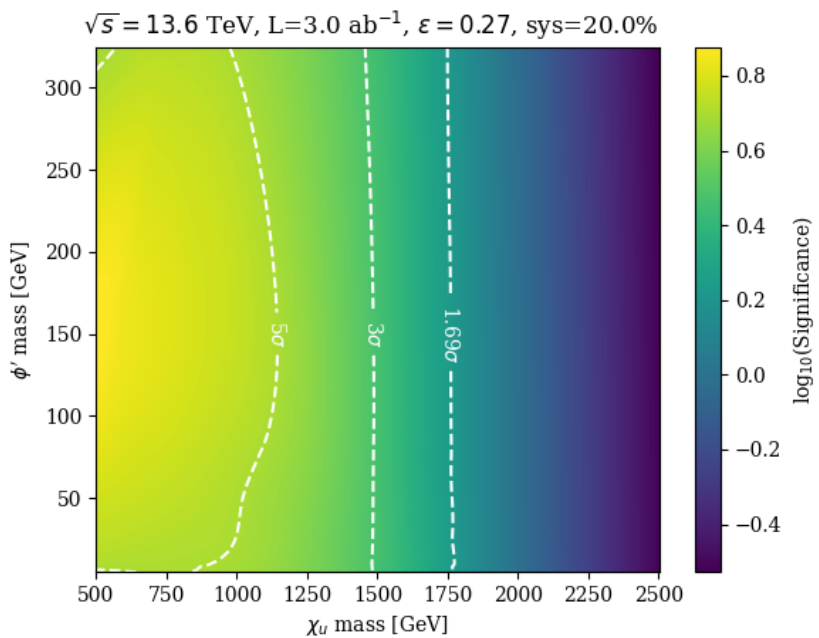


Figure 4.14: Signal significance for the high luminosity LHC era, considering with 3000 fb^{-1} of collected data.

5

DISCUSSION AND RESULTS

5.1 U1

The LHC will continue to run with pp collisions at $\sqrt{s} = 13.6$ TeV for the next decade. Given the increase in the integrated luminosity expected from the high-luminosity program, it is important to consider unexplored new physics phase space that diverges from the conventional assumptions made in many BSM theories, and which could have remained hidden in processes that have not yet been thoroughly examined. It is additionally crucial to explore advanced analysis techniques, in particular the use of artificial intelligence algorithms, to enhance the probability of detecting these rare corners where production cross sections are lower and discrimination from SM backgrounds is difficult.

In this work, we examine a model based on a $U(1)_{T_R^3}$ extension of the SM, which can address various conceptual and experimental issues with the SM, including the mass hierarchy between generations of fermions, the thermal dark matter abundance, and the muon $g - 2$, $R_{(D)}$, and $R_{(D^*)}$ anomalies. This model contains a light scalar boson ϕ' , with potential masses below the electroweak scale, and TeV-scale vector-like quarks χ_u . We consider the scenario where the scalar ϕ' has family non-universal fermion couplings and $m(\phi') \geq 1$ GeV, as was suggested in Ref. (Dutta2020), and thus the ϕ' can primarily decay to a pair of muons. Previous works in Refs. (Dutta2023; Banerjee_2016) considered scenarios motivating a search methodology with a merged diphoton system from $\phi' \rightarrow \gamma\gamma$ decays. The authors of Ref (Dutta2023), in which $m(\phi') < 1$ GeV, indeed pointed out that if the ϕ' is heavier than about 1 GeV, then decays to $\mu^+\mu^-$ can become the preferable mode for discovery, which is the basis for the work presented in this paper. We further note that the final state topology studied in this paper would represent the most important mode for discovery at $m(\phi') < 2m_t$ where the $\phi' \rightarrow t\bar{t}$ decay is kinematically forbidden.

The main result of this paper is that we have shown that the LHC can probe the visible decays of new bosons with masses below the electroweak scale, down to the GeV-scale, by considering the simultaneous production of heavy QCD-coupled particles, which then decay to the SM particles that contain large momentum values and can be observed in the central regions of the CMS and ATLAS detectors. The boosted system combined with innovative machine learning algorithms allows for the signal extraction above the lower-energy SM background. The LHC search strategy described here can be used to discover the prompt decay of new light particles. An important conclusion from this paper is that the detection prospects for low-mass particles are enhanced when it is kinematically possible to simultaneously access the heavy degrees of freedom which arise in the UV completion of the low-energy model. This specific scenario in which the couplings of the light scalars are generationally dependent, with important coupling values

to the top quark, is an ideal example which would be difficult to directly probe at low energy beam experiments.

The proposed data analysis represents a competitive alternative to complement searches already being conducted at the LHC, allowing us to probe ϕ' masses from 1 to 325 GeV, for $m(\chi_u)$ values up to almost 2 TeV, at the HL-LHC. Therefore, we strongly encourage the ATLAS and CMS Collaborations to consider the proposed analysis strategy in future new physics searches.

5.2 LEPTOQUARK

Experimental searches for LQs with preferential couplings to third generation fermions are currently of great interest due to their potential to explain observed tensions in the $R(D)$ and $R(D^*)$ decay ratios of B mesons with respect to the SM predictions. Although the LHC has a broad physics program on searches for LQs, it is very important to consider the impact of each search within wide range of different theoretical assumptions within a specific model. In addition, in order to improve the sensitivity to detect possible signs of physics beyond the SM, it is also important to strongly consider new computational techniques based on machine learning (ML). Therefore, we have studied the production of U_1 LQs with preferential couplings to third generation fermions, considering different couplings, masses and chiral currents. These studies have been performed considering $p\ p$ collisions at $\sqrt{s} = 13$ TeV and 13.6 TeV and different luminosity scenarios, including projections for the high luminosity LHC. A ML algorithm based on boosted decision trees is used to maximize the signal significance. The signal to background discrimination output of the algorithm is taken as input to perform a profile binned-likelihood test statistic to extract the expected signal significance.

The expected signal significance for sLQ, dLQ and non-res production, and their combination, is presented as contours on a two dimensional plane of g_U versus M_{U_1} . We present results for the case of exclusive couplings to left-handed, mixed, and exclusive right-handed currents. For the first two, the region of the phase space that could explain the B meson anomalies is also presented. We confirm the findings of previous works that the largest production cross-section and best overall significance comes from the combination of dLQ and non-res production channels. We also find that the sensitivity to probe the parameter space of the model is highly dependent on the chirality of the couplings. Nevertheless, the region solving the B-meson anomalies also changes with each choice, such that in all evaluated cases we find ourselves just starting to probe this region at large M_{U_1} .

Our studies compare our exclusion regions with respect to the latest reported results from the ATLAS and CMS Collaborations. The comparison suggests that our ML approach has a better sensitivity than the standard cut-based analyses, especially at large values of g_U . In addition, our projections for the HL-LHC cover the whole region solving the B-anomalies, for masses up to 5.00 TeV.

Finally, we consider the effects of a companion Z' boson on non-res production. We find that such a contribution can have a considerable impact on the LQ sensitivity regions, depending on the specific masses and couplings. In spite of this, we still consider non-res production as an essential channel for probing LQs in the future.

BIBLIOGRAPHY

- Aaboud, M. et al. (2018). "Measurement of the W-boson mass in pp collisions at $\sqrt{s} = 7$ TeV with the ATLAS detector". In: *The European Physical Journal C* 78.2. doi: 10.1140/epjc/s10052-017-5475-4.
- Aaij, R. et al. (2015). "Measurement of the Ratio of Branching Fractions $\mathcal{B}(\bar{B}^0 \rightarrow D^{*+}\tau^-\bar{\nu}_\tau)/\mathcal{B}(\bar{B}^0 \rightarrow D^{*+}\mu^-\bar{\nu}_\mu)$ ". In: *Phys. Rev. Lett.* 115 (11), p. 111803. doi: 10.1103/PhysRevLett.115.111803.
- Abazov, V. M. et al. (2012). "Measurement of the W Boson Mass with the Do Detector". In: *Physical Review Letters* 108.15. doi: 10.1103/physrevlett.108.151804.
- Abdullah, Mohammad et al. (2018). "Probing a simplified W' model of $R(D^{(*)})$ anomalies using b tags, τ leptons, and missing energy". In: *Phys. Rev. D* 98 (5), p. 055016. doi: 10.1103/PhysRevD.98.055016.
- Abe, S. et al. (2008). "Precision Measurement of Neutrino Oscillation Parameters with KamLAND". In: *Physical Review Letters* 100.22. doi: 10.1103/physrevlett.100.221803.
- Abi, B. et al. (2021). "Measurement of the Positive Muon Anomalous Magnetic Moment to 0.46 ppm". In: *Physical Review Letters* 126.14. doi: 10.1103/physrevlett.126.141801.
- Adler, Ronald J., Brendan Casey, and Ovid C. Jacob (July 1995). "Vacuum catastrophe: An elementary exposition of the cosmological constant problem". In: *American Journal of Physics* 63 (7), pp. 620–626. ISSN: 0002-9505. doi: 10.1119/1.17850.
- Albert, Andreas (n.d.). *lhereader*. Version 1.0.11. URL: <https://pypi.org/project/lhereader/>.
- Alloul, Adam et al. (2014). "FeynRules 2.0 A complete toolbox for tree-level phenomenology". In: *Computer Physics Communications* 185.8, pp. 2250–2300. ISSN: 0010-4655. doi: <https://doi.org/10.1016/j.cpc.2014.04.012>.
- Altmannshofer, Wolfgang and David M. Straub (2015). "New physics in b → s transitions after LHC run 1". In: *The European Physical Journal C* 75.8. doi: 10.1140/epjc/s10052-015-3602-7.
- Altmannshofer, Wolfgang et al. (2017). "Status of the $B \rightarrow K^*\mu^+\mu^-$, anomaly after Moriond 2017". In: *The European Physical Journal C* 77.6, p. 377. ISSN: 1434-6052. doi: 10.1140/epjc/s10052-017-4952-0.
- Alwall, J. et al. (2014). "The automated computation of tree-level and next-to-leading order differential cross sections, and their matching to parton shower simulations". In: *Journal of High Energy Physics* 2014.7. doi: 10.1007/jhep07(2014)079.
- Amhis, Y. et al. (2021). "Averages of b-hadron, c-hadron, and τ -lepton properties as of 2018". In: *The European Physical Journal C* 81.3. doi: 10.1140/epjc/s10052-020-8156-7.
- Antoniadis, I. et al. (2014). "The Volkov-Akulov-Starobinsky supergravity". In: *Physics Letters, Section B: Nuclear, Elementary Particle and High-Energy Physics* 733, pp. 32–35. ISSN: 03702693. doi: 10.1016/j.physletb.2014.04.015. arXiv: 1403.3269 [hep-th].
- Aoude, Rafael et al. (2020). "The impact of flavour data on global fits of the MFV SMEFT". In: *Journal of High Energy Physics* 2020.12. doi: 10.1007/jhep12(2020)113.

- Ask, Stefan et al. (Sept. 2012). "From Lagrangians to Events: Computer Tutorial at the MC4BSM-2012 Workshop". In.
- Assad, N., B. Fornal, and B. Grinstein (2018). "Baryon Number and Lepton Universality Violation in Leptoquark and Diquark Models". In: *Phys. Lett. B* 777, pp. 324–331. DOI: 10.1016/j.physletb.2017.12.042. arXiv: 1708.06350 [hep-ph].
- Baker, Michael J. et al. (n.d.). *Vector-leptoquark model*. URL: <https://feynrules.irmp.ucl.ac.be/wiki/LeptoQuark>.
- Baker, Michael J. et al. (2019). "High-\$p_T\$ signatures in vector-leptoquark models". In: *The European Physical Journal C* 79.4, p. 334. ISSN: 1434-6052. DOI: 10.1140/epjc/s10052-019-6853-x.
- Barbieri, R., S. Ferrara, and C. A. Savoy (1982). "Gauge models with spontaneously broken local supersymmetry". In: *Physics Letters B* 119.4-6, pp. 343–347. ISSN: 03702693. DOI: 10.1016/0370-2693(82)90685-2.
- Barbieri, R., C. W. Murphy, and F. Senia (2017). "B-decay anomalies in a composite leptoquark model". In: *Eur. Phys. J. C* 77.1, p. 8. DOI: 10.1140/epjc/s10052-016-4578-7. arXiv: 1611.04930 [hep-ph].
- Barbieri, R. and A. Tesi (2018). "B-decay anomalies in Pati-Salam SU(4)". In: *Eur. Phys. J. C* 78.3, p. 193. DOI: 10.1140/epjc/s10052-018-5680-9. arXiv: 1712.06844 [hep-ph].
- Bergshoeff, Eric A. et al. (2015). "Pure de Sitter supergravity". In: *Physical Review D - Particles, Fields, Gravitation and Cosmology* 92.8, p. 85040. ISSN: 15502368. DOI: 10.1103/PhysRevD.92.085040. arXiv: 1507.08264.
- Bhaskar, Arvind et al. (2024). "Fresh look at the LHC limits on scalar leptoquarks". In: *Phys. Rev. D* 109.5, p. 055018. DOI: 10.1103/PhysRevD.109.055018. arXiv: 2312.09855 [hep-ph].
- Bierlich, Christian et al. (2022). *A comprehensive guide to the physics and usage of PYTHIA 8.3*. DOI: 10.48550/ARXIV.2203.11601.
- Bilal, Adel (2001). "Introduction to Supersymmetry". In: *arXiv*. arXiv: 0101055 [hep-th].
- Binetruy, Pierre et al. (2004). "Fayet-Iliopoulos terms in supergravity and cosmology". In: *Classical and Quantum Gravity* 21.13, pp. 3137–3169. ISSN: 0264-9381. DOI: 10.1088/0264-9381/21/13/005. arXiv: 0402046 [hep-th].
- Blanke, M. and A. Crivellin (2018). "B Meson anomalies in a Pati-Salam model within the Randall-Sundrum background". In: *Phys. Rev. Lett.* 121.1, p. 011801. DOI: 10.1103/PhysRevLett.121.011801. arXiv: 1801.07256 [hep-ph].
- Blankenburg, Gianluca, Gino Isidori, and Joel Jones-Perez (2012). "Neutrino Masses and LFV from Minimal Breaking of $U(3)^5$ and $U(2)^5$ flavor Symmetries". In: *Eur. Phys. J. C* 72, p. 2126. DOI: 10.1140/epjc/s10052-012-2126-7. arXiv: 1204.0688 [hep-ph].
- Blum, Thomas et al. (2013). *The Muon $(g-2)$ Theory Value: Present and Future*. DOI: 10.48550/ARXIV.1311.2198.
- Bols, E. et al. (2020). "Jet flavour classification using DeepJet". In: *Journal of Instrumentation* 15.12, P12012. DOI: 10.1088/1748-0221/15/12/P12012.
- Bordone, M. et al. (2018a). "A three-site gauge model for flavor hierarchies and flavor anomalies". In: *Phys. Lett. B* 779, pp. 317–323. DOI: 10.1016/j.physletb.2018.02.011. arXiv: 1712.01368 [hep-ph].
- Bordone, M. et al. (2018b). "Low-energy signatures of the PS³ model: from B-physics anomalies to LFV". In: *JHEP* 10, p. 148. DOI: 10.1007/JHEP10(2018)148. arXiv: 1805.09328 [hep-ph].

- Bordone, Marzia, Gino Isidori, and Andrea Pattori (2016). "On the standard model predictions for R_K and R_{K^*} ". In: *The European Physical Journal C* 76.8, p. 440. ISSN: 1434-6052. doi: 10.1140/epjc/s10052-016-4274-7.
- Burdman, Gustavo, Bogdan A. Dobrescu, and Eduardo Pontón (2006). "Resonances from two universal extra dimensions". In: *Phys. Rev. D* 74 (7), p. 075008. doi: 10.1103/PhysRevD.74.075008.
- Buttazzo, Dario et al. (2017). "B-physics anomalies: a guide to combined explanations". In: *Journal of High Energy Physics* 2017.11. doi: 10.1007/jhep11(2017)044.
- COllaboration, CDF et al. (2022). "High-precision measurement of the W boson mass with the CDF II detector". In: *Science* 376.6589, pp. 170–176. doi: 10.1126/science.abk1781.
- Calibbi, L., A. Crivellin, and T. Li (2018). "Model of vector leptoquarks in view of the B-physics anomalies". In: *Phys. Rev. D* 98.11, p. 115002. doi: 10.1103/PhysRevD.98.115002. arXiv: 1709.00692 [hep-ph].
- Camargo-Molina, José Eliel, Alejandro Celis, and Darius A. Faroughy (2018). "Anomalies in bottom from new physics in top". In: *Physics Letters B* 784, pp. 284–293. doi: 10.1016/j.physletb.2018.07.051.
- Capdevila, Bernat et al. (2017). "Hadronic uncertainties in $B \rightarrow K?\mu+\mu?$: a state-of-the-art analysis". In: *Journal of High Energy Physics* 2017.4, p. 16. ISSN: 1029-8479. doi: 10.1007/JHEP04(2017)016.
- Capdevila, Bernat et al. (2018). "Patterns of New Physics in $b \rightarrow s\ell^+\ell^-$ transitions in the light of recent data". In: *Journal of High Energy Physics* 2018.1. doi: 10.1007/jhep01(2018)093.
- Carlos, B. de et al. (1993). "Model-independent properties and cosmological implications of the dilaton and moduli sectors of 4D strings". In: *Physics Letters B* 318.3, pp. 447–456. ISSN: 03702693. doi: 10.1016/0370-2693(93)91538-X. arXiv: 9308325 [hep-ph].
- Celis, Alejandro et al. (2017). "Gauge-invariant implications of the LHCb measurements on lepton-flavor nonuniversality". In: *Physical Review D* 96.3. doi: 10.1103/physrevd.96.035026.
- Chamseddine, A H, R Arnowitt, and Pran Nath (1982). "Locally Supersymmetric Grand Unification". In: *Phys. Rev. Lett.* 49.14, pp. 970–974. doi: 10.1103/PhysRevLett.49.970.
- Cheung, Clifford, Francesco D'Eramo, and Jesse Thaler (2011). "Supergravity computations without gravity complications". In: *Phys. Rev. D* 84.8, p. 85012. doi: 10.1103/PhysRevD.84.085012.
- Chobanova, V. G. et al. (2017). "Large hadronic power corrections or new physics in the rare decay $B \rightarrow K?\mu+\mu??$ ". In: *Journal of High Energy Physics* 2017.7, p. 25. ISSN: 1029-8479. doi: 10.1007/JHEP07(2017)025.
- Cline, James M. (2006). *Baryogenesis*. doi: 10.48550/ARXIV.HEP-PH/0609145.
- Collaboration, Belle (2021). "Test of lepton-flavor universality in $B \rightarrow K^*\ell^+\ell^-$ decays at Belle". In: *Physical Review Letters* 126.16. doi: 10.1103/physrevlett.126.161801.
- Collaboration, The CMS (2008). "The CMS experiment at the CERN LHC". In: *Journal of Instrumentation* 3.08, S08004–S08004. doi: 10.1088/1748-0221/3/08/S08004.
- Conte, Eric, Benjamin Fuks, and Guillaume Serret (2013). "MadAnalysis 5, a user-friendly framework for collider phenomenology". In: *Computer Physics Communications* 184.1, pp. 222–256. ISSN: 0010-4655. doi: 10.1016/j.cpc.2012.09.009.

- Cornella, C., J. Fuentes-Martín, and G. Isidori (2019). "Revisiting the vector leptoquark explanation of the B-physics anomalies". In: *JHEP* 07, p. 168. DOI: [10.1007/JHEP07\(2019\)168](https://doi.org/10.1007/JHEP07(2019)168). arXiv: [1903.11517 \[hep-ph\]](https://arxiv.org/abs/1903.11517).
- Cornella, C. et al. (2021a). "Reading the footprints of the B-meson flavor anomalies". In: *JHEP* 08, p. 050. DOI: [10.1007/JHEP08\(2021\)050](https://doi.org/10.1007/JHEP08(2021)050). arXiv: [2103.16558 \[hep-ph\]](https://arxiv.org/abs/2103.16558).
- Cornella, Claudia, Javier Fuentes-Martín, and Gino Isidori (2019). "Revisiting the vector leptoquark explanation of the B-physics anomalies". In: *Journal of High Energy Physics* 2019.7. DOI: [10.1007/jhep07\(2019\)168](https://doi.org/10.1007/jhep07(2019)168).
- Cornella, Claudia et al. (2021b). "Reading the footprints of the B-meson flavor anomalies". In: *Journal of High Energy Physics* 2021.8, p. 50. ISSN: 1029-8479. DOI: [10.1007/JHEP08\(2021\)050](https://doi.org/10.1007/JHEP08(2021)050).
- Cosenza, Mario (2016). *Mecánica Clásica - Apuntes de Clase*. A-2016. Mérida: Universidad de Los Andes.
- Coy, Rupert et al. (2020). "New physics in $b \rightarrow s\ell\ell$ transitions at one loop". In: *The European Physical Journal C* 80.1, p. 52. ISSN: 1434-6052. DOI: [10.1140/epjc/s10052-019-7581-y](https://doi.org/10.1140/epjc/s10052-019-7581-y).
- Crivellin, Andreas, Giancarlo D'Ambrosio, and Julian Heeck (2015). "Addressing the LHC flavor anomalies with horizontal gauge symmetries". In: *Physical Review D* 91.7. DOI: [10.1103/physrevd.91.075006](https://doi.org/10.1103/physrevd.91.075006).
- Crivellin, Andreas and Martin Hoferichter (2020). " β Decays as Sensitive Probes of Lepton Flavor Universality". In: *Phys. Rev. Lett.* 125 (11), p. 111801. DOI: [10.1103/PhysRevLett.125.111801](https://doi.org/10.1103/PhysRevLett.125.111801).
- (2021). "Hints of lepton flavor universality violations". In: *Science* 374.6571, pp. 1051–1052. DOI: [10.1126/science.abk2450](https://doi.org/10.1126/science.abk2450).
- Crivellin, Andreas et al. (2015). "Lepton-flavor violating B decays in generic Z' models". In: *Phys. Rev. D* 92 (5), p. 054013. DOI: [10.1103/PhysRevD.92.054013](https://doi.org/10.1103/PhysRevD.92.054013).
- Descotes-Genon, Sébastien et al. (2013). "Implications from clean observables for the binned analysis of $B \rightarrow K^? \mu^+ \mu^-$ at large recoil". In: *Journal of High Energy Physics* 2013.1, p. 48. ISSN: 1029-8479. DOI: [10.1007/JHEP01\(2013\)048](https://doi.org/10.1007/JHEP01(2013)048).
- Di Luzio, L., A. Greljo, and M. Nardecchia (2017). "Gauge leptoquark as the origin of B-physics anomalies". In: *Phys. Rev. D* 96.11, p. 115011. DOI: [10.1103/PhysRevD.96.115011](https://doi.org/10.1103/PhysRevD.96.115011). arXiv: [1708.08450 \[hep-ph\]](https://arxiv.org/abs/1708.08450).
- Dienes, Keith R., Emilian Dudas, and Tony Gherghetta (1999). "Grand unification at intermediate mass scales through extra dimensions". In: *Nuclear Physics B* 537.1, pp. 47–108. ISSN: 0550-3213. DOI: [https://doi.org/10.1016/S0550-3213\(98\)00669-5](https://doi.org/10.1016/S0550-3213(98)00669-5).
- Dimopoulos, Savas and Howard Georgi (1981). "Softly broken supersymmetry and SU(5)". In: *Nuclear Physics, Section B* 193.1, pp. 150–162. ISSN: 05503213. DOI: [10.1016/0550-3213\(81\)90522-8](https://doi.org/10.1016/0550-3213(81)90522-8).
- Doršner, Ilja and Admir Greljo (2018). "Leptoquark toolbox for precision collider studies". In: *Journal of High Energy Physics* 2018.5. DOI: [10.1007/jhep05\(2018\)126](https://doi.org/10.1007/jhep05(2018)126).
- Dyson, F. J. (1949). "The Radiation Theories of Tomonaga, Schwinger, and Feynman". In: *Phys. Rev.* 75 (3), pp. 486–502. DOI: [10.1103/PhysRev.75.486](https://doi.org/10.1103/PhysRev.75.486).
- Ellis, John, Dimitri V Nanopoulos, and Keith A Olive (2013). "No-Scale Supergravity Realization of the Starobinsky Model of Inflation". In: *Phys. Rev. Lett.* 111.11, p. 111301. DOI: [10.1103/PhysRevLett.111.111301](https://doi.org/10.1103/PhysRevLett.111.111301).
- Evans, Lyndon and Philip Bryant (2008). "LHC Machine". In: *Journal of Instrumentation* 3.08, S08001–S08001. DOI: [10.1088/1748-0221/3/08/s08001](https://doi.org/10.1088/1748-0221/3/08/s08001).
- Everett, L L (2013). "Models of Supersymmetry Breaking". In: *The Dark Secrets of the Terascale*, pp. 259–281. DOI: [10.1142/9789814390163_0006](https://doi.org/10.1142/9789814390163_0006).

- Farakos, F., A. Kehagias, and A. Riotto (2013). "On the Starobinsky model of inflation from supergravity". In: *Nuclear Physics B* 876.1, pp. 187–200. ISSN: 05503213. DOI: 10.1016/j.nuclphysb.2013.08.005. arXiv: 1305.1247.
- Favereau, J. de et al. (2014). "DELPHES 3: a modular framework for fast simulation of a generic collider experiment". In: *Journal of High Energy Physics* 2014.2. DOI: 10.1007/jhep02(2014)057.
- Fayet, P. (1977). "Spontaneously broken supersymmetric theories of weak, electromagnetic and strong interactions". In: *Physics Letters B* 69.4, pp. 489–494. ISSN: 03702693. DOI: 10.1016/0370-2693(77)90852-8.
- Fernández-Navarro, M. and S. F. King (2023). "B-anomalies in a twin Pati-Salam theory of flavour including the 2022 LHCb $R_{K^{(*)}}$ analysis". In: *JHEP* 2023.2. DOI: 10.1007/jhep02(2023)188.
- Ferrara, S. and A. Sagnotti (2017). "Supergravity at 40: Reflections and Perspectives". In: *Riv. Nuovo Cim* 40.6, pp. 279–295. DOI: 10.1393/ncr/i2017-10136-6. arXiv: 1702.00743v2.
- Ferrara, S., B. Zumino, and J. Wess (1974). "Supergauge multiplets and superfields". In: *Physics Letters B* 51.3, pp. 239–241. ISSN: 03702693. DOI: 10.1016/0370-2693(74)90283-4.
- Ferrara, Sergio, Renata Kallosh, and Andrei Linde (2014). "Cosmology with nilpotent superfields". In: *Journal of High Energy Physics* 2014.10, p. 143. ISSN: 1029-8479. DOI: 10.1007/JHEP10(2014)143.
- Ferrara, Sergio et al. (2013). "Minimal supergravity models of inflation". In: *Phys. Rev. D* 88.8, p. 85038. DOI: 10.1103/PhysRevD.88.085038. arXiv: 1307.7696.
- Freedman, Daniel Z, P van Nieuwenhuizen, and S Ferrara (1976). "Progress toward a theory of supergravity". In: *Phys. Rev. D* 13.12, pp. 3214–3218. DOI: 10.1103/PhysRevD.13.3214.
- Freedman, Daniel Z, Diederik Roest, and Antoine Van Proeyen (2017). "Off-shell Poincaré supergravity". In: *JHEP* 0.2, p. 102. ISSN: 1029-8479. DOI: 10.1007/JHEP02(2017)102. arXiv: 1701.05216.
- Freedman, Daniel Z. and Antoine Van Proeyen (2011). "Ingredients of supergravity". In: *Fortschr. Phys.* 59.11-12, pp. 1118–1126. DOI: 10.1002/prop.201100059. arXiv: 1106.1097.
- (2012). *Supergravity*. Cambridge University Press. ISBN: 9780521194013.
- Fuentes-Martín, Javier et al. (2022). "Flavor hierarchies, flavor anomalies, and Higgs mass from a warped extra dimension". In: *Phys. Lett. B* 834, p. 137382. DOI: 10.1016/j.physletb.2022.137382. arXiv: 2203.01952 [hep-ph].
- Gallego, Diego (2009). "An effective description of the landscape". In: *AIP Conference Proceedings* 1200, pp. 537–540. ISSN: 0094243X. DOI: 10.1063/1.3327666. arXiv: 0812.0369.
- (2015a). "Effective upliftings in Large volume compactifications". In: *Nucl. Part. Phys. Proc.* 267-269, pp. 186–193. DOI: 10.1016/j.nuclphysbps.2015.10.101. arXiv: 1502.01214 [hep-th].
- (2015b). "Light field integration in SUGRA theories". In: *Int. J. Mod. Phys. A* 30.01, p. 1550003. DOI: 10.1142/S0217751X15500037. arXiv: 1301.6177 [hep-th].
- (2016). *Estudio de uplifts efectivos en compactificaciones de supercuerdas tipo-IIB*. Tech. rep. Tunja: Universidad Pedagógica y Tecnológica de Colombia, p. 96.
- Gallego, Diego et al. (2017). "A New Class of de Sitter Vacua in Type IIB Large Volume Compactifications". In: *JHEP* 10, p. 193. DOI: 10.1007/JHEP10(2017)193. arXiv: 1707.01095 [hep-th].

- Georgi, Howard (1999). *Lie Algebras In Particle Physics: from Isospin To Unified Theories*. Frontiers in Physics. Avalon Publishing, p. 344. ISBN: 0738202339. DOI: 10.1038/278692b0.
- Georgi, Howard and S. L. Glashow (1974). "Unity of All Elementary-Particle Forces". In: *Phys. Rev. Lett.* 32 (8), pp. 438–441. DOI: 10.1103/PhysRevLett.32.438.
- Girardello, L. and M. T. Grisaru (1982). "Soft breaking of supersymmetry". In: *Nuclear Physics, Section B* 194.1, pp. 65–76. ISSN: 05503213. DOI: 10.1016/0550-3213(82)90512-0. arXiv: 0402046 [hep-th].
- Giudice, G. F. and A. Masiero (1988). "A natural solution to the μ -problem in supergravity theories". In: *Physics Letters B* 206.3, pp. 480–484. ISSN: 03702693. DOI: 10.1016/0370-2693(88)91613-9. arXiv: 9711178 [arXiv:hep-th].
- Glashow, Sheldon L. (1961). "Partial-symmetries of weak interactions". In: *Nuclear Physics* 22.4, pp. 579–588. ISSN: 0029-5582. DOI: [https://doi.org/10.1016/0029-5582\(61\)90469-2](https://doi.org/10.1016/0029-5582(61)90469-2).
- Goldstein, Herbert, Charles P Poole, and John L Safko (2001). *Classical mechanics*. 3rd ed. Addison Wesley. ISBN: 9780201657029, 0201657023.
- Greiner, W (2000). *Relativistic Quantum Mechanics. Wave Equations*. Springer. ISBN: 9783540674573.
- Greljo, Admir and Ben A. Stefanek (2018). "Third family quark-lepton unification at the TeV scale". In: *Phys. Lett. B* 782, pp. 131–138. DOI: 10.1016/j.physletb.2018.05.033. arXiv: 1802.04274 [hep-ph].
- Gripaios, B. (2010). "Composite leptoquarks at the LHC". In: *JHEP* 02, p. 045. DOI: 10.1007/JHEP02(2010)045. arXiv: 0910.1789 [hep-ph].
- Hackeling, G. (2017). *Mastering Machine Learning with scikit-learn*. Packt Publishing. ISBN: 9781788298490.
- Hardy, J. C. and I. S. Towner (2020). "Superallowed $0^+ \rightarrow 0^+$ nuclear β decays: 2020 critical survey, with implications for V_{ud} and CKM unitarity". In: *Phys. Rev. C* 102 (4), p. 045501. DOI: 10.1103/PhysRevC.102.045501.
- Hasegawa, Fuminori and Yusuke Yamada (2015). "Component action of nilpotent multiplet coupled to matter in 4 dimensional $\mathcal{N} = 1$ supergravity". In: *Journal of High Energy Physics* 2015.10, p. 106. ISSN: 1029-8479. DOI: 10.1007/JHEP10(2015)106. arXiv: 1507.08619.
- Herr, Werner and B Muratori (2006). *Concept of luminosity*. DOI: 10.5170/CERN-2006-002.361. URL: <http://cds.cern.ch/record/941318>.
- Hill, Christopher T. (1995). "Topcolor assisted technicolor". In: *Physics Letters B* 345.4, pp. 483–489. ISSN: 0370-2693. DOI: 10.1016/0370-2693(94)01660-5.
- Hiller, Gudrun and Frank Krüger (2004). "More model-independent analysis of $\bar{b} \rightarrow s$ processes". In: *Phys. Rev. D* 69 (7), p. 074020. DOI: 10.1103/PhysRevD.69.074020.
- Hiller, Gudrun and Martin Schmaltz (2014). " R_K and future $b \rightarrow s\ell\ell$ BSM opportunities". In: *Physical Review D* 90.5. DOI: 10.1103/physrevd.90.054014.
- (2015). "Diagnosing lepton-nonuniversality in $b \rightarrow s\ell\ell$ ". In: *Journal of High Energy Physics* 2015.2. DOI: 10.1007/jhep02(2015)055.
- Hooft, G. 't (1976). "Symmetry Breaking through Bell-Jackiw Anomalies". In: *Phys. Rev. Lett.* 37 (1), pp. 8–11. DOI: 10.1103/PhysRevLett.37.8.
- Hurth, T., F. Mahmoudi, and S. Neshatpour (2016a). "On the anomalies in the latest LHCb data". In: *Nuclear Physics B* 909, pp. 737–777. DOI: 10.1016/j.nuclphysb.2016.05.022.
- (2016b). "On the anomalies in the latest LHCb data". In: *Nuclear Physics B* 909, pp. 737–777. ISSN: 0550-3213. DOI: 10.1016/j.nuclphysb.2016.05.022.

- Iguro, S. et al. (2021). "TeV-scale vector leptoquark from Pati-Salam unification with vectorlike families". In: *Phys. Rev. D* 104.7, p. 075008. doi: 10.1103/PhysRevD.104.075008. arXiv: 2103.11889 [hep-ph].
- Jones-Perez, Joel (2013). "RGE behaviour of $U(2)^3$ symmetry in SUSY". In: *J. Phys. Conf. Ser.* 447. Ed. by Gustavo C. Branco et al., p. 012060. doi: 10.1088/1742-6596/447/1/012060. arXiv: 1302.6133 [hep-ph].
- José, J V and E J Saletan (1998). *Classical Dynamics: A Contemporary Approach*. Cambridge University Press. ISBN: 9780521636360.
- Jung, Martin and David M. Straub (2019). *Constraining new physics in $b \mapsto c\ell$ transitions*. doi: 10.1007/JHEP01(2019)009.
- Kallosh, R E (2016). "Matter-coupled de Sitter supergravity". In: *Theoretical and Mathematical Physics* 187.2, pp. 695–705. ISSN: 1573-9333. doi: 10.1134/S0040577916050068. arXiv: 1509.02136.
- Kallosh, Renata, Andrei Linde, and Tomas Rube (2011). "General inflaton potentials in supergravity". In: *Phys. Rev. D* 83.4, p. 43507. doi: 10.1103/PhysRevD.83.043507. arXiv: 1011.5945.
- Kallosh, Renata and Timm Wrane (2015). "de Sitter supergravity model building". In: *Phys. Rev. D* 92.10, p. 105010. doi: 10.1103/PhysRevD.92.105010. arXiv: 1509.02137.
- Kallosh, Renata et al. (2000). "Superconformal symmetry, supergravity and cosmology". In: *Classical and Quantum Gravity* 17.20, p. 4269. doi: 10.1088/0264-9381/17/20/308. arXiv: 0006179 [hep-th].
- Kaplan, David B. and Howard Georgi (1984). "SU(2) \times U(1) breaking by vacuum misalignment". In: *Physics Letters B* 136.3, pp. 183–186. ISSN: 0370-2693. doi: 10.1016/0370-2693(84)91177-8.
- Kaplan, David B., Howard Georgi, and Savas Dimopoulos (1984). "Composite Higgs scalars". In: *Physics Letters B* 136.3, pp. 187–190. ISSN: 0370-2693. doi: 10.1016/0370-2693(84)91178-X.
- King, S. F. (2021). "Twin Pati-Salam theory of flavour with a TeV scale vector leptoquark". In: *JHEP* 11, p. 161. doi: 10.1007/JHEP11(2021)161. arXiv: 2106.03876 [hep-ph].
- Kugo, Taichiro and Shozo Uehara (1983). "Conformal and poincaré tensor calculi in N=1 supergravity". In: *Nuclear Physics B* 226.1, pp. 49–92. ISSN: 05503213. doi: 10.1016/0550-3213(83)90463-7.
- LHCb Collaboration et al. (2021). *Test of lepton universality in beauty-quark decays*. doi: 10.48550/ARXIV.2103.11769.
- Lahiri, Amitabha and Palash B Pal (2006). *A First Book of Quantum Field Theory*. Alpha Science International, p. 380. ISBN: 1842652494.
- Lees, J. P. et al. (2012). "Evidence for an Excess of $\bar{B} \rightarrow D^{(*)}\tau^-\bar{\nu}_\tau$ Decays". In: *Phys. Rev. Lett.* 109 (10), p. 101802. doi: 10.1103/PhysRevLett.109.101802.
- Luzio, Luca Di et al. (Nov. 13, 2018). "Maximal flavour violation: a Cabibbo mechanism for leptoquarks". In: *Journal of High Energy Physics* 2018.11, p. 81. ISSN: 1029-8479. doi: 10.1007/JHEP11(2018)081. URL: [https://doi.org/10.1007/JHEP11\(2018\)081](https://doi.org/10.1007/JHEP11(2018)081).
- M. P. Hobson G. P. Efstathiou, A. N. Lasenby (2005). *General relativity: an introduction for physicists*. Cambridge University Press. ISBN: 9780521536394.
- Maldacena, Juan (1999). "The Large-N Limit of Superconformal Field Theories and Supergravity". In: *International Journal of Theoretical Physics* 38.4, pp. 1113–1133. ISSN: 1572-9575. doi: 10.1023/A:1026654312961. arXiv: 9711200 [hep-th].
- Malkawi, Ehab, Tim Tait, and C.-P. Yuan (1996). "A model of strong flavor dynamics for the top quark". In: *Physics Letters B* 385.1, pp. 304–310. ISSN: 0370-2693. doi: [https://doi.org/10.1016/0370-2693\(96\)00859-3](https://doi.org/10.1016/0370-2693(96)00859-3).

- Martin, Stephen P. (2011). "A Supersymmetry Primer". In: *Perspectives on Supersymmetry*. World Scientific, pp. 1–98. doi: 10.1142/9789812839657_0001. arXiv: 9709356 [hep-ph].
- (2012). "TASI 2011 lectures notes: two-component fermion notation and supersymmetry". In: *arXiv*. arXiv: 1205.4076.
- Martínez, Roberto (2002). *Teoría cuántica de campos*. Colección Textos. Universidad Nacional de Colombia, Facultad de Ciencias, Departamento de Física. ISBN: 9789587011203.
- Michael E. Peskin, Dan V. Schroeder (1995). *An Introduction To Quantum Field Theory*. Frontiers in Physics. Westview Press. ISBN: 9780201503975,0201503972.
- Muller, David J and Satyanarayan Nandi (1996). "Topflavor: a separate SU(2) for the third family". In: *Physics Letters B* 383.3, pp. 345–350. ISSN: 0370-2693. doi: 10.1016/0370-2693(96)00745-9.
- N. D. Birrell, P C W Davies (1984). *Quantum fields in curved space*. CUP. Cambridge Monographs on Mathematical Physics. Cambridge University Press. ISBN: 9780521278584,0521278589.
- Nakano, Tadao and Kazuhiko Nishijima (Nov. 1953). "Charge Independence for V-particles*". In: *Progress of Theoretical Physics* 10.5, pp. 581–582. ISSN: 0033-068X. doi: 10.1143/PTP.10.581.
- Neutelings, Izaak (n.d.). CMS coordinate system. URL: https://tikz.net/axis3d_cms.
- Nilles, H.P. P (1984). "Supersymmetry, supergravity and particle physics". In: *Physics Reports* 110.1-2, pp. 1–162. ISSN: 03701573. doi: 10.1016/0370-1573(84)90008-5.
- Noether, Emmy and M. A. Tavel (1971). "Invariant Variation Problems". In: *Transp Theory Stat Phys* 1, pp. 186–207. doi: 10.1080/00411457108231446. arXiv: 0503066 [physics].
- Odom, B. et al. (2006). "New Measurement of the Electron Magnetic Moment Using a One-Electron Quantum Cyclotron". In: *Phys. Rev. Lett.* 97 (3), p. 030801. doi: 10.1103/PhysRevLett.97.030801.
- Pedregosa, F. et al. (2011). "Scikit-learn: Machine Learning in Python". In: *Journal of Machine Learning Research* 12, pp. 2825–2830.
- Perelstein, Maxim (2007). "Little Higgs models and their phenomenology". In: *Progress in Particle and Nuclear Physics* 58.1, pp. 247–291. ISSN: 0146-6410. doi: 10.1016/j.ppnp.2006.04.001.
- "Physics: 1963-1970" (1972). In: Nobel lectures, including presentation speeches and laureates' biographies. Elsevier Publishing Company.
- Pokorski, Stefan (2000). *Gauge field theories*. Cambridge Monographs on Mathematical Physics. Cambridge University Press. ISBN: 9780521478168.
- Qureshi, Umar Sohail et al. (2025). "Probing light scalars and vector-like quarks at the high-luminosity LHC". In: *Eur. Phys. J. C* 85.4, p. 379. doi: 10.1140/epjc/s10052-025-14085-1. arXiv: 2410.17854 [hep-ph].
- R. Aaij, and et al. (2022). "Measurement of the W boson mass". In: *Journal of High Energy Physics* 2022.1. doi: 10.1007/jhep01(2022)036.
- Rivero, Alejandro and Andre Gsponer (2005). *The strange formula of Dr. Koide*. doi: 10.48550/ARXIV.HEP-PH/0505220.
- Robinson, M (2011). *Symmetry and the Standard Model: Mathematics and Particle Physics*. 1st ed. SpringerLink : Bucher. New York: Springer-Verlag. ISBN: 9781441982674. doi: 10.1007/978-1-4419-8267-4.
- Rodriguez, Cristian (2018). "Evaluacion del Lagrangiano de Supergravedad $\mathcal{N} = 1$ utilizando el formalismo Superconforme." BA thesis. UPTC.

- Rovelli, Carlo (2007). *Quantum gravity*. Cambridge Monographs on Mathematical Physics. Cambridge University Press. ISBN: 9780521715966, 0521715962.
- Sakharov, A.D. (Jan. 1967). "Violation of CP Invariance, C Asymmetry, and Baryon Asymmetry of the Universe". In: *Soviet Journal of Experimental and Theoretical Physics Letters* 5, p. 24.
- Sakurai, J J and J Napolitano (2011). *Modern Quantum Mechanics*. Addison-Wesley. ISBN: 9780805382914.
- Salam, Abdus and J. Strathdee (1974). "Super-gauge transformations". In: *Nuclear Physics B* 76.3, pp. 477–482. ISSN: 05503213. DOI: 10.1016/0550-3213(74)90537-9.
- Schael, S. et al. (2006). "Measurement of the W boson mass and width in e+e- collisions at LEP". In: *The European Physical Journal C* 47.2, pp. 309–335. DOI: 10.1140/epjc/s2006-02576-8.
- Schillo, Marjorie, Ellen van der Woerd, and Timm Wräse (2016). "The general de Sitter supergravity component action". In: *Fortschritte der Physik* 64.4-5, pp. 292–302. ISSN: 00158208. DOI: 10.1002/prop.201500074. arXiv: 1511.01542.
- Susskind, Leonard (1979). "Dynamics of spontaneous symmetry breaking in the Weinberg-Salam theory". In: *Phys. Rev. D* 20 (10), pp. 2619–2625. DOI: 10.1103/PhysRevD.20.2619.
- Takahashi, Yuta (2019). *Leptoquark searches in CMS*. DOI: 10.48550/ARXIV.1901.03570.
- The Belle Collaboration (2017). *Precise determination of the CKM matrix element $|V_{cb}|$ with $B^0 \rightarrow D^* - \ell^+ \nu_\ell$ decays with hadronic tagging at Belle*. DOI: 10.48550/ARXIV.1702.01521.
- The LHCb collaboration (2014). "Differential branching fractions and isospin asymmetries of $B \rightarrow K^{(*)}\mu^+\mu^-$ decays". In: *Journal of High Energy Physics* 2014.6, p. 133. ISSN: 1029-8479. DOI: 10.1007/JHEP06(2014)133.
- Thomson, Mark (2013). *Modern Particle Physics*. Cambridge University Press. ISBN: 978-1-107-03426-6.
- Tong, David (1995). *Quantum Field Theory University of Cambridge Part III Mathematical Tripos*. Vol. 45. 12.
- Tung, W K (1985). *Group Theory in Physics*. World Scientific. ISBN: 9789971966560.
- Van Proeyen, Antoine (1999). "Tools for Supersymmetry". In: *Physics AUC* 9.I, pp. 1–49. arXiv: 9910030 [hep-th].
- (2014). "Superconformal symmetry and higher-derivative Lagrangians". In: *Breaking of Supersymmetry and Ultraviolet Divergences in Extended Supergravity: Proceedings of the INFN-Laboratori Nazionali di Frascati School 2013*. Ed. by Stefano Bellucci. Springer International Publishing, pp. 1–21. DOI: 10.1007/978-3-319-03774-5_1. arXiv: 1306.2169.
- VanderPlas, J. (2016). *Python Data Science Handbook: Essential Tools for Working with Data*. O'Reilly Media. ISBN: 9781491912133.
- Walter Greiner Joachim Reinhardt, D.A. Bromley (1996). *Field quantization*. 1st ed. Springer. ISBN: 3540591796, 9783540591795.
- Wang, Lei, Jin Min Yang, and Yang Zhang (2022). "Two-Higgs-doublet models in light of current experiments: a brief review". In: *Communications in Theoretical Physics* 74.9, p. 097202. DOI: 10.1088/1572-9494/ac7fe9. URL: <https://dx.doi.org/10.1088/1572-9494/ac7fe9>.
- Weinberg, Steven (1967). "A Model of Leptons". In: *Phys. Rev. Lett.* 19 (21), pp. 1264–1266. DOI: 10.1103/PhysRevLett.19.1264.
- (2005). *The Quantum Theory of Fields, Volume 3: Supersymmetry*. Cambridge University Press. ISBN: 0521670551, 9780521670555.

- Wu, C. S. et al. (1957). "Experimental Test of Parity Conservation in Beta Decay". In: *Phys. Rev.* 105 (4), pp. 1413–1415. DOI: [10.1103/PhysRev.105.1413](https://doi.org/10.1103/PhysRev.105.1413).
- Zyla, P.A. et al. (2020). "Review of Particle Physics". In: *PTEP* 2020.8, p. 083Co1. DOI: [10.1093/ptep/ptaa104](https://doi.org/10.1093/ptep/ptaa104).
- collaboration, The CMS (2021). "Search for resonant and nonresonant new phenomena in high-mass dilepton final states at $\sqrt{s} = 13$ TeV". In: *Journal of High Energy Physics* 2021.7, p. 208. ISSN: 1029-8479. DOI: [10.1007/JHEP07\(2021\)208](https://doi.org/10.1007/JHEP07(2021)208).
- collaboration, The LHCb (2017). "Test of lepton universality with $B^0 \rightarrow K^* \ell^+ \ell^-$ decays". In: *Journal of High Energy Physics* 2017.8, p. 55. ISSN: 1029-8479. DOI: [10.1007/JHEP08\(2017\)055](https://doi.org/10.1007/JHEP08(2017)055).

PUBLICATIONS

Lorem ipsum dolor sit amet, consectetuer adipiscing elit. Ut purus elit, vestibulum ut, placerat ac, adipiscing vitae, felis. Curabitur dictum gravida mauris. Nam arcu libero, nonummy eget, consectetuer id, vulputate a, magna. Donec vehicula augue eu neque. Pellentesque habitant morbi tristique senectus et netus et malesuada fames ac turpis egestas. Mauris ut leo. Cras viverra metus rhoncus sem. Nulla et lectus vestibulum urna fringilla ultrices. Phasellus eu tellus sit amet tortor gravida placerat. Integer sapien est, iaculis in, pretium quis, viverra ac, nunc. Praesent eget sem vel leo ultrices bibendum. Aenean faucibus. Morbi dolor nulla, malesuada eu, pulvinar at, mollis ac, nulla. Curabitur auctor semper nulla. Donec varius orci eget risus. Duis nibh mi, congue eu, accumsan eleifend, sagittis quis, diam. Duis eget orci sit amet orci dignissim rutrum.

Nam dui ligula, fringilla a, euismod sodales, sollicitudin vel, wisi. Morbi auctor lorem non justo. Nam lacus libero, pretium at, lobortis vitae, ultricies et, tellus. Donec aliquet, tortor sed accumsan bibendum, erat ligula aliquet magna, vitae ornare odio metus a mi. Morbi ac orci et nisl hendrerit mollis. Suspendisse ut massa. Cras nec ante. Pellentesque a nulla. Cum sociis natoque penatibus et magnis dis parturient montes, nascetur ridiculus mus. Aliquam tincidunt urna. Nulla ullamcorper vestibulum turpis. Pellentesque cursus luctus mauris.

Nulla malesuada porttitor diam. Donec felis erat, congue non, volutpat at, tincidunt tristique, libero. Vivamus viverra fermentum felis. Donec nonummy pellentesque ante. Phasellus adipiscing semper elit. Proin fermentum massa ac quam. Sed diam turpis, molestie vitae, placerat a, molestie nec, leo. Maecenas lacinia. Nam ipsum ligula, eleifend at, accumsan nec, suscipit a, ipsum. Morbi blandit ligula feugiat magna. Nunc eleifend consequat lorem. Sed lacinia nulla vitae enim. Pellentesque tincidunt purus vel magna. Integer non enim. Praesent euismod nunc eu purus. Donec bibendum quam in tellus. Nullam cursus pulvinar lectus. Donec et mi. Nam vulputate metus eu enim. Vestibulum pellentesque felis eu massa.

Quisque ullamcorper placerat ipsum. Cras nibh. Morbi vel justo vitae lacus tincidunt ultrices. Lorem ipsum dolor sit amet, consectetuer adipiscing elit. In hac habitasse platea dictumst. Integer tempus convallis augue. Etiam facilisis. Nunc elementum fermentum wisi. Aenean placerat. Ut imperdiet, enim sed gravida sollicitudin, felis odio placerat quam, ac pulvinar elit purus eget enim. Nunc vitae tortor. Proin tempus nibh sit amet nisl. Vivamus quis tortor vitae risus porta vehicula.

Fusce mauris. Vestibulum luctus nibh at lectus. Sed bibendum, nulla a faucibus semper, leo velit ultricies tellus, ac venenatis arcu wisi vel nisl. Vestibulum diam. Aliquam pellentesque, augue quis sagittis posuere, turpis lacus congue quam, in hendrerit risus eros eget felis. Maecenas eget erat in sapien mattis porttitor. Vestibulum porttitor. Nulla facilisi. Sed a turpis eu lacus commodo facilisis. Morbi fringilla, wisi in dignissim interdum, justo lectus sagittis dui, et vehicula libero dui cursus dui. Mauris tempor ligula sed lacus. Duis cursus enim ut augue. Cras ac magna. Cras nulla. Nulla egestas. Curabitur a leo. Quisque egestas wisi eget nunc. Nam feugiat lacus vel est. Curabitur consectetur.

Suspendisse vel felis. Ut lorem lorem, interdum eu, tincidunt sit amet, laoreet vitae, arcu. Aenean faucibus pede eu ante. Praesent enim elit, rutrum at, molestie non, nonummy vel, nisl. Ut lectus eros, malesuada sit amet, fermentum eu, sodales

cursus, magna. Donec eu purus. Quisque vehicula, urna sed ultricies auctor, pede lorem egestas dui, et convallis elit erat sed nulla. Donec luctus. Curabitur et nunc. Aliquam dolor odio, commodo pretium, ultricies non, pharetra in, velit. Integer arcu est, nonummy in, fermentum faucibus, egestas vel, odio.

Sed commodo posuere pede. Mauris ut est. Ut quis purus. Sed ac odio. Sed vehicula hendrerit sem. Duis non odio. Morbi ut dui. Sed accumsan risus eget odio. In hac habitasse platea dictumst. Pellentesque non elit. Fusce sed justo eu urna porta tincidunt. Mauris felis odio, sollicitudin sed, volutpat a, ornare ac, erat. Morbi quis dolor. Donec pellentesque, erat ac sagittis semper, nunc dui lobortis purus, quis congue purus metus ultricies tellus. Proin et quam. Class aptent taciti sociosqu ad litora torquent per conubia nostra, per inceptos hymenaeos. Praesent sapien turpis, fermentum vel, eleifend faucibus, vehicula eu, lacus.



On the sensitivity reach of LQ production with preferential couplings to third generation fermions at the LHC

A. Flórez^{1,a}, J. Jones-Pérez^{2,b}, A. Gurrola^{3,c}, C. Rodriguez^{1,d}, J. Peñuela-Parra^{1,e}

¹ Departamento de Física, Universidad de Los Andes, Cra. 1 # 18a-12, Bogotá, Colombia

² Sección Física, Departamento de Ciencias, Pontificia Universidad Católica del Perú, Apartado 1761, Lima, Peru

³ Department of Physics and Astronomy, Vanderbilt University, Nashville, TN 37235, USA

Received: 31 July 2023 / Accepted: 22 October 2023 / Published online: 11 November 2023
© The Author(s) 2023

Abstract Leptoquarks (LQs) are hypothetical particles that appear in various extensions of the Standard Model (SM), that can explain observed differences between SM theory predictions and experimental results. The production of these particles has been widely studied at various experiments, most recently at the Large Hadron Collider (LHC), and stringent bounds have been placed on their masses and couplings, assuming the simplest beyond-SM (BSM) hypotheses. However, the limits are significantly weaker for LQ models with family non-universal couplings containing enhanced couplings to third-generation fermions. We present a new study on the production of a LQ at the LHC, with preferential couplings to third-generation fermions, considering proton-proton collisions at $\sqrt{s} = 13$ TeV and $\sqrt{s} = 13.6$ TeV. Such a hypothesis is well motivated theoretically and it can explain the recent anomalies in the precision measurements of B-meson decay rates, specifically the $R_{D^{(*)}}$ ratios. Under a simplified model where the LQ masses and couplings are free parameters, we focus on cases where the LQ decays to a τ lepton and a b quark, and study how the results are affected by different assumptions about chiral currents and interference effects with other BSM processes with the same final states, such as diagrams with a heavy vector boson, Z' . The analysis is performed using machine learning techniques, resulting in an increased discovery reach at the LHC, allowing us to probe new physics phase space which addresses the B-meson anomalies, for LQ masses up to 5.00 TeV, for the high luminosity LHC scenario.

1 Introduction

After more than ten years collecting data, the LHC has confirmed that the Standard Model (SM) is indeed the correct theory describing particle physics for energies below the TeV scale. Nevertheless, there exist reasons to expect the SM to be a low-energy effective realization of a more complete theory. On the theoretical side, we do not know if gravity should be quantized, or if the gauge interactions should be unified, and if so, we do not know how to solve the associated hierarchy problems on the Higgs mass. Moreover, we have no explanation for fermion family replication, nor for the lack of CP violation in the strong sector. This expectation for physics beyond the SM (BSM) is reinforced experimentally, where the observation of neutrino masses, dark matter, and the baryon asymmetry in the Universe, cannot be explained by the SM.

Leptoquarks (LQs) are hypothetical bosons carrying both baryon and lepton number, thus interacting jointly with a lepton and a quark. They are a common ingredient in SM extensions where quarks and leptons share the same multiplet. Typical examples of these can be found in the Pati-Salam [1] and $SU(5)$ GUT [2] models. In addition, they can also be found in theories with strong interactions, such as compositeness [3]. Due to their exotic coupling which allows quark-lepton transitions, they have a diverse phenomenology, which naturally leads to several constraints. An important one comes from proton decay, which forces the LQ mass to values close to the Planck scale, unless baryon and lepton numbers are not violated. Furthermore, in models where the latter are conserved, the LQ can still be subject to a wide variety of bounds [4–9]. Examples of these come from meson mixing, electric and magnetic dipole moments, atomic parity violation tests, rare decays, and direct searches. Nevertheless, the significance of each bound is a model dependent question.

^a e-mail: ca.florez@uniandes.edu.co (corresponding author)

^b e-mail: jones.j@pucp.edu.pe

^c e-mail: alfredo.gurrola@vanderbilt.edu

^d e-mail: c.rodriguez45@uniandes.edu.co

^e e-mail: j.penuela@uniandes.edu.co

In the last years, an increased interest in low scale LQs has emerged due to the anomalies in the precision measurements of the B-meson decay rates. As it is well known, these corresponded mainly to deviations in the $R_{K^{(*)}}$ [10–13] and $R_{D^{(*)}}$ [14–25] ratios, which measure the violation of lepton flavour universality (LFU). What followed was a very intense theoretical development, aiming to explain the anomalies by TeV scale LQ exchange at tree level [26–41]. Before the end of 2022, it was generally agreed that, within proposed single LQ solutions, the only candidate capable of addressing all B-meson anomalies simultaneously and surviving all other constraints was a vector LQ (U_1), transforming as $(\mathbf{3}, \mathbf{1}, 2/3)$, and coupling mainly to third-generation fermions via $b \tau$ and $t \nu_\tau$ vertices [36, 39]. In spite of a recent re-analysis of $R_{K^{(*)}}$ data showing this ratio to be compatible with the SM prediction [42–45], the solution to the $R_{D^{(*)}}$ anomaly is still an open question and remains a valid motivation for the study of scenarios where new particles have preferential couplings to third-generation fermions. Thus, it is still of interest to continue exploring the possibility of observing the U_1 LQ at the LHC [41].

As expected, the theoretical community has extensively participated in probing LQ models by scrutinizing search strategies, recasting LHC results, and predicting the reach in the parameter space via different searches involving third-generation fermions (see for instance [46–55]). In addition, several 13 TeV searches for LQs decaying into t/b and τ/ν final states have been performed by the CMS [56–64] and ATLAS [65–71] collaborations.

Of the searches above, we find [62] particularly interesting. Here, the CMS collaboration explores signals corresponding to $t \nu b \tau$ and $t \nu \tau$ final states, with 137 fb^{-1} of proton-proton (pp) collision data. The former is motivated by LQ pair production, with one LQ decaying into $t \nu$ and the other into $b \tau$, while the latter arises from a single LQ produced in association with a τ , with a subsequent LQ decay into $t \nu$ (see Fig. 1 for the corresponding diagrams). From the combination of both production channels, the search excludes U_1 masses under $1.3 - 1.7 \text{ TeV}$, with this range depending on the U_1 coupling to gluons and on its coupling g_U in the $b_L \tau_L$ vertex.

What makes this search particularly attractive is that, for the first time, an LHC collaboration directly places (mass dependent) bounds on g_U . This is important, since having information on this parameter is crucial in order to understand if the U_1 is really responsible for the $R_{D^{(*)}}$ anomaly. The inclusion of the single-LQ production mode is important, since its cross-section is directly proportional to g_U^2 . However, as can be seen in Fig. 6 of [62], the current constraints are dominated by pair production, with single-LQ production playing a subleading role. While this is expected [49], it still leads us to ponder the possibility of improving the sensitivity of LHC searches to single-LQ production, and thus

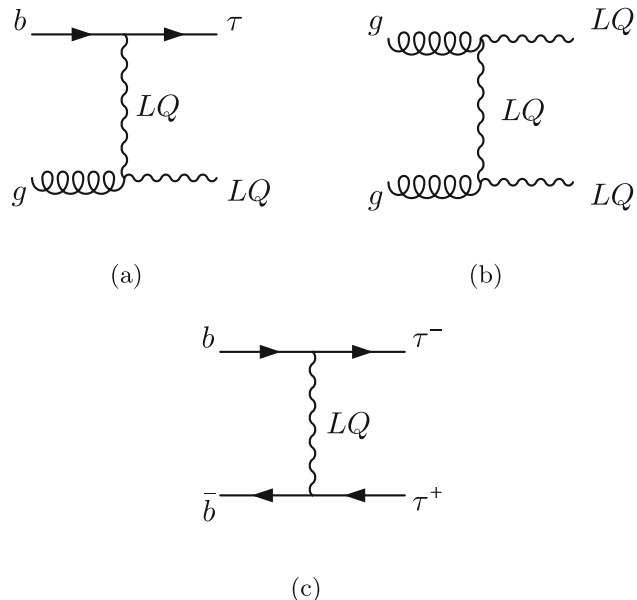


Fig. 1 Representative Feynman diagrams of single (a), pair (b), and non-resonant (c) leptoquark production in proton-proton collision experiments. In single and pair production, the diagrams shown involve t-channel LQ exchange, dominant for lower LQ mass. However, for larger mass there exist s-channel diagrams featuring a virtual bottom quark and gluon, respectively

on achieving better constraints on g_U . Other complementary and similar searches to [62] were carried out by both ATLAS [70] and CMS [64].

It is also well known, though, that searches for an excess in the high- p_T tails of τ lepton distributions can strongly probe g_U , up to very large LQ masses. Indeed, as shown in [41, 72], the new physics effective operators contributing to $R_{D^{(*)}}$ also contribute to an enhancement in the $\text{p p} \rightarrow \tau\tau$ production rates. This has motivated a large number of recasts [39, 41, 49, 51, 73–77], as well as a CMS search explicitly providing constraints in terms of U_1 [63]. Nevertheless, it is important to note that for these $\text{p p} \rightarrow \tau\tau$ processes, the LQ participates non-resonantly, so contributions to the $\text{p p} \rightarrow \tau\tau$ rates and kinematic distributions from non-LQ BSM diagrams containing possible virtual particles, such as a heavy neutral vector boson Z' , could spoil a straightforward interpretation of any possible excess [51]. Thus, it is also necessary to understand how the presence of other virtual particles can affect the sensitivity of an analysis probing g_U .

In this work we study the projected LQ sensitivity at the LHC, considering already available pp data as well as the expected amount of data to be acquired during the High-Luminosity LHC (HL-LHC) runs. We explore a proposed analysis strategy which utilizes a combination of single-, double-, and non-resonant-LQ production, targeting final states with varying τ -lepton and b-jet multiplicities. The

studies are performed considering various benchmark scenarios for different LQ masses and couplings, also taking into account distinct chiralities for the third-generation fermions in the LQ vertex. We also assess the impact of a companion Z' , which is typical of gauge models, in non-resonant LQ probes, and find that interference effects can have a significant effect on the discovery reach. We consider this effect to be of high interest, given that non-resonant LQ production can have the largest cross-section, and thus could be an important channel in terms of discovery potential.

An important aspect of this work is that the analysis strategy is developed using a machine learning (ML) algorithm based on Boosted Decision Trees (BDT)[78]. The output of the event classifier is used to perform a profile-binned likelihood test to extract the overall signal significance for each model considered in the analysis. The advantage of using BDTs and other ML algorithms has been demonstrated in several experimental and phenomenological studies [50, 79–84]. In our studies, we find that the BDT algorithm gives sizeable improvement in signal significance.

This paper is organized as follows. In Sect. 2 we present our simplified model and review the model parameters which are relevant for solving the B-meson anomalies. Section 3 describes the details associated with the analysis strategy and the simulation of signal and background samples. Section 4 contains the results of the study, including the projected sensitivity for different benchmark scenarios considered. Finally, in Sect. 5 we discuss the implication of our results and prospects for future studies.

2 A simplified model for the U_1 leptoquark

Extending the SM with a massive U_1 vector LQ is not straightforward, as one has to ensure the renormalizability of the model. Most of the theoretical community has focused on extensions of the Pati-Salam (PS) models which avoid proton decay, such as the scenario found in [85]. Other examples include PS models with vector-like fermions [86–88], the so-called 4321 models [89–91], the twin PS² model [92, 93], the three-site PS³ model [94–96], as well as composite PS models [97–99].

In what follows, we shall restrict ourselves to a simplified non-renormalizable lagrangian, understood to be embedded into a more complete model. The SM is thus extended by adding the following terms featuring the U_1 LQ:

$$\begin{aligned} \mathcal{L}_{U_1} = & -\frac{1}{2} U_{\mu\nu}^\dagger U^{\mu\nu} + M_U^2 U_{1\mu}^\dagger U_1^\mu \\ & -ig_s U_{1\mu}^\dagger T^a U_{1\nu} G^{a\mu\nu} - i\frac{2}{3}g' U_{1\mu}^\dagger U_{1\nu} B^{\mu\nu} \\ & + \frac{g_U}{\sqrt{2}} [U_{1\mu} (\bar{Q}_3 \gamma^\mu L_3 + \beta_L^{st} \bar{Q}_2 \gamma^\mu L_3 \\ & + \beta_R \bar{b}_R \gamma^\mu \tau_R) + h.c.] \end{aligned} \quad (1)$$

where $U_{\mu\nu} \equiv \mathcal{D}_\mu U_{1\nu} - \mathcal{D}_\nu U_{1\mu}$, and $\mathcal{D}_\mu \equiv \partial_\mu + ig_s T^a G_\mu^a + i\frac{2}{3}g' B_\mu$. As evidenced by the second line above, we assume that the LQ has a gauge origin.¹

The third and fourth lines in Eq. (1) shows the LQ interactions with SM fermions, with coupling g_U , which we have chosen as preferring the third generation.² These are particularly relevant for the LQ decay probabilities, as well as for the single-LQ production cross-section. The β_L^{st} parameter, which is the $LQ \rightarrow s\tau$ coupling in the β_L matrix (see footnote), is chosen to be equal to 0.2, following the fit done in [75], in order to simultaneously solve the $R_{D^{(*)}}$ anomaly and satisfy the $p p \rightarrow \tau^+ \tau^-$ constraints. Although β_L^{st} technically alters the single-LQ production cross-section and LQ branching fractions, we have confirmed that a value of $\beta_L^{st} = 0.2$ results in negligible impact on our collider results, and thus is ignored in our subsequent studies.

The LQ right-handed coupling is modulated with respect to the left-handed one by the β_R parameter. The choice of β_R is important phenomenologically, as it affects the LQ branching ratios,³ as well as the single-LQ production cross-section. To illustrate the former, Fig. 2 (top) shows the LQ $\rightarrow b\tau$ and LQ $\rightarrow t\nu$ branching ratios as functions of the LQ mass, for two values of β_R . For large LQ masses, we confirm that with $\beta_R = 0$ then $BR(LQ \rightarrow b\tau) \approx BR(LQ \rightarrow t\nu) \approx \frac{1}{2}$. However, for $\beta_R = -1$, as was chosen in [38], the additional coupling adds a new term to the total amplitude, leading to $BR(LQ \rightarrow b\tau) \approx \frac{2}{3}$. The increase in this branching ratio can thus weaken bounds from LQ searches targeting decays into $t\nu$ final states, which motivates exploring the sensitivity in $b\tau$ final states exclusively. Note that although a $BR(LQ \rightarrow b\tau) \approx 1$ scenario is possible by having the LQ couple exclusively to right-handed currents (i.e., $g_U \rightarrow 0$, but $g_U \beta_R \neq 0$), it does not solve the observed anomalies in the $R_{D^{(*)}}$ ratios. Therefore, although some LHC searches assume $BR(LQ \rightarrow b\tau) = 1$, we stress that in our studies we assume values of the model parameters and branching ratios that solve the $R_{D^{(*)}}$ ratios.

To further understand the role of β_R at colliders, Fig. 2 (bottom) shows the cross-section for single-LQ (sLQ), double-LQ (dLQ), and non-resonant (non-res) production, as a function of mass and for a fixed coupling $g_U = 1.8$, assuming $p p$ collisions at $\sqrt{s} = 13$ TeV. We note that this benchmark scenario with $g_U = 1.8$ results in a LQ $\rightarrow b\tau$ decay width that is <5% of the LQ mass, for mass values

¹ The couplings in the second line of Eq. (1) can be found in the literature as $g_s \rightarrow g_s(1 - \kappa_U)$ and $g' \rightarrow g'(1 - \tilde{\kappa}_U)$, in order to take into account the possibility of an underlying strong interaction.

² Before the demise of the $R_{K^{(*)}}$ anomaly [42–45], a 3×3 β_L matrix would be used instead, with values fitted to solve all B meson anomalies.

³ Having β_L^{st} different from zero also opens new decay channels. These, however, are either suppressed by β_L^{st} and powers of λ_{CKM} . In any case, this effect would decrease $BR(LQ \rightarrow b\tau)$ and $BR(LQ \rightarrow t\nu)$ by less than 3%.

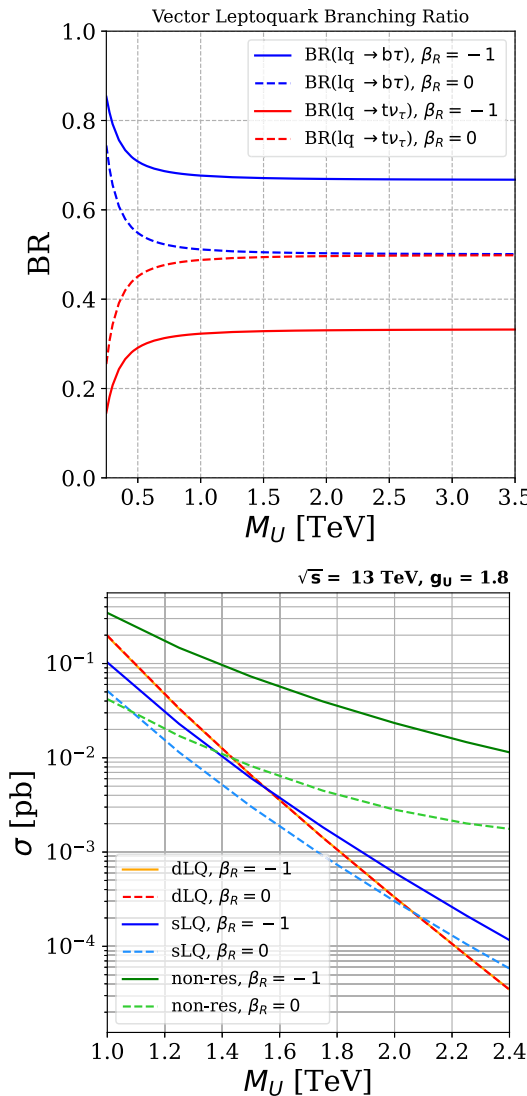


Fig. 2 Top: The LQ $\rightarrow \text{b}\tau$ and LQ $\rightarrow \text{t}\nu$ branching ratios for $\beta_R = 0$ (solid lines) and $\beta_R = -1$ (dashed lines). Bottom: Signal cross-section as a function of the LQ mass, for $\sqrt{s} = 13 \text{ TeV}$, with $g_U = 1.8$. We show single, pair, and non-resonant production, for $\beta_R = -1, 0$ in solid and dashed lines, respectively

from 250 GeV to 2.5 TeV. In the figure, we observe that, since dLQ production is mainly mediated by events from quantum chromodynamic processes, the choice of β_R does not affect the cross-section. However, for sLQ production, a non-zero value for β_R increases the cross-section by about a factor of 2 and by almost one order of magnitude in the case of non-res production. These results shown in Fig. 2 are easily understood by considering the diagrams shown in Fig. 1. The LQ mass value where the sLQ production cross-section exceeds the dLQ cross-section depends on the choice of g_U .

We also note that to solve the $R_{D^{(*)}}$ anomaly, the authors of [75] point out that the wilson coefficient $C_U \equiv g_U^2 v_{SM}^2 / (4 M_U^2)$ is constrained to a specific range of values,

and this range depends on the value of the β_R parameter. Therefore, the allowed values of the coupling g_U depend on M_U and β_R , and thus our studies are performed in this multi-dimensional phase space.

As noted in Sect. 1, we study the role of a Z' boson in $\text{pp} \rightarrow \tau\tau$ production. The presence of a Z' boson in LQ models has been justified in various papers, for example, in [51]. The argument is that minimal extensions of the SM which include a massive gauge U_1 LQ, uses the gauge group $SU(4) \times SU(3)' \times SU(2)_L \times U(1)_{T_R^3}$. Such an extension implies the presence of an additional massive boson, Z' , and a color-octet vector, G' , arising from the spontaneous symmetry breaking into the SM.⁴ The Z' in particular can play an important role in the projected LQ discovery reach, as it can participate in $\text{pp} \rightarrow \tau\tau$ production by s-channel exchange, both resonantly and as a virtual mediator. To study the effect of a Z' on the $\text{pp} \rightarrow \tau\tau$ production cross-sections and kinematics, we extend our benchmark Lagrangian in Eq. (1) with further non-renormalizable terms involving the Z' . Accordingly, we assume the Z' only couples to third-generation fermions. Our simplified model is thus extended by:

$$\begin{aligned} \mathcal{L}_{Z'} = & -\frac{1}{4} Z'_{\mu\nu} Z'^{\mu\nu} + \frac{1}{2} M_{Z'}^2 Z'_\mu Z'^\mu \\ & + \frac{8Z'}{2\sqrt{6}} Z'^\mu (\zeta_q \bar{Q}_3 \gamma_\mu Q_3 + \zeta_t \bar{t}_R \gamma_\mu t_R \\ & + \zeta_b \bar{b}_R \gamma_\mu b_R - 3\zeta_\ell \bar{L}_3 \gamma_\mu L_3 - 3\zeta_\tau \bar{\tau}_R \gamma_\mu \tau_R) \end{aligned} \quad (2)$$

where the constants $M_{Z'}$, $g_{Z'}$, ζ_q , ζ_t , ζ_b , ζ_ℓ , ζ_τ , are model dependent.

We study two extreme cases for the Z' mass, following [100], namely $M_{Z'} = \sqrt{\frac{1}{2}} M_U < M_U$ and $M_{Z'} = \sqrt{\frac{3}{2}} M_U > M_U$. We also assume the LQ and Z' are uniquely coupled to left-handed currents, i.e. $\zeta_q = \zeta_\ell = 1$ and $\zeta_t = \zeta_b = \zeta_\tau = 0$. With these definitions, Fig. 3 shows the effect of the Z' on the $\tau\tau$ production cross-section, considering $g_U = 1$, $\beta_R = 0$, and different $g_{Z'}$ couplings. On the top panel, the cross-sections corresponding to the cases where $M_{Z'} = \sqrt{\frac{1}{2}} M_U$ are shown. As expected, the $\tau\tau$ production cross-section for the inclusive case (i.e., $g_{Z'} \neq 0$) is larger than that for the LQ-only non-res process ($g_{Z'} = 0$, depicted in blue). This effect increases with $g_{Z'}$ and, within the evaluated values, can exceed the LQ-only cross-section by up to two orders of magnitude. In contrast, a more intricate behaviour can be seen in the bottom panel of Fig. 3, which corresponds to $M_{Z'} = \sqrt{\frac{3}{2}} M_U$. Here, for low values of M_U , a similar

⁴ Naively, the LQs are associated to the breaking of $SU(4) \rightarrow SU(3)_{[4]} \times U(1)_{B-L}$, the G' arises from $SU(3)_{[4]} \times SU(3)' \rightarrow SU(3)_c$, and the Z' comes from the breaking of $U(1)_{B-L} \times U(1)_{T_R^3} \rightarrow U(1)_Y$. Notice that the specific pattern of breaking, and the relations between the masses and couplings, are connected to the specific scalar potential used.

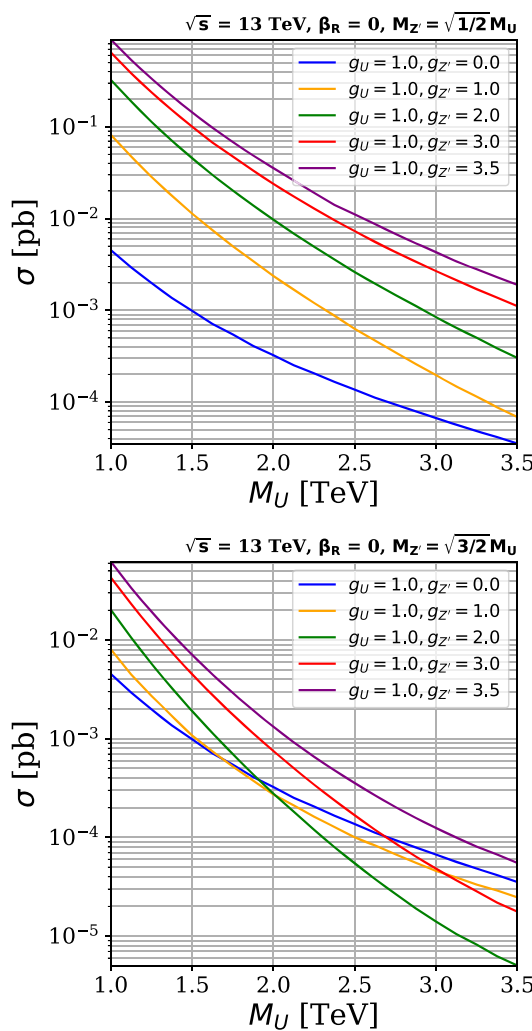


Fig. 3 $\tau\tau$ cross-section as a function of the LQ mass for different values of g_U and $g_{Z'}$. The estimates are performed at $\sqrt{s} = 13$ TeV, $\beta_R = 0$, $M_{Z'} = \sqrt{1/2}M_U$ (top), and $M_{Z'} = \sqrt{3/2}M_U$ (bottom)

increase in the cross-section is observed. However, for higher values of M_U , the inclusive $p p \rightarrow \tau\tau$ cross-section is smaller than the LQ-only $\tau\tau$ cross-section. This behaviour suggests the presence of a dominant destructive interference at high masses, leaving its imprint on the results.

In order to further illustrate the effect, Fig. 4 shows the relative kinematic interference (RKI) as a function of the reconstructed invariant mass $m_{\tau\tau}$, for $g_{Z'} = 1$ and varying values of M_U . The RKI parameter is defined as

$$\text{RKI}(m_{\tau\tau}) = \frac{1}{\sigma_{\text{LQ}+Z'}} \left[\frac{d\sigma_{\text{LQ}+Z'}}{dm_{\tau\tau}} - \left(\frac{d\sigma_{\text{LQ}}}{dm_{\tau\tau}} + \frac{d\sigma_{Z'}}{dm_{\tau\tau}} \right) \right], \quad (3)$$

where σ_X is the production cross-section arising due to contributions from X particles. For example, $\sigma_{\text{LQ}+Z'}$ represents the inclusive cross-section where both virtual LQ and s-channel Z' exchange contribute. For both cases, we can

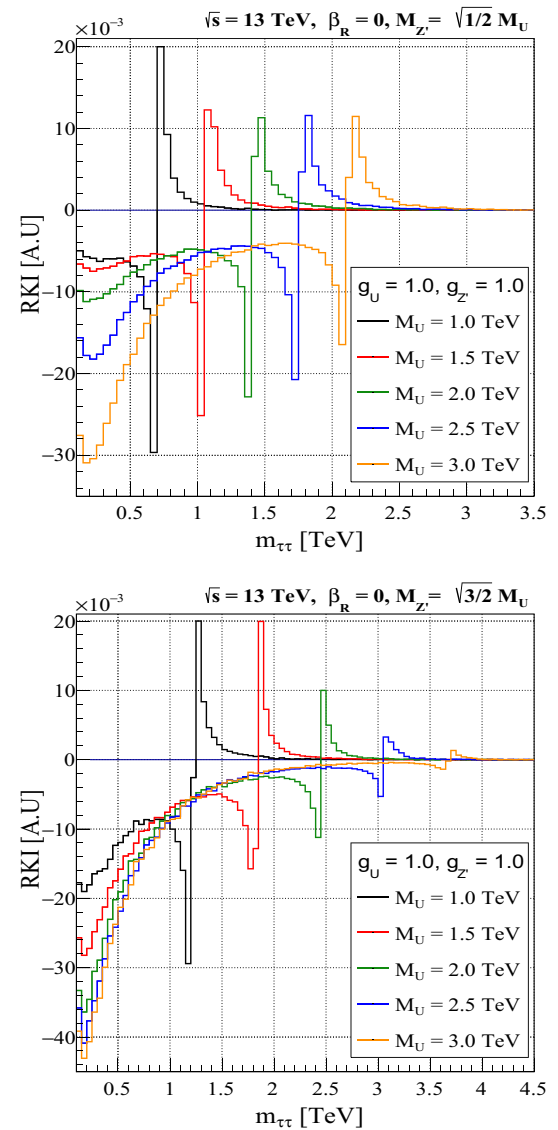


Fig. 4 The relative kinematic interference (RKI), as a function of the reconstructed mass of two taus, for different LQ masses. The studies are performed assuming $\sqrt{s} = 13$ TeV, $\beta_R = 0$, $g_U = 1.0$, $g_{Z'} = 1.0$, $M_{Z'} = \sqrt{1/2}M_U$ (top), and $M_{Z'} = \sqrt{3/2}M_U$ (bottom)

observe the presence of deep valleys in the RKI curves when $m_{\tau\tau} \rightarrow 0$, indicating destructive interference between the LQ and the Z' contributions. This interference generates a suppression of the differential cross-section for lower values of $m_{\tau\tau}$ and, therefore, in the integrated cross-section.

The observed interference effects are consistent with detailed studies on resonant and non-resonant $p p \rightarrow t\bar{t}$ production, performed in reference [101].

3 LQ search strategy and simulation

Our proposed analysis strategy utilizes single-LQ (i.e. $p p \rightarrow \tau\tau$ LQ), double-LQ (i.e. $p p \rightarrow \text{LQ LQ}$), and non-resonant LQ

production (i.e. $p p \rightarrow \tau\tau$) as shown in Fig. 1. At leading order in α_s , since we focus on $U_1 \rightarrow b\tau$ decays, the sLQ process results in the $b\tau\tau$ mode, the dLQ process results in the $bb\tau\tau$ mode, and the non-res process results in the $\tau\tau$ mode. Therefore, in all cases we obtain two τ leptons, with either 0, 1, or 2 b jets. The τ leptons decay to hadrons (τ_h) or semi-leptonically to electrons or muons (τ_ℓ , $\ell = e$ or μ). To this end, we study six final states: $\tau_h\tau_{h/\ell}$, $b\tau_h\tau_{h/\ell}$, and $bb\tau_h\tau_{h/\ell}$, which can be naively associated to non-res, sLQ and dLQ production, respectively. Nevertheless, experimentally it is possible for b jets to not be properly identified or reconstructed, leading, for instance, to a fraction of dLQ signal events falling into the $b\tau_h\tau_{h/\ell}$ and $\tau_h\tau_{h/\ell}$ categories. Similarly, soft jets can fake b jets, such that non-res processes can contribute to the $b\tau_h\tau_{h/\ell}$ and $bb\tau_h\tau_{h/\ell}$ final states. This kind of signal loss and mixing is taken into account in our analysis.⁵

The contributions of signal and background events are estimated using Monte Carlo (MC) simulations. We implemented the U_1 model from [51], adjusted to describe the lagrangian in Eqs. (1) and (2), using FeynRules (v2.3.43) [102, 103]. The branching ratios and cross-sections have been calculated using MadGraph5_aMC (v3.1.0) [104, 105], the latter at leading order in α_s . The corresponding samples are generated considering $p p$ collisions at $\sqrt{s} = 13$ TeV and $\sqrt{s} = 13.6$ TeV. All samples are generated using the NNPDF3.0 NLO [106] set for parton distribution functions (PDFs) and using the full amplitude square SDE strategy for the phase-space optimization due to strong interference effects with the Z' boson. Parton level events are then interfaced with the PYTHIA (v8.2.44) [107] package to include parton fragmentation and hadronization processes, while DELPHES (v3.4.2) [108] is used to simulate detector effects, using the input card for the CMS detector geometric configurations, and for the performance of particle reconstruction and identification.

At parton level, jets and leptons are required to have a minimum transverse momentum (p_T) of 20 GeV, while b jets are required to have a minimum p_T of 30 GeV. Additionally, we constrain the pseudorapidity (η) to $|\eta| < 2.5$ for b jets and leptons, and $|\eta| < 5.0$ for jets. The production cross-sections shown in the bottom panel of Figs. 2 and 3 are obtained with the aforementioned selection criteria.

Table 1 shows the preliminary event selection criteria for each channel at analysis level. The channels are divided based on the multiplicity of b jets, $N(b)$, number of light leptons, $N(\ell)$, number of hadronic tau leptons, $N(\tau_h)$, and kinematic

⁵ Note that further signal mixing can also occur at the event generation level by including terms at larger order in α_s . For example, in the non-res diagram in Fig. 1, one of the initial b could come from a $g \rightarrow b\bar{b}$ splitting, leading to non resonant production of $b\tau_h\tau_{h/\ell}$. Simulating and studying the role of such NLO contributions is outside the scope of this work.

Table 1 Preliminary event selection criteria used to filter events before feeding them to the BDT algorithm. A $\Delta R(p_i, p_j) > 0.3$ requirement is imposed between all pairs of reconstructed particle candidates p_i, p_j

Variable	Threshold					
	$\tau_h\tau_h$	$b\tau_h\tau_h$	$bb\tau_h\tau_h$	$\tau_h\tau_\ell$	$b\tau_h\tau_\ell$	$bb\tau_h\tau_\ell$
$N(b)$	= 0	= 1	≥ 2	= 0	= 1	≥ 2
$p_T(b)$	–	≥ 30 GeV	–	≥ 30 GeV	–	≤ 2.4
$ \eta(b) $	–	≤ 2.4	–	≤ 2.4	–	≤ 2.4
$N(\ell)$	= 0	–	–	= 1	–	–
$p_T(e)$	–	–	≥ 35 GeV	–	–	–
$p_T(\mu)$	–	–	≥ 30 GeV	–	–	–
$ \eta(\ell) $	–	–	≤ 2.4	–	–	–
$N(\tau_h)$	= 2	–	–	= 1	–	–
$p_T(\tau_h)$	≥ 50 GeV	–	–	–	–	–
$ \eta(\tau_h) $	≤ 2.3	–	–	–	–	–
$\Delta R(p_i, p_j)$	≥ 0.3	–	–	–	–	–

criteria based on η , p_T and spatial separation of particles in the detector volume ($\Delta R = \sqrt{(\Delta\eta)^2 + (\Delta\phi)^2}$). The minimum p_T thresholds for leptons are chosen following references [62, 63, 67], based on experimental constraints associated to trigger performance. Following reference [109], we use a flat identification efficiency for b jets of 70% across the entire p_T spectrum with misidentification rate of 1%. These values correspond with the “medium working point” of the CMS algorithm to identify b jets, known as DeepCSV. We also explored the “Loose” (“Tight”) working point using an efficiency of 85% (45%) and mis-identification rate of 10% (0.1%). The “medium working point” was selected as it gives the best signal significance for the analysis.

For the performance of τ_h identification in DELPHES, we consider the latest technique described in [110], which is based on a deep neural network (i.e. DeepTau) that combines variables related to isolation and τ -lepton lifetime as input to identify different τ_h decay modes. Following [110], we consider three possible DeepTau “working points”: (i) the “Medium” working point of the algorithm, which gives a 70% τ_h -tagging efficiency and 0.5% light-quark and gluon jet mis-identification rate; (ii) the “Tight” working point, which gives a 60% τ_h -tagging efficiency and 0.2% light-quark and gluon jet mis-identification rate; and (iii) the “VTight” working point, which gives a 50% τ_h -tagging efficiency and 0.1% light-quark and gluon jet mis-identification rate. Similar to the choice of b-tagging working point, the choice of τ_h -tagging working point is determined through an optimization process which maximizes discovery reach. The “Medium” working point was ultimately shown to provide the best sensitivity and therefore chosen for this study. For muons (electrons), the assumed identification efficiency is 95% (85%), with a 0.3% (0.6%) mis-identification rate [111–113].

Table 2 The number of simulated events for the signal and background samples

Sample	$t\bar{t}$	single t	VV	$V+\text{jets}$	signals
$N_{\text{events}} \times 10^{-6}$	24.31	11.50	32.35	39.45	0.60

After applying the preliminary selection criteria, the primary sources of background are production of top quark pairs ($t\bar{t}$), and single-top quark processes (single t), followed by production of vector bosons with associated jets from initial or final state radiation ($V+\text{jets}$), and pair production of vector bosons (VV). The number of simulated MC events used for each sample is shown in Table 2.

We use two different sets of signal samples. The first set includes various $\{M_U, g_U\}$ scenarios, for two different values of $\beta_R \in \{0, -1\}$. We generate signal samples for M_U values between 250 and 5000 GeV, in steps of 250 GeV. The considered g_U coupling values are between 0.25 and 3.5, in steps of 0.25. Although the signal cross-sections depend on both M_U and g_U , the efficiencies of our selections only depend on M_U (for all practical purposes) since the decay widths are relatively small compared to the mass of M_U ($\frac{\Gamma_U}{M_U} < 5\%$), and thus more sensitive to experimental resolution. In total there are 280 $\{M_U, g_U, \beta_R\}$ scenarios simulated for this first set of signal samples, and for each of these scenarios two subsets of samples are generated, which are used separately for the training and testing of the machine learning algorithm. The second set of signal samples is used to evaluate interference effects between LQs and the Z' bosons in non-res production. Using benchmark values $g_U = 1.8$ and $\beta_R = 0$, we consider various $\{M_U, g_{Z'}\}$ scenarios for two different Z' mass hypotheses, $(M_{Z'}/M_U)^2 \in \{\frac{1}{2}, \frac{3}{2}\}$. The M_U values vary between 500 and 5000 GeV, in steps of 250 GeV. The $g_{Z'}$ coupling values are between 0.25 and 3.5, in steps of 0.25. Therefore, in total there are 280 $\{M_U, g_{Z'}, (M_{Z'}/M_U)^2\}$ scenarios simulated for this second set of signal samples, and for each of these scenarios a total of 6.0×10^5 MC events are generated.

As noted previously, the simulated signal and background events are initially filtered using selections which are motivated by experimental constraints, such as the geometric constraints of the CMS detector, the typical kinematic thresholds for reconstruction of particle objects, and the available triggers. The remaining events after the preliminary event selection criteria are used to train and execute a BDT algorithm for each signal point in the $\{M_U, g_U\}$ space, in order to maximize the probability to detect signal amongst background events. The BDT algorithm is implemented using the scikit-learn [114] and xgboost (XGB) [115] python libraries. We use the XGBClassifier class from the xgboost library, a 10-fold cross validation using

the scikit-learn method (GridCV⁶) for a grid in a hyperparameter space with 75, 125, 250, and 500 estimators, maximum depth in 3, 5, 7, 9, as well as learning rates of 0.01, 0.1, 1, and 10. For the cost function, we utilize the default mean square error (MSE). Additionally, we use the tree method based on the approximate greedy algorithm (histogram-optimized), referred to as hist, with a uniform sample method. These choices allow us to maximize the detection capability of the BDT algorithm by carefully tuning the hyperparameters, selecting an appropriate cost function, and utilizing an optimized tree construction method.

For each of the six analysis channels and $\{M_U, g_U\}$ signal point, the binary XGB classifier was trained (tested) with 20% (80%) of the simulated events, for each signal and background MC sample. Over forty kinematic and topological variables were studied as input for the XGB. These included the momenta of b jets and $\tau_{h,\ell}$ candidates; both invariant and transverse masses of pairs of τ objects and of b τ combinations; angular differences between b jets, between τ objects, and between the $\tau_{h,\ell}$ and b jets; and additional variables derived from the missing momentum in the events. After studying correlations between variables and their impact on the performance of the BDT, we found that only eight variables were necessary and responsible for the majority of the sensitivity of the analysis. The variable that provides the best signal to background separation is the scalar sum of the p_T of the final state objects (τ_h , $\tau_{h/\ell}$, and b jets) and the missing transverse momentum, referred to as S_T^{MET} :

$$S_T^{MET} = |\vec{p}_T^{miss}| + \sum_{\tau_h, \tau_{h/\ell}, b} |\vec{p}_T| \quad (4)$$

The S_T^{MET} variable has been successfully used in LQ searches at the LHC, since it probes the mass scale of resonant particles involved in the production processes. Other relevant variables include the magnitude of the vectorial difference in p_T between the two lepton candidates ($|\Delta \vec{p}_T|_{\tau_h \tau_{h/\ell}}$), the $\Delta R_{\tau_h \tau_{h/\ell}}$ separation between them, the reconstructed dilepton mass $m_{\tau_h \tau_{h/\ell}}$, and the product of their electric charges ($Q_{\tau_h} \times Q_{\tau_{h/\ell}}$). We also use the $|\Delta \vec{p}_T|$ between the τ_h candidate and \vec{p}_T^{miss} , and (if applicable) the $|\Delta \vec{p}_T|$ between the τ_h candidate and the leading b jet. For the final states including two τ_h candidates, the one with the highest p_T is used.

Figure 5 shows some relevant topological distributions, including S_T^{MET} on the top, for the b $\tau_h \tau_\ell$ category. In the Figure we include all signal production modes to this channel, with each component weighted with respect to their total contribution to the combined signal. The combined signal distribution is normalised to unity. We also show all background processes contributing to this channel, each of them

⁶ GridCV is a method that allows to find the best combination of hyperparameter values for the model, as this choice is crucial to achieve an optimal performance.

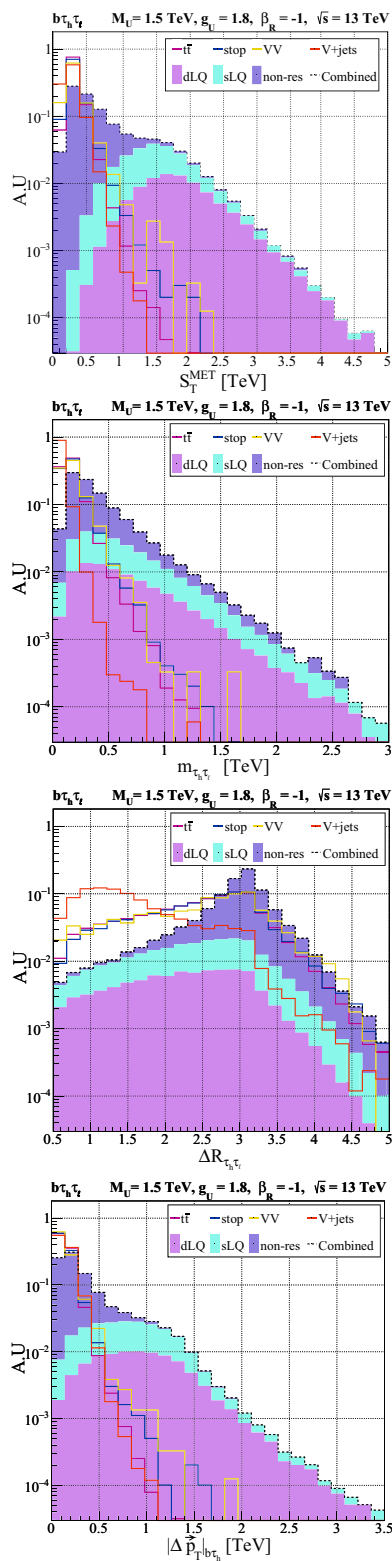


Fig. 5 S_T^{MET} , $m_{\tau_h \tau_\ell}$, $\Delta R_{\tau_h \tau_\ell}$, $|\Delta \vec{p}_T|_{b\tau_h}$ signal and background distributions for the $b\tau_h \tau_\ell$ channel. The signal distributions are generated for a benchmark sample with LQ mass of 1.5 TeV maximally coupled to right-handed currents. The combined distribution (shown as a stacked histogram) is the sum of the distributions, correctly weighted according to their respective cross-sections, assuming a coupling $g_U = 1.8$

individually normalised to unity. We find that the combined signal is dominated by sLQ production for large values of S_T^{MET} , while non-res production dominates for small S_T^{MET} . Interestingly, the backgrounds also sit at low S_T^{MET} values, since S_T^{MET} is driven by the mass scale of the SM particles being produced, in this case top quarks and Z/W bosons. This suggest that the sLQ and dLQ signals can indeed be separated from the SM background. As expected, the S_T^{MET} slQ and dLQ signal distributions have a mean near M_U , representative of resonant production, and a broad width as expected for large mass M_U hypotheses when information about the z -components of the momenta of objects is not utilised in the S_T^{MET} calculation.

Figure 5 (second from the top) shows the reconstructed mass of the ditau system, for the $b\tau_h \tau_\ell$ search channel. Since the two τ candidates in signal events arise from different production vertices (e.g., each τ candidate in dLQ production comes from a different LQ decay chain), the ditau mass distribution for signal scales as $m_{\tau_h \tau_\ell} \sim p_T(\tau_h) + p_T(\tau_\ell)$, and thus has a tail which depends on M_U and sits above the expected SM spectrum. On the other hand, the SM $m_{\tau_h \tau_\ell}$ distributions sit near $m_{Z/W}$ since the τ candidates in SM events arise from Z/W decays.

Figure 5 (third from the top) shows the $\Delta R_{\tau_h \tau_\ell}$ distribution for the $b\tau_h \tau_\ell$ channel. In the case of the $p p \rightarrow \tau \tau$ non-res signal distribution, the two τ leptons must be back-to-back to preserve conservation of momentum. Therefore, the visible τ candidates, τ_h and τ_ℓ , give rise to a $\Delta R_{\tau_h \tau_\ell}$ distribution that peaks near π radians. In the case of sLQ production, although the LQ and associated τ candidate must be back-to-back, the second τ candidate arising directly from the decay of the LQ does not necessarily move along the direction of the LQ (since the LQ also decays to a b quark). As a result, the $\Delta R_{\tau_h \tau_\ell}$ distribution for the sLQ signal process is smeared out, is broader, and has a mean below π radians. On the other hand, the τ_h candidate in $t\bar{t}$ events is often a jet being misidentified as a genuine τ_h . When this occurs, the fake τ_h candidate can arise from the same top quark decay chain as the τ_ℓ candidate, thus giving rise to small $\Delta R_{\tau_h \tau_\ell}$ values. This difference in the signal and background distributions provides a nice way for the ML algorithm to help decipher signal and background processes.

As noted above, the $|\Delta \vec{p}_T|$ distribution between the visible τ candidates and the b-quark jets is an important variable to help the BDT distinguish between signal and background processes. The discriminating power can be seen in Fig. 5 (bottom), which shows the $|\Delta \vec{p}_T|$ between the τ_h and b-jet candidate of the $b\tau_h \tau_\ell$ channel. In the case of dLQ production, the b quarks and τ leptons from the LQ $\rightarrow b\tau$ decay acquire transverse momentum of $p_T \sim M_U/2$. However, when the τ lepton decays hadronically (i.e. $\tau \rightarrow \tau_h \nu$), a large fraction of the momentum is lost to the neutrino. Therefore, the $|\Delta \vec{p}_T|_{b\tau_h}$ distribution for the dLQ (and sLQ)

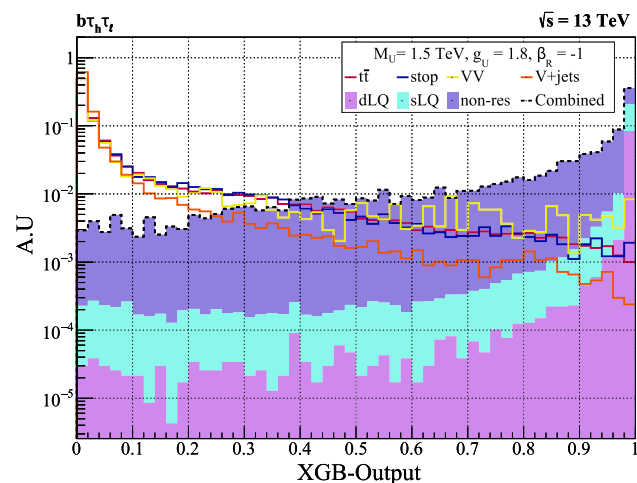


Fig. 6 Postfit XGB-output normalised distribution in the $b\tau_h\tau_\ell$ channel, for LQ mass of 1.5 TeV, constant coupling $g_U = 1.8$, and maximally coupled to right-handed currents

process peaks below $M_U/2$. On the other hand, for a background process such as V+jets, the b jet arises due to initial state radiation, and thus must balance the momentum of the associated vector boson (i.e. $p_T(b) \sim p_T(V) \sim m_V$). Since the visible τ candidate is typically produced from the V boson decay chain, its momentum (on average) is approximately $p_T(\tau_h) \sim p_T(V)/4 \sim m_V/4$. Therefore, to first order, the $|\Delta\vec{p}_T|$ distribution for the V+jets background is expected to peak below the m_V mass.

Lets us turn to the results of the $b\tau_h\tau_\ell$ BDT classifier, which is shown in Fig. 6 for the different signal production modes and backgrounds. Similar to Fig. 5, the distribution for each individual signal production mode is weighted with respect to their total contribution to the combined signal. The background distributions and combined signal distribution are normalized to an area under the curve of unity. Figure 6 shows the XGB distributions for a signal benchmark point with $M_U = 1.5$ TeV, $g_U = 1.8$, and $\beta_R = -1$. The XGB output is a value between 0 and 1, which quantifies the likelihood that an event is either signal-like (XGB output near 1) or background-like (XGB output near 0). We see that the presence of the sLQ and dLQ production modes is observed as an enhancement near a XGB output of unity, while the backgrounds dominate over the low end of the XGB output spectrum, especially near zero. In fact, over eighty percent of the sLQ and dLQ distributions reside in the last two bins, XGB output greater than 0.96, while more than sixty percent of the backgrounds fall in the first two bins, XGB output less than 0.04. It is also interesting to note that in comparison to the sLQ and dLQ distributions in Fig. 6, non-res is broader and not as narrowly peaked near XGB output of 1, which is expected due to the differences in kinematics described

above. Overall, if we focus on the last bin in this distribution, we find approximately 0.2% of the background, in contrast to 22% of the non-res, 78% of the sLQ, and 91% of the dLQ signal distributions. These numbers highlight the effectiveness of the XGB output in reducing the background in the region where the signal is expected.

The output signal and background distributions of the XGB classifier, normalised to their cross section times pre-selection efficiency times luminosity, are used to perform a profile binned likelihood statistical test in order to determine the expected signal significance. The estimation is performed using the `RooFit` [116] package, following the same methodology as in Refs. [117–132]. The value of the significance (Z_{sig}) is measured using the probability to obtain the same outcome from the test statistic in the background-only hypothesis, with respect to the signal plus background hypothesis. This allows for the determination of the local p-value and thus the calculation of the signal significance, which corresponds to the point where the integral of a Gaussian distribution between Z_{sig} and ∞ results in a value equal to the local p-value.

Systematic uncertainties are incorporated as nuisance parameters, considering log-priors for normalization and Gaussian priors for shape uncertainties. Our consideration of systematic uncertainties includes both experimental and theoretical effects, focusing on the dominant sources of uncertainty. Following [133], we consider a 3% systematic uncertainty on the measurement of the integrated luminosity at the LHC. A 5% uncertainty arises due to the choice of the parton distribution function used for the MC production, following the PDF4LHC prescription [134]. The chosen PDF set only has an effect on the overall expected signal and background yields, but the effect on the shape of the XGB output distribution is negligible. Reference [110] reports a systematic uncertainty of 2–5%, depending on the p_T and η of the τ_h candidate. Therefore, we utilize a conservative 5% uncertainty per τ_h candidate, independent of p_T and η , which is correlated between signal and background processes with genuine τ_h candidates, and correlated across XGB bins for each process. We assumed a 5% τ_h energy scale uncertainty, independent of p_T and η , following the CMS measurements described in [110]. Finally, we assume a conservative 3% uncertainty per b-jet candidate, following reference [135], and an additional 10% uncertainty in all the background predictions to account for possible mismodeling by the simulated samples. The uncertainties on the background estimates are typically derived from collision data using dedicated control samples that have negligible signal contamination and are enriched with events from the specific targeted background. The systematic uncertainties on the background estimates are treated as uncorrelated between background processes.

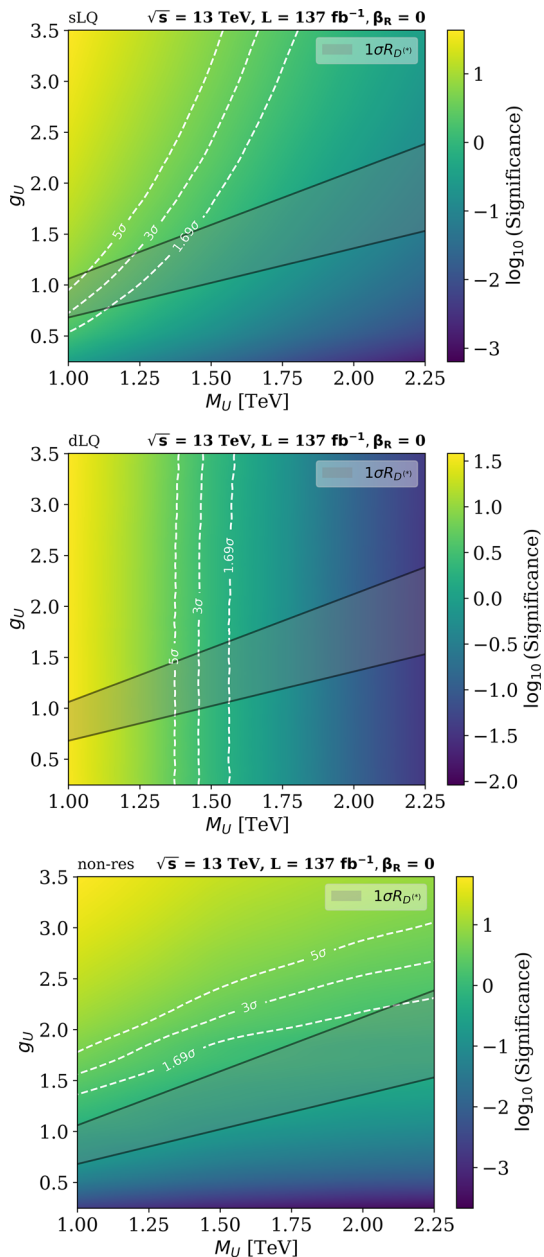


Fig. 7 Signal significance for different coupling scenarios and LQ masses, without right-handed currents, using the combination of all search channels. The results pertaining to sLQ, dLQ and non-res production are displayed respectively from the top. These results are for $\sqrt{s} = 13 \text{ TeV}$ and 137 fb^{-1}

4 Results

The expected signal significance for sLQ, dLQ and non-res production, and their combination, is presented in Fig. 7. Here, the significance is shown as a heat map in a two dimensional plane of g_U versus M_U , considering exclusive couplings to left-handed currents, i.e. $\text{BR}(\text{LQ} \rightarrow b\tau) = \frac{1}{2}$. The dashed lines show the contours of constant signal significance. The 1.69σ contour represents exclusion at 95%

confidence level, and the $3-5\sigma$ contours represent potential discovery. The grey band defines the set of $\{M_U, g_U\}$ values that can explain the B-meson anomalies, $C_U \sim 0.01$ for this scenario. The estimates are performed under the conditions for the second run, RUN-II, of the LHC ($\sqrt{s} = 13 \text{ TeV}$ and $L = 137 \text{ fb}^{-1}$). We find that the dLQ interpretation plot (Fig. 7 second from the top) does not depend on g_U , which is expected due to dLQ production arising exclusively from interactions with gluons. For this reason, the dLQ production process provides the best mode for discovery when g_U is small. On the other hand, the non-res channel is more sensitive to changes in the coupling parameter g_U , as its production cross-section depends on g_U^4 . Therefore, the non-res production process provides the best mode for discovery when g_U is large. These results confirm the expectations from previous analyses (see for instance [49]), in the sense that the dLQ and non-res processes complement each other nicely at low and high g_U scenarios. The sLQ channel combines features from both the dLQ and non-res channels, in principle making it an interesting option to explore different scenarios and gain a better understanding of LQ properties, but the evolution of the signal significance in the full phase space is more complicated as it involves resonant LQ production with a cross-section that depends non-trivially on M_U , g_U , and the LQ coupling to gluons. However, Fig. 7 shows that the sLQ production process can provide complementary and competitive sensitivity to the non-res and dLQ processes, in certain parts of the phase space.

The top panel of Fig. 8 presents the sensitivity of all signal production processes combined, and compares our expected exclusion region with the latest one from the ATLAS Collaboration [70]. The comparison suggests that our proposed analysis strategy provides better sensitivity than current methods being carried out at ATLAS, especially at large values of g_U . In particular, we find that with the pp data already available from RUN-II, our expected exclusion curves begin to probe solutions to the B-anomalies for LQ masses up to 2.25 TeV .

Figure 8 shows the expected signal significance considering $\text{BR}(\text{LQ} \rightarrow b\tau) = 1$, in order to compare our analysis with the corresponding results from the CMS [64] and ATLAS [71] Collaborations. Let us emphasize again that $\text{BR}(\text{LQ} \rightarrow b\tau)$ depends on β_R , as illustrated on the top panel of Fig. 2. Thus, although the $\text{BR}(\text{LQ} \rightarrow b\tau) = 1$ scenario is a possible physical case, it does not solve the observed anomalies in the $R_{D^{(*)}}$ ratios, as it corresponds to the case where LQs couple exclusively to right-handed currents.

With this in mind, the scenario studied by CMS in [64] considers couplings only to left-handed currents, setting artificially the condition $\text{BR}(\text{LQ} \rightarrow b\tau) = 1$. In order to compare, we scale the efficiency \times acceptance of our selection criteria for $\beta_R = 0$, by a factor of 2.0 for sLQ and 4.0 for dLQ. According to Fig. 8, the ML approach that we have followed

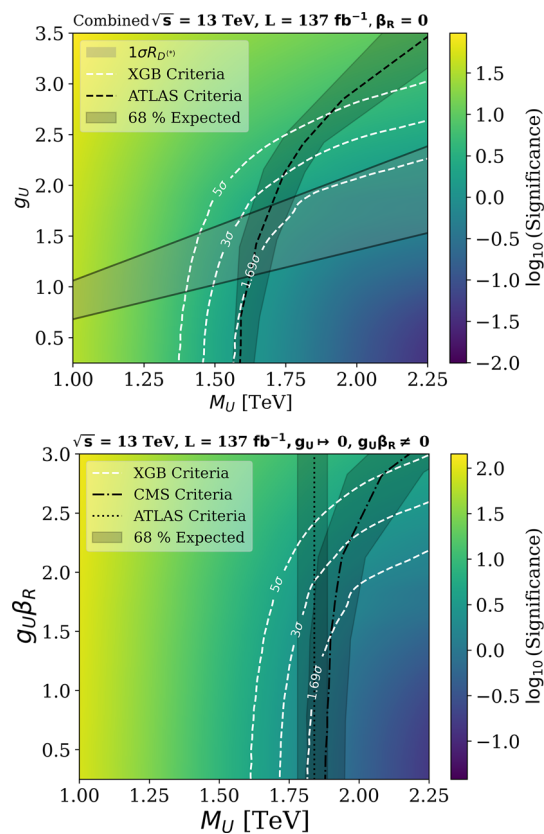


Fig. 8 The top (bottom) panel shows signal significance comparison with ATLAS [70] (CMS and ATLAS [64, 71]) background only hypothesis, for the combination of all channels, with uniquely coupling to left-handed (right-handed) currents. The estimates are performed at $\sqrt{s} = 13$ TeV and 137 fb^{-1}

again suggests an optimisation of the signal and background separation, having the potential of improving the regions of exclusion (1.69σ) with respect to that of CMS. In the bottom panel of the figure we have also included a similar exclusion by ATLAS [71]. However, since ATLAS only considers dLQ production in the analysis, the results are not entirely comparable, so are included only as a reference.

We now turn to the role of β_R , and our capacity of probing the regions solving the B-meson anomalies. Figure 9 shows the maximum significant contours, under LHC RUN-II conditions, for the different LQ production mechanisms and their combination, considering scenarios with only left-handed currents ($\beta_R = 0$, top) and with maximal right-handed currents ($\beta_R = -1$, bottom). We find a noticeable improvement in signal significance in all channels when taking $\beta_R = -1$, as is expected from the increase in $\text{BR}(\text{LQ} \rightarrow b\tau)$ branching ratio and production cross-sections (see Fig. 2). However, the region solving the B-meson anomalies also changes, preferring lower values of g_U , such that in both cases we find ourselves just starting to probe this region at large M_U .

The combined significance contours for the different BR scenarios that have been considered is presented in Fig. 10.

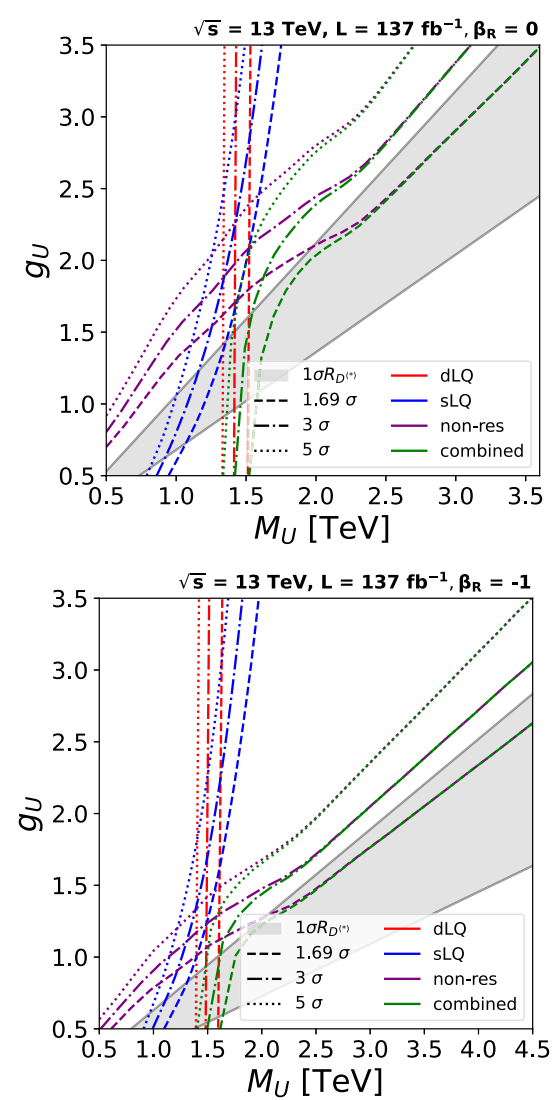


Fig. 9 Signal significance for different coupling scenarios and LQ masses for all channels. This plot summarizes our results with $\beta_R = 0$ (without right-handed currents) and $\beta_R = -1$ (maximally coupled to right-handed currents). The estimates are performed at $\sqrt{s} = 13$ TeV and 137 fb^{-1}

These contours illustrate the regions of exclusion for the three cases of interest, namely exclusive left-handed currents ($\text{BR}(\text{LQ} \rightarrow b\tau) = \frac{1}{2}, \beta_R = 0$), maximal left and right couplings ($\text{BR}(\text{LQ} \rightarrow b\tau) = \frac{2}{3}, \beta_R = -1$), and exclusive right-handed currents ($\text{BR}(\text{LQ} \rightarrow b\tau) = 1, g_U \rightarrow 0, g_U \beta_R = 1$). For small g_U , we find that the exclusive right-handed scenario is most sensitive, while the exclusive left-handed case is the worst. The reason for this is that this region is excluded principally by dLQ production, such that having the largest branching ratio is crucial in order to have a large number of events. For larger couplings, both exclusive scenarios end up having similar exclusion regions, with the $\beta_R = -1$ case being significantly more sensitive. The reason in this case is that the exclusion is dominated by

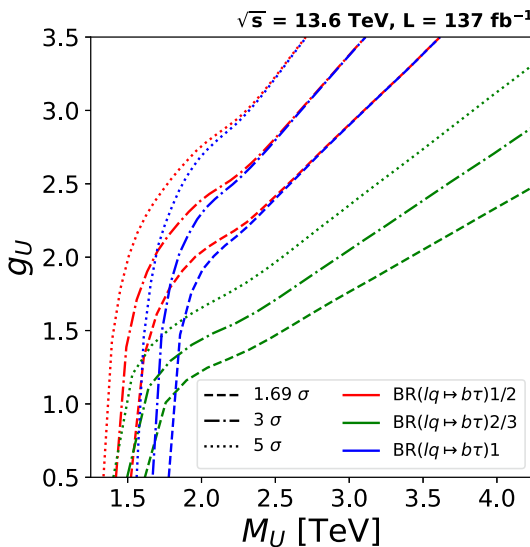


Fig. 10 Signal significance for different coupling scenarios and LQ masses, considering the case without coupling to right-handed currents $\text{BR}(\text{LQ} \rightarrow b\tau) = \frac{1}{2}$, the case maximally coupled to right- and left-handed currents $\text{BR}(\text{LQ} \rightarrow b\tau) = \frac{2}{3}$, and the case uniquely coupled to right-handed currents $\text{BR}(\text{LQ} \rightarrow b\tau) = 1$. The estimates are performed at $\sqrt{s} = 13 \text{ TeV}$ and 137 fb^{-1}

non-res, which has a much larger production cross-section if both currents are turned on.

In order to finalise our analysis of the LQ-only model, we show in Fig. 11 the expected combined significance in the relatively near future. For this, considering $\sqrt{s} = 13.6 \text{ TeV}$, we show contours for the sensitivity corresponding to integrated luminosities of 137 fb^{-1} , 300 fb^{-1} , and 3000 fb^{-1} , for scenarios with only left-handed currents (top) and with maximal coupling to right-handed currents (bottom). Note that for $\beta_R = 0$ ($\beta_R = -1$), couplings g_U close to 3.18 (1.85) and $M_U = 5.0 \text{ TeV}$ can be excluded with 1.69σ significance for the high luminosity LHC era, allowing us to probe the practically the entirety of the B-meson anomaly favored region. Note that the background yields for the high luminosity LHC might be larger due to pileup effects. Nevertheless, as it was mentioned in Sect. 3, we have included a conservative 10% systematic uncertainty associated with possible fluctuations on the background estimations. Although effects from larger pileup might be significant, they can be mitigated by improvements in the algorithms for particle reconstruction and identification, and also on the data-analysis techniques.

As commented on the Introduction, non-res production can be significantly affected by the presence of a companion Z' , which provides additional s-channel diagrams that add to the total cross-section and can interfere destructively with the LQ t-channel process (see Figs. 3 and 4). From our previous results, we see that non-res always is of high importance in determining the exclusion region, particularly at large M_U .

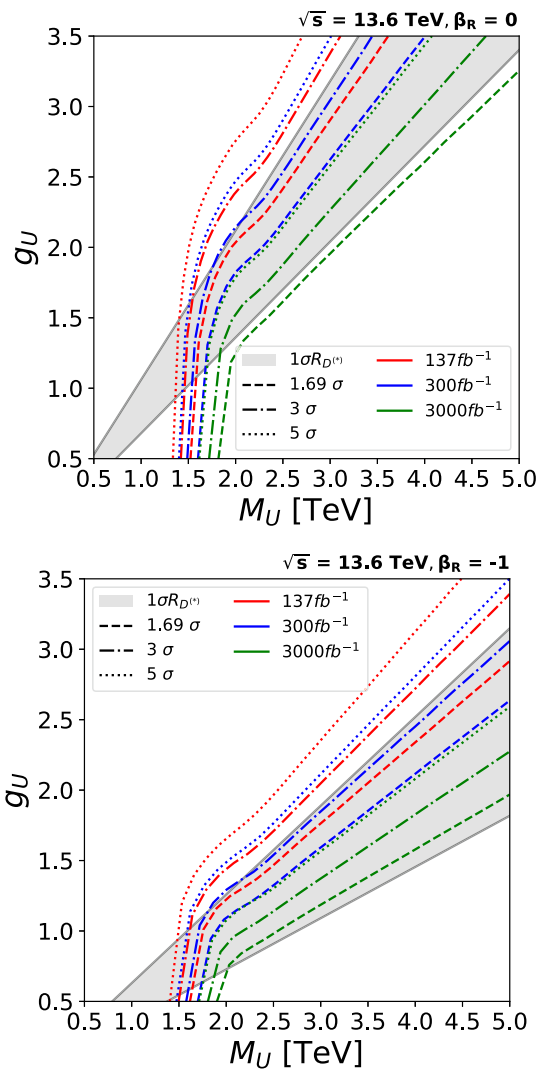


Fig. 11 Projected signal significance for different coupling scenarios and LQ masses maximally coupled to right-handed currents. The estimates are performed at $\sqrt{s} = 13.6 \text{ TeV}$, 137 fb^{-1} , 300 fb^{-1} and 3000 fb^{-1}

and g_U , meaning it is crucial to understand how this role is affected in front of a Z' with similar mass.

The change in sensitivity on the non-res signal significance due this interference effect with the Z' boson is shown in Fig. 12. We consider two opposite cases for the Z' mass: $M_{Z'}^2 = M_U^2/2$ (top) and $M_{Z'}^2 = 3M_U^2/2$ (bottom). Our results are shown on the $g_{Z'} - M_U$ plane, for a fixed $g_U = 1.8$ and $\beta_R = 0$. For the $M_{Z'}^2 = M_U^2/2$ scenario, there is an overall increase in the total cross-section, with a larger $g_{Z'}$ implying a larger sensitivity. This means that our ability to probe smaller values of g_U could be enhanced, as a given observation would be reproduced with both a specific g_U and vanishing $g_{Z'}$, or a smaller g_U with large $g_{Z'}$. Thus, for a large enough $g_{Z'}$, it could be possible to enhance non-res to the point that the entire region favoured by B-anomalies could

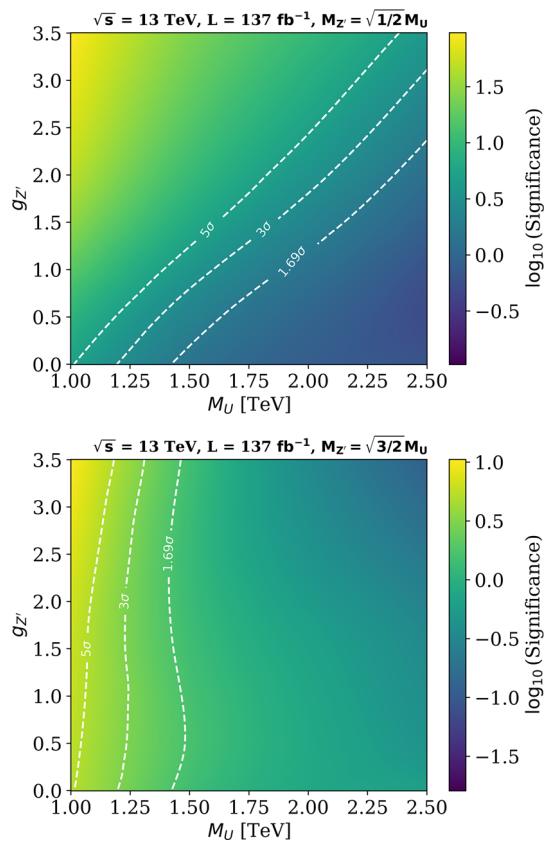


Fig. 12 Change on the non-res signal significance for different Z' coupling scenarios and LQ masses. The estimates are performed at $\sqrt{s} = 13.0$ TeV, $\beta_R = 0$, $g_U = 1.8$, $M_{Z'} = \sqrt{1/2}M_U$ (top), and $M_{Z'} = \sqrt{3/2}M_U$ (bottom)

be ruled out. In contrast, for $M_{Z'}^2 = 3M_U^2/2$ the cross-section is strongly affected by the large destructive interference, such that a larger $g_{Z'}$ does not necessarily imply an increase in sensitivity. In fact, as can be seen in the bottom panel, for large M_U the significance is reduced as $g_{Z'}$ increases, leading to the opposite conclusion than above, namely, that a large $g_{Z'}$ could reduce the effectiveness of non-res.

The impact of the above can be seen in Fig. 13, which shows our previous sensitivity curves on the $M_U - g_U$ plane, but this time with a Z' contribution to non-res. We use the same values of $M_{Z'}$ as before, but fix $g_{Z'} = 3.5$. For smaller $M_{Z'}$ (top), the non-res contribution is enhanced so much, that both sLQ and dLQ play no role whatsoever in determining the exclusion region. We find that, for small g_U , the sensitivity is dominated by Z' production such that, since M_U is related to $M_{Z'}$, LQ masses up to ~ 3 TeV are excluded. This bound is slightly relaxed for larger values of g_U , which is attributed to destructive interference effects due to an increased LQ contribution.

The bottom panel of Fig. 13 shows that case where $M_{Z'}$ is larger than M_U . As expected from our previous discussion, the behaviour and impact of non-res is modified. For small

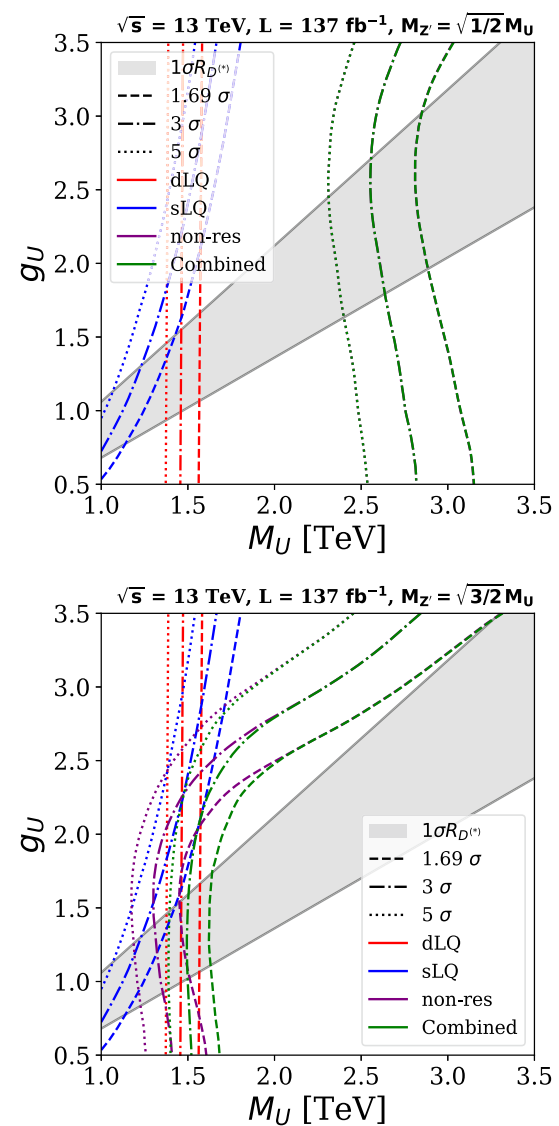


Fig. 13 Signal significance for different coupling scenarios and LQ masses, for all channels, with an additional Z' contribution to non-res production. We set $\beta_R = 0$ and $g_{Z'} = 3.5$, taking $M_{Z'}^2$ equal to $M_U^2/2$ (top) ($3M_U^2/2$) on the bottom panel

g_U , we again have the pure Z' production dominating the non-res cross-section, leading to a null sensitivity on g_U , similar to what happens in dLQ. In contrast, for very large g_U , we find that the pure LQ non-res production is the one that dominates, and we recover sensitivity regions with a slope similar to those shown in Figs. 7, 8, 9, 10 and 11, shifted towards larger values of g_U . For intermediate values of this coupling, the destructive interference have an important effect again, twisting the exclusion region slightly towards the left. Still, even in this case, we find that sLQ plays a marginal role in defining the combined exclusion region, and that the final result again depends primarily on dLQ and non-res production.

5 Discussion and conclusions

Experimental searches for LQs with preferential couplings to third generation fermions are currently of great interest due to their potential to explain observed tensions in the $R_{(D)}$ and $R_{(D^*)}$ decay ratios of B mesons with respect to the SM predictions. Although the LHC has a broad physics program on searches for LQs, it is very important to consider the impact of each search within wide range of different theoretical assumptions within a specific model. In addition, in order to improve the sensitivity to detect possible signs of physics beyond the SM, it is also important to strongly consider new computational techniques based on machine learning (ML). Therefore, we have studied the production of U_1 LQs with preferential couplings to third generation fermions, considering different couplings, masses and chiral currents. These studies have been performed considering p p collisions at $\sqrt{s} = 13$ TeV and 13.6 TeV and different luminosity scenarios, including projections for the high luminosity LHC. A ML algorithm based on boosted decision trees is used to maximize the signal significance. The signal to background discrimination output of the algorithm is taken as input to perform a profile binned-likelihood test statistic to extract the expected signal significance.

The expected signal significance for sLQ, dLQ and non-res production, and their combination, is presented as contours on a two dimensional plane of g_U versus M_U . We present results for the case of exclusive couplings to left-handed, mixed, and exclusive right-handed currents. For the first two, the region of the phase space that could explain the B meson anomalies is also presented. We confirm the findings of previous works that the largest production cross-section and best overall significance comes from the combination of dLQ and non-res production channels. We also find that the sensitivity to probe the parameter space of the model is highly dependent on the chirality of the couplings. Nevertheless, the region solving the B-meson anomalies also changes with each choice, such that in all evaluated cases we find ourselves just starting to probe this region at large M_U .

Our studies compare our exclusion regions with respect to the latest reported results from the ATLAS and CMS Collaborations. The comparison suggests that our ML approach has a better sensitivity than the standard cut-based analyses, especially at large values of g_U . In addition, our projections for the HL-LHC cover the whole region solving the B-anomalies, for masses up to 5.00 TeV.

Finally, we consider the effects of a companion Z' boson on non-res production. We find that such a contribution can have a considerable impact on the LQ sensitivity regions, depending on the specific masses and couplings. In spite of this, we still consider non-res production as an essential channel for probing LQs in the future.

Acknowledgements The authors would like to thank Gino Isidori for fruitful discussions. A.F, J.P, and C.R thank the constant and enduring financial support received for this project from the faculty of science at Universidad de Los Andes (Bogotá, Colombia) and the Colombian Science Ministry MinCiencias, with the grant program 70141, contract number 164-2021. J.J.P. acknowledges funding by the *Dirección de Gestión de la Investigación* at PUCP, through grant No. DGI-2021-C-0020. A.G acknowledges the funding received from the Physics & Astronomy department at Vanderbilt University and the US National Science Foundation. This work is supported in part by NSF Award PHY-1945366 and a Vanderbilt Seeding Success Grant.

Data availability statement This manuscript has no associated data or the data will not be deposited. [Authors' comment: This is a theoretical study and no experimental data].

Open Access This article is licensed under a Creative Commons Attribution 4.0 International License, which permits use, sharing, adaptation, distribution and reproduction in any medium or format, as long as you give appropriate credit to the original author(s) and the source, provide a link to the Creative Commons licence, and indicate if changes were made. The images or other third party material in this article are included in the article's Creative Commons licence, unless indicated otherwise in a credit line to the material. If material is not included in the article's Creative Commons licence and your intended use is not permitted by statutory regulation or exceeds the permitted use, you will need to obtain permission directly from the copyright holder. To view a copy of this licence, visit <http://creativecommons.org/licenses/by/4.0/>.

Funded by SCOAP³. SCOAP³ supports the goals of the International Year of Basic Sciences for Sustainable Development.

References

1. J.C. Pati, A. Salam, Lepton number as the fourth color. *Phys. Rev. D* **10**, 275–289 (1974). (**Erratum:** *Phys. Rev. D* **11**, 703–703 (1975))
2. H. Georgi, S.L. Glashow, Unity of all elementary particle forces. *Phys. Rev. Lett.* **32**, 438–441 (1974)
3. B. Schrempp, F. Schrempp, Light leptoquarks. *Phys. Lett. B* **153**, 101–107 (1985)
4. M. Leurer, A comprehensive study of leptoquark bounds. *Phys. Rev. D* **49**, 333–342 (1994)
5. S. Davidson, D.C. Bailey, B.A. Campbell, Model independent constraints on leptoquarks from rare processes. *Z. Phys. C* **61**, 613–644 (1994)
6. M. Leurer, Bounds on vector leptoquarks. *Phys. Rev. D* **50**, 536–541 (1994)
7. J.L. Hewett, T.G. Rizzo, Much ado about leptoquarks: a comprehensive analysis. *Phys. Rev. D* **56**, 5709–5724 (1997)
8. F.S. Queiroz, K. Sinha, A. Strumia, Leptoquarks, dark matter, and anomalous LHC events. *Phys. Rev. D* **91**(3), 035006 (2015)
9. I. Doršner, S. Fajfer, A. Greljo, J.F. Kamenik, N. Košnik, Physics of leptoquarks in precision experiments and at particle colliders. *Phys. Rep.* **641**, 1–68 (2016)
10. LHCb Collaboration, Test of lepton universality using $B^+ \rightarrow K^+ \ell^+ \ell^-$ decays. *Phys. Rev. Lett.* **113**(2014)
11. LHCb Collaboration, Test of lepton universality with $B^0 \rightarrow K^{*0} \ell^+ \ell^-$ decays. *JHEP* **08**, 055 (2017)
12. LHCb Collaboration, Search for lepton-universality violation in $B^+ \rightarrow K^+ \ell^+ \ell^-$ decays. *Phys. Rev. Lett.* **122**(19), 191801 (2019)
13. LHCb Collaboration, Test of lepton universality in beauty-quark decays. *Nat. Phys.* **18**(3), 277–282 (2022)

14. B.B. Collaboration, Evidence for an excess of $\bar{B} \rightarrow D^{(*)}\tau^-\bar{\nu}_\tau$ decays. *Phys. Rev. Lett.* **109**, 101802 (2012)
15. B.B. Collaboration, Measurement of an excess of $\bar{B} \rightarrow D^{(*)}\tau^-\bar{\nu}_\tau$ decays and implications for charged Higgs bosons. *Phys. Rev. D* **88**(7), 072012 (2013)
16. Belle Collaboration, Measurement of $\mathcal{R}(D)$ and $\mathcal{R}(D^*)$ with a semileptonic tagging method (2019)
17. B. Collaboration, Measurement of the τ lepton polarization and $R(D^*)$ in the decay $\bar{B} \rightarrow D^*\tau^-\bar{\nu}_\tau$ with one-prong hadronic τ decays at Belle. *Phys. Rev. D* **97**, 012004 (2018)
18. B. Collaboration, Measurement of the branching ratio of $\bar{B}^0 \rightarrow D^{*+}\tau^-\bar{\nu}_\tau$ relative to $\bar{B}^0 \rightarrow D^{*+}\ell^-\bar{\nu}_\ell$ decays with a semileptonic tagging method. *Phys. Rev. D* **94**, 072007 (2016)
19. B. Collaboration, Measurement of the τ lepton polarization and $R(D^*)$ in the decay $\bar{B} \rightarrow D^*\tau^-\bar{\nu}_\tau$. *Phys. Rev. Lett.* **118**, 211801 (2017)
20. B. Collaboration, Measurement of the branching ratio of $\bar{B} \rightarrow D^{(*)}\tau^-\bar{\nu}_\tau$ relative to $\bar{B} \rightarrow D^{(*)}\ell^-\bar{\nu}_\ell$ decays with hadronic tagging at Belle. *Phys. Rev. D* **92**, 072014 (2015)
21. LHCb Collaboration, Measurement of the ratio of branching fractions $\mathcal{B}(\bar{B}^0 \rightarrow D^{*+}\tau^-\bar{\nu}_\tau)/\mathcal{B}(\bar{B}^0 \rightarrow D^{*+}\mu^-\bar{\nu}_\mu)$. *Phys. Rev. Lett.* **115**(11), 111803 (2015). [Erratum: *Phys. Rev. Lett.* **115**, 159901 (2015)]
22. LHCb Collaboration, Measurement of the ratio of branching fractions $\mathcal{B}(\bar{B}^0 \rightarrow D^{*+}\tau^-\bar{\nu}_\tau)/\mathcal{B}(\bar{B}^0 \rightarrow D^{*+}\mu^-\bar{\nu}_\mu)$. *Phys. Rev. Lett.* **115**, 111803 (2015). [Erratum: *Phys. Rev. Lett.* **115**, 159901 (2015)]
23. LHCb Collaboration, Measurement of the ratio of the $B^0 \rightarrow D^{*-}\tau^+\nu_\tau$ and $B^0 \rightarrow D^{*-}\mu^+\nu_\mu$ branching fractions using three-prong τ -lepton decays. *Phys. Rev. Lett.* **120**, 171802 (2018)
24. LHCb Collaboration, Test of lepton flavor universality by the measurement of the $B^0 \rightarrow D^{*-}\tau^+\nu_\tau$ branching fraction using three-prong τ decays. *Phys. Rev. D* **97**(7), 072013 (2018)
25. LHCb Collaboration, Measurement of the ratios of branching fractions $\mathcal{R}(D^*)$ and $\mathcal{R}(D^0)$ (2023)
26. G. Hiller, M. Schmaltz, R_K and future $b \rightarrow s\ell\ell$ physics beyond the standard model opportunities. *Phys. Rev. D* **90**, 054014 (2014)
27. B. Gripaios, M. Nardecchia, S.A. Renner, Composite leptoquarks and anomalies in B -meson decays. *JHEP* **05**, 006 (2015)
28. R. Alonso, B. Grinstein, J.M. Camalich, Lepton universality violation and lepton flavor conservation in B -meson decays. *JHEP* **10**, 184 (2015)
29. L. Calibbi, A. Crivellin, T. Ota, Effective field theory approach to $b \rightarrow s\ell\ell^{(\prime)}$, $B \rightarrow K^{(*)}\nu\bar{\nu}$ and $B \rightarrow D^{(*)}\tau\nu$ with third generation couplings. *Phys. Rev. Lett.* **115**, 181801 (2015)
30. S. Fajfer, N. Košnik, Vector leptoquark resolution of R_K and $R_{D^{(*)}}$ puzzles. *Phys. Lett. B* **755**, 270–274 (2016)
31. M. Bauer, M. Neubert, Minimal leptoquark explanation for the $R_{D^{(*)}}$, R_K , and $(g-2)_\mu$ anomalies. *Phys. Rev. Lett.* **116**(14), 141802 (2016)
32. D. Bećirević, N. Košnik, O. Sumensari, R. Zukanovich-Funchal, Palatable leptoquark scenarios for lepton flavor violation in exclusive $b \rightarrow s\ell_1\ell_2$ modes. *JHEP* **11**, 035 (2016)
33. A. Crivellin, D. Müller, T. Ota, Simultaneous explanation of $R(D^*)$ and $b \rightarrow \mu^+\mu^-$: the last scalar leptoquark standing. *JHEP* **09**, 040 (2017)
34. G. D'Amico, M. Nardecchia, P. Panci, F. Sannino, A. Strumia, R. Torre, A. Urbano, Flavour anomalies after the R_{K^*} measurement. *JHEP* **09**, 010 (2017)
35. G. Hiller, I. Nisandžić, R_K and R_{K^*} beyond the standard model. *Phys. Rev. D* **96**(3), 035003 (2017)
36. D. Buttazzo, A. Greljo, G. Isidori, D. Marzocca, B-physics anomalies: a guide to combined explanations. *JHEP* **11**, 044 (2017)
37. D. Bećirević, I. Doršner, S. Fajfer, N. Košnik, D.A. Faroughy, O. Sumensari, Scalar leptoquarks from grand unified theories to accommodate the B -physics anomalies. *Phys. Rev. D* **98**(5), 055003 (2018)
38. C. Cornellà, J. Fuentes-Martín, G. Isidori, Revisiting the vector leptoquark explanation of the B -physics anomalies. *JHEP* **07**, 168 (2019)
39. A. Angelescu, D. Bećirević, D.A. Faroughy, F. Jaffredo, O. Sumensari, Single leptoquark solutions to the B -physics anomalies. *Phys. Rev. D* **104**(5), 055017 (2021)
40. G. Belanger et al., Leptoquark manœuvres in the dark: a simultaneous solution of the dark matter problem and the $R_{D^{(*)}}$ anomalies. *JHEP* **02**, 042 (2022)
41. J. Aebrischer, G. Isidori, M. Pesut, B.A. Stefanek, F. Wilsch, Confronting the vector leptoquark hypothesis with new low- and high-energy data. *JHEP* **02**, 153 (2023)
42. LHCb Collaboration, Test of lepton universality in $b \rightarrow \ell^+\ell^-$ decays (2022)
43. LHCb Collaboration, Measurement of lepton universality parameters in $B^+ \rightarrow K^+\ell^+\ell^-$ and $B^0 \rightarrow K^{*0}\ell^+\ell^-$ decays (2022)
44. A. Greljo, J. Salko, A. Smolkovič, P. Stangl, Rare b decays meet high-mass Drell-Yan. *JHEP* **5**, 2023 (2023)
45. M. Ciuchini, M. Fedele, E. Franco, A. Paul, L. Silvestrini, M. Valli, Constraints on lepton universality violation from rare b decays. *Phys. Rev. D* **107**, 055036 (2023)
46. B. Diaz, M. Schmaltz, Y. Zhong, The leptoquark Hunter's guide: Pair production. *JHEP* **10**, 097 (2017)
47. I. Doršner, A. Greljo, Leptoquark toolbox for precision collider studies. *JHEP* **05**, 126 (2018)
48. N. Vignaroli, Seeking leptoquarks in the $t\bar{t}$ plus missing energy channel at the high-luminosity lhc. *Phys. Rev. D* **99**, 035021 (2019)
49. M. Schmaltz, Y. Zhong, The leptoquark Hunter's guide: large coupling. *JHEP* **01**, 132 (2019)
50. A. Biswas, D. Kumar-Ghosh, N. Ghosh, A. Shaw, A.K. Swain, Collider signature of U_1 leptoquark and constraints from $b \rightarrow c$ observables. *J. Phys. G* **47**(4), 045005 (2020)
51. M.J. Baker, J. Fuentes-Martín, G. Isidori, M. König, High- p_T signatures in vector-leptoquark models. *Eur. Phys. J. C* **79**(4), 334 (2019)
52. U. Haisch, G. Polesello, Resonant third-generation leptoquark signatures at the Large Hadron Collider. *JHEP* **05**, 057 (2021)
53. A. Bhaskar, T. Mandal, S. Mitra, M. Sharma, Improving third-generation leptoquark searches with combined signals and boosted top quarks. *Phys. Rev. D* **104**(7), 075037 (2021)
54. J. Bernigaud, M. Blanke, I.M. Varzielas, J. Talbert, J. Zurita, LHC signatures of τ -flavoured vector leptoquarks. *JHEP* **08**, 127 (2022)
55. R. Leonardi, O. Panella, F. Romeo, A. Gurrola, H. Sun, S. Xue, Phenomenology at the LHC of composite particles from strongly interacting Standard Model fermions via four-fermion operators of NJL type. *EPJC* **80**(309) (2020)
56. C.M.S. Collaboration, Search for heavy neutrinos or third-generation leptoquarks in final states with two hadronically decaying τ leptons and two jets in proton-proton collisions at $\sqrt{s} = 13$ TeV. *JHEP* **03**, 077 (2017)
57. C.M.S. Collaboration, Search for third-generation scalar leptoquarks and heavy right-handed neutrinos in final states with two tau leptons and two jets in proton-proton collisions at $\sqrt{s} = 13$ TeV. *JHEP* **07**, 121 (2017)
58. C.M.S. Collaboration, Search for third-generation scalar leptoquarks decaying to a top quark and a τ lepton at $\sqrt{s} = 13$ TeV. *Eur. Phys. J. C* **78**, 707 (2018)
59. C.M.S. Collaboration, Constraints on models of scalar and vector leptoquarks decaying to a quark and a neutrino at $\sqrt{s} = 13$ TeV. *Phys. Rev. D* **98**(3), 032005 (2018)
60. C.M.S. Collaboration, Search for a singly produced third-generation scalar leptoquark decaying to a τ lepton and a bottom

- quark in proton-proton collisions at $\sqrt{s} = 13$ TeV. *JHEP* **07**, 115 (2018)
61. C.M.S. Collaboration, Search for heavy neutrinos and third-generation leptoquarks in hadronic states of two τ leptons and two jets in proton-proton collisions at $\sqrt{s} = 13$ TeV. *JHEP* **03**, 170 (2019)
 62. C.M.S. Collaboration, Search for singly and pair-produced leptoquarks coupling to third-generation fermions in proton-proton collisions at $s=13$ TeV. *Phys. Lett. B* **819**, 136446 (2021)
 63. CMS Collaboration, Searches for additional Higgs bosons and for vector leptoquarks in $\tau\tau$ final states in proton-proton collisions at $\sqrt{s} = 13$ TeV (2022)
 64. CMS Collaboration, The search for a third-generation leptoquark coupling to a τ lepton and a b quark through single, pair and nonresonant production at $\sqrt{s} = 13$ TeV (2022)
 65. ATLAS Collaboration, Searches for third-generation scalar leptoquarks in $\sqrt{s} = 13$ TeV pp collisions with the ATLAS detector. *JHEP* **06**, 144 (2019)
 66. ATLAS Collaboration, Search for a scalar partner of the top quark in the all-hadronic $t\bar{t}$ plus missing transverse momentum final state at $\sqrt{s} = 13$ TeV with the ATLAS detector. *Eur. Phys. J. C* **80**(8), 737 (2020)
 67. ATLAS Collaboration, Search for pair production of third-generation scalar leptoquarks decaying into a top quark and a τ -lepton in pp collisions at $\sqrt{s} = 13$ TeV with the ATLAS detector. *JHEP* **06**, 179 (2021)
 68. ATLAS Collaboration, Search for new phenomena in final states with b -jets and missing transverse momentum in $\sqrt{s} = 13$ TeV pp collisions with the ATLAS detector. *JHEP* **05**, 093 (2021)
 69. ATLAS Collaboration, Search for new phenomena in pp collisions in final states with tau leptons, b-jets, and missing transverse momentum with the ATLAS detector. *Phys. Rev. D* **104**(11), 112005 (2021)
 70. ATLAS Collaboration, Search for leptoquarks decaying into the $b\tau$ final state in pp collisions at $\sqrt{s} = 13$ TeV with the ATLAS detector (2023)
 71. ATLAS Collaboration, Search for pair production of third-generation leptoquarks decaying into a bottom quark and a τ -lepton with the atlas detector (2023)
 72. D.A. Faroughy, A. Greljo, J.F. Kamenik, Confronting lepton flavor universality violation in B decays with high- p_T tau lepton searches at LHC. *Phys. Lett. B* **764**, 126–134 (2017)
 73. A. Angelescu, D. Bećirević, D.A. Faroughy, O. Sumensari, Closing the window on single leptoquark solutions to the B-physics anomalies. *JHEP* **10**, 183 (2018)
 74. A. Bhaskar, D. Das, T. Mandal, S. Mitra, C. Neeraj, Precise limits on the charge-2/3 U1 vector leptoquark. *Phys. Rev. D* **104**(3), 035016 (2021)
 75. C. Cornellà, D.A. Faroughy, J. Fuentes-Martín, G. Isidori, M. Neubert, Reading the footprints of the B-meson flavor anomalies. *JHEP* **08**, 050 (2021)
 76. L. Allwicher, D.A. Faroughy, F. Jaffredo, O. Sumensari, F. Wilsch, Drell-Yan tails beyond the standard model. *JHEP* **3**, 2023 (2023)
 77. U. Haisch, L. Schnell, S. Schulte, Drell-Yan production in third-generation gauge vector leptoquark models at NLO+PS in QCD. *JHEP* **2**, 2023 (2023)
 78. J. H. Friedman, Greedy function approximation: A gradient boosting machine. *Ann. Stat.* **29**(5), 1189–1232 (2001). Publisher: Institute of Mathematical Statistics
 79. X. Ai, S.C. Hsu, K. Li, C.T. Lu, Probing highly collimated photon-jets with deep learning. *JPCS* **2438**(1), 012114 (2023)
 80. ATLAS Collaboration, Search for the standard model Higgs boson produced in association with top quarks and decaying into a $b\bar{b}$ pair in pp collisions at $\sqrt{s} = 13$ TeV with the ATLAS detector. *Phys. Rev. D* **97**(7), 072016 (2018)
 81. S. Chigusa, S. Li, Y. Nakai, W. Zhang, Y. Zhang, J. Zheng, Deeply learned preselection of Higgs dijet decays at future lepton colliders. *Phys. Lett. B* **833**, 137301 (2022)
 82. Y.L. Chung, S.C. Hsu, B. Nachman, Disentangling boosted Higgs boson production modes with machine learning. *JINST* **16**, P07002 (2021)
 83. J. Feng, M. Li, Q.S. Yan, Y.P. Zeng, H.H. Zhang, Y. Zhang, Z. Zhao, Improving heavy Dirac neutrino prospects at future hadron colliders using machine learning. *JHEP* **9**, 2022 (2022)
 84. D. Barbosa, F. Díaz, L. Quintero, A. Flórez, M. Sanchez, A. Gurrola, E. Sheridan, and F. Romeo, Probing a Z' with non-universal fermion couplings through top quark fusion, decays to bottom quarks, and machine learning techniques. *EPJC* **83**(413) (2023)
 85. N. Assad, B. Fornal, B. Grinstein, Baryon Number and Lepton Universality Violation in Leptoquark and Diquark Models. *Phys. Lett. B* **777**, 324–331 (2018)
 86. L. Calibbi, A. Crivellin, T. Li, Model of vector leptoquarks in view of the B-physics anomalies. *Phys. Rev. D* **98**(11), 115002 (2018)
 87. M. Blanke, A. Crivellin, B Meson anomalies in a Pati-Salam model within the Randall-Sundrum background. *Phys. Rev. Lett.* **121**(1), 011801 (2018)
 88. S. Iguro, J. Kawamura, S. Okawa, Y. Omura, TeV-scale vector leptoquark from Pati-Salam unification with vectorlike families. *Phys. Rev. D* **104**(7), 075008 (2021)
 89. L. Di Luzio, A. Greljo, M. Nardecchia, Gauge leptoquark as the origin of B-physics anomalies. *Phys. Rev. D* **96**(11), 115011 (2017)
 90. A. Greljo, B.A. Stefanek, Third family quark-lepton unification at the TeV scale. *Phys. Lett. B* **782**, 131–138 (2018)
 91. L. Di Luzio, J. Fuentes-Martín, A. Greljo, M. Nardecchia, S. Renner, Maximal flavour violation: a Cabibbo mechanism for leptoquarks. *JHEP* **11**, 081 (2018)
 92. S.F. King, Twin Pati-Salam theory of flavour with a TeV scale vector leptoquark. *JHEP* **11**, 161 (2021)
 93. M. Fernández-Navarro, S.F. King, B-anomalies in a twin Pati-Salam theory of flavour including the 2022 LHCb $R_{K^{(*)}}$ analysis. *JHEP* **2**, 2023 (2023)
 94. M. Bordone, C. Cornellà, J. Fuentes-Martín, G. Isidori, A three-site gauge model for flavor hierarchies and flavor anomalies. *Phys. Lett. B* **779**, 317–323 (2018)
 95. M. Bordone, C. Cornellà, J. Fuentes-Martín, G. Isidori, Low-energy signatures of the PS³ model: from B-physics anomalies to LFV. *JHEP* **10**, 148 (2018)
 96. J. Fuentes-Martín, G. Isidori, J.M. Lizana, N. Selimovic, B.A. Stefanek, Flavor hierarchies, flavor anomalies, and Higgs mass from a warped extra dimension. *Phys. Lett. B* **834**, 137382 (2022)
 97. B. Gripaios, Composite leptoquarks at the LHC. *JHEP* **02**, 045 (2010)
 98. R. Barbieri, C.W. Murphy, F. Senia, B-decay anomalies in a composite leptoquark model. *Eur. Phys. J. C* **77**(1), 8 (2017)
 99. R. Barbieri, A. Tesi, B-decay anomalies in Pati-Salam SU(4). *Eur. Phys. J. C* **78**(3), 193 (2018)
 100. J. Fuentes-Martín, G. Isidori, M. König, N. Selimović, Vector leptoquarks beyond tree level. III. Vectorlike fermions and flavor-changing transitions. *Phys. Rev. D* **102**, 115015 (2020)
 101. A. Djouadi, J. Ellis, A. Popov, J. Quevillon, Interference effects in $t\bar{t}$ production at the LHC as a window on new physics. *JHEP* **03**, 119 (2019)
 102. N.D. Christensen, C. Duhr, FeynRules - Feynman rules made easy. *Comput. Phys. Commun.* **180**, 1614–1641 (2009)
 103. A. Alloul, N.D. Christensen, C. Degrande, C. Duhr, B. Fuks, FeynRules 2.0 - A complete toolbox for tree-level phenomenology. *Comput. Phys. Commun.* **185**, 2250–2300 (2014)
 104. J. Alwall, C. Duhr, B. Fuks, O. Mattelaer, D.G. Öztürk, C.H. Shen, Computing decay rates for new physics theories with FeynRules

- and MadGraph 5_aMC@NLO. *Comput. Phys. Commun.* **197**, 312–323 (2015)
105. J. Alwall, R. Frederix, S. Frixione, V. Hirschi, F. Maltoni, O. Mattelaer, H.S. Shao, T. Stelzer, P. Torrielli, M. Zaro, The automated computation of tree-level and next-to-leading order differential cross sections, and their matching to parton shower simulations. *JHEP* **07**, 079 (2014)
 106. NNPDF Collaboration. Parton distributions for the LHC Run II. *JHEP* **04**, 040 (2015)
 107. T. Sjöstrand, S. Ask, J.R. Christiansen, R. Corke, N. Desai, P. Ilten, S. Mrenna, S. Prestel, C.O. Rasmussen, P.Z. Skands, An introduction to PYTHIA 8.2. *Comput. Phys. Commun.* **191**, 159–177 (2015)
 108. DELPHES 3 Collaboration. DELPHES 3, A modular framework for fast simulation of a generic collider experiment. *JHEP* **02**, 057 (2014)
 109. C.M.S. Collaboration, Identification of heavy-flavour jets with the CMS detector in pp collisions at 13 TeV. *JINST* **13**(04), P05011 (2018)
 110. C.M.S. Collaboration, Identification of hadronic tau lepton decays using a deep neural network. *JINST* **17**(07), P07023 (2022)
 111. CMS Collaboration. Study of the Discovery Reach in Searches for Supersymmetry at CMS with 3000/fb. CMS Physics Analysis Summary CMS-PAS-FTR-13-014, CERN, 2013. Accessed on January 07, (2023)
 112. A.M. Sirunyan et al., Performance of the reconstruction and identification of high-momentum muons in proton-proton collisions at $\sqrt{s} = 13$ TeV. *JINST* **15**(02), P02027 (2020)
 113. A.M. Sirunyan et al., Electron and photon reconstruction and identification with the CMS experiment at the CERN LHC. *JINST* **16**(05), P05014 (2021)
 114. F. Pedregosa, G. Varoquaux, A. Gramfort, V. Michel, B. Thirion, O. Grisel, M. Blondel, P. Prettenhofer, R. Weiss, V. Dubourg, J. Vanderplas, A. Passos, D. Cournapeau, M. Brucher, M. Perrot, É. Duchesnay, Scikit-learn: Machine Learning in Python. *J. Mach. Learn. Res.* **12**, 2825–2830 (2011)
 115. T. Chen and C. Guestrin. XGBoost: A scalable tree boosting system. In *Proceedings of the 22nd ACM SIGKDD International Conference on Knowledge Discovery and Data Mining*, KDD ’16, pages 785–794, New York, NY, USA, 2016. Association for Computing Machinery
 116. The ROOT team. Root - an object oriented data analysis framework. *Nucl. Inst. & Meth. in Phys. Res. A*, 389:81–86, 1997. Proceedings AIHENP’96 Workshop, Lausanne, Sep. 1996. See also “ROOT”[software], Release v6.18/02, and <https://root.cern/manual/root/>
 117. D. Barbosa, F. Díaz, L. Quintero, A. Flórez, M. Sanchez, A. Gurrola, E. Sheridan, F. Romeo, Probing a Z' with non-universal fermion couplings through top quark fusion, decays to bottom quarks, and machine learning techniques. *Eur. Phys. J. C* **83**(5), 413 (2023)
 118. A. Flórez, A. Gurrola, W. Johns, P. Sheldon, E. Sheridan, K. Sinha, B. Soubasis, Probing axionlike particles with $\gamma\gamma$ final states from vector boson fusion processes at the LHC. *Phys. Rev. D* **103**(9), 095001 (2021)
 119. A. Flórez, A. Gurrola, W. Johns, J. Maruri, P. Sheldon, K. Sinha, S.R. Starko, Anapole dark matter via vector boson fusion processes at the LHC. *Phys. Rev. D* **100**(1), 016017 (2019)
 120. A. Flórez, Y. Guo, A. Gurrola, W. Johns, O. Ray, P. Sheldon, S. Starko, Probing heavy spin-2 bosons with $\gamma\gamma$ final states from vector boson fusion processes at the LHC. *Phys. Rev. D* **99**(3), 035034 (2019)
 121. A. Flórez, K. Gui, A. Gurrola, C. Patiño, D. Restrepo, Expanding the reach of heavy neutrino searches at the LHC. *Phys. Lett. B* **778**, 94–100 (2018)
 122. A. Flórez, A. Gurrola, W. Johns, Y. Do Oh, P. Sheldon, D. Teague, T. Weiler, Searching for new heavy neutral gauge bosons using vector boson fusion processes at the LHC. *Phys. Lett. B* **767**, 126–132 (2017)
 123. A. Flórez, L. Bravo, A. Gurrola, C. Ávila, M. Segura, P. Sheldon, W. Johns, Probing the stau-neutralino coannihilation region at the LHC with a soft tau lepton and a jet from initial state radiation. *Phys. Rev. D* **94**(7), 073007 (2016)
 124. B. Dutta, S. Ghosh, A. Gurrola, D. Julson, T. Kamon, J. Kumar, Probing an MeV-Scale Scalar Boson in Association with a TeV-Scale Top-Quark Partner at the LHC. *JHEP* **03**(164) (2023)
 125. R. Arnowitt, B. Dutta, A. Gurrola, T. Kamon, A. Krislock, D. Toback, Determining the Dark Matter Relic Density in the Minimal Supergravity Stau-Neutralino Coannihilation Region at the Large Hadron Collider. *Phys. Rev. Lett.* **100**, 231802 (2008)
 126. B. Dutta, A. Gurrola, T. Kamon, A. Krislock, A.B. Lahanas, N.E. Mavromatos, D. V. Nanopoulos, Supersymmetry Signals of Super-critical String Cosmology at the Large Hadron Collider. *Phys. Rev. D* **79**, 055002 (2009)
 127. C. Avila, A. Flórez, A. Gurrola, D. Julson, S. Starko, Connecting Particle Physics and Cosmology: Measuring the Dark Matter Relic Density in Compressed Supersymmetry at the LHC. *Phys. Dark Univ.* **27**, 100430 (2020)
 128. B. Dutta, A. Gurrola, W. Johns, T. Kamon, P. Sheldon, K. Sinha, Vector Boson Fusion Processes as a Probe of Supersymmetric Electroweak Sectors at the LHC. *Phys. Rev. D* **87**, 035029 (2013)
 129. A. Delannoy, B. Dutta, A. Gurrola, W. Johns, T. Kamon, E. Luiggi, A. Melo, P. Sheldon, K. Sinha, K. Wang, S. Wu, Probing Dark Matter at the LHC using Vector Boson Fusion Processes. *Phys. Rev. Lett.* **111**, 061801 (2013)
 130. B. Dutta, T. Ghosh, A. Gurrola, W. Johns, T. Kamon, P. Sheldon, K. Sinha, S. Wu, Probing Compressed Sleptons at the LHC using Vector Boson Fusion Processes. *Phys. Rev. D* **91**, 055025 (2015)
 131. B. Dutta, W. Flanagan, A. Gurrola, W. Johns, T. Kamon, P. Sheldon, K. Sinha, K. Wang, S. Wu, Probing Compressed Top Squarks at the LHC at 14 TeV. *Phys. Rev. D* **90**, 095022 (2014)
 132. B. Dutta, W. Flanagan, A. Gurrola, W. Johns, T. Kamon, P. Sheldon, K. Sinha, K. Wang, S. Wu, Probing Compressed Bottom Squarks with Boosted Jets and Shape Analysis. *Phys. Rev. D* **92**, 095009 (2015)
 133. Paul Lujan The Pixel Luminosity Telescope: A detector for luminosity measurement at CMS using silicon pixel sensors. Technical Report CMS-DN-21-008, et al., Accepted by Eur (Phys. J. C., 2022)
 134. J. Butterworth, S. Carrazza, A. Cooper-Sarkar, A. De Roeck, J. Feltesse, S. Forte, J. Gao, S. Glazov, J. Huston, Z. Kassabov, R. McNulty, A. Morsch, P. Nadolsky, V. Radescu, J. Rojo, R. Thorne, PDF4LHC recommendations for LHC Run II. *J. Phys. G* **43**, 023001 (2016)
 135. A.M. Sirunyan et al., Identification of heavy-flavour jets with the CMS detector in pp collisions at 13 TeV. *JINST* **13**, P05011 (2018)



Probing light scalars and vector-like quarks at the high-luminosity LHC

U. S. Qureshi^{1,a}, A. Gurrola^{1,b}, A. Flórez^{2,c}, C. Rodriguez^{2,d}

¹ Department of Physics and Astronomy, Vanderbilt University, Nashville, TN, USA

² Physics Department, Universidad de los Andes, Bogotá, Colombia

Received: 30 October 2024 / Accepted: 15 March 2025

© The Author(s) 2025

Abstract A model based on a $U(1)_{T_R^3}$ extension of the Standard Model can address the mass hierarchy between generations of fermions, explain thermal dark matter abundance, and the muon $g - 2$, $R_{(D)}$, and $R_{(D^*)}$ anomalies. The model contains a light scalar boson ϕ' and a heavy vector-like quark χ_u that can be probed at CERN's large hadron collider (LHC). We perform a phenomenology study on the production of ϕ' and χ_u particles from proton–proton (pp) collisions at the LHC at $\sqrt{s} = 13.6$ TeV, primarily through $g-g$ and $t-\chi_u$ fusion. We work under a simplified model approach and directly take the χ_u and ϕ' masses as free parameters. We perform a phenomenological analysis considering χ_u final states to b-quarks, muons, and neutrinos, and ϕ' decays to $\mu^+\mu^-$. A machine learning algorithm is used to maximize the signal sensitivity, considering an integrated luminosity of 3000 fb^{-1} . The proposed methodology can be a key mode for discovery over a large mass range, including low masses, traditionally considered difficult due to experimental constraints.

1 Introduction

The Standard Model (SM) of particle physics, despite its successful account of numerous experimental findings involving strong, electromagnetic, and weak interactions, confirmed by CERN's large hadron collider (LHC) is regarded as a lower-energy manifestation of a more comprehensive theory. This perspective arises from unresolved questions regarding the origins of dark matter, electroweak symmetry breaking scales, lepton flavor universality, the anomalous muon mag-

netic moment [1–8], discrepancies in the $R_{(D)}$ and $R_{(D^*)}$ ratios from b-meson decays [9–21], as well as theoretical conundrums about whether gravity should be quantized, how gauge interactions can be unified, and the fine-tuning problem associated with the Higgs boson mass. Furthermore, the SM offers no explanation for fermion family replication nor for the lack of CP violation in the strong sector. These theoretical gaps, coupled with the experimental observation of phenomena such as neutrino masses, dark matter, and the baryon asymmetry in the universe, which cannot be explained by the SM, reinforce the expectation for physics beyond the SM (BSM).

As a result, several theoretical models have been put forth to address the limitations of the SM over the past decade. Despite differing theoretical motivations and resulting implications, a common thread among these ideas is the introduction of new particles, that, depending on the model, might be probed via proton–proton (pp) collisions at the LHC. A myriad of ideas have been suggested to investigate BSM physics, driving a substantial amount of exploration at the LHC. Said research has significantly limited the scope of theories and established exclusion bounds, extending to multi-TeV ranges for the masses of newly predicted particles within certain models [22–28]. Possible reasons for the absence of evidence could be attributed to new particle masses being at the scale where they are too large to be produced at the LHC energies and likely with exceptionally low production rates. In the scenario where the masses of the new particles might be probed at the LHC, a vast amount of data might be needed, together with advanced analysis techniques, to enhance the probability of detection. Alternatively, it is conceivable that new physics diverges from the conventional assumptions made in many BSM theories and the associated explorations. As a result, these new physics phenomena could remain hidden in processes that have not yet been thoroughly examined.

^a e-mail: umar.sohail.qureshi@vanderbilt.edu

^b e-mail: alfredo.gurrola@vanderbilt.edu

^c e-mail: ca.florez@uniandes.edu.co (corresponding author)

^d e-mail: c.rodriguez45@uniandes.edu.co

Minimal extensions to the SM, considering new $U(1)_\chi$ symmetry groups, are among the most studied BSM scenarios. For example, the $U(1)_{T_R^3}$ symmetry, where families of right-handed fermions of the SM and possible extensions, such as right-handed neutrinos, are charged, was originally studied in the context of left-right symmetry models [29–31]. In these studies, $U(1)_{T_R^3}$ is identified as the subgroup of $SU(2)_R$ defined by its diagonal (electric-charge neutral) generator, T_R^3 . In addition, it is often suggested that $U(1)_{T_R^3}$ is a subspecies of a $U(1)_{B-L}$ symmetry since the breaking of the $U(1)_{B-L} \times U(1)_{T_R^3}$ leads to the $U(1)_Y$ symmetry. This naturally motivates the presence of a massive and electrically neutral Z' gauge boson [32–36]. However, in the breaking of $U(1)_{B-L} \times U(1)_{T_R^3} \rightarrow U(1)_Y$, it follows that the Higgs doublet H , since it is a singlet of $U(1)_{B-L}$, acquires its hypercharge by inheritance from a charge under $U(1)_{T_R^3}$. Consequently, the vacuum expectation value (VEV) of H couples both symmetry-breaking scales for $U(1)_Y$ and $U(1)_{T_R^3}$. Alternatively, these symmetry-breaking scales can be decoupled by adding an additional $U(1)_G$ group where fermions of the SM are singlets and H is not. Therefore, the hypercharge comes from $U(1)_G$ for the H and from $U(1)_{T_R^3}$ for fermions, i.e. $Y = Q_{T_R^3} + \frac{1}{2}Q_{B-L} + Q_G$ [37]. Moreover, one can ask for scenarios where the hypercharge is not related to the $U(1)_{T_R^3}$ charge.

Recently, theoretical and phenomenological efforts have emerged around scenarios where the low-energy gauge symmetry of the SM is extended by appending the Abelian gauge group $U(1)_{T_R^3}$, whose spontaneous symmetry-breaking is not linked to the electroweak one [38–43]. In these scenarios, the gauge boson of $U(1)_{T_R^3}$ is associated with a massive dark photon A' whose longitudinal mode arises from a Higgs-like mechanism involving a complex scalar field, ϕ . This field is a singlet under the SM group, with its CP-odd component associated with the A' mass and the CP-even giving rise to a dark Higgs, ϕ' . To cancel gauge anomalies, a right-handed ν_R neutrino must be included for each generation of the SM that couples to $U(1)_{T_R^3}$. Furthermore, to correctly explain the origin of fermion masses in a UV-complete theory, a set of new vector-like quarks ($\chi_u, \chi_d, \chi_\ell, \chi_\nu$) must be included. These new particles are singlets under $U(1)_{T_R^3}$ and charged like SM right-handed fermions, as in the universal see-saw mechanism [44–49].

In this phenomenology study, we devise a LHC search strategy for the light GeV-scale scalar boson ϕ' produced in association with a heavy TeV-scale χ_u , the partner particle of the top quark, through a previously unexplored production and final state channel. Particularly, we explore the production of $pp \rightarrow t\chi_u\phi'$, in contrast to $pp \rightarrow TT \rightarrow t\phi't\phi'$ with hadronic [50–52] di-photon ϕ' [53, 54] decays. Due to the non-trivial $\chi - t - \phi'$ coupling, processes where the final state includes $t\chi_u\phi'$ are allowed in pp colliders through the $\chi_u - t$

fusion, see Fig. 1. Since the χ_u couples to SM quarks and gluons, it can be produced in large quantities. Furthermore, its energetic decay products can be detected alongside the ϕ' mediator particle that has significant transverse momentum. Therefore, if the ϕ' decays into SM particles that are observable in the detector's central region, this strategy can be very effective at reducing the SM background, and thus improve the long-term LHC discovery reach for heavy top partners and GeV-scale mediators, which are typically hard to detect using conventional methods at hadron colliders. Moreover, since it is possible to have $\chi_u \rightarrow t\phi'$ decays (and $\bar{\chi}_u \rightarrow \bar{t}\phi'$), the same $pp \rightarrow t\chi_u\phi'$ state may arise from $\chi_u\bar{\chi}_u$ production diagrams with quantum chromodynamic (QCD) vertices, where one χ_u decays to $t\phi'$, as shown in Fig. 2. As a consequence, the energetic products from $\chi_u\bar{\chi}_u$ decays can be readily detected, particularly when they occur alongside a mediator particle that carries substantial transverse momentum, providing greater sensitivity than that of searches where either χ_u or ϕ' are considered in isolation.

We probe the scenario where the scalar ϕ' has family non-universal fermion couplings, as was suggested in [39], and thus can address several issues with the SM. We focus on the ϕ' decay to a pair of muons since, at the experimental level, muons generally have high reconstruction and identification efficiencies, which allow for the development of relatively low $p_T(\mu)$ triggers, and provide clean signatures to remove the copious QCD multijet SM background. A key component of this study is the development of an analysis strategy utilizing a machine learning (ML) algorithm based on Boosted Decision Trees (BDT) [55]. The event classifier's output is employed to conduct a profile-binned likelihood test, which is used to determine the overall signal significance for each model examined in the analysis. The effectiveness of BDTs and other ML algorithms has been validated in numerous experimental and phenomenological studies [36, 56–65]. Our findings indicate that the BDT algorithm significantly enhances signal significance.

The rest of this paper is structured as follows. Section 3 discusses details of the minimal $U(1)_{T_R^3}$ model. Section 2 provides an overview of current relevant results at the LHC. Section 4 explains how the Monte Carlo (MC) simulation samples are produced for this study. In Sect. 5 we discuss the motivation and details of our machine learning workflow, and in Sect. 6, the main results are presented. We conclude with a short discussion in Sect. 7.

2 Experimental considerations

The ATLAS and CMS collaborations at CERN have conducted various searches for heavy vector-like quarks (T). These searches utilized pp collisions at center-of-mass energies of $\sqrt{s} = 8$ and 13 TeV. The studies primarily focused

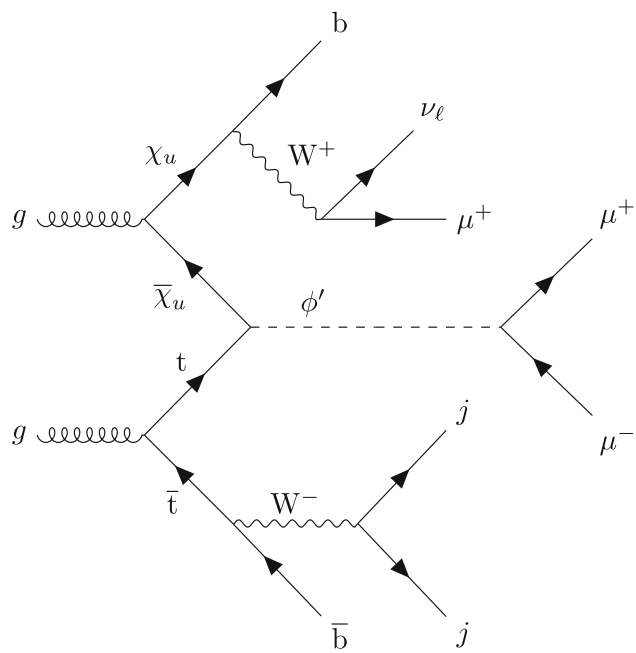


Fig. 1 Representative Feynman diagram for the production of a ϕ' boson in association with a χ_u vector-like quark through the fusion of a top quark and χ_u vector-like quark. Once again, the ϕ' decays to a pair of muons, the top quark decays fully hadronically, and the χ_u decays semi-leptonically to muons, neutrinos and b -jets

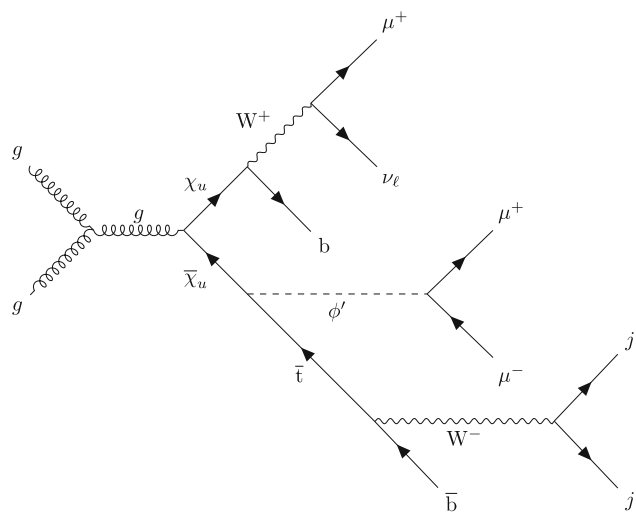


Fig. 2 Representative Feynman diagram for the production of a ϕ' boson in association with a χ_u vector-like quark through the fusion of a gluon pair from incoming protons. The ϕ' decays to a pair of muons, the top quark that decays fully hadronically, and the χ_u decay semi-leptonically to muons, neutrinos and jets

on T production through gluon-mediated QCD processes, either in pair production from quark-antiquark annihilation (Fig. 3) or in single-T production from electroweak processes involving associated quarks (Fig. 4).

In those studies, T decays into bW , tZ , or tH have been considered. In the context of T pair production, $T\bar{T}$, via

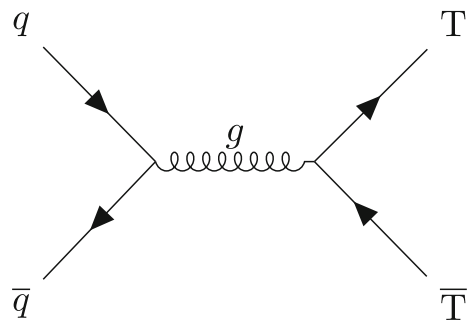


Fig. 3 Representative Feynman diagram for T pair production via gluon-mediated QCD processes

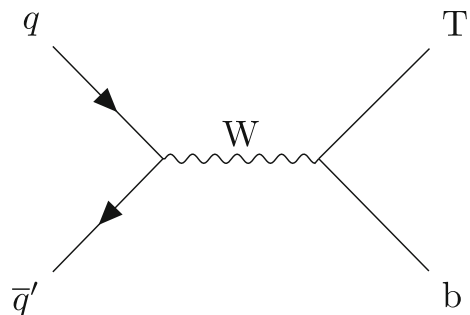


Fig. 4 Representative Feynman diagram for single T production via electroweak processes

QCD processes, the cross sections are well-known and solely depend on the mass of the vector-like quark. Assuming a narrow T decay width ($\Gamma/m(T) < 0.05$ or 0.1) and a 100% branching fraction to bW , tZ , or tH , these searches have set stringent bounds on $m(T)$, excluding masses below almost 1.5 TeV at 95% confidence level [66–73]. The most recent analysis from the CMS collaboration probes T-quark production via $pp \rightarrow Tqb$, in final states with $T \rightarrow tZ$ or $T \rightarrow tH$, considering scenarios with preferential couplings to third-generation fermions. The analysis sets 95% confidence level upper limits of 68–1260 fb on the production cross section, for T masses ranging from 600–1200 GeV [67]. The latest studies from ATLAS probe vector-like quarks using the single-T production mode with the $T \rightarrow tH$ decay channel leading to a fully hadronic final state [68], the single-T production mode with the $T \rightarrow tZ$ decay channel leading to a multileptonic final state [69], the TT pair production mode with various T decay channels leading to multileptonic final states [70], and the TT pair production mode with various T decay channels leading to a single lepton plus missing momentum final state [71, 72]. The multilepton search offers the greatest sensitivity in most of the phase space, but the missing transverse energy based search has better sensitivity for low branching fraction $\mathcal{B}(T \rightarrow Wb)$ and high $\mathcal{B}(T \rightarrow Ht)$. These searches have similar sensitivities for the singlet and doublet models, resulting in exclusion bounds for masses below about 1.25 TeV and 1.41 TeV, respectively.

A key consideration in the model interpretations summarized above is that the T branching fractions depend on the chosen model. The excluded mass range is less restrictive for specific branching fraction scenarios, such as $\{\mathcal{B}(T \rightarrow tZ), \mathcal{B}(T \rightarrow bW), \mathcal{B}(T \rightarrow tH)\} = \{0.2, 0.6, 0.2\}$, excluding masses below about 0.95 TeV. Moreover, if the $T \rightarrow \phi't$ decay is allowed, or if the branching fractions $\mathcal{B}(T \rightarrow tH/bW)$ are lower, the limits previously quoted must be re-evaluated. The authors of Ref. [74] emphasize that bounds on $m(T)$ can be around 500 GeV when $T \rightarrow t\phi'$ decays are permitted. Therefore, to facilitate a comprehensive study, benchmark scenarios in this paper are considered down to $m(\chi_u) = 500$ GeV.

3 The minimal $U(1)_{T_R^3}$ model

3.1 Scalar potential

In this model, the SM is extended by the Abelian gauge symmetry $U(1)_{T_R^3}$, where only right-handed fermions are charged. We assume two independent Higgs mechanisms, one with a Higgs doublet H for electroweak symmetry breaking and the other with a Higgs singlet ϕ for the $U(1)_{T_R^3}$ symmetry breaking. Both scalars have independent vacuum expectation values (VEVs), $\langle H \rangle = v_h/\sqrt{2}$ and $\langle \phi \rangle = v_\phi/\sqrt{2}$, allowing us to express the doublet and singlet Higgs fields, following a Kibble parametrization, as

$$H = \begin{pmatrix} G_+ \\ \frac{1}{\sqrt{2}}(v_h + \rho_0 + iG_0) \end{pmatrix} \quad (1)$$

$$\phi = \frac{1}{\sqrt{2}}(v_\phi + \rho_\phi + iG_\phi). \quad (2)$$

In Eqs. (1) and (2), G_\pm , G_0 , and G_ϕ are the Goldstone bosons that allow the SM W^\pm and Z bosons and the dark photon A' , associated with the $U(1)_{T_R^3}$ symmetry, to acquire mass. The ρ_h and ρ_ϕ are an orthogonal mixture of the SM Higgs boson and the dark Higgs

$$\begin{pmatrix} h \\ \phi' \end{pmatrix} = \begin{pmatrix} \cos \alpha & -\sin \alpha \\ \sin \alpha & \cos \alpha \end{pmatrix} \begin{pmatrix} \rho_0 \\ \rho_\phi \end{pmatrix}, \quad (3)$$

that results from the diagonalization of the mass matrices arising from the gauge invariant potential

$$\begin{aligned} \mathcal{V}(\phi, H) = & \mu_H^2 H^\dagger H + \mu_\phi^2 \phi^* \phi \\ & + \lambda (H^\dagger H)(\phi^* \phi) + \lambda_H (H^\dagger H)^2 + \lambda_\phi (\phi^* \phi)^2. \end{aligned} \quad (4)$$

The tadpole equations are given from the minimization of the potential as

$$\frac{\partial \mathcal{V}}{\partial H} = \frac{v_h}{\sqrt{2}} \left(\mu_H^2 + \lambda_H v_h^2 + \frac{1}{2} \lambda v_\phi^2 \right) = 0, \quad (5)$$

$$\frac{\partial \mathcal{V}}{\partial \phi} = \frac{v_\phi}{\sqrt{2}} \left(\mu_\phi^2 + \lambda_\phi v_\phi^2 + \frac{1}{2} \lambda v_h^2 \right) = 0. \quad (6)$$

The masses of the scalar bosons can be written as

$$\begin{aligned} m_{h,\phi'}^2 = & \frac{1}{2} \left(\lambda_H v_h^2 + \lambda_\phi v_\phi^2 \right) \\ & \pm \sqrt{\lambda^2 v_h^2 v_\phi^2 + \left(\lambda_H v_h^2 - \lambda_\phi v_\phi^2 \right)^2}, \end{aligned} \quad (7)$$

and the mixing angle α as

$$\tan \alpha = \frac{-\lambda v_h v_\phi}{\lambda_H v_h^2 - \lambda_\phi v_\phi^2 - \sqrt{\lambda^2 v_h^2 v_\phi^2 + \left(\lambda_H v_h^2 - \lambda_\phi v_\phi^2 \right)^2}}. \quad (8)$$

3.2 The universal seesaw mechanism

In the model, each electrically charged SM fermion f has a mass protected by both VEVs. In turn, they acquire mass from the mixture with a vector-like fermion χ_f , which is charged as the right-handed component of the respective SM fermion, in a UV complete theory. The terms in the Lagrangian density that contribute to the mass of physical fermions are,

$$\begin{aligned} -\mathcal{L} \supset & Y_{f_L} \bar{f}'_L \chi'_{fR} H + Y_{f_R} \bar{\chi}'_{fL} f'_R \phi^* + m_{\chi'_f} \bar{\chi}'_{fL} \chi'_{fR} \\ & + \text{h.c.} \end{aligned} \quad (9)$$

Therefore, in the vacuum, the mass matrix is

$$M_f = \begin{pmatrix} 0 & Y_{f_L} v_h / \sqrt{2} \\ Y_{f_R} v_\phi / \sqrt{2} & m_{\chi'_f} \end{pmatrix}. \quad (10)$$

The left- and right-handed components of the physical fermions (f , χ_f) are given by two rotations $\mathcal{R}(\theta_{f_{L,R}})$ as,

$$\begin{pmatrix} f_{L,R} \\ \chi_{f_{L,R}} \end{pmatrix} = \begin{pmatrix} \pm \cos \theta_{f_{L,R}} & \mp \sin \theta_{f_{L,R}} \\ \sin \theta_{f_{L,R}} & \cos \theta_{f_{L,R}} \end{pmatrix} \begin{pmatrix} f'_{L,R} \\ \chi'_{f_{L,R}} \end{pmatrix}, \quad (11)$$

in a way that $\mathcal{R}(\theta_{f_L}) M_f \mathcal{R}^{-1}(\theta_{f_R}) = \text{diag}(m_f, m_{\chi_f})$ up to a phase. Assuming real parameters, the physical masses and the mixing angles are given by

$$m_f m_{\chi_f} = \frac{(Y_{f_L} v_h)(Y_{f_R} v_\phi)}{2}, \quad (12)$$

$$m_f^2 + m_{\chi_f}^2 = m_{\chi'_f}^2 + \frac{1}{2} \left(Y_{f_L}^2 v_h^2 + Y_{f_R}^2 v_\phi^2 \right), \quad (13)$$

$$\tan \theta_{f_{L,R}} = \frac{\sqrt{2}}{m_{\chi'_f}} \left(\frac{Y_{f_{L,R}} v_{h,\phi}}{2} - \frac{m_f^2}{Y_{f_{L,R}} v_{h,\phi}} \right). \quad (14)$$

The Yukawa interactions of the physical fermions with the scalar bosons have the form

$$-\mathcal{L}_{\text{yuk}} = h \bar{\psi}_{f_L} \mathcal{Y}_h \psi_{f_R} + \phi' \bar{\psi}_{f_L} \mathcal{Y}_\phi \psi_{f_R}, \quad (15)$$

with $\psi_f = (f, \chi_f)^T$, and the matrices $\mathcal{Y}_{f_{L,R}}$ given by

$$\mathcal{Y}_h = \frac{1}{\sqrt{2}} \mathcal{R}(\theta_{f_L}) (Y_{f_L} \sigma_+ \cos \alpha - Y_{f_R} \sigma_- \sin \alpha) \mathcal{R}^{-1}(\theta_{f_R}) \quad (16)$$

$$\mathcal{Y}_\phi = \frac{1}{\sqrt{2}} \mathcal{R}(\theta_{f_L}) (Y_{f_L} \sigma_+ \sin \alpha + Y_{f_R} \sigma_- \cos \alpha) \mathcal{R}^{-1}(\theta_{f_R}), \quad (17)$$

where $\sigma_\pm = (\sigma_1 \pm i \sigma_2)/2$ are the ladder Pauli matrices.

3.3 Minimal UV-complete theory

The model must provide non-zero masses for all the SM fermions and be free of gauge anomalies. So, we must have at least one full generation of vector-like fermions $\{\chi_u, \chi_d, \chi_\ell, \chi_v\}$ and the right-handed component of the SM neutrinos, ν_R , charged as shown in Table 1. Therefore, the Yukawa interactions in the UV-complete theory must be of the form

$$\begin{aligned} -\mathcal{L} \supset & Y_{Lu}^i \bar{q}_L^i \chi'_{uR} \tilde{H} + Y_{Ru}^i \bar{\chi}'_{uL} u_R^i \phi^* + m_{\chi_u} \bar{\chi}'_{uL} \chi'_{uR} \\ & + Y_{Ld}^i \bar{q}_L^i \chi'_{dR} H + Y_{Rd}^i \bar{\chi}'_{dL} d_R^i \phi + m_{\chi_d} \bar{\chi}'_{dL} \chi'_{dR} \\ & + Y_{L\ell}^i \bar{\ell}_L^i \chi'_{\ell R} H + Y_{R\ell}^i \bar{\chi}'_{\ell L} \ell_R^i \phi + m_{\chi_\ell} \bar{\chi}'_{\ell L} \chi'_{\ell R} \\ & + Y_{Lv}^i \bar{\ell}_L^i \chi'_{vR} \tilde{H} + Y_{Rv}^i \bar{\chi}'_{vL} \nu_R^i \phi^* + m_{\chi_v} \bar{\chi}'_{vL} \chi'_{vR} \\ & + \text{h.c.}, \end{aligned} \quad (18)$$

where the i index runs over the three generations of fermions. The simultaneous diagonalization of the mass matrices of each fermion sector will have a similar structure to the one presented in Eqs. (12) and (13) and the Yukawa matrices will have a similar structure of Eqs. (16) and (17) but codifying the CKM matrix. For the neutrino sector, the structure of the mass matrix will be more complex due to the presence of the additional Majorana mass term for the vector-like neutrino χ'_v .

Table 1 Minimal field content of the model and their representations under the SM and $U(1)_{T_R^3}$ gauge groups

Field	$SU(3)_C$	$SU(2)_L$	$U(1)_Y$	$U(1)_{T_R^3}$
q'_L	3	2	1/6	0
ℓ'_L	1	2	-1/2	0
H	1	2	1/2	0
u'^c_R	3	1	-2/3	-2
d'^c_R	3	1	1/3	2
ℓ'^c_R	1	1	1	2
ν'^c_R	1	1	0	-2
ϕ	1	1	0	2
χ'_{uL}	3	1	2/3	0
χ'^c_{uR}	3	1	-2/3	0
χ'_{dL}	3	1	-1/3	0
χ'^c_{dR}	3	1	1/3	0
$\chi'_{\ell L}$	1	1	-1	0
$\chi'^c_{\ell R}$	1	1	1	0
χ'_{vL}	1	1	0	0
χ'^c_{vR}	1	1	0	0

The numbers in bold indicate the dimensional representation under $SU(2)_L$ and $SU(3)_C$ in which the field transforms

4 Samples and simulation

The minimal $U(1)_{T_R^3}$ model described in Sect. 3 is implemented into the `FeynRules` package [75], which generates the Feynman rules and exports them into a Universal `FeynRules Output` (`UFO`) [76]. The resulting `UFO` is utilized as input for a generator to produce the MC samples. Both signal and background events are generated with the `MadGraph5_aMC@NLO` v3.2.0 program [77, 78] at leading order (LO) in QCD, considering pp beams colliding with a center-of-mass energy of $\sqrt{s} = 13.6$ TeV. Each signal and background sample is generated separately, with no interference effects between the signal and background considered. The impact of these interference effects has been evaluated, and for all values of χ_u and ϕ' masses considered, the effect on the signal plus background cross section is found to be less than $< 0.5\%$. Additionally, the effect on the shape of the b-jet p_T distribution is less than 6% for $p_T < 300$ GeV and less than 2% for b-jet $p_T > 300$ GeV. We use the `NNPDF3.0 NLO` [79] set for parton distribution functions (PDFs) for all event generation. Parton-level events are then interfaced with `PYTHIA` (v8.2.44) [80] to account for parton showering and hadronization processes. Finally, we use `DELPHES` (v3.4.2) [81] to simulate smearing and other detector effects using the CMS detector geometric configurations and parameters for particle identification and reconstruction, using the CMS input card with 140 average pileup interactions. All signal cross sections used

in this analysis are obtained requiring the following kinematic criteria on leptons (ℓ), b quarks, and light-quark/gluon jets (j) at parton level in MadGraph: $p_T(\ell) > 35$ GeV, $|\eta(b)| < 2.5$, $|\eta(\ell)| < 2.3$, $p_T(j) > 20$ GeV, and $|\eta(j)| < 5$. These parton-level selections were applied exclusively to the signal processes to restrict event generation to the relevant phase space regions. For background processes, these default parton level requirements in MadGraph were imposed: $p_T(\ell) > 10$ GeV, $|\eta(\ell)| < 2.5$, $p_T(j) > 20$ GeV, $|\eta(j)| < 5$, and $|\eta(b)| < 5$. This ensures that the phase space regions for the background near the analysis-level selection criteria are adequately described after parton showering since the pre-selections at the analysis level are more stringent than the parton-level requirements. Furthermore, we use the MLM algorithm for jet matching and jet merging. The parameters $x_{q\bar{q}cut}$ and $qcut$ of the MLM algorithm are set to 30 and 45 respectively to ensure continuity of the differential jet rate as a function of jet multiplicity. Each simulated signal and background sample is produced separately at LO, with one million events at the generation level, neglecting potential interference effects between the signal and background due to the suppression caused by the different orders of magnitude in the coupling constants of the signal and background.

Signal samples are generated considering the production of a ϕ' boson, an associated χ_u vector-like quark, and a top quark ($pp \rightarrow \chi_u t \phi'$), inclusive in both α and α_s (see Figs. 1 and 2). We have used the implementation of the $U(1)_{T_R^3}$ model in Ref. [43]. Signal samples were created considering coupling values of $Y_{t_R} = Y_L = 2\sqrt{2}$ in the range of masses $m(\phi') \in \{5, 10, 50, 100, 325\}$ GeV for the dark higgs and $m(\chi_u) \in \{0.50, 0.75, 1.0, 1.5, 2.0, 2.5\}$ TeV for the vector-like quark χ_u [82]. The production cross section for $pp \rightarrow \chi_u t \phi'$ is highly dependent on the choice of the Yukawa couplings in the Lagrangian. The χ_u-t fusion process shown in Fig. 1 is dominated by the Y_{t_R} coupling. However, the decay $\chi_u \rightarrow t \phi'$ shown in Fig. 2 is inversely proportional to the Y_{t_L} coupling. This effect is shown in Fig. 5, which displays the total signal cross section, as a function of Y_{t_R} and Y_{t_L} , for a benchmark point with $m(\phi') = 100$ GeV and $m(\chi_u) = 1.0$ TeV.

We target signal events where the top quark decays hadronically into a bottom quark and two jets ($t \rightarrow bW \rightarrow bqq\bar{q}'$), the χ_u decays semileptonically into a b quark, lepton, and neutrino (via $\chi_u \rightarrow bW$ and $W \rightarrow \mu\nu_\mu$), and the ϕ' produces two muons. We note that the scalar ϕ' particle could result from the mixture of the SM Higgs boson and additional scalar fields, and the Yukawas of the fermions could additionally arise from the mixing of the SM fermions with additional copies of the associated vector-like fermions. Therefore, the ϕ' branching ratios are dependent on the chosen mechanism and model by which this mixture occurs, see for example, Refs. [83–86]. For the purpose of this work, and similar to Refs. [39, 43], the considered bench-

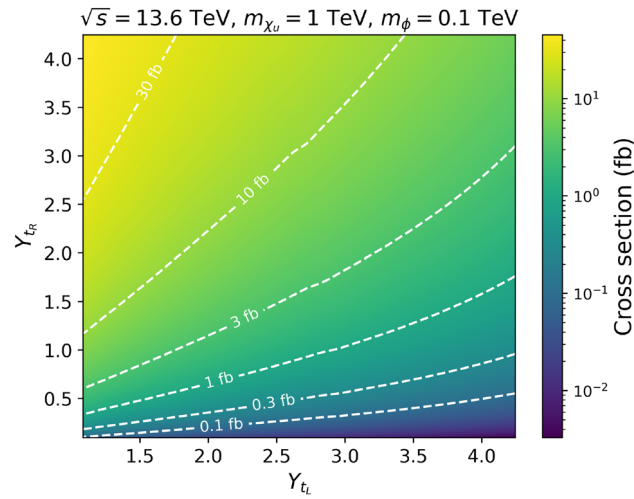


Fig. 5 Signal production cross section, $pp \rightarrow \chi_u t \phi'$, in the Y_{t_R} versus Y_{t_L} plane, for a benchmark point with $m(\phi') = 100$ GeV and $m(\chi_u) = 1.00$ TeV. The white-dashed contours show specific cross section values in the two dimensional plane

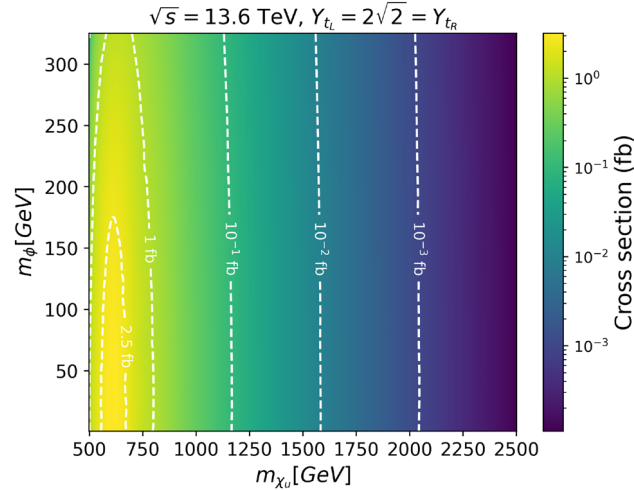


Fig. 6 Projected cross section (fb) plot for $pp \rightarrow t \chi_u \phi'$ and subsequent decay as a function of $m(\chi_u)$ and $m(\phi')$

mark signal scenarios have $\mathcal{B}(\chi_u \rightarrow b W)$ of about 0.5 and $\mathcal{B}(\phi' \rightarrow \mu^+ \mu^-) = 0.98$. Figure 6 shows the production cross section in fb, as a function of $m(\phi')$ and $m(\chi_u)$ masses, assuming the aforementioned decays, branching ratios, and couplings.

We note that for the parameter space of focus in this paper, the total mass of the $t-\chi_u$ system is larger than $m(\phi')$, thus the large rest energy of the $t-\chi_u$ system is converted into potentially large momentum values for the ϕ' . Similarly, the t -quark produced through the χ_u-t fusion interaction can also have large momentum values, and thus in some cases the hadronic t decay products cannot be fully reconstructed independently of each other. This results in three possible t reconstruction scenarios: a fully merged scenario where the

$W \rightarrow jj$ system and the b quarks are very collimated and reconstructed as a single “fat jet” (henceforth referred to as a FatJet, FJ); a partially merged scenario, where the decay products of the W boson form a single FatJet but the b quark can still be separately identified; and an un-merged scenario where all decay products can be independently identified. Jets are clustered using the anti- k_t algorithm [87] using the FastJet (v3.4.2) [88] package with a distance parameter of $R = 0.4$ for standard jets and $R = 0.8$ for fat jet objects. Each scenario has an associated identification efficiency and misidentification rate, which depends on the choice of the boosted t/W algorithm (our choice of efficiency and misidentification rates is described later).

Based on the above details, the final state of interest in this paper consists of three muons (two from the ϕ' decay and one from the χ_u decay), a (possibly boosted) top-tagged system, at least one b -tagged jet, and large missing transverse momentum (\vec{p}_T^{miss}). For the partially merged and un-merged scenarios, there will be two b quarks present in the final state (one of which is part of the top tagged system).

We consider background sources from SM processes which can give similar objects in the final state as those expected for signal. Several background sources were considered and studied, such as QCD multijet events, production of vector boson pairs (VV : WW, ZZ, WZ), vector boson triplets (VVV : WWZ, WZZ, ZZZ, WWW), top-quark pairs in association with weak bosons ($t\bar{t}X$), and $t\bar{t}\bar{t}\bar{t}$ processes. The dominant sources of SM background events are from the $t\bar{t}X$, ZZW, and $t\bar{t}\bar{t}\bar{t}$ processes. The $t\bar{t}X$ background is primarily associated production of a Z/γ^* from $t\bar{t}$ fusion processes. The ZZW process becomes a background when one Z decays $b\bar{b}$, another Z decays to a pair of muons, and the W decays to a muon and a neutrino. Events from ZZW and $t\bar{t}\bar{t}\bar{t}$ have been combined, after being weighted by their corresponding production cross section. The combination is presented as the “ $b\bar{b}\mu\mu\nu\nu$ ” background in the remainder of this paper. The $t\bar{t}X$ process is presented as part of the “ $t\bar{t}\mu^+\mu^-$ ” background. Table 2 shows the production cross sections for the dominant background sources. The rest of the aforementioned background processes do not contribute meaningfully in our context, accounting for $\ll 1\%$ of the total expected background yield.

The identification of leptons, boosted top quarks, and bottom quarks plays an important role in the ability to identify signal events, the ability to minimize the rate of SM backgrounds, and thus also the discovery reach in the high-luminosity environment of the LHC. It is worth noting that the reconstruction and identification of leptons and the decay products of the top/bottom quarks may be non-trivial at the High-Luminosity LHC (HL-LHC) due to the presence of a potentially large number of secondary pp interactions (pileup). The impact of pileup on the new physics discovery reach, and the importance of pileup mitigation at CMS

Table 2 A summary of dominant SM backgrounds produced by pp collisions and their cross sections in pb, as computed by MadGraph with $n = 10^6$ events

Background process	Cross-section σ [pb]
$pp \rightarrow t\bar{t} \mu^+ \mu^-$	2.574×10^{-3}
$pp \rightarrow b\bar{b} \mu\mu\nu\nu$	4.692×10^{-4}

and ATLAS has been outlined in many papers, for example in Ref. [89]. We note the expected performance of the upgraded ATLAS and CMS detectors for the HL-LHC is beyond the scope of this work; however, the studies presented here do attempt to provide reasonable expectations by conservatively assuming some degradation in lepton and hadron identification efficiencies, using Ref. [89] as a benchmark, and considering the case of 140 average pileup interactions.

For muons with $|\eta| < 1.5$, the assumed identification efficiency is 95% with a 0.3% misidentification rate [89, 90]. The performance degrades linearly with η for $1.5 < |\eta| < 2.5$, and we assume an identification efficiency of 65% with a 0.5% misidentification rate at $|\eta| = 2.5$. Similarly, the charged hadron tracking efficiency, which contributes to the jet clustering algorithm and missing transverse momentum (\vec{p}_T^{miss}) calculation, is 97% for $1.5 < |\eta| < 2.5$, and degrades to about 85% at $|\eta| = 2.5$. These potential inefficiencies due to the presence of secondary pp interactions contribute to how well the lepton and top kinematics can be reconstructed. Following Refs. [91, 92], we consider the “Loose” working point for the identification of the fully merged (partially merged) t decays, which results in 80–85% top (W) identification efficiency and 11–25% misidentification rate, depending on the FatJet transverse momentum (p_T^{FJ}). Following Ref. [93], we consider the “Loose” working point of the DeepCSV algorithm [94], which gives a 70–80% b-tagging efficiency and 10% light quark mis-identification rate. The choice of boosted t/W and b-tagging working points is determined through an optimization process that maximizes discovery reach. It is noted the contribution from SM backgrounds with a misidentified boosted t/W is negligible, and thus our discovery projections are not sensitive to uncertainties related to the boosted t/W misidentification rates (Fig. 7).

5 Data analysis using machine learning

The analysis of signal and background events is performed utilizing machine learning techniques. A machine learning-based approach offers sizeable advantages when compared to traditional event classification techniques. Unlike conventional methods, machine learning models have the capability to simultaneously consider all kinematic variables, allowing them to efficiently navigate the complex and

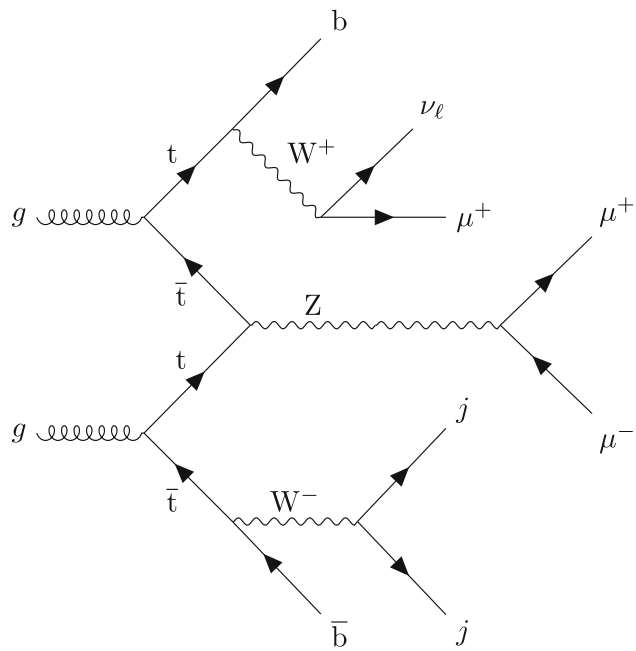


Fig. 7 Representative Feynman diagram for a background event. A Z boson is produced in association with a top quark through the fusion of a top, anti top pair from incoming protons. The Z boson subsequently decays to a pair of muons and the two spectator top quarks decay semi-leptonically and purely hadronically to muons, neutrinos and jets, resulting in the same final states as the signal event

high-dimensional space of event kinematics. Consequently, machine learning models can effectively enact sophisticated selection criteria that take into account the entirety of this high-dimensional space. This makes them ideal for high-energy physics applications.

The BDT method is a powerful machine learning technique that has proven its effectiveness in various applications, particularly in the field of collider physics. In this method, decision trees are trained greedily in a sequential manner, with each tree focusing on learning the discrepancies or residuals between its predictions and the expected values obtained from the previously trained tree. This iterative process aims to progressively minimize errors, making BDTs a particularly effective approach for enhancing model performance.

In the context of collider physics, BDTs have demonstrated their utility in addressing classification problems. In particular, BDTs can effectively discriminate between signal and background events, enabling accurate and efficient event classification. Their ability to handle subtle non-linear relationships within the data with high interpretability makes BDTs a valuable tool to handle large amounts of data with a large number of parameters for each event.

The first step in our workflow involves the use of a specialized *MadAnalysis Expert Mode C++* script [95]. This script extracts essential kinematic and topological information from the simulated samples. The script will process the aforementioned variables contained within these

files and transform them into a structured and informative CSV (Comma-Separated Values) format that can be used to train our machine learning models. These kinematic variables include crucial details about the events, such as particle momenta, energies, and topologies, providing the fundamental building blocks for our machine learning analysis. Figure 13 shows the features that are used for training the machine learning models and their importance for a benchmark point.

To account for the differential significance of various events, we apply cross-section weighting. This ensures that the relative importance of signal and background events is appropriately balanced in the dataset. This weighting is crucial for addressing the varying likelihood of observing different types of events in high-energy physics experiments. The prepared and weighted datasets are then passed to our *MadAnalysis Expert Mode C++* script, where the simulated signal and background events are initially filtered, before being passed to the CSV file for use by the machine learning algorithm. The filtering process requires at least one well-reconstructed and identified b -jet candidate, at least one jet (regular or FJ) not tagged as a b jet, and exactly three identified muons. The filtering selections are motivated by experimental constraints, such as the geometric constraints of the CMS/ATLAS detectors, the typical kinematic thresholds for the reconstruction of particle objects, and the available lepton triggers which also drive the minimal kinematic thresholds. Selected jets must have $p_T > 30 \text{ GeV}$ and $|\eta(j)| < 5.0$, while b -jet candidates with $p_T > 20 \text{ GeV}$ and $|\eta(b)| < 2.5$ are chosen. The μ object must pass a $p_T > 35 \text{ GeV}$ threshold and be within a $|\eta(\ell)| < 2.3$. We will refer to this filtering criteria as pre-selections. The efficiency of the pre-selections depends on $m(\phi')$ and $m(\chi_u)$, but is typically about 25–30% for the signal samples. Events passing this pre-selection are used as input for the machine learning algorithm, which classifies them as signal or background, using a probability factor.

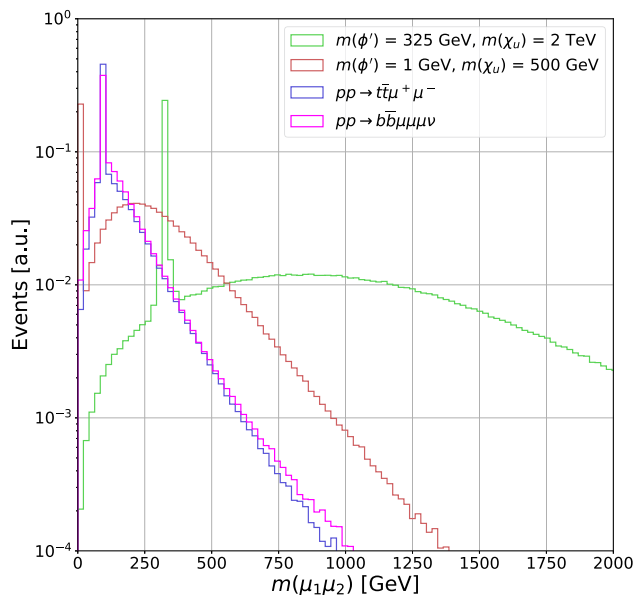
We explore the performance of a diverse set of machine learning models, specifically three neural networks of differing architectures and a BDT algorithm. To ensure robust model assessment, we employed a standard 90–10 train-test split of the dataset, partitioning it into a 90% portion for training and a 10% portion for testing. This division allows us to gauge the generalization capabilities of our models on unseen data.

The training and evaluation of the BDT were carried out in a high-performance computing environment. Specifically, an Nvidia A100 GPU was used. The canonical PyTorch [96] deep learning framework was employed for configuring, training, and evaluating the neural networks. PyTorch is well-regarded for its flexibility and performance in deep learning applications.

For the BDT algorithm, we used hyperparameters $\eta = 0.3$, $\gamma = 0$, and $\text{max_depth} = 6$. The XGBoost [97]

Table 3 Train/test results for the ML models

Model	Train/test acc.	Training time
BDT	N.A./0.9993	6s
Neural network 1	0.9999/0.9997	1 h 58 min
Neural network 2	0.9999/0.9998	2 h 12 min
Neural network 3	0.9999/0.9998	2 h 32 min

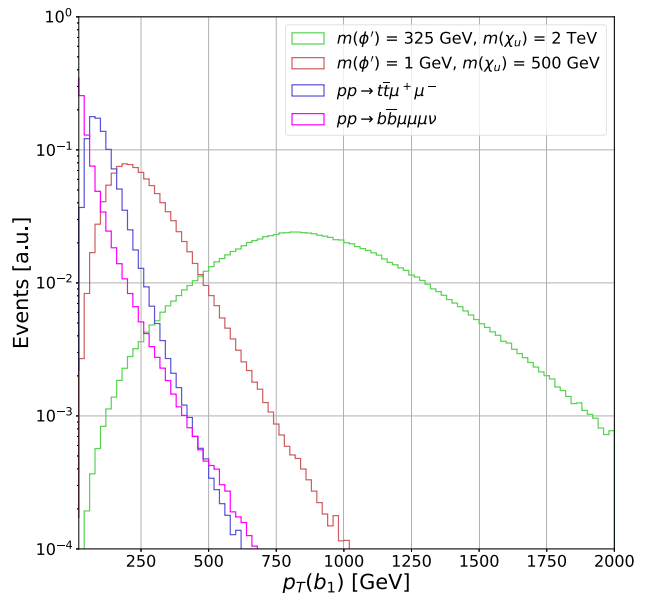
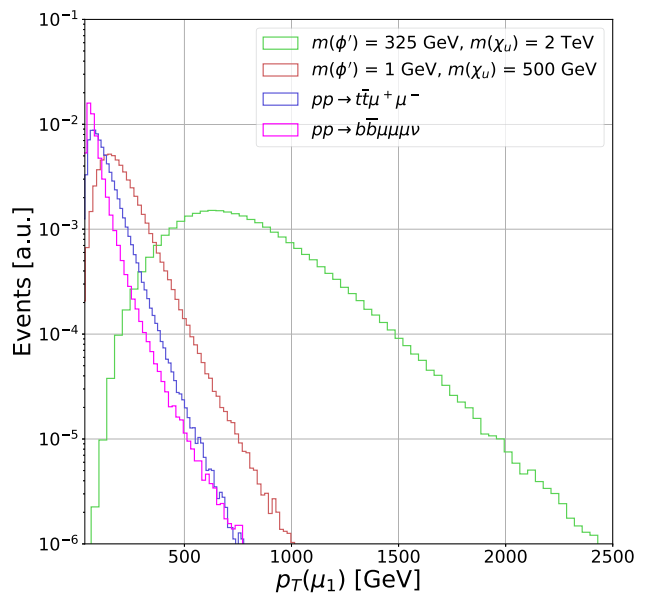
**Fig. 8** Invariant mass distribution of the muon pair with the highest and second highest transverse momentum. The distributions are shown for the two main SM background processes and two signal benchmark points

library was used for the implementation of the Boosted Decision Tree algorithm. It offers high efficiency, optimization, and interpretability, making it a suitable choice for this particular task (Table 3).

It is worth mentioning that we experimented with deep neural networks of various architectures. Although we found that they yield similar signal sensitivity to the BDT, the complex nature of the studies in this work (particle objects considered, experimental constraints in a high luminosity LHC, etc.) motivates the use of a BDT over a deep neural network because of its usefulness, efficiency, and simplicity in understanding the machine learning output in addition to significantly shorter training times. Therefore, we perform our proceeding analysis using the BDT. The outcomes of our model training and evaluation are presented in Table 3.

6 Results

Figures 8, 9, and 10 show relevant kinematic distributions for two benchmark signal points and the dominant SM back-

**Fig. 9** Transverse momentum distribution of the leading b-quark jet candidate. The distributions are shown for the two main SM background processes and two signal benchmark points**Fig. 10** Transverse momentum distribution of the leading muon candidate. The distributions are shown for the two main SM background processes and two signal benchmark points

grounds, using the subset of events passing the pre-selections defined above. The signal benchmark points in these figures are $m(\phi') = 325 \text{ GeV}, m(\chi_u) = 2 \text{ TeV}$, and $m(\phi') = 1 \text{ GeV}, m(\chi_u) = 500 \text{ GeV}$. The distributions are normalized such that the area under the curve is unity. These distributions correspond to the reconstructed mass, $m(\mu_1, \mu_2)$, between the two muon candidates with the highest transverse momentum (μ_1 and μ_2), the transverse momentum of the b-jet can-

dicate with the highest transverse momentum p_T (b_1), and the muon candidate with the highest transverse momentum p_T (μ_1), respectively. These distributions are among the variables identified by the BDT algorithm with the highest signal to background discrimination power (see Fig. 13).

As can be seen from Fig. 8, the ϕ' mass can be reconstructed through its associated muon decay pair, which is observed as a peak in the $m(\mu_1, \mu_2)$ distribution around the expected $m(\phi')$ value, and has low- and high-mass tails which are a consequence of cases where the leading and/or sub-leading muon is not from the ϕ' decay, but rather from the associated W boson from the χ_u decay. For the backgrounds, muons come from Z (W) decays. Therefore, the $m(\mu_1, \mu_2)$ background distributions show a peak near $m_{W/Z}$, combined with a broad distribution indicative of the combination of two muon candidates from different decay vertices. We note that the $\phi' \rightarrow \mu^+ \mu^-$ decay width depends on the square of the $\phi' \rightarrow \mu^+ \mu^-$ coupling and $\frac{m_\mu^2}{m(\phi')^2}$ and is thus suppressed by the relatively small muon mass. For the new physics phase space considered in this paper, the ϕ' decay width is less than 1% of the ϕ' resonant mass. Furthermore, as indicated previously, the signal/background interference effects are small and negligible compared to effects from experimental resolution. Therefore, the width of the $m(\mu_1, \mu_2)$ signal distributions is driven by the experimental resolution in the reconstruction of the muon momenta, as well as the probability that the two leading muons are the correct pair from the ϕ' decay. Since the probability that the two highest- p_T muons are the correct pair from the $\phi' \rightarrow \mu^+ \mu^-$ decay depends on $m(\phi')$ and $m(\chi_u)$, it is important to include all possible combinations of dimuon pairs (i.e., $m(\mu_1, \mu_3)$ and $m(\mu_2, \mu_3)$) in the training of the BDT.

Figure 9 shows the distribution for the b-jet candidate with the highest p_T , $p_T(b_1)$, for the same simulated samples shown in Fig. 8. Based on the signal topology and our choice of parameter space (i.e., $m(\chi_u) > m_t$), it is expected that the leading b-jet candidate comes from the χ_u decay, with an average p_T close to $\frac{m(\chi_u) - m_W}{2}$, as observed in Fig. 9. For the $t\bar{t}\mu^+ \mu^-$ background, the b-jet candidates come from top-quark decays. Therefore, their average transverse momentum is expected to be $\frac{m_t - m_W}{2} \approx 45$ GeV, as observed in Fig. 9. On the other hand, the b-jet candidates for the $bb\bar{\mu}\mu\mu\nu$ background can come from off-mass-shell Z^*/γ^* , and thus typically have an even softer spectrum in comparison to the $t\bar{t}\mu^+ \mu^-$ background.

Figure 10 shows the distribution for the muon candidate with the highest p_T , $p_T(\mu_1)$. Similar to Fig. 9, when $m(\chi_u) > m_t$ it is expected that the leading muon candidate comes from the χ_u decay, with an average p_T of approximately $\frac{m(\chi_u) - m_W}{4}$, as observed in Fig. 10. For the major SM backgrounds, the muon candidates come from Z/W/ γ^* decays. Therefore, their average transverse momentum is expected to be much lower,

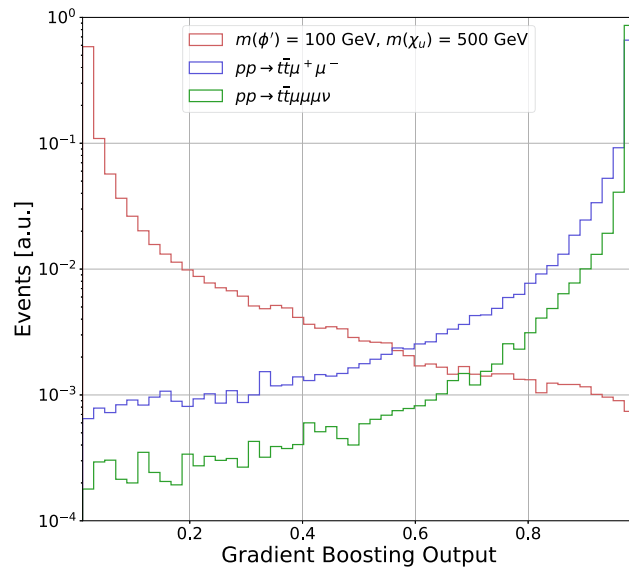


Fig. 11 Output of the gradient boosting algorithm for a benchmark $m(\phi') = 100$ GeV and $m(\chi_u) = 500$ GeV signal, and dominant backgrounds. The distributions are normalized to unity

$\frac{m_{Z/W}}{4} \approx 40 - 45$ GeV. This kinematic feature provides a nice handle to discriminate high $m(\chi_u)$ signal events amongst the large SM backgrounds, which have lower average $p_T(\mu)$ constrained by the SM weak boson masses.

In addition to these aforementioned variables in Figs. 8, 9 and 10, several other kinematic variables were included as inputs to the BDT algorithm. In particular, 27 such variables were used in total, and these included the momenta of b and muon candidates; invariant masses of pairs of muons; angular differences between b jets and between the muons.

As mentioned above, the variables $m(\mu_i, \mu_j)$ for $i, j \neq 1$ provide some additional discrimination between signal and background when the leading muons are not a ϕ' decay candidate. The angular separation variables, such as $\Delta R(\mu_i, \mu_j)$, are designed to be sensitive to lower mass ϕ' , since the low rest mass of those particles means they acquire more boost, and thus smaller angular separation ΔR between the muon candidates. The trained BDT returns the discriminating power of each of its inputs, and the feature importance for each variable is shown in Fig. 13 for a signal benchmark point with $m(\phi') = 325$ GeV and $m(\chi_u) = 2000$ GeV.

Figure 11 shows the distributions for the output of the BDT algorithm, normalized to unity, for the representative signal benchmark point of $m(\phi') = 1$ GeV, $m(\chi_u) = 0.5$ TeV and the two dominant backgrounds. The output of the BDT algorithm is a value between 0 and 1, which quantifies the likelihood that an event is either background-like (BDT output near 1) or signal-like (BDT output near 0). Figure 12 illustrates the true positive rate (TPR), defined as the probability of correctly selecting signal events using the BDT output, plotted against the false positive rate (FPR), defined as the

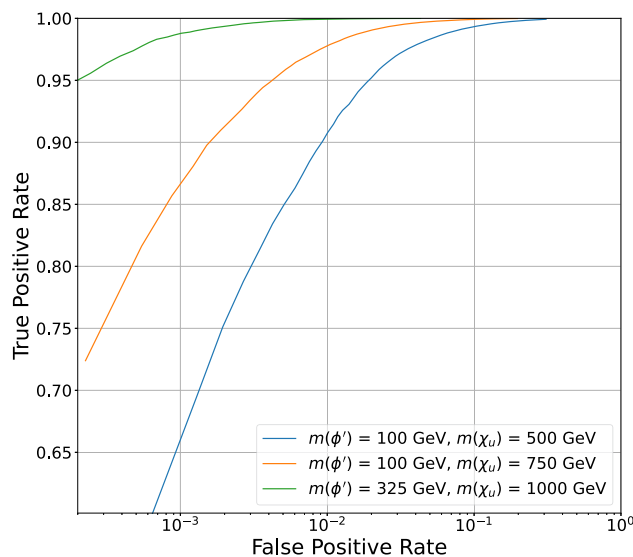


Fig. 12 Receiver operating characteristic curve of the BDT algorithm for three different signal benchmark scenarios

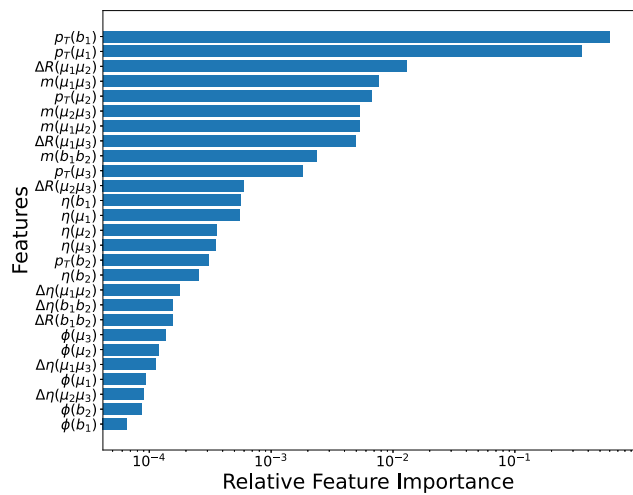


Fig. 13 Relative importance of features in training for a benchmark signal scenario with $m(\phi') = 325 \text{ GeV}$ and $m(\chi_u) = 2000 \text{ GeV}$

probability of incorrectly selecting background events. For example, for $m(\phi') = 100 \text{ GeV}$ and $m(\chi_u) = 500 \text{ GeV}$, when signal events are selected at 65% probability, the background is selected at about 10^{-3} probability. We note that the primary discriminating feature between the signal and background is the boosted b-jet p_T coming from the χ_u vector-like quark. The p_T of said b jet increases with $m(\chi_u)$, peaking at around $[m(\chi_u) - m(W)]/2$. This enhanced boost increases the separation between signal and background, improving the performance of the BDT algorithm as $m(\chi_u)$ increases (Fig. 13).

The outputs from the BDT machine learning algorithm are used to perform a profile-bin likelihood analysis to estimate the signal significance for a luminosity of 3000 fb^{-1} ,

corresponding to the expected amount of collected data by the end of the LHC era. For this purpose, the BDT distributions are normalized to cross section times pre-selection efficiency times luminosity for the different signal models. The significance is then calculated using the expected bin-by-bin yields of the BDT output distribution in a profile likelihood fit, using the ROOTFit [98] package developed by CERN. The expected signal significance Z_{sig} is calculated using the probability of obtaining the same test statistic for the signal plus background and the signal-null hypotheses, defined as the local p -value. Similar to Refs. [99–105], the significance corresponds to the point where the integral of a Gaussian distribution between Z_{sig} and ∞ results in a value equal to the local p -value. The estimation of Z_{sig} incorporates systematic uncertainties. The uncertainty values have been included as nuisance parameters, considering lognormal priors for normalization and Gaussian priors for uncertainties associated with the modeling of the shapes similar to Refs. [106, 107].

The systematic uncertainties that have been included result from experimental and theoretical constraints. A 1–5% systematic uncertainty, depending on the simulated MC sample, has been included to account for the choice of Parton Distribution Function (PDF) set. The systematic uncertainty effect was incorporated following the PDF4LHC [98] recommendations. This systematic uncertainty has a small impact on the expected event yields for signal and background, but it does not affect the shape of the BDT output distribution. We additionally considered theoretical uncertainties related to the absence of higher-order contributions to the signal cross sections, which can change the pre-selection efficiencies and the shapes of kinematic variables used as inputs to the BDT algorithm. This uncertainty was calculated by varying the renormalization and factorization scales by $\times 2$, and studying the resulting change in the bin-by-bin yields of the BDT distributions. They are found to be at most 2% in a given bin.

Regarding experimental uncertainties, following experimental measurements from CMS on the estimation of the integrated luminosity, a conservative 3% effect has been included [108]. A 5% systematic uncertainty associated with the reconstruction and identification of b-quark jets has been included, independent of p_T and η of the b-jet candidates. According to Ref. [93], this uncertainty is correlated between signal and background processes with genuine b-jets and is also correlated across BDT bins for each process. For muons, we include a 2% uncertainty associated with the reconstruction, identification, and isolation requirements, and a 3% systematic uncertainty to account for scale and resolution effects on the momentum and energy measurement. We consider jet energy scale uncertainties ranging from 2–5%, contingent on η and p_T , resulting in shape-based uncertainties on the BDT output distribution. Jet energy scale uncertainties were assumed to range from 1–5%, contingent on η and p_T . These assumptions lead to shape-based uncertainties on the

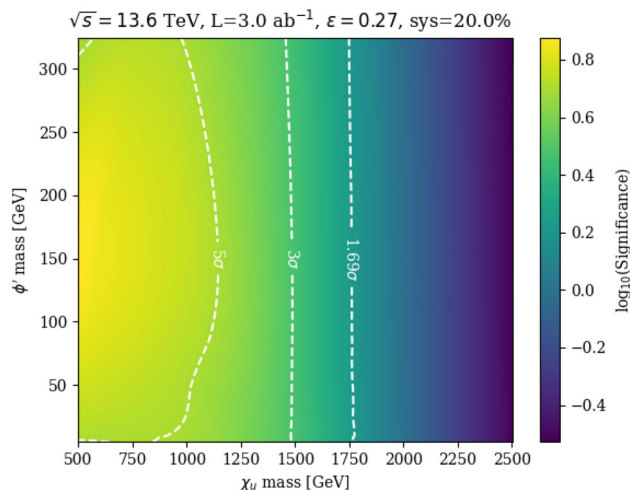


Fig. 14 Signal significance for the high luminosity LHC era, considering with 3000 fb^{-1} of collected data

BDT output distribution, varying from 1–2%. Additionally, we include a 10% systematic uncertainty to account for errors in the signal and background predictions. Considering all the various sources of systematic uncertainties, our conservative estimate yields a total effect of about 20%.

Figure 14 shows the expected signal significance considering an integrated luminosity of 3000 fb^{-1} . The significance is shown as a heat map in a two-dimensional plane for different ϕ' and χ_u masses. The x-axis corresponds to $m(\chi_u)$, the y-axis to $m(\phi')$, and the heat map to $\log_{10}(Z_{\text{sig}})$. The white dashed lines are contours of constant signal significances of 1.69σ , 3σ and 5σ to represent regions of possible exclusion, evidence of new physics, and discovery, respectively. Under these conditions, $\phi'(\chi_u)$ masses ranging from 1 to 325 GeV (500 to 1800 GeV) can be probed. The range for a discovery with 5σ signal significance varies from χ_u masses from $m(\chi_u) = 770$ – 1100 GeV, depending $m(\phi')$. For large $m(\chi_u)$, the significance is almost independent of $m(\phi')$ because the primary discriminating feature—the boosted b -quark originating from ϕ' —is driven predominantly by the large $m(\chi_u)$, with the kinematic impact of $m(\phi')$ being relatively negligible.

7 Discussion

The LHC will continue to run with pp collisions at $\sqrt{s} = 13.6$ TeV for the next decade. Given the increase in the integrated luminosity expected from the high-luminosity program, it is important to consider unexplored new physics phase space that diverges from the conventional assumptions made in many BSM theories, and which could have remained hidden in processes that have not yet been thoroughly examined. It is additionally crucial to explore advanced analysis techniques, in particular the use of artificial intelligence

algorithms, to enhance the probability of detecting these rare corners where production cross sections are lower and discrimination from SM backgrounds is difficult.

In this work, we examine a model based on a $U(1)_{T_R^3}$ extension of the SM, which can address various conceptual and experimental issues with the SM, including the mass hierarchy between generations of fermions, the thermal dark matter abundance, and the muon $g - 2$, $R_{(D)}$, and $R_{(D^*)}$ anomalies. This model contains a light scalar boson ϕ' , with potential masses below the electroweak scale, and TeV-scale vector-like quarks χ_u . We consider the scenario where the scalar ϕ' has family non-universal fermion couplings and $m(\phi') \geq 1$ GeV, as was suggested in Ref. [39], and thus the ϕ' can primarily decay to a pair of muons. Previous works in Refs. [43, 53] considered scenarios motivating a search methodology with a merged diphoton system from $\phi' \rightarrow \gamma\gamma$ decays. The authors of Ref [43], in which $m(\phi') < 1$ GeV, indeed pointed out that if the ϕ' is heavier than about 1 GeV, then decays to $\mu^+\mu^-$ can become the preferable mode for discovery, which is the basis for the work presented in this paper. We further note that the final state topology studied in this paper would represent the most important mode for discovery at $m(\phi') < 2m_t$ where the $\phi' \rightarrow t\bar{t}$ decay is kinematically forbidden.

The main result of this paper is that we have shown that the LHC can probe the visible decays of new bosons with masses below the electroweak scale, down to the GeV-scale, by considering the simultaneous production of heavy QCD-coupled particles, which then decay to the SM particles that contain large momentum values and can be observed in the central regions of the CMS and ATLAS detectors. The boosted system combined with innovative machine learning algorithms allows for the signal extraction above the lower-energy SM background. The LHC search strategy described here can be used to discover the prompt decay of new light particles. An important conclusion from this paper is that the detection prospects for low-mass particles are enhanced when it is kinematically possible to simultaneously access the heavy degrees of freedom which arise in the UV completion of the low-energy model. This specific scenario in which the couplings of the light scalars are generationally dependent, with important coupling values to the top quark, is an ideal example which would be difficult to directly probe at low energy beam experiments.

The proposed data analysis represents a competitive alternative to complement searches already being conducted at the LHC, allowing us to probe ϕ' masses from 1 to 325 GeV, for $m(\chi_u)$ values up to almost 2 TeV, at the HL-LHC. Therefore, we strongly encourage the ATLAS and CMS Collaborations to consider the proposed analysis strategy in future new physics searches.

Acknowledgements The authors would like to thank Prof. Joel Jones-Pérez for fruitful discussions. A.F. and C.R. thank the constant and enduring financial support received for this project from the Faculty of Science at Universidad de Los Andes (Bogotá, Colombia) through the projects INV-2023-178-2999 and INV-2023-175-2957. A.G. and U.Q. acknowledge the funding received from the Physics & Astronomy Department at Vanderbilt University and the US National Science Foundation. This work is supported in part by NSF Award PHY-1945366 and a Vanderbilt Seeding Success Grant.

Data Availability Statement Data will be made available on reasonable request. [Authors' comment: The datasets generated during and/or analysed during the current study are available from the corresponding author on reasonable request.]

Code Availability Statement Code/software will be made available on reasonable request. [Authors' comment: The code/software generated during and/or analysed during the current study is available from the corresponding author on reasonable request.]

Open Access This article is licensed under a Creative Commons Attribution 4.0 International License, which permits use, sharing, adaptation, distribution and reproduction in any medium or format, as long as you give appropriate credit to the original author(s) and the source, provide a link to the Creative Commons licence, and indicate if changes were made. The images or other third party material in this article are included in the article's Creative Commons licence, unless indicated otherwise in a credit line to the material. If material is not included in the article's Creative Commons licence and your intended use is not permitted by statutory regulation or exceeds the permitted use, you will need to obtain permission directly from the copyright holder. To view a copy of this licence, visit <http://creativecommons.org/licenses/by/4.0/>.

Funded by SCOAP³.

References

1. G.W. Bennett et al., Phys. Rev. D **73**, 072003 (2006). <https://doi.org/10.1103/PhysRevD.73.072003>
2. M. Tanabashi et al., Phys. Rev. D **98**, 030001 (2018). <https://doi.org/10.1103/PhysRevD.98.030001>
3. M. Davier, A. Hoecker, B. Malaescu, Z. Zhang, Eur. Phys. J. C **77**(12), 827 (2017). <https://doi.org/10.1140/epjc/s10052-017-5161-6>
4. M. Davier, A. Hoecker, B. Malaescu, Z. Zhang, Eur. Phys. J. C **80**(3), 241 (2020). <https://doi.org/10.1140/epjc/s10052-020-7792-2>
5. T. Blum, P.A. Boyle, V. Gülpers, T. Izubuchi, L. Jin, C. Jung, A. Jüttner, C. Lehner, A. Portelli, J.T. Tsang, Phys. Rev. Lett. **121**, 022003 (2018). <https://doi.org/10.1103/PhysRevLett.121.022003>
6. A. Keshavarzi, D. Nomura, T. Teubner, Phys. Rev. D **97**, 114025 (2018). <https://doi.org/10.1103/PhysRevD.97.114025>
7. T. Blum, N. Christ, M. Hayakawa, T. Izubuchi, L. Jin, C. Jung, C. Lehner, Phys. Rev. Lett. **124**, 132002 (2020). <https://doi.org/10.1103/PhysRevLett.124.132002>
8. F. Campanario, H. Czyż, J. Gluza, T. Jeliński, G. Rodrigo, S. Tracz, D. Zhuridov, Phys. Rev. D **100**, 076004 (2019). <https://doi.org/10.1103/PhysRevD.100.076004>
9. B. Collaboration, Phys. Rev. Lett. **109**, 101802 (2012). <https://doi.org/10.1103/PhysRevLett.109.101802>
10. B. Collaboration, Phys. Rev. D **88**(7), 072012 (2013). <https://doi.org/10.1103/PhysRevD.88.072012>
11. Belle Collaboration, Phys. Rev. D **92**, 072014 (2015). <https://doi.org/10.1103/PhysRevD.92.072014>
12. L. Collaboration, Phys. Rev. Lett. **115**(11), 111803 (2015). <https://doi.org/10.1103/PhysRevLett.115.111803>. [Erratum: Phys. Rev. Lett. **115**, 159901 (2015)]
13. LHCb Collaboration, Phys. Rev. Lett. **115**, 111803 (2015). <https://doi.org/10.1103/PhysRevLett.115.111803>. [Erratum: Phys. Rev. Lett. **115**, 159901 (2015)]
14. Belle Collaboration, Phys. Rev. D **94**, 072007 (2016). <https://doi.org/10.1103/PhysRevD.94.072007>
15. Belle Collaboration, Phys. Rev. Lett. **118**, 211801 (2017). <https://doi.org/10.1103/PhysRevLett.118.211801>
16. LHCb Collaboration, Phys. Rev. Lett. **120**, 171802 (2018). <https://doi.org/10.1103/PhysRevLett.120.171802>
17. Belle Collaboration, Phys. Rev. D **97**, 012004 (2018). <https://doi.org/10.1103/PhysRevD.97.012004>
18. L. Collaboration, Phys. Rev. D **97**(7), 072013 (2018). <https://doi.org/10.1103/PhysRevD.97.072013>
19. Belle Collaboration, (2019). <https://doi.org/10.48550/arXiv.1904.08794>
20. Belle Collaboration, Phys. Rev. Lett. **124**, 161803 (2020). <https://doi.org/10.1103/PhysRevLett.124.161803>
21. L. Collaboration, (2023). <https://doi.org/10.48550/arXiv.2302.02886>
22. S. Navas et al., Phys. Rev. D **110**(3), 030001 (2024). <https://doi.org/10.1103/PhysRevD.110.030001>
23. A.M. Sirunyan et al., JHEP **03**, 170 (2019). [https://doi.org/10.1007/JHEP03\(2019\)170](https://doi.org/10.1007/JHEP03(2019)170)
24. V. Khachatryan et al., Phys. Rev. Lett. **118**(2), 021802 (2017). <https://doi.org/10.1103/PhysRevLett.118.021802>
25. V. Khachatryan et al., JHEP **02**, 048 (2017). [https://doi.org/10.1007/JHEP02\(2017\)048](https://doi.org/10.1007/JHEP02(2017)048)
26. V. Khachatryan et al., JHEP **03**, 077 (2017). [https://doi.org/10.1007/JHEP03\(2017\)077](https://doi.org/10.1007/JHEP03(2017)077)
27. A.M. Sirunyan et al., JHEP **07**, 121 (2017). [https://doi.org/10.1007/JHEP07\(2017\)121](https://doi.org/10.1007/JHEP07(2017)121)
28. V. Khachatryan et al., JHEP **11**, 189 (2015). [https://doi.org/10.1007/JHEP11\(2015\)189](https://doi.org/10.1007/JHEP11(2015)189)
29. J.C. Pati, A. Salam, Phys. Rev. D **10**(1), 275 (1974). <https://doi.org/10.1103/PhysRevD.10.275>
30. R.N. Mohapatra, J.C. Pati, Phys. Rev. D **11**(9), 2558 (1975). <https://doi.org/10.1103/PhysRevD.11.2558>
31. G. Senjanovic, R.N. Mohapatra, Phys. Rev. D **12**(5), 1502 (1975). <https://doi.org/10.1103/PhysRevD.12.1502>
32. L. Di Luzio, J. Fuentes-Martin, A. Greljo, M. Nardecchia, S. Renner, J. High Energy Phys. **2018**(11), 81 (2018). [https://doi.org/10.1007/JHEP11\(2018\)081](https://doi.org/10.1007/JHEP11(2018)081)
33. M.J. Baker, J. Fuentes-Martín, G. Isidori, M. König, Eur. Phys. J. C **79**(4), 334 (2019). <https://doi.org/10.1140/epjc/s10052-019-6853-x>
34. L. Michaels, F. Yu, JHEP **03**, 120 (2021). [https://doi.org/10.1007/JHEP03\(2021\)120](https://doi.org/10.1007/JHEP03(2021)120)
35. P.S.B. Dev, W. Rodejohann, X.J. Xu, Y. Zhang, JHEP **06**, 039 (2021). [https://doi.org/10.1007/JHEP06\(2021\)039](https://doi.org/10.1007/JHEP06(2021)039)
36. A. Flórez, J. Jones-Pérez, A. Gurrola, C. Rodríguez, J. Peñuela-Parra, Eur. Phys. J. C **83**(11), 1023 (2023). <https://doi.org/10.1140/epjc/s10052-023-12177-4>
37. B. Dutta, S. Ghosh, J. Kumar, in *Snowmass 2021* (2022)
38. B. Dutta, S. Ghosh, J. Kumar, Phys. Rev. D **100**(7), 075028 (2019). <https://doi.org/10.1103/PhysRevD.100.075028>
39. B. Dutta, S. Ghosh, J. Kumar, Phys. Rev. D **102**(7), 075041 (2020). <https://doi.org/10.1103/PhysRevD.102.075041>
40. B. Dutta, S. Ghosh, J. Kumar, Phys. Rev. D **102**(1), 015013 (2020). <https://doi.org/10.1103/PhysRevD.102.015013>
41. B. Dutta, S. Ghosh, P. Huang, J. Kumar, Phys. Rev. D **105**(1), 015011 (2022). <https://doi.org/10.1103/PhysRevD.105.015011>

42. V. De Romeri, J. Nava, M. Puerta, A. Vicente, Phys. Rev. D **107**, 095019 (2023). <https://doi.org/10.1103/PhysRevD.107.095019>
43. B. Dutta, S. Ghosh, A. Gurrola, D. Julson, T. Kamon, J. Kumar, J. High Energy Phys. **2023**(3), 164 (2023). [https://doi.org/10.1007/JHEP03\(2023\)164](https://doi.org/10.1007/JHEP03(2023)164)
44. Z. Berezhiani, Phys. Lett. B **129**(1), 99 (1983). [https://doi.org/10.1016/0370-2693\(83\)90737-2](https://doi.org/10.1016/0370-2693(83)90737-2)
45. D. Chang, R.N. Mohapatra, Phys. Rev. Lett. **58**, 1600 (1987). <https://doi.org/10.1103/PhysRevLett.58.1600>
46. A. Davidson, K.C. Wali, Phys. Rev. Lett. **59**, 393 (1987). <https://doi.org/10.1103/PhysRevLett.59.393>
47. S. Rajpoot, Mod. Phys. Lett. A **02**(05), 307 (1987). <https://doi.org/10.1142/S0217732387000422>
48. K.S. Babu, R.N. Mohapatra, Phys. Rev. Lett. **62**, 1079 (1989). <https://doi.org/10.1103/PhysRevLett.62.1079>
49. K.S. Babu, R.N. Mohapatra, Phys. Rev. D **41**, 1286 (1990). <https://doi.org/10.1103/PhysRevD.41.1286>
50. A. Bhardwaj, T. Mandal, S. Mitra, C. Neeraj, Phys. Rev. D (2022). <https://doi.org/10.1103/physrevd.106.095014>
51. A. Bhardwaj, K. Bhide, T. Mandal, S. Mitra, C. Neeraj, Phys. Rev. D (2022). <https://doi.org/10.1103/physrevd.106.075024>
52. J. Bardhan, T. Mandal, S. Mitra, C. Neeraj, Phys. Rev. D (2023). <https://doi.org/10.1103/physrevd.107.115001>
53. S. Banerjee, D. Barducci, G. Bélanger, C. Delaunay, J. High Energy Phys. (2016). [https://doi.org/10.1007/jhep11\(2016\)154](https://doi.org/10.1007/jhep11(2016)154)
54. J.M. Alves, G. Branco, A. Cherchiglia, C. Nishi, J. Penedo, P.M. Pereira, M. Rebelo, J. Silva-Marcos, Phys. Rep. **1057**, 1–69 (2024). <https://doi.org/10.1016/j.physrep.2023.12.004>
55. J.H. Friedman, Ann. Stat. **29**(5), 1189 (2001). <https://doi.org/10.1214/aos/1013203451>. (Publisher: Institute of Mathematical Statistics)
56. X. Ai, S.C. Hsu, K. Li, C.T. Lu, JPCS **2438**(1), 012114 (2023). <https://doi.org/10.1088/1742-6596/2438/1/012114>
57. A. Collaboration, Phys. Rev. D **97**(7), 072016 (2018). <https://doi.org/10.1103/PhysRevD.97.072016>
58. A. Biswas, D. Kumar-Ghosh, N. Ghosh, A. Shaw, A.K. Swain, J. Phys. G **47**(4), 045005 (2020). <https://doi.org/10.1088/1361-6471/ab6948>
59. Y.L. Chung, S.C. Hsu, B. Nachman, JINST **16**, P07002 (2021). <https://doi.org/10.1088/1748-0221/16/07/P07002>
60. J. Feng, M. Li, Q.S. Yan, Y.P. Zeng, H.H. Zhang, Y. Zhang, Z. Zhao, JHEP (2022). [https://doi.org/10.1007/jhep09\(2022\)141](https://doi.org/10.1007/jhep09(2022)141)
61. D. Barbosa, F. Díaz, L. Quintero, A. Flórez, M. Sanchez, A. Gurrola, E. Sheridan, F. Romeo, EPJC (2023). <https://doi.org/10.1140/epjc/s10052-023-11506-x>
62. S. Chigusa, S. Li, Y. Nakai, W. Zhang, Y. Zhang, J. Zheng, Phys. Lett. B **833**, 137301 (2022). <https://doi.org/10.1016/j.physletb.2022.137301>
63. E. Arganda, D.A. Díaz, A.D. Perez, R.M. Sandá Seoane, A. Szynkman, Phys. Rev. D **109**, 055032 (2024). <https://doi.org/10.1103/PhysRevD.109.055032>
64. S. Ajmal, J.T. Gaglione, A. Gurrola, O. Panella, M. Presilla, F. Romeo, H. Sun, S.S. Xue, J. High Energy Phys. (2024). [https://doi.org/10.1007/jhep08\(2024\)176](https://doi.org/10.1007/jhep08(2024)176)
65. B. Dutta, A. Gurrola, K. Hatakeyama, W. Johns, T. Kamon, P. Sheldon, K. Sinha, S. Wu, Z. Wu, Phys. Rev. D (2015). <https://doi.org/10.1103/physrevd.92.095009>
66. C. Collaboration, Review of searches for vector-like quarks, vector-like leptons, and heavy neutral leptons in proton-proton collisions at $\sqrt{s} = 13$ TeV at the CMS experiment (2024)
67. C. Collaboration, Search for production of a single vector-like quark decaying to Th or Tz in the all-hadronic final state in pp collisions at $\sqrt{s} = 13$ TeV (2024)
68. G. Aad et al., Phys. Rev. D **105**(9), 092012 (2022). <https://doi.org/10.1103/PhysRevD.105.092012>
69. G. Aad et al., Phys. Rev. D **109**(11), 112012 (2024). <https://doi.org/10.1103/PhysRevD.109.112012>
70. G. Aad et al., Phys. Lett. B **843**, 138019 (2023). <https://doi.org/10.1016/j.physletb.2023.138019>
71. G. Aad et al., Eur. Phys. J. C **83**(8), 719 (2023). <https://doi.org/10.1140/epjc/s10052-023-11790-7>
72. G. Aad et al., JHEP **08**, 153 (2023). [https://doi.org/10.1007/JHEP08\(2023\)153](https://doi.org/10.1007/JHEP08(2023)153)
73. G. Aad et al., arXiv:2403.09292
74. G. Cacciapaglia, T. Flacke, M. Park, M. Zhang, Phys. Lett. B **798**, 135015 (2019). <https://doi.org/10.1016/j.physletb.2019.135015>
75. A. Alloul, N.D. Christensen, C. Degrande, C. Duhr, B. Fuks, Comput. Phys. Commun. **185**, 2250 (2014). <https://doi.org/10.1016/j.cpc.2014.04.012>
76. C. Degrande, C. Duhr, B. Fuks, D. Grellscheid, O. Mattelaer, T. Reiter, Comput. Phys. Commun. **183**, 1201 (2012). <https://doi.org/10.1016/j.cpc.2012.01.022>
77. J. Alwall, R. Frederix, S. Frixione, V. Hirschi, F. Maltoni, O. Mattelaer, H.S. Shao, T. Stelzer, P. Torrielli, M. Zaro, JHEP **07**, 079 (2014). [https://doi.org/10.1007/JHEP07\(2014\)079](https://doi.org/10.1007/JHEP07(2014)079)
78. J. Alwall, C. Duhr, B. Fuks, O. Mattelaer, D.G. Öztürk, C.H. Shen, Comput. Phys. Commun. **197**, 312 (2015). <https://doi.org/10.1016/j.cpc.2015.08.031>
79. N. Collaboration, JHEP **04**, 040 (2015). [https://doi.org/10.1007/JHEP04\(2015\)040](https://doi.org/10.1007/JHEP04(2015)040)
80. T. Sjöstrand, S. Ask, J.R. Christiansen, R. Corke, N. Desai, P. Ilten, S. Mrenna, S. Prestel, C.O. Rasmussen, P.Z. Skands, Comput. Phys. Commun. **191**, 159 (2015). <https://doi.org/10.1016/j.cpc.2015.01.024>
81. D. Collaboration, JHEP **02**, 057 (2014). [https://doi.org/10.1007/JHEP02\(2014\)057](https://doi.org/10.1007/JHEP02(2014)057)
82. A.C. Canbay, O. Cakir, Phys. Rev. D **108**, 095006 (2023). <https://doi.org/10.1103/PhysRevD.108.095006>
83. G. Cacciapaglia, A. Deandrea, S. Vatani, Phys. Rev. D (2023). <https://doi.org/10.1103/physrevd.108.016010>
84. G. Blankenburg, G. Isidori, J. Jones-Perez, Eur. Phys. J. C **72**, 2126 (2012). <https://doi.org/10.1140/epjc/s10052-012-2126-7>
85. J. Jones-Perez, J. Phys. Conf. Ser. **447**, 012060 (2013). <https://doi.org/10.1088/1742-6596/447/1/012060>
86. L. Calibbi, J. Jones-Perez, A. Masiero, J.h. Park, W. Porod, O. Vives, PoS EPS-HEP2009, 167 (2009). <https://doi.org/10.22323/1.084.0167>
87. M. Cacciari, G.P. Salam, G. Soyez, J. High Energy Phys. **2008**(04), 063 (2008). <https://doi.org/10.1088/1126-6708/2008/04/063>
88. M. Cacciari, G.P. Salam, G. Soyez, Eur. Phys. J. C (2012). <https://doi.org/10.1140/epjc/s10052-012-1896-2>
89. Study of the discovery reach in searches for supersymmetry at CMS with 3000/fb. Geneva (2013). <https://cds.cern.ch/record/1607141>. CMS-PAS-FTR-13-014
90. A. Sirunyan et al., JINST **15**(02), P02027 (2020). <https://doi.org/10.1088/1748-0221/15/02/P02027>
91. A.M. Sirunyan et al., JINST **15**(06), P06005 (2020). <https://doi.org/10.1088/1748-0221/15/06/P06005>
92. M. Aaboud et al., Eur. Phys. J. C **79**(5), 375 (2019). <https://doi.org/10.1140/epjc/s10052-019-6847-8>
93. A. Sirunyan et al., JINST **13**, P05011 (2018). <https://doi.org/10.1088/1748-0221/13/05/P05011>
94. E. Bols, J. Kieseler, M. Verzetti, M. Stoye, A. Stakia, J. Instrum. **15**(12), P12012 (2020). <https://doi.org/10.1088/1748-0221/15/12/P12012>
95. E. Conte, B. Fuks, G. Serret, Comput. Phys. Commun. **184**(1), 222 (2013). <https://doi.org/10.1016/j.cpc.2012.09.009>
96. A. Paszke et al., Pytorch: an imperative style, high-performance deep learning library. (2019)
97. T. Chen, C. Guestrin, in *Proceedings of the 22nd ACM SIGKDD International Conference on Knowledge Discovery and Data*

- Mining (Association for Computing Machinery, New York, 2016), KDD '16, pp. 785–794. <https://doi.org/10.1145/2939672.2939785>
98. J. Butterworth, S. Carrazza, A. Cooper-Sarkar, A. De Roeck, J. Feltesse, S. Forte, J. Gao, S. Glazov, J. Huston, Z. Kassabov, R. McNulty, A. Morsch, P. Nadolsky, V. Radescu, J. Rojo, R. Thorne, *J. Phys. G* **43**, 023001 (2016). <https://doi.org/10.1088/0954-3899/43/2/023001>
99. A. Flórez, A. Gurrola, W. Johns, P. Sheldon, E. Sheridan, K. Sinha, B. Soubasis, *Phys. Rev. D* **103**(9), 095001 (2021). <https://doi.org/10.1103/PhysRevD.103.095001>
100. A. Flórez, A. Gurrola, W. Johns, J. Maruri, P. Sheldon, K. Sinha, S.R. Starko, *Phys. Rev. D* **100**(1), 016017 (2019). <https://doi.org/10.1103/PhysRevD.100.016017>
101. A. Flórez, Y. Guo, A. Gurrola, W. Johns, O. Ray, P. Sheldon, S. Starko, *Phys. Rev. D* **99**(3), 035034 (2019). <https://doi.org/10.1103/PhysRevD.99.035034>
102. A. Flórez, K. Gui, A. Gurrola, C. Patiño, D. Restrepo, *Phys. Lett. B* **778**, 94 (2018). <https://doi.org/10.1016/j.physletb.2018.01.009>
103. A. Florez, A. Gurrola, W. Johns, Y. Do Oh, P. Shendon, D. Teague, T. Weiler, *Phys. Lett. B* **767**, 126 (2017). <https://doi.org/10.1016/j.physletb.2017.01.062>
104. A. Flórez, L. Bravo, A. Gurrola, C. Ávila, M. Segura, P. Sheldon, W. Johns, *Phys. Rev. D* **94**(7), 073007 (2016). <https://doi.org/10.1103/PhysRevD.94.073007>
105. R. Leonardi, O. Panella, F. Romeo, A. Gurrola, H. Sun, S.S. Xue, *Eur. Phys. J. C* (2020). <https://doi.org/10.1140/epjc/s10052-020-7822-0>
106. C. Natalia, F. Andrés, G. Alfredo, J. Will, S. Paul, T. Cheng, Long-term LHC discovery reach for compressed higgsino-like models using VBF processes. (2021)
107. A. Flórez, A. Gurrola, W. Johns, P. Sheldon, E. Sheridan, K. Sinha, B. Soubasis, *Phys. Rev. D* **103**, 095001 (2021). <https://doi.org/10.1103/PhysRevD.103.095001>
108. P. Lujan et al., The Pixel Luminosity Telescope: a detector for luminosity measurement at CMS using silicon pixel sensors. *Tech. Rep. CMS-DN-21-008* (2022). Accepted by *Eur. Phys. J. C*